UNIVERSITÀ DEGLI STUDI DI PALERMO
DEPARTMENT OF ENGINEERING

PHD PROGRAMME IN INFORMATION AND COMMUNICATION TECHNOLOGIES (ICT)
XXXVIII CYCLE

DOCTORAL THESIS

Exploring Complex System Behaviors via Information-Theoretic Measures: Applications to Physiological Dynamics and Machine Learning

---

Author:
Chiara BARÀ

Supervisor:
Prof. Luca FAES

Co-Supervisor:
Dr. Riccardo PERNICE

A thesis submitted in the fulfillment of the requirements for the degree of Doctor of Philosophy

in the

Biosignals and Information Theory Laboratory (BIT Lab)

ACADEMIC YEAR 2024-2025

Abstract

Recent advances in data-driven modeling of complex systems have identified information-theoretic metrics as powerful tools for extracting meaningful insights by exploiting the stochastic nature of investigated phenomena. In this perspective, these metrics have been widely applied to the study of intertwined physiological dynamics within the framework of network physiology. Nevertheless, the literature still presents a fragmented characterization of the several aspects that should be taken into account when applying these metrics, that are related to both theoretical foundations and practical computation, which in turn affect their meaningful interpretation in the context of neuroscience and physiology.

This thesis provides a comprehensive investigation of established information-theoretic measures designed for the analysis of the individual components of a complex system and their pairwise interactions, as well as more recent approaches aimed at capturing emergent behaviors arising from the interaction of multiple components. Particular emphasis is given to the challenges associated with the practical computation of these metrics, highlighting how the choice of an appropriate estimation strategy should account for data characteristics – such as nonlinearity, nonstationary, and dimensionality – as well as for the desired trade-offs between feasibility, robustness, and computational cost.

The effectiveness of these approaches in enabling a hierarchical evaluation of interactions in complex systems is first demonstrated on simulation studies and then illustrated on different applications in the fields of network physiology and machine learning. In the former domain, the use of metrics quantifying the complexity of individual physiological systems, along with pairwise measures of coupling and causality, and high-order measures of redundant and synergistic interactions, reveals the intrinsically intricate nature of healthy physiological dynamics. More-

over, the combined use of estimation approaches capable of capturing both linear and nonlinear dynamics enables a more comprehensive characterization of well-established regulatory mechanisms, such as those governing cardiovascular and cardiorespiratory interactions among heart rate, arterial pressure, and respiratory activity, as well as less explored parameters, such as arterial compliance. In the context of machine learning, the adoption of information-theoretic measures capturing high-order feature interactions is shown to improve learning models performance through advanced feature selection and importance strategies. Applications to physiological feature sets further highlight the enhanced interpretability achieved by integrating these metrics into machine learning frameworks.

Overall, the findings of this thesis demonstrate the effectiveness of information theory in providing a unified analytical framework for the study of network systems, enabling a stratified characterization and a comprehensive understanding of the underlying complex behaviors.

Contents

Abstract i

Contents iii

List of abbreviations vii

I Preface 1

1 Introduction 2

1.1 Overview . . . 2
1.2 Problem statement and aim of the thesis . . . 5
1.3 Structure of the thesis . . . 7

2 Fundamentals of Information Theory 12

2.1 Concepts of probability and Shannon information content . . . 13
2.2 Grounding measures of information theory . . . 13
2.3 Estimation methods . . . 16
2.3.1 Linear parametric approach . . . 16
2.3.2 Nearest-neighbor approach . . . 17
2.3.3 Binning approach . . . 20
2.3.4 Permutation approach . . . 22
2.3.5 Other estimation approaches . . . 22
2.4 Estimation matters . . . 23
2.5 Overview and conclusions of chapter 2 . . . 25

II Estimating complex system behaviors through information-theoretic approaches 27

3 Analysis of individual node dynamics 28

3.1 Conditional entropy as a measure of complexity 28
3.1.1 Entropy rate estimation approaches 30
3.1.2 Validation on stationary autoregressive and mixed nonlinear deterministic/linear stochastic dynamics processes 35
3.2 Local estimation of conditional entropy and information storage . . . 40
3.2.1 Local information storage estimation approaches 42
3.2.2 Validation on time-varying stochastic autoregressive and noisy deterministic processes 44
3.3 Overview and conclusions of chapter 3 48

4 Pairwise analysis of link dynamics 53
4.1 Mutual Information Rate and its decomposition terms 53
4.1.1 Mutual information rate estimation strategies 56
4.1.2 Validation on bivariate autoregressive and chaotic processes . 59
4.2 Predictive Information framework 65
4.2.1 Predictive information estimation strategies 67
4.3 Multivariate analysis of pairwise link dynamics 70
4.3.1 Conditional transfer estimation strategies 71
4.4 Overview and conclusions of chapter 4 72

5 High-order investigation of group dynamics 76
5.1 Overview on multivariate analytical frameworks 76
5.2 Partial Information Decomposition 78
5.2.1 Redundancy measures 81
5.2.2 Estimation strategies 83
5.2.3 Validation on boolean logic gates 87
5.3 Overview and conclusions of chapter 5 91

III Applications on physiological data 95

6 Physiological and methodological grounds 96
6.1 Overview of the investigated physiological control mechanisms . . . 96
6.1.1 Cardiovascular and cardiorespiratory dynamics 97
6.1.2 Brain-heart interaction 99
6.2 Extracting time series from physiological signals 100
6.3 Explored databases 103
6.4 Overview and conclusions of chapter 6 110

7 Univariate analysis of physiological signals 112
7.1 Cardiac and breathing dynamics complexity during spontaneous and controlled breathing 112

7.2 Ultra-short term analysis of cardiac and vascular dynamics complexity during postural and mental stress . . . 114
7.3 Case report: respiratory dynamics during sleep apneas through local predictability measures . . . 118
7.4 Local predictability analysis of heartbeat-evoked cortical responses . 120
7.5 Overview and conclusions of chapter 7 . . . 124

8 Pairwise analysis of physiological dynamics 128
8.1 Mutual Information Rate decomposition in cardiorespiratory and cardiovascular systems . . . 128
8.2 Testing coupling and nonlinearities in cardiovascular dynamics during postural stress . . . 133
8.3 Comparison of linear and nonlinear directional coupling measures in cardiovascular and cardiorespiratory interactions . . . 137
8.4 Analysis of cardiorespiratory interactions in heart failure patients . . 138
8.5 Cardiovascular dynamic networks uncovered through direct causality measures . . . 144
8.6 Overview and conclusions of chapter 8 . . . 149

9 High-order analysis of physiological networks 155
9.1 Application of different redundancy measures on arterial pressure signals . . . 155
9.2 Exploring high-order dynamics between ventilatory activity phases and cardiovascular dynamics . . . 158
9.3 Investigating modes of interactions within cardiorespiratory systems with physiological stressors . . . 159
9.4 Overview and conclusions of chapter 9 . . . 164

IV Applications to machine learning 168

10 Information-theoretic foundations of machine learning 169
10.1 Machine learning paradigms and feature representation . . . 169
10.2 Probability and information-theoretic foundations of machine learning 171
10.3 Applications of information-theoretic measures in machine learning . 172
10.4 Overview and conclusions of chapter 10 . . . 173

11 Feature analysis strategies based on conditional Mutual Information measures and Partial Information Decomposition framework 175
11.1 Information-theoretic approaches for feature analysis . . . 176
11.2 Introduction to a novel feature selection strategy . . . 178
11.2.1 Description of the feature selection algorithm . . . 178
11.2.2 Estimation strategy . . . 178

11.2.3 Validation on a set of known relevant and irrelevant features . 179
11.3 Introduction to a novel feature importance strategy 181
11.3.1 Description of the feature importance algorithm 181
11.3.2 Estimation strategies 183
11.3.3 Validation on Gaussian and non-Gaussian simulated features 185
11.4 A machine learning approach based on the Partial Information Decomposition framework 189
11.4.1 state Partial Information Decomposition framework and estimation strategy 190
11.4.2 Validation on multiple features system 191
11.5 Overview and conclusions of chapter 11 193

12 Application of information-theoretic machine learning strategies to physiological data 196
12.1 Conditional Mutual Information-based feature selection for sex differences characterization 196
12.2 Feature importance assessment in cardiovascular variability data for physiological stress classification 198
12.3 Feature importance assessment in gene expression measurements for breast cancer detection 200
12.4 state Partial Information Decomposition application on cortical data 202
12.5 Overview and conclusions of chapter 12 206

V Conclusions 208

13 Concluding remarks and future directions 209
13.1 Opportunities and challenges in estimating complex system behavior using information-theoretic measures 209
13.2 Information-theoretic insights into physiological dynamics 211
13.3 Enhancing machine learning interpretability via information-theoretic methods 213
13.4 Future directions 213

Appendix: Surrogate data analysis 216

Bibliography 220

Scientific curriculum 256

List of publications 257

Acknowledgements 266

List of abbreviations

2AR	bivariate Autoregressive
ABP	Arterial Blood Pressure
AC	Arterial Compliance
ACC	Anterior Cingulate Cortex
AIC	Akaike Information Criterion
AMI	Acute Myocardial Infarction
ANS	Autonomic Nervous System
AR	Autoregressive
ARX	Auto- and Cross- regressive
B	Bankssts
BIC	Bayesian Information Criterion
bpm	beats per minute
BPV	Blood Pressure Variability
Breath	Respiratory signal
C	Central
CaCg	Caudal Lanterior Cingulate
CAN	Central Autonomic Network
CB	Controlled Breathing
CCE	Corrected Conditional Entropy
CE	Conditional Entropy
CFA	Cardiac Field Artifact
CMF	Caudal Middle Frontal
CMI	Conditional Mutual Information
CMINN	Conditional Mutual Information with Nearest Neighbors

CO	Cardiac Output
CrossEn	Cross-Entropy
CRPS	Cardio-Respiratory Phase Synchronization
CRT	Cardiac Resynchronization Therapy
cSE	conditional Self-Entropy
CTE	Conditional Transfer Entropy
Cu	Cuneus
CV	Coefficient Variation
DAN	Dorsal Attention Network
DAP	Diastolic Arterial Pressure
DK	Desikan-Killany atlas
DMN	Default Mode Network
EC	Eyes Closed
ECG	Electrocardiographic signal
EEG	Electroencephalographic signal
En	Enterhinal
EO	Eyes Open
ER	Entropy Rate
exp	Expiration
F	Frontal
FDR	False Discovery Rate
FE	Feature Extraction
FEF	Frontal Eyes Field
fHf	Peak frequency within the High Frequency band
FI	Feature Importance
Fpol	Frontal Pol
FS	Feature Selection
Fu	Fusiform
FWR	Feature-Wise Redundancy
FWS	Feature-Wise Synergy
GMM	Gaussian Mixture Model
H	Entropy
HEP	Heartbeat-Evoked Potential
HF	High Frequency band

HFn	High Frequency normalized power
HFSin	Heart Failure patients with Sinus rhythm
HFVES	Heart Failure patients with Extrasystole
Hi-Fi	High-order effects in Feature Importance
HOBs	High-Order Behaviors
HOIs	High-Order Interactions
HOMs	High-Order Mechanisms
HP	Heart Period
HR	Heart Rate
HRV	Heart Rate Variability
HUT	Head-Up Tilt
IAAFT	Iterative Amplitude Adjusted Fourier Transforms
IC	Instantaneous Causality
ICA	Independent Component Analysis
ICG	Impedance Cardiography signal
ICNS	Intrinsic Cardiac Nervous System
IG	Information Gain
II	Interaction Information
Ins	Insula
insp	Inspiration
IP	Inferior Parietal
IS	Information Storage
IstCg	Isthmus Cingulate
IT	Inferior Temporal
ITL	Information Theoretic Learning
kCMI-FS	k-nearest neighbor Conditional Mutual Information method for Feature Selection
KL	Kullback-Leibler
knn	k-nearest neighbor
KS	Kolmogorov-Sinai
KSG	Kraskov-Stögbauer-Grassberger
L	Lateral
LF	Low Frequency band
LFn	Low Frequency normalized power
Lg	Lingual
lin	linear

LO	Lateral Occipital
LOCO	Leave-One-Covariate-Out
LOrF	Lateral Orbitofrontal
LVET	Left Ventricular Ejection Time
M	Mental Arithmetic
MA	Mental Arithmetic
MAP	Mean Arterial Pressure
MB	Model-Based
MC	Monte Carlo
MDL	Minimum Description Length
MEAN	Mean
MF	Model-Free
MI	Mutual Information
MIR	Mutual Information Rate
ML	Machine Learning
MMI-PID	Minimal Mutual Information PID
MODWT	Maximal Overlap Discrete Wavelet Transform method
MOrF	Medial Orbitofrontal
mRMR	minimum Redundancy Maximum Relevance
MT	Middle Temporal
NTS	Nucleus Tractus Solitarii
O	Occipital
OI	O-Information
OIR	O-Information Rate
OLS	Ordinary Least-Squares
Op	Pars Opercularis
Or	Pars Orbitalis
P	Parietal
PaC	Para Central
PaH	Para Hippocampal
PerCa	Pericalcarin
PF	Prefrontal
PI	Partial Information
PID	Partial Information Decomposition

PIRD	Partial Information Rate Decomposition
pNN50	percentage of successive interbeats intervals differencing more than 50 ms
PoC	Post Central
PoCg	Posterior Cingulate
PP	Pulse Pressure intervals
PreC	Pre Central
PreCu	Pre Cuneus
PrI	Predictive Information
PVR	Peripheral Vascular Resistance
PWV	Pulse Wave Velocity
R	Resting state
RCGA-BRCA	The Cancer Genome Atlas - Breast Invasive Carcinoma
RESP	Respiration
REST	Resting state
RMSSD	Root Mean Square of Successive Differences
RoACg	Rostral Anterior Cingulate
RoMF	Rostral Middle Frontal
RR	Interbeat intervals
RSA	Respiratory Sinus Arrhythmia
SAP	Systolic Arterial Pressure
SB	Spontaneous Breathing
SE	Self-Entropy
SF	Superior Frontal
SM	Supra Marginal
SP	Superior Parietal
sPID	state-PID
SS	State-Space
SSSBL	Spectral Structured Sparse Bayesian Learning
ST	Short-Term
STD	Standard Deviation
SupT	Superior Temporal
SV	Stroke Volume
SVB	Symphato-Vagal Balance
T	Head-Up Tilt

TE	Transfer Entropy
TP	Total Power
Tpol	Temporal Pole
Tr	Pars Triangularis
TrT	Transverse Temporal
TV	Time-Varying
UST	Ultra-Short-Term
VAR	Variance
VLF	Very Low Frequency band
vmPFC	ventro-medial Prefrontal Cortex
VN	Visual Network
WMS	Whole-Minus-Sum
X	Cross-Regressive
XAI	Explainable Artificial Intelligence
YW	Yule-Walker

Part I

Preface

Chapter 1

Introduction

1.1. Overview

Complex systems are representative of most real-world physical and social dynamics, ranging from those characterizing climatic and physiological systems to the evolutionary and financial ones (Boccaletti et al. (2006); Lizier (2012a); Siegenfeld and Bar-Yam (2020); Ivanov (2021)). These are generally referred to as nonlinear systems involving interactions of multiple interdependent parts (Goldberger (2006); Foote (2007); Ladyman et al. (2013)), exhibiting self-organized behavior (Arshinov and Fuchs (2003)), self-similarity across multiple scales (Cannon (1984)), and emergent dynamics in response to small variations of single parts within the whole system (Arshinov and Fuchs (2003); Ladyman et al. (2013); Mihailović et al. (2015)).

With a large number of control mechanisms operating simultaneously to maintain the homeostatic balance, the *human organism* represents a perfect example of complex system (Kaplan and Glass (2012); Goldberger (2006)). The combined effects of multiple coupling and feedback interactions among physiological subsystems or organs give rise to time-varying nonlinear dynamics characterized by high variability and long-term self-similarity (Glass (2001); Goldberger et al. (2002); Valente et al. (2018)). Reflecting the ability of physiological mechanisms to preserve a balanced state in response to external stimuli or intrinsic physiological perturbations (Lehrer and Eddie (2013); Shaffer et al. (2014)), *physiological complexity* typically varies when specific tasks are performed, leading to the dominance of particular regulatory mechanisms, or when cooperation among physiological systems is reduced due to pathological states (Javorka et al. (2008); Pincus (1994)).

In recent years, these concepts have converged in the emerging field of *Network Physiology* (Bashan et al. (2012); Ivanov and Bartsch (2014)). Within this field, the hu-

man organism can be modeled as a dynamic network in which nodes – representing organ systems – and the links – representing the functional dependencies between systems – continuously reorganize across different physiological states. Accordingly, the collective behavior of the global network cannot be reduced to the simple combination of the actions of its components, as it is strongly influenced by the interactions among its multiple parts (Ivanov (2021)). Alterations occurring within specific organ systems or involving individual regulatory mechanisms may lead to global modifications in network interactions, which in certain conditions may result in a cascade of system failures and the emergence of pathological events (Deitch (1992); Buchman (2006)). From this perspective, the dynamics of the complex human organism cannot be fully understood by examining only the self-dynamics of individual nodes or the pairwise interactions between them. Instead, it is necessary to investigate interdependencies involving more than two organs or physiological systems in order to account for the so-called *high-order interactions*. In order to quantitatively characterize such complex hierarchically-organized interactions, suitable mathematical frameworks capable of capturing the stochastic and multiscale nature of physiological dynamics are required.

Complex systems are rarely completely deterministic or purely chaotic (Foote (2007)), making stochastic representations of their dynamics a valuable tool for their analysis. In this context, the mathematical framework of *information theory* is widely employed to exploit the statistical properties of the data generated by a system in order to investigate its dynamical behavior. Originally introduced by Claude Shannon in 1948 to optimize communication systems by focusing on the fundamental aspects of information transmission and processing, information theory provides a principled way to quantify the information carried by a signal in terms of its randomness and uncertainty (Shannon (1948)). In a network system, information-theoretic measures can be used to analyze the dynamics of individual subsystems by evaluating the predictability of a single node (Cover (1999)). Furthermore, these measures can be employed to describe pairwise dynamics in terms of coupling and causal relations between two nodes. In particular, non-directional coupling relations capture associations that do not specify the direction of influence, reflecting symmetrical statistical dependencies between components. In contrast, causality measures are essential for identifying driver-response relations, as they focus on time-lagged interactions under the principle that causes precede their effects (Schreiber (2000); Sparacino et al. (2026)). In addition, when considering the dynamics of more than two subsystems in a groupwise fashion, information-theoretic measures can be used to quantify synergistic and redundant interactions arising from the cooperation among multiple subsystems or from overlapping contributions across them, which cannot be detected when these are considered separately (Rosas et al. (2018); Faes et al. (2025)).

The acquisition of physiological signals from multiple body districts enable the extraction of synchronous time series representing their dynamical activity, to which information-theoretic metrics can be applied to gain insights into complex physiological dynamic. As an illustrative example, Fig. 1.1 depicts *physiological signals* synchronously acquired from brain, heart, vasculature, and lung, observed as nodes of a physiological network. From these organs, physiological signals of different nature can be acquired, ranging from electrical signals representative of the neural and cardiac dynamics – such as the fast and highly irregular electroencephalographic (EEG) signal and the more regular electrocardiographic (ECG) signal – to mechanical signals representative of vascular and respiratory activities – such as the arterial blood pressure (ABP) waveform and the slower respiratory volume signal (Breath). To investigate individual, pairwise and high-order dynamics within the analyzed network of physiological systems, acquired signals must be processed to extract *physiological time series* characterized by a comparable time scale, selected according to the physiological phenomena of interest. For instance, from the aforementioned signals it is possible to derive time series representing interbeat interval duration (RR), systolic and diastolic arterial pressure amplitudes (SAP and DAP), or breath amplitude, as well as time series describing spectral dynamic characteristics of neural activity. The quantitative features obtained from these signals – often

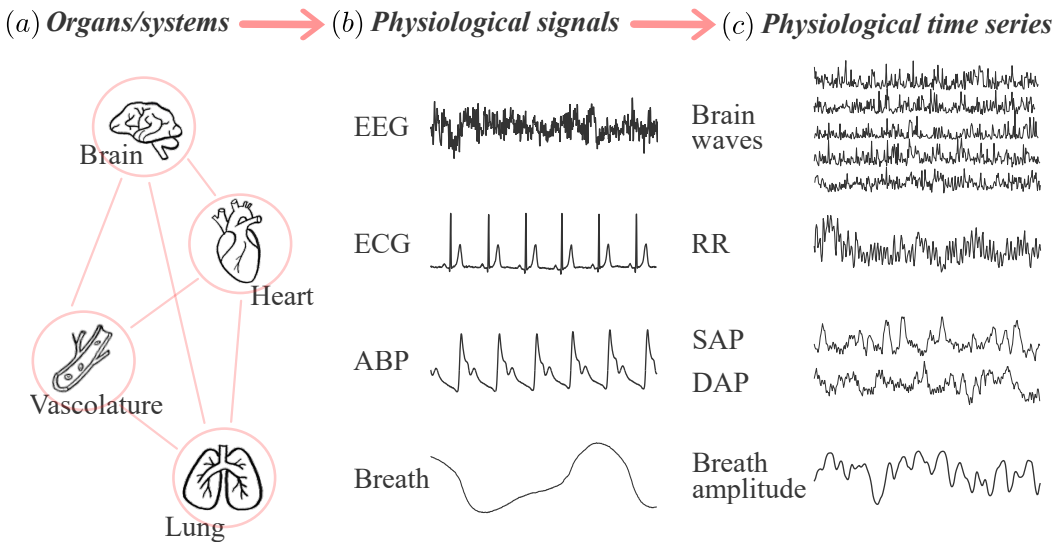

Figure 1.1: Network representation of interactions among multiple organ systems (panel (*a*)), i.e., brain, heart, circulatory system, and lung, investigated through recorded physiological signals (panel (*b*)), i.e., electroencephalogram (EEG), electrocardiogram (ECG), arterial blood pressure (ABP), and respiratory volume (Breath), respectively. Generally, for each of these signals, time series representative of the dynamical activity of the physiological systems are extracted (panel (*c*)), e.g., brain dynamic characteristics for the EEG, interbeat intervals (RR) for the ECG, systolic (SAP) and diastolic (DAP) arterial pressure for the ABP, and breath amplitude for Breath.

computed through information-theoretic metrics – can then be used to characterize physiological states and their underlying regulatory mechanisms.

In the perspective of multivariate data analysis, information-theoretic measures also play an important role in the field of *machine learning* (ML). Beyond their traditional use within statistical learning frameworks (Amigó et al. (2015); Sepúlveda-Fontaine and Amigó (2024)), recent studies have highlighted their effectiveness in addressing contemporary challenges in ML applications. The development and understanding of complex ML models require computationally efficient resources, optimized training strategies, and robust performance metrics – requirements that can be effectively supported by the information-theoretic framework (Vergara and Estévez (2014); Wollstadt et al. (2023)). In this perspective, the pairwise and high-order measures previously mentioned for the analysis of physiological time series can also be leveraged to investigate interactions between features and class variables. Accordingly, their use in ML approaches – ranging from feature selection and feature importance analysis to classification tasks – can enhance the interpretability of ML models when characterizing and distinguishing different physio-pathological states (Dastgoshadeh and Rabiei (2023); Parbat and Chakraborty (2024); Iovino et al. (2024b)).

1.2. Problem statement and aim of the thesis

Estimating information-theoretic measures from time series representing physiological dynamics is a challenging task. An important aspect concerning the computation of the measures within the information-theoretic framework is the assumption of data stationarity, whereby the statistical properties of the data remain constant over the time interval on which the measures are evaluated (Wibral et al. (2014b)). However, physiological data are often characterized by *nonstationary* behaviors due to the presence of trends and local changes. These may arise from disturbances in the acquisition environment (e.g., electromagnetic field, power supply, electrode motion) (Allen et al. (2000); Tatum et al. (2011)), from the cross-influences among physiological activities (e.g., slow fluctuation in ECG due to ventilatory movement, blinking or cardiac field in EEG traces) (Clifford et al. (2006); Mannan et al. (2018)), as well as to abrupt signal variations related to physiological phenomena such as arrhythmic beats, respiratory apnea, or epileptic events. Additionally, transient changes may occur in response to task execution or pathological conditions (Peng et al. (1995); Ivanov (2003)). Another important aspect concerns the strongly *nonlinear* nature of physiological signals. The activity of organs and physiological systems is governed by multiple regulatory mechanisms interacting across different scales, leading to complex nonlinear dynamics that complicate the application of simple modeling approaches and the reliable estimation of statistical dependencies (Glass

(2001); Goldberger et al. (2002)). Moreover, analyses must account for the limitation of working with *finite-size* data. Physiological recordings are often restricted to relatively short time windows due to experimental protocol constraints, acquisition device limitations, and the difficulty of collecting long artifact-free signals. While shorter recordings may facilitate the identification of stationary segments, limited data length can hinder the analysis of high-dimensional systems or long-range dynamical interactions (Xiong et al. (2017); Faes et al. (2019b)).

Within this framework, the objective of this thesis is to exploit the potential of information-theoretic approaches to disentangle the complex functioning of physiological systems explicitly addressing the challenges posed by nonstationarity, nonlinearity, and limited data length. By carefully accounting for these factors, the thesis aims to improve the reliability and interpretability of entropy-based analyses applied to physiological data. The ultimate goal is to enhance the understanding of complex physiological dynamics and to identify informative indices capable of characterizing and discriminating physio-pathological conditions, thereby contributing to both medical research and clinical practice.

To this end, a comprehensive analysis of well-established information-theoretic measures (Cover (1999); Lizier (2012a); Faes et al. (2015a,c)) and sophisticated information decomposition strategies (Williams and Beer (2010)) is presented, thus providing a systematic exploration on methodologies whose treatment is often fragmented across the literature and restricted to specific theoretical or computational aspects. The thesis considers a wide spectrum of information-theoretic measures to characterize physiological dynamics at different organizational levels, from individual subsystems (*univariate analysis*) and pairwise interactions between physiological processes (*bivariate analysis*) to high-order interactions among groups of physiological processes (*multivariate analysis*), reflecting the hierarchical organization of the human organism. Furthermore, both static and dynamic representations of physiological networks are investigated. While *static analyses* describe the system disregarding the temporal correlations within and between network subsystems and models the system through random variables, *dynamic analyses* explicitly account for temporal dependencies within and between the random processes that represent the dynamics of the subsystems. Particular attention is devoted to the choice of the most appropriate *estimation method*, which depends on the characteristics of the available data, the underlying physiological phenomena, and the specific physiological insights of interest. Both simplified approaches based on linear modeling or discretized representations of continuous physiological dynamics and more advanced methods that preserve a continuous and detailed description of the data are employed to investigate physiological networks in a hierarchical and complementary manner. In this context, the main outcomes of the research activity conducted during my doctoral studies – reported in Barà et al. (2023b), Barà et al. (2023c), Barà

et al. (2024c), and Barà et al. (2025a) – are presented and discussed.

1.3. Structure of the thesis

This thesis is organized into five main sections. In *Part I - Preface*, comprising two chapters, the main objectives of the thesis are presented, providing an overview of both the analytical framework employed – information theory – and the application domain – computational physiology. *Part II - Estimating complex system behaviors through information-theoretic approaches*, structured in three chapters, presents the mathematical formulation of information-theoretic measures used to evaluate complex dynamics at multiple levels: from single-node properties to pairwise interactions and, ultimately, groupwise behaviors. Particular emphasis is given on the different estimation strategies that can be used for the practical computation of these measures from finite-length data. *Part III - Application on physiological data* reports a chapter presenting an overview of relevant physiological foundations and three chapters of illustrative examples applying the information-theoretic tool detailed in the previous part to physiological time series. *Part IV - Application to machine learning* presents three chapters focused on the integration of information-theoretic analyses with machine learning approaches to predict physiological states. Finally, *Part V - Remarks and final conclusions* summarizes the main findings of the thesis, highlights the broader implications of the results, and outlines potential directions for future research.

A more detailed description of each chapter is outlined in the follow.

Part I - Preface

Chapter 1 - Introduction is the current chapter. It provides an overview of the context in which the thesis is set, namely the study of the human organism as a complex network system. Particular emphasis is placed on the advantages pertaining to the employment of tools within the information-theoretic framework of analysis. These account for both the hierarchical evaluation of physiological dynamics involving individual organ/systems and the organism as a whole, as well as for the development of sophisticated machine learning techniques that allow for the classification of physio-pathological states. In this context, the goal of the thesis is defined: to provide a comprehensive analytical framework that integrates well-established and more recently developed information-theoretic measures, together with multiple computational approaches for their estimation, to gain insights into complex physiological mechanisms and dynamics that characterize the human organism's functioning, with the aim of contributing to medical research and clinical practice.

Chapter 2 - Fundamentals of Information Theory is concerned with the concepts of probability and information content for stochastic random variables. It provides an overview of the main measures of the information-theoretic framework used to

characterize a static system and of the estimation strategies more widely used for their computation. Particular attention is devoted to the practical challenges associated with the implementation of these computational approaches, as well as to the solutions proposed in the literature to mitigate such issues and obtain reliable estimates.

Part II - Estimating complex system behaviors through information-theoretic approaches

Chapter 3 - Analysis of individual node dynamics focuses on the main information-theoretic measures employed for the investigation of univariate processes. In particular, entropy rate and information storage are discussed as quantities respectively associated with the complexity and regularity of system dynamics. The chapter further examines their use both as global descriptors of overall system behavior and as local measures, enabling a time-resolved characterization of transient dynamics. The content of this chapter mainly builds upon two of the main works resulting from the doctoral study, namely Barà et al. (2024c) and Barà et al. (2023c). In particular, my contribution consists in extending and validating entropy-based measures in systems exhibiting both linear stochastic and chaotic deterministic dynamics, and in systematically assessing their performance under different estimation strategies.

Chapter 4 - Pairwise analysis of link dynamics focuses on two widely used frameworks for the analysis of bivariate processes: the mutual information rate and predictive information. It emphasizes their complementary roles in disentangling the overall information exchanged between two processes and discusses the distinct interpretations of the resulting measures of coupling and causality. It reviews estimation strategies for each framework, highlighting their advantages, limitations, and practical considerations. My methodological contribution is mainly based on Barà et al. (2023b), where I developed and systematically evaluated discrete estimation strategies across different simulation settings. Finally, it discusses partial information-theoretic measures investigating the presence of a direct link between two nodes when they are part of a network, as explored in Barà et al. (2026b).

Chapter 5 - High-order investigation of group dynamics addresses the analysis of multivariate interactions and the assessment of synergistic and redundant interplay among multiple variables. The chapter introduces a range of the most widely employed measures that are used to examine the presence of a predominant synergistic or redundant interaction among several nodes sharing information. It then focuses on the analytical framework of the partial information decomposition that can be used to disentangle redundant and synergistic information shared by several sources and a target. Issues pertaining to the definition, estimation, and interpretability of the measures computed in this framework are addressed and considered when outlining application strategies. In this context, the estimation strategy

presented in Barà et al. (2025a), one of the main outputs of my doctoral research, plays a central role.

Part III - Applications on physiological data

Chapter 6 - Physiological and methodological grounds introduces the physiological regulatory mechanisms investigated throughout the thesis using information-theoretic tools. Particular attention is devoted to cardiovascular and cardiorespiratory dynamics, as well as to brain-heart interactions. It focuses on outlining the approaches necessary to extract time series that accurately capture the physiological dynamics of interest from the acquired signals. Finally, an overview of the databases employed in the subsequent chapters is provided.

Chapter 7 - Univariate analysis of physiological signals presents the findings of univariate analyses conducted on physiological time series, aiming at evaluate the regularity and complexity of cardiac, vascular, and respiratory dynamics under different physio-pathological states, encompassing varying breathing rates, postural orthostatic stress, mental arithmetic tasks, or during sleep apnea events. Additionally, findings on the modulation of multichannel neural dynamics in relation to cardiac activity are shown. The chapter collects results from some of my main papers, namely Barà et al. (2023c) and Barà et al. (2024c), as well as from Volpes et al. (2022a); Antonacci et al. (2025a), where I provided methodological and/or interpretative contributions.

Chapter 8 - Pairwise analysis of physiological dynamics collects the findings of several studies investigating pairwise interactions within the cardiovascular and cardiorespiratory systems. Specifically, the mutual information rate and predictive information, along with their decomposition terms, are evaluated during the transition from a resting state to the presence of physiological stressors. Furthermore, applications aimed at elucidating the functioning of regulatory mechanisms under pathological conditions, such as myocardial infarction or heart failure, are reported. The findings are mainly drawn from two of my journal papers, i.e., Barà et al. (2023b) and Barà et al. (2026b), a conference paper, i.e., Barà et al. (2023a), and collaborative works including, i.e., Sparacino et al. (2025c); Cimignolo et al. (2025a) and Platiša et al. (2023).

Chapter 9 - High-order analysis of physiological networks presents the findings of two applicative studies employing the partial information decomposition analytical framework to investigate the relationship among arterial pressure components and the high-order behaviors of cardiovascular dynamics during ventilatory phases. These analyses are respectively reported in Sparacino et al. (2025d) and in one of the main outputs of my doctoral research, namely Barà et al. (2025a). Moreover, it presents the results reported in Saputo et al. (2026), in which the high-order analytical framework is employed to disambiguate complex cardiorespiratory bivariate

dynamics.

Part IV - Applications to machine learning

Chapter 10 - Information-theoretic foundations of machine learning highlights the relationship between the analytical framework of information theory and the field of machine learning. After recalling the probabilistic foundations underlying both paradigms and providing an overview of the main entropy-based quantities and their main applications in machine learning, it emphasized the potentiality of information tools in addressing challenges related to scalability and interpretability, particularly important in biomedical and healthcare applications.

Chapter 11 - Feature analysis strategies based on conditional Mutual Information measures and Partial Information Decomposition framework focuses on recently proposed information-theoretic feature selection and importance strategies that explicitly account for high-order interaction among multiple features in determining class outputs. In particular, it presents the selection strategy grounded on conditional mutual information terms proposed in Iovino et al. (2026) and the feature importance assessment framework introduced in Lazic et al. (2026). Additionally, an alternative framework of the partial information decomposition proposed in Barà et al. (2025b) is discussed, which enables the analysis of synergistic and redundant contributions of feature pairs in large datasets with respect to a class variable. Given that ML problems typically involve discrete class variables and continuous feature variables, particular attention is devoted to the adoption of appropriate estimation techniques. In this context, my principal contribution was in the development and adaptation of methods suitable for handling data of mixed nature.

Chapter 12 - Application of information-theoretic machine learning strategies to physiological data presents the results of feature analysis conducted on neurophysiological and gene expression data. In particular, it reports the findings obtained in Iovino et al. (2024b) and Iovino et al. (2026), where feature selection strategies were applied to cardiovascular features to discriminate cardiovascular autonomic control mechanisms between sexes or across different stress conditions. Furthermore, it reports the results of feature importance analysis presented in Lazic et al. (2026), aimed at evaluating the relevance of gene expression data in distinguishing breast cancer tissues, and in Barà et al. (2025b), which investigates the role of cortical areas in differentiating between eyes-open and eyes-closed conditions.

Part V - Conclusion

Chapter 13 - Concluding remarks and future directions summarizes the key findings of the comprehensive investigation conducted in this thesis on complex systems through the application of information-theoretic measures. It highlights opportunities and challenges associated with this analytical framework, with a particular focus on the critical and nontrivial aspects related to estimation strategies required

for the practical computation of the metrics considered. Subsequently, the main results and insights obtained from the analysis of complex physiological networks and large-scale machine learning settings are reviewed. Finally, the chapter outlines potential directions for future research aimed at overcoming the limitations identified throughout the thesis with a view toward methodological advancements applicable across a wide range of domains that deal with complex systems.

Appendix

Surrogate data analysis provides an overview of the statistical strategies employed to assess the significance of the information-theoretic measures considered throughout the thesis. After outlining the general principles of these methods, specific approaches developed to evaluate statistical significance and to detect nonlinear dynamics for each of the investigated quantities are presented.

Chapter 2

Fundamentals of Information Theory

This chapter first introduces the concept of probability for random variables and the associated notion of information content (Sect. 2.1), with focus on the main measures of the information-theoretic framework (Sect. 2.2). The quantities under investigation are defined in terms of generic scalar and vector systems, $\mathcal{V}$ and $\boldsymbol{\mathcal{W}} = \{\mathcal{W}_1, \ldots, \mathcal{W}_d\}$, which constitute the $(d+1)$-dimensional static network illustrated in Fig. 1.1. The chapter then reviews different data-driven approaches that can be used to estimate these quantities from realizations of the random variables composing the network (Sect. 2.3). Finally, it addresses practical considerations and challenges related to the application and implementation of these estimation strategies (Sect. 2.4).

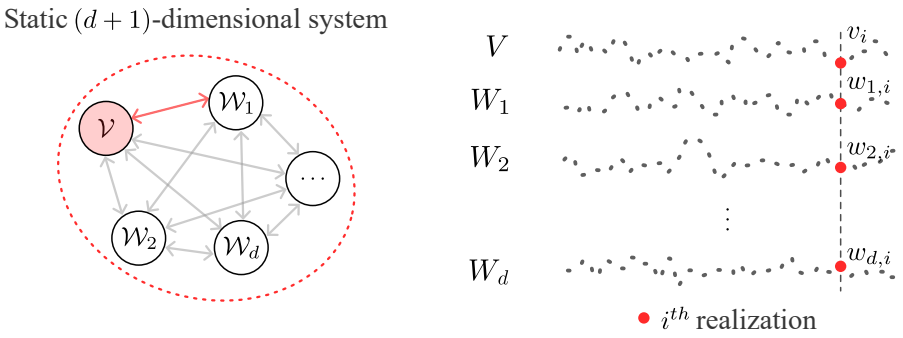

Figure 2.1: Graphical representation of a $(d+1)$-dimensional system represented by the random variable V and the vector random variable $\boldsymbol{W}$, whose realizations are assumed as temporally independent. It is used to investigate static network at the level of the individual system (colored node), of the link involving couples of systems (highlighted arrow), and of groups of systems or whole network (dotted line).

2.1. Concepts of probability and Shannon information content

In the framework of probability, a *random* (or *stochastic*) *variable* is a mathematical function that maps the outcomes of a random experiment. It does not assume predetermined numerical values, but it is subjected to the chance associated to the event of which it is representative (Papoulis (1965)). A generic scalar random variable V can be *discrete*, when its values belong to a finite-size set (i.e., the alphabet $\mathcal{A}_V$), or *continuous*, when it takes values inside a continuous set of values (i.e., the domain $\mathcal{D}_V$). If the random variable is discrete, it is possible to define a *probability distribution function* which maps for each possible outcome of the variable $v \in \mathcal{A}_V$ the probability of occurrence, i.e., $p(v) = Pr\{V = v\}$. Otherwise, if the random variable V is continuous, it is possible to refer to the *probability density function*, defined as the derivative of the cumulative distribution function $F_V(v) = Pr\{V \leq v\}$ which quantifies the probability that v is the upper bound of the variable V, i.e., $p(v) = \frac{dF_V(v)}{dv}$ for each $v \in \mathcal{D}_V$. These definitions can be easily extended to a generic d-dimensional vector random variable $\boldsymbol{W} = [W_1, \ldots, W_d]$ collecting the results of multiple random experiments, by defining the *joint probability distribution* $p(\boldsymbol{w}) = Pr\{W_1 = w_1, \ldots, W_d = w_d\}$, with $w_j \in \mathcal{A}_{W_j}$, or the *joint probability density* $p(\boldsymbol{w}) = \frac{dF_{\boldsymbol{W}}(\boldsymbol{w})}{d\boldsymbol{w}}$ with $dF_{\boldsymbol{W}}(\boldsymbol{w}) = Pr\{W_1 \leq w_1, \ldots, W_d \leq w_d\}$ and $w_j \in \mathcal{D}_{W_j}$, for $j = 1, \ldots, d$, when working with discrete and continuous vector variables, respectively. Moreover, considering both variables V and $\boldsymbol{W}$, the *conditional probability distribution* (or *density*) functions can be defined as the probability that V takes a specific value v given that $\boldsymbol{W}$ assumes the value $\boldsymbol{w}$. It can be expressed as the ratio between the joint probability of the two variables $p(v, \boldsymbol{w})$ and the probability of the conditioning variable $p(\boldsymbol{w})$, i.e., $p(v|\boldsymbol{w}) = \frac{p(v,\boldsymbol{w})}{p(\boldsymbol{w})}$.

Closely related to the probability framework is that of information theory. This allows to define the information associated to an event by looking at its probability of occurrence (Shannon (1948)). Specifically, the uncertainty associated to the specific outcome v of the random variable V is quantified by the *Shannon information content* $h(v) = -\log p(v)$. The probability and the content of information of a random variable outcome are linked by an inverse relation: the occurrence of an event whose probability is lower is more uncertain, thus brings more information. This quantity is typically expressed in nats for continuous variables and in bits for discrete variables, as respectively obtained by using the natural or the base 2 logarithm (Cover (1999)).

2.2. Grounding measures of information theory

The notions of probability and information content presented in the paragraph above allow to define the basic measures of the information-theoretic framework

here presented. Considering a generic scalar random variable V, its information content, intended as the average uncertainty about all its outcomes, is represented by the *entropy* measure $H(V)$, defined as (Shannon (1948); Cover (1999)):

$$H(V) = \mathbb{E}[h(v)] = -\mathbb{E}[\log p(v)], \tag{2.1}$$

with $\mathbb{E}[\cdot]$ being the expectation operator implemented as the sum or integral (over the alphabet or the domain of V) for discrete and continuous variables, respectively. The entropy value is zero if all the outcomes of the variable V are the same, thus if only one outcome occurs with unit probability, whereas it has the maximum value if all the outcomes occur with the same probability. Similarly, it is possible to define the entropy measure for the random vector variable $\boldsymbol{W}$ or for the joint vector variable $[V, \boldsymbol{W}]$ by using the joint probability $p(\boldsymbol{w})$ and $p(v, \boldsymbol{w})$, respectively, i.e., $H(\boldsymbol{W}) = \mathbb{E}[h(\boldsymbol{w})] = -\mathbb{E}[\log p(\boldsymbol{w})]$ and $H(V, \boldsymbol{W}) = \mathbb{E}[h(v, \boldsymbol{w})] = -\mathbb{E}[\log p(v, \boldsymbol{w})]$.

Two important information measures characterizing the interaction between two random variables V and $\boldsymbol{W}$ (either scalar or vectorial) are the Conditional Entropy (CE) and the Mutual Information (MI). The *conditional entropy* $H(V|\boldsymbol{W})$ of the random variable V given $\boldsymbol{W}$ quantifies the average uncertainty that remains about the outcomes of V when the outcomes of $\boldsymbol{W}$ are known and is defined as (Lizier (2012a)):

$$H(V|\boldsymbol{W}) = \mathbb{E}[h(v|\boldsymbol{w})] = -\mathbb{E}[\log p(v|\boldsymbol{w})]. \tag{2.2}$$

Considering the relation that allows to compute the conditional entropy for specific outcomes v and $\boldsymbol{w}$ from the Shannon information contents $h(v, \boldsymbol{w})$ and $h(\boldsymbol{w})$, i.e., $h(v|\boldsymbol{w}) = h(v, \boldsymbol{w}) - h(\boldsymbol{w})$, this quantity can be equally expressed as the difference between the joint entropy of the two variables and that of the conditioning variable, i.e., $H(V|\boldsymbol{W}) = H(V, \boldsymbol{W}) - H(\boldsymbol{W})$. It assumes maximum value and is equal to the entropy of V when the two variables are independent, while it is equal to zero if the two variables are deterministically related.
On the other hand, the *mutual information* $I(V; \boldsymbol{W})$ of V and $\boldsymbol{W}$ represents the information shared by the two variables intended as the average reduction in uncertainty about the outcomes of V when the outcomes of $\boldsymbol{W}$ are known. This measure is defined as (Lizier (2012a)):

$$I(V; \boldsymbol{W}) = \mathbb{E}[i(v; \boldsymbol{w})] = \mathbb{E}\left[\log \frac{p(v|\boldsymbol{w})}{p(v)}\right], \tag{2.3}$$

where $i(v; \boldsymbol{w})$ is the specific mutual information that the two outcomes v and $\boldsymbol{w}$ contain when they are taken individually but not together, i.e., $i(v; \boldsymbol{w}) = h(v) + h(\boldsymbol{w}) - h(v, \boldsymbol{w})$. Accordingly, the average measure $I(V; \boldsymbol{W})$ can be also expressed as the sum of the entropy terms associated to the two variables minus their joint entropy, i.e., $I(V; \boldsymbol{W}) = H(V) + H(\boldsymbol{W}) - H(V, \boldsymbol{W})$. This symmetric measure is equal to zero when

the two variables are independent, while it coincides with the entropy of V when this latter is related to $\boldsymbol{W}$ through a deterministic function.

Another measure of interest when investigating the interaction of two variables accounting for the presence of other variables is the conditional mutual information (CMI) measure. The *conditional mutual information* $I(V;W_j|\boldsymbol{W}_{\setminus j})$ of V and a generic scalar variable W_j, $j \in \{1,\dots,d\}$, inside the vector random variable $\boldsymbol{W}$ when conditioning on the rest of the scalar variables composing $\boldsymbol{W}$, i.e., $\boldsymbol{W}_{\setminus j} = \boldsymbol{W} \setminus W_j$, represents the information shared by V and W_j that is not already present in $\boldsymbol{W}_{\setminus j}$. This quantity is intended as the average reduction in uncertainty about the outcomes of V when the outcomes of W_j are known and are not related to the knowledge of $\boldsymbol{w}_{\setminus j}$. Accordingly, it is defined as (Lizier (2012a)):

$$I(V;W_j|\boldsymbol{W}_{\setminus j}) = \mathbb{E}\left[i(v;w_j|\boldsymbol{w}_{\setminus j})\right] = \mathbb{E}\left[\log \frac{p(v,w_j|\boldsymbol{w}_{\setminus j})}{p(v|\boldsymbol{w}_{\setminus j})p(w_j|\boldsymbol{w}_{\setminus j})}\right], \tag{2.4}$$

and can be expressed as the combination of CE or MI terms, i.e., $I(V;W_j|\boldsymbol{W}_{\setminus j}) = H(V|\boldsymbol{W}_{\setminus j}) - H(V|W_j,\boldsymbol{W}_{\setminus j}) = I(V;W_j,\boldsymbol{W}_{\setminus j}) - I(V;\boldsymbol{W}_{\setminus j})$. This quantity is equal to zero when V and W_j are independent conditioning on $\boldsymbol{W}_{\setminus j}$, while it can assume values greater than $I(V;W_j)$ when V and W_j are independent but became dependent conditioning on $\boldsymbol{W}_{\setminus j}$.

Finally, other measures that should be mentioned when statistically evaluating random variables are the Kullback-Leibler divergence and the Cross-Entropy. The *Kullback-Leibler* (KL) *divergence*, also called as *relative entropy*, measures the statistical distance between two probability distributions (or probability densities) $p(v)$ and $q(v)$ defined over the same alphabet (or domain) for the variable V. Accordingly, defined as (Csiszár, 1975)

$$D_{KL}(p||q) = \mathbb{E}_p\left[\log \frac{p(v)}{q(v)}\right], \tag{2.5}$$

to quantify the divergence of p from q, it measures the expected information gained when considering the distribution q instead of p. This asymmetric quantity is always nonnegative, being equal to zero only when the two probability distributions are identical. Contrarily, the *cross-entropy* term, defined as the expectation of the negative log-probability of $q(v)$ calculated with respect to $p(v)$ (Cover, 1999), i.e.,

$$H(p,q) = \mathbb{E}_p\left[-\log q(v)\right], \tag{2.6}$$

quantifies the average surprise when assuming a distribution q for a variable that comes from the distribution p. Being in some sense complementary, these two quantities are related through the entropy $H(p)$ of the variable V drawn from its own probability p, i.e., $H(p,q) = H(p) + D_{KL}(p||q)$.

2.3. Estimation methods

The information-theoretic measures outlined in Sect. 2.2 can be computed using several estimation approaches based on different data distribution assumptions and different operating methods to estimate probability distributions. A first broad categorization can be made between methods assuming a specific probability distribution and using its descriptive parameters to derive entropy measures, i.e., the *model-based* (MB) approaches, and methods approximating the probability density directly from the data, i.e., *model-free* (MF) approaches (Xiong et al. (2017)). The MB approaches are simpler and computationally faster but lack generality failing in describing complex dynamics, contrarily to the MF ones which are not constrained in observing specific data behaviors but are data-demanding and computationally onerous. Furthermore, a second categorization can be made by considering estimators working with *continuous* or *discrete* variables. The formers are more reliable but less data-efficient and more time-consuming, while the latters can be implemented in faster algorithms which lead to loss of accuracy due to a coarse grained representation of the continuous dynamics. Indeed, the variables describing physiological dynamics are typically continuous and the use of discrete estimators makes it necessary the manipulate data nature to provide a symbolic representation of their continuous values (Azami et al. (2023)).

In the following, two continuous estimation approaches, i.e., the linear model-based and the model-free nearest neighbor, as well as two model-free discrete estimation approaches, i.e., the binning- and the permutation-based, are described in detail. For each of these approaches, the formulas of the main terms of entropy, CE, and MI terms are derived.

2.3.1. Linear parametric approach

The linear estimator is a model-based approach relying on the assumption that data follow a *Gaussian probability distribution* (Barrett et al. (2010)). Specifically, given a zero-mean generic d-dimensional Gaussian variable $\boldsymbol{W}$ following the probability density

$$p(\boldsymbol{w}) = \frac{1}{\sqrt{(2\pi)^d |\Sigma_{\boldsymbol{W}}|}} e^{-\frac{1}{2}\boldsymbol{w}\Sigma_{\boldsymbol{W}}^{-1}\boldsymbol{w}^\top}, \tag{2.7}$$

with $\Sigma_{\boldsymbol{W}} = \mathbb{E}\left[\boldsymbol{W}^\top \boldsymbol{W}\right]$ being the covariance matrix of $\boldsymbol{W}$, its joint entropy can be expressed in terms of $\Sigma_{\boldsymbol{W}}$ as

$$H(\boldsymbol{W}) = \frac{1}{2}\ln\left((2\pi e)^d |\Sigma_{\boldsymbol{W}}|\right). \tag{2.8}$$

When considering the scalar variable V, the formula in Eq. 2.8 is reduced by replacing the covariance matrix with the variance σ_V^2 of V, i.e., $H(V) = \frac{1}{2}\ln\left(2\pi e\sigma_V^2\right)$.

Following the general formula reported in Sect. 2.2, the model-based linear estimators of CE and MI are obtained respectively as:

$$H(V|\boldsymbol{W}) = \frac{1}{2}\ln\left(2\pi e\sigma^2_{V|\boldsymbol{W}}\right), \tag{2.9}$$

$$I(V;\boldsymbol{W}) = \frac{1}{2}\ln\left(\frac{\sigma^2_V}{\sigma^2_{V|\boldsymbol{W}}}\right), \tag{2.10}$$

where $\sigma^2_{V|\boldsymbol{W}}$ is the partial variance of V given $\boldsymbol{W}$, which can be expressed as the ratio between $|\Sigma_{V\boldsymbol{W}}|$ and $|\Sigma_{\boldsymbol{W}}|$, i.e., $\sigma^2_{V|\boldsymbol{W}} = \frac{|\Sigma_{V\boldsymbol{W}}|}{|\Sigma_{\boldsymbol{W}}|}$.

To compute these quantities, it is possible to exploit the duality between information measures and linear prediction for Gaussian variables (Barrett et al. (2010)). Considering the *linear regression model* establishing the relation between the scalar variable V and vector variable $\boldsymbol{W}$, i.e., $V = \boldsymbol{W}\boldsymbol{A} + U$ where $\boldsymbol{A}$ is the d-dimensional vector of the regression coefficient and U the zero-mean prediction error vector, the partial variance of V given $\boldsymbol{W}$ can be expressed as the variance of the prediction error, i.e., $\sigma^2_{V|\boldsymbol{W}} = \sigma^2_U$. The identification procedure of the regression model is usually performed by using the *ordinary least-squares* (OLS) method, which minimizes the difference between the true and the predicted data, i.e., the prediction error U (Lütkepohl (2005)). Let us denote the collection of the realizations of the variable V as the $N \times 1$ data matrix $v = [v_1, \ldots, v_N]^\top$, with $i = 1, \ldots, N$, and the realizations of the variable $\boldsymbol{W}$ as the $N \times d$ data matrix $\boldsymbol{w} = [\boldsymbol{w}_1, \ldots, \boldsymbol{w}_N]^\top$, where the i^{th} row is a realization of $\boldsymbol{W}_i$, i.e., $\boldsymbol{w}_i = [w_{1,i}, \ldots, w_{d,i}]$, and the j^{th} column collects all realizations of W_j, i.e., $[w_{j,1}, \ldots, w_{j,N}]^\top$, with $j = 1, \ldots, d$. The OLS formula estimates the regression coefficients as $\hat{\boldsymbol{A}} = (\boldsymbol{w}^\top\boldsymbol{w})^{-1}\boldsymbol{w}^\top v$, allowing to obtain the prediction error $\hat{u} = v - \boldsymbol{w}\hat{\boldsymbol{A}}$ of which it is possible to compute the variance value σ^2_U as shown in Fig. 2.2 (*a*).

2.3.2. *Nearest-neighbor approach*

One of the most widely used non-parametric estimation approach for continuous variables is the nearest-neighbor method, based on the idea that the probability density around a data point is constant and inversely related to the distance from its nearest samples (Kozachenko (1987)). Considering the N observations of the generic d-dimensional continuous random variable $\boldsymbol{W}$, the probability density around the i^{th} sample of $\boldsymbol{w}$ is expressed as:

$$p(\boldsymbol{w}_i) = \frac{k}{(N-1)c_{d,L}\epsilon^d_{i,k}}, \tag{2.11}$$

thus considering the probability mass of a sphere of diameter $\epsilon_{i,k}$ and volume $c_{d,L}$ centered at the reference point $\boldsymbol{w}_i$ and reaching its k^{th} neighbor sample.

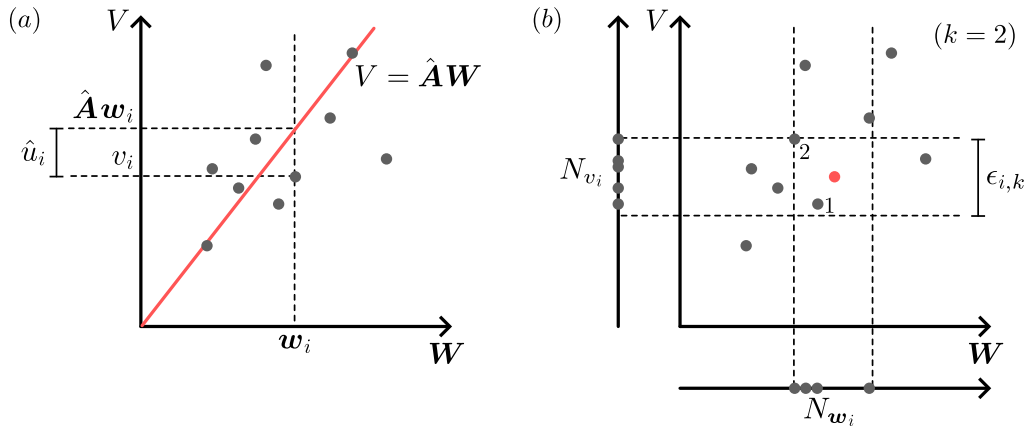

Figure 2.2: Graphical representation of the continuous estimation methods detailed in Sects. 2.3.1 and 2.3.2, i.e., the linear model-based (panel (*a*)) and the model-free nearest neighbor (panel (*b*)) approaches. Given nine realizations (gray dots) of the random variables V and $\boldsymbol{W}$, in panel (*a*) these are used to fill the $(d+1)$-dimensional space $\{V\ \boldsymbol{W}\}$ and to obtain the linear regression model $V = \hat{\boldsymbol{A}}\boldsymbol{W}$ (red line, case with $d = 1$). As depicted for the generic i^{th} realization, the residual prediction $\hat{u}_i$ is obtained as the deviation of the true value v_i from the estimated one $\hat{v}_i = \hat{\boldsymbol{A}}\boldsymbol{w}_i$. Repeating this procedure for all the realizations, the residual prediction vector U_i is obtained and its variance $\sigma^2_{V|\boldsymbol{W}}$ evaluated allowing the estimation of $H(V|\boldsymbol{W})$ and $I(V;\boldsymbol{W})$ by using Eqs. 2.9 and 2.10. Otherwise, considering the nonlinear estimation approach, the searching neighbor strategy is illustrated in panel (*b*) for the i^{th} realization of the vector variable $[V\,\boldsymbol{W}]$ (red dot). Fixing the parameter k to 2, the nearest samples (numbered dots) are searched in the highest-dimensional space $\{V\ \boldsymbol{W}\}$ and then the double of the distance of the more distant neighbor to the reference one is considered as range in the projected spaces $\{V\}$ and $\{\boldsymbol{W}\}$. Specifically, in the depicted example, projecting samples on the lower-dimensional spaces, $N_{v_i} = 5$ and $N_{\boldsymbol{w}_i} = 4$ samples are counted. Iterating the searching procedure for the N realizations, the interaction measures of CE and MI can be computed through Eqs. 2.18 and 2.19. The figure was modified from Xiong et al. (2017).

Differently from other estimation approaches, the nearest-neighbor method cannot be applied by directly substituting the derived probability density into the formulas of the information-theoretic measures previously reported. Indeed, estimation errors arising from finite sample sizes, the use of distance as a proxy for density, and the handling of variables defined in spaces of differing dimensionality must be explicitly accounted for. First, the bias-correction term $\log(k) - \psi(k)$ was added to the specific information measure $h(\boldsymbol{w}_i)$ to correct for systematic estimation offsets, thus yielding

$$h(\boldsymbol{w}_i) = -\log p(\boldsymbol{w}_i) = \log(N-1) - \psi(k) + \log c_{d,L} + d\log\epsilon_{i,k}, \tag{2.12}$$

with $\psi(\cdot)$ being the digamma function, $c_{d,L} = 1$ when using the maximum norm distance to find the neighbors (as done in practice), and $\log(N-1) \approx \psi(N)$ (Kozachenko (1987)). Furthermore, the estimation bias resulting from the combination of entropy

terms associated with variables defined in spaces of different dimensions must be taken into account. Among the formulations proposed to compensate for the presence of this bias, the most widely used was introduced by Kraskov, Stögbauer, and Grassberger (KSG) (Kraskov et al. (2004)). This approach defines the *searching distance* in the highest-dimensional space and then searches for neighbors in the lower-dimensional ones using the same *searching range*. Exploiting this approach, the entropy measure for the generic d-dimensional random variable is expressed as:

$$H(\boldsymbol{W}) = -\psi(k) + \psi(N) + \frac{d}{N}\sum_{i=1}^{N}\log\epsilon_{i,k}, \tag{2.13}$$

while the entropy of its j^{th} scalar component W_j as:

$$H(W_j) = \psi(N) + \frac{1}{N}\sum_{i=1}^{N}\left(\log\epsilon_{i,k} - \psi(N_{w_{j,i}} - 1)\right), \tag{2.14}$$

where $N_{w_{j,i}}$ is the number of samples of W_j whose distance from its i^{th} sample is smaller than $\epsilon_{i,k}/2$.

According to the KSG formulation, the searching space has to be properly defined considering the space involved by the measures we want to compute. For example, to evaluate the interaction measures between the random variables V and $\boldsymbol{W}$, the three entropy terms considering both jointly and separately the two variables have to be computed considering as searching space the highest-dimensional one, i.e., $\{V\ \boldsymbol{W}\}$, and then the same range has to be used in the lower-dimensional spaces for counting neighbors as depicted in Fig. 2.2 (*b*). Specifically, the aforementioned entropy terms are obtained as:

$$H(V, \boldsymbol{W}) = -\psi(k) + \psi(N) + \frac{1}{N}\sum_{i=1}^{N}(d+1)\log\epsilon_{i,k}, \tag{2.15}$$

$$H(\boldsymbol{W}) = \psi(N) + \frac{1}{N}\sum_{i=1}^{N}\left(d\log\epsilon_{i,k} - \psi(N_{\boldsymbol{w}_i} - 1)\right), \tag{2.16}$$

$$H(V) = \psi(N) + \frac{1}{N}\sum_{i=1}^{N}\left(\log\epsilon_{i,k} - \psi(N_{v_i} - 1)\right), \tag{2.17}$$

where $\epsilon_{i,k}$ is twice the distance from each of the samples in $\{V\ \boldsymbol{W}\}$ and its k^{th} neighbor, and $N_{\boldsymbol{w}_i}$ and N_{v_i} are the number of samples falling within half of this distance when considering the realizations of the variable $\boldsymbol{W}$ and V, respectively. Combining

these entropy measures, the interaction CE and MI terms can be computed as:

$$H(V|\boldsymbol{W}) = -\psi(k) + \frac{1}{N}\sum_{i=1}^{N}\left(\log \epsilon_{i,k} + \psi(N_{\boldsymbol{w}_i} - 1)\right), \tag{2.18}$$

$$I(V;\boldsymbol{W}) = \psi(k) + \psi(N) - \frac{1}{N}\sum_{i=1}^{N}\left(\psi(N_{\boldsymbol{w}_i} - 1) + \psi(N_{v_i} - 1)\right). \tag{2.19}$$

The estimation parameter k used to evaluate the probability distribution needs to be set finding a trade-off between the bias, i.e., the deviation of the estimated mean value from the theoretical one, and the variance, i.e., the statistical error of the estimates around the mean. Specifically, for increasing values of k, the estimation bias increases while the estimation variance decreases (Xiong et al. (2017)). Moreover, a good practice when applying the nearest-neighbor approach on multivariate variables is to normalize the scalar variables to zero mean and unit variance, as to work within comparable search ranges when computing entropy terms for variables of different dimensions.

2.3.3. *Binning approach*

Based on the discretization of continuous random variables through quantization and on the computation of their probability distribution via the frequentistic approach, the most intuitive approach for estimating entropy measures is the binning method (Azami et al. (2023)). Considering a generic random variable $\boldsymbol{W}$ whose scalar components take values in the continuous domain $\mathcal{D}_{W_j} = \left[w_{j,min}, w_{j,max}\right]$, it is possible to have a symbolic representation of W_j by associating to each sample $w_{j,i}$, $i = 1, \ldots, N$, a discrete value $w_{j,i}^{(b)}$ belonging to the alphabet $\mathcal{A}_{W_j^{(b)}} = \{1, \ldots, b\}$, with b the number of bins, i.e., the number of symbols used to give a coarse grained representation of the continuous values of W_j. To estimate the entropy of $\boldsymbol{W}$, the probability of all possible patterns of the quantized d-dimensional variable $\boldsymbol{W}^{(b)}$ and taking values inside the alphabet $\mathcal{A}_{\boldsymbol{W}^{(b)}}$ of b^d symbols, is measured as the frequency of occurrence of each possible realization over the N observations of the variable. Once the probability distribution is obtained considering all possible symbolic patterns for $\boldsymbol{W}^{(b)}$, this can be plugged in the definition of the entropy measure by implementing the sum over the alphabet $\mathcal{A}_{\boldsymbol{W}^{(b)}}$ to obtain the term $H(\boldsymbol{W})$. The same approach can be used to estimate the probability distributions $p(v)$ and $p(v, \boldsymbol{w})$, thus to compute the entropy terms $H(V)$ and $H(V, \boldsymbol{W})$, and to combine them to obtain the CE and MI quantities.

Different procedures can be used to quantize a generic continuous scalar random variable W_j based on the definition of bins with equal amplitude or equal sample density. The first method, known as *uniform quantization* approach and graphically depicted in Fig. 2.3 (*a*), defines b quantization levels of amplitude

$q = (w_{j,max} - w_{j,min})/b$ and associates the value $w_{j,i}^{(b)} \in \{1, \ldots, b\}$ to the i^{th} sample $w_{j,i}$ when it takes a value such that $w_{j,min} + (w_{j,i}^{(b)} - 1)q \leq w_{j,i} < w_{j,min} + w_{j,i}^{(b)} q$. Contrarily, the second method, known as *non-uniform quantization* approach, varies the size of the bins so as to have smaller bins where the amplitude of the samples is more likely and larger ones where the probability of occurrence of the samples is lower, thus keeping constant the number of samples falling into the bins. The uniform approach is the simplest to implement and works well when the signals are affected by a quite homogeneously distributed level of noise, while the non-uniform one allows to reduce the quantization error when the variables are not uniformly distributed. The number of bins b used to discretize the original continuous values of the variables determines the level of detail used to represent them and reflects a trade-off between the estimation probability precision and feasibility (Sturges (1926)) as more deeply discussed in Sect. 2.4.

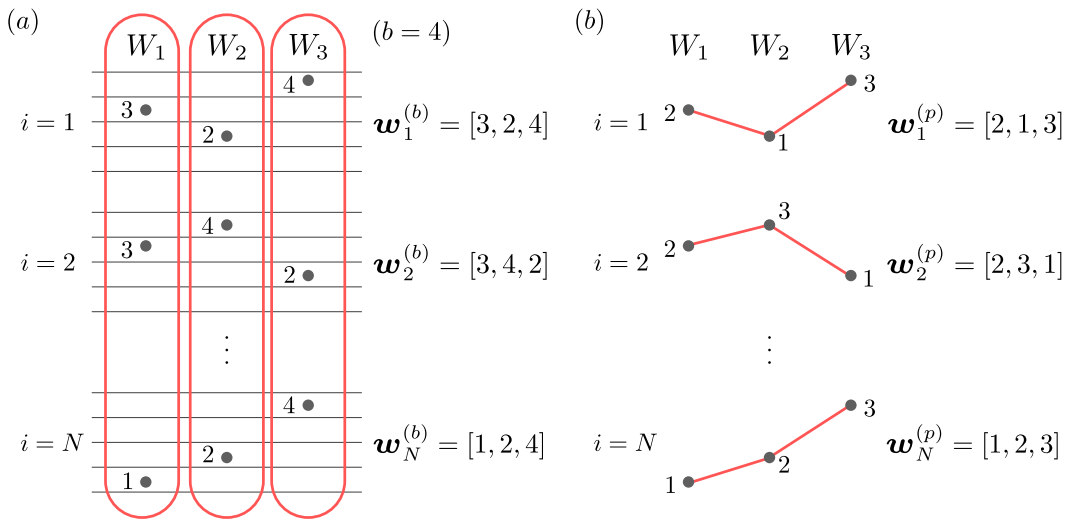

Figure 2.3: Graphical representation of the symbolization procedures performed to apply the discrete estimation methods detailed in Sects. 2.3.3 and 2.3.4, i.e., the binning-based (panel (*a*)) and the permutation-based (panel (*b*)) approaches. Considering three realizations of the random vector variable $\boldsymbol{W}$, the uniform quantization procedure in panel (*a*) associates to each of the samples $w_{j,i}$ a symbol in the alphabet $\mathcal{A}_{W_j^{(b)}} = \{1, \ldots, b\}$ with $b = 4$ being the number of bins. To simplify the graphical representation, the scalar variables of $\boldsymbol{W}$, i.e., W_j with $j = \{1, 2, 3\}$, are assumed to have the same domain $\mathcal{D}_{W_j}$. Contrarily, as shown in panel (*b*), the rank-ordering procedure looks at the realizations of the vector variable $\boldsymbol{W}$, i.e., $\boldsymbol{w}_i$, and assigns a symbol to each of its samples that indicates the sample's rank when its continuous amplitude values are ordered in ascending order. Once the three scalar variables are discretized, the occurrence of the realizations of the symbolic variables $\boldsymbol{W}^{(b)}$ with cardinality $|\boldsymbol{W}^{(b)}| = 4^3$ for the binning approach or of $\boldsymbol{W}^{(p)}$ with cardinality $|\boldsymbol{W}^{(p)}| = 3!$ for the permutation approach is counted to estimate $H(\boldsymbol{W})$.

2.3.4. Permutation approach

The permutation-based model-free estimation approach does not take into account the information carried by the amplitude value of the samples in the variable and instead relies only on their rank ordering within multidimensional patterns, thus working only on vector variables (Bandt and Pompe (2002)). Specifically, given a realization of the generic d-dimensional continuous variable $\boldsymbol{W}$, i.e., $\boldsymbol{w}_i = \left[w_{1,i}, \ldots, w_{d,i}\right]$, the symbolic representation $\boldsymbol{w}_i^{(p)} = \left[w_{1,i}^{(p)}, \ldots, w_{d,i}^{(p)}\right]$, with $w_{j,i}^{(p)} \in \{1, \ldots, d\}$, is obtained through the *rank-ordering procedure* which rank the order of $w_{j,i}$ inside the sequence $\boldsymbol{w}_i$. Specifically, $w_{j,i}^{(p)} = 1$ if $w_{j,i} = \min(\boldsymbol{w}_i)$ and $w_{j,i}^{(p)} = d$ if $w_{j,i} = \max(\boldsymbol{w}_i)$, while the other symbols are assigned according to ascendant order of the samples within $\boldsymbol{w}_i$ as graphically shown in Fig. 2.3 (*b*); if two equal components are found, the smallest rank is assigned to the component appearing last. Similarly to the binning approach, the probability of the symbolic patterns representing the realizations the discrete variable $\boldsymbol{W}^{(p)}$ with alphabet $\mathcal{A}_{\boldsymbol{W}^{(p)}}$ of dimension $d!$ is used to estimate the entropy measure of the variable $\boldsymbol{W}$, and the same can be done with the symbolic vector jointly representing V and $\boldsymbol{W}$ with alphabet of dimension $(d+1)!$ to estimate $H(V, \boldsymbol{W})$, thus to obtain $H(V|\boldsymbol{W})$. Being not possible to estimate probability distributions and entropy terms for scalar variables, the estimation of the MI term $I(V; \boldsymbol{W})$ cannot be performed via the permutation-based approach. This model-free approach appears data-efficient and has the great advantage of being a *parameter-free* estimation method.

2.3.5. Other estimation approaches

The estimation approaches detailed in the paragraphs above include only a restricted part of the plethora of methodologies that can be used to quantitatively evaluate the probability distribution of random variables and thus the related entropy-based measures. Among the strategies based on the use of continuous-valued variables, the *kernel estimator* is one of the most widely used model-free approaches on which the well-known CE estimators of Approximate Entropy (Pincus (1991)) and Sample Entropy (Richman and Moorman (2000)) are based. This quantifies the probability distribution of a variable assigning to each sample a weighted importance according to its distance from the reference sample. Starting from this estimator, other strategies have been developed like those based on *fuzzy approaches*, which make use of smoother similarity metrics (Xie et al. (2008); Chen et al. (2009); He et al. (2018); Girault and Humeau-Heurtier (2018)), or the *distribution entropy*, which evaluates information measures directly in state space of the distances among the variables (Li et al. (2015)). Furthermore, with regard to strategies able to address the nonlinearity of functionals relating the stochastic variables, it is important to mention some MB estimation approaches. Strategies based on the definition of *nonlinear*

models have been shown to be less affected by data length and dimensionality than the nearest-neighbor strategy (Draper and Smith (1998); Marinazzo et al. (2006)). However, the feasibility of these estimates is strongly related to the model assumptions and constraints and therefore, in the absence of prior knowledge on the system behaviour, their use is not recommended. In this context, it is also pertinent to mention approaches based on *local linear modeling*, which have the capacity to observe the nonlinearity of the system while considering a linear behavior for nearby points (Farmer and Sidorowich (1987)).

Looking at the strategies requiring the discretization of the continuous variables, different works have been established to modify the original algorithm of the permutation-based entropy accounting for the amplitude of the samples (Fadlallah et al. (2013); Xiao-Feng and Yue (2009)) and some others have been developed leading to novel entropy estimation approaches, e.g., the slope, the dispersion, and the bubble entropy. All these strategies are based on the frequentistic approach for the computation of the probability distribution of the variables and differ in the adopted discretization strategy. Indeed, while the *slope* approach assigns symbols according to the difference between consecutive values in a pattern looking at its deviation from zero and at the direction of the variation (Cuesta-Frau (2019)), the *dispersion* one discretizes the samples of the variables by using various mapping functions as the sigmoid-like one (Rostaghi and Azami (2016)). Differently, the *bubble entropy* evaluates the entropy of a vector accounting for the number of swaps needed to sort the pattern in ascending order (Manis et al. (2017)).

Among the various estimation approaches proposed in the literature, strategies that enable to jointly work with continuous and discrete variables are of particular relevance for application involving mixed data type. In this context, the approach introduced by Ross (2014) – which will be exploited in Sect. 5.2.2 and in the ML strategies presented in Chapter 11 – deserves particular attention. Specifically, this method applies the nearest-neighbor estimation strategy originally developed for continuous variables by defining search spaces conditioned on the observations of the discrete variable, thus effectively accounting for the association between continuous observations and specific values of the discrete variable.

2.4. Estimation matters

Among the estimation approaches described in the section above, the linear parametric one is the most widely used for its simplicity, even if limited in the identification of linear relations within and among variables that are assumed to follow Gaussian probability distributions (Barrett et al. (2010)). From this perspective, nonlinear model-free approaches emerge as more versatile and effective in investigating complex dynamics, despite typically requiring longer data sequences and attention

in their practical application. Among these, discretization strategies are easier to implement, with drastically reduced time and costs compared to the nearest-neighbor one. However, these strategies generally require a change in the nature of the variables representing real-world processes (as in the case of physiological processes), thus leading to an intrinsic loss of the information carried by the original variables. For instance, by applying the permutation-based approach the information provided by the amplitude values is completely disregarded.

The main issue that needs to be dealt with when using model-free estimation methods is the so-called *curse of dimensionality*, which refers to the difficulty of obtaining reliable entropy estimates for high-dimension variables (Runge et al. (2012)). Indeed, due to the increasing sparsity of data in spaces of growing dimension, the feasibility of the estimated entropy measures decreases, leading conditional entropy towards zero even for independent variables (Faes and Porta (2014)). Nevertheless, a proper choice of the estimation parameters can be useful in controlling the feasibility of the estimated quantities and in facing the curse of dimensionality.

The nearest-neighbor strategy has been observed to be the most efficient to implement for computing information-theoretic quantities in multidimensional variable spaces; indeed, it has been proven to suffer less than discretization-based approaches from the curse of dimensionality (Porta et al. (2015)). There are no established rules that help in finding the optimal parameter k: values ranging between 3 and 10 are generally used (Kraskov et al. (2004)), preferring small k values to have lower estimation bias (Khan et al. (2007)). Nevertheless, the parameter k should also account for the dimension of the explored space, for the number of realizations N of the variable, and for the characteristics of the investigated system (Papana and Kugiumtzis (2009)). When working in high-dimensional spaces, data sparsity increases resulting in more neighbors at comparable distances to the reference sample, so that small k leads to less reliable estimates suggesting the use of greater values. In Trujillo (2019), it is recommended to use a k value at least equal to the dimension of the investigated space. Although computationally demanding, an effective approach to determine the most appropriate number of neighbors k consists in searching for the optimal value that stabilizes the estimated values (Papana and Kugiumtzis (2009)). In general, lower values of k are preferred when the system under investigation is predominantly linear, whereas higher values are more suitable for capturing nonlinear dynamics.

Regarding the application of symbolization methods, an empirical criteria suggests to optimize the estimation parameters in a way such that the alphabet size remains as low as the number of realizations N of the variables (Faes and Porta (2014)). According to this criterion, we should have at least b^d or $d!$ samples for the binning- and permutation-based approaches, respectively, to obtain feasible entropy estimates of the generic d-dimensional variable $\boldsymbol{W}$. Considering how the rank-ordering

procedure leads to a lower number of symbolized patterns than the quantization strategy, the permutation approach usually works better for higher-dimensional variables (Kugiumtzis (2012, 2013)). Moreover, while the estimation performance of the permutation-based approach relies only on the dimension d of the variable, the feasibility of the binning estimates strongly depends also on the number of bins b used to discretize the variables. Different rules have been proposed to find an appropriate number of bins for discretization (Papana and Kugiumtzis (2009)). These range from the simple heuristic accounting only for the number of realization of the variable, i.e., $b = \sqrt{N}$ (Mosteller and Tukey (1977)), to the more refined formulation that also account for the shape of the underlying probability distribution, such as the Doane's formula (Doane (1976)). Specifically, this latter defines the number of quantization levels as $b = 1 + \log_2(N) + \log_2\left(1 + \frac{s}{\sigma_s}\right)$, where s denotes the estimated skewness and $\sigma_s = \sqrt{\frac{6(N-2)}{(N+1)(N+3)}}$ represents the expected variability of the skewness. This formula reduces to Sturges' formula, i.e., $b = 1 + \log_2(N)$, when the distribution is almost symmetric (Sturges (1926)), while using additional bins thereby improving the representation of asymmetric distributions.

2.5. Overview and conclusions of chapter 2

This chapter resumes the fundamental concepts of information theory and their connection with the theory of probability in order to provide a review of the measures of entropy, conditional entropy, and mutual information used to describe stochastic phenomena. These quantities are employed to describe the uncertainty associated with a random variable within a static network and how this is influenced by the other variables in the network. Among the several estimation strategies that can be applied to quantify these measures, a linear model-based approach assuming data normality and a nonlinear model-free approach based on the nearest-neighbors strategy have been discussed in deep when using continuous-valued data, while symbolic strategies based on binning and permutation approaches have been considered when using discrete estimation methods. The advantages and disadvantages of these approaches have been reported, highlighting the simplicity of the linear parametric approach among the continuous estimators against the greater adaptability of the nearest-neighbor one, as well as the approximation made by discrete estimators while manipulating the information content of the data in favor of a lower computational cost and time than the model-free continuous estimator. Although a reasoned selection of the estimation parameters allows to have control of the feasibility of the computed measures, even for high-dimensional variables thus limiting the curse of dimensionality, choosing the most appropriate estimation approach is not a simple task.

The measures recalled in this chapter for the analysis of static networks mapped

by random variables will be exploited to investigate the random processes constituting dynamic networks. As highlighted in Sect. 1.2, physiological signals are often nonstationary, nonlinear, and noisy, making the estimation process even more difficult, also precluding the use of some estimation strategies (further reasoning are reported in Sect. 3.1.1). Furthermore, when accounting for the dynamic evolution of a process, using an embedding vector that collects the present and past states of the process results in working in higher-dimensional spaces. This exacerbates the curse of dimensionality, which is particularly problematic when working with variables of finite size, as occurring with physiological signals often acquired over short time periods. Recognizing this challenge, this thesis will conduct a dynamic analysis of the activity of individual nodes (Chapters 3 and 7) or links (Chapters 4 and 8) within physiological dynamic networks, while overall limiting the investigation of group behaviors to a static analysis (Chapters 5 and 9). It is worth noting that examining individual nodes and node pairs within the static network in Fig. 2.1 merely reduces to the application of the formulations presented in this chapter.

Part II

Estimating complex system behaviors through information-theoretic approaches

Chapter 3

Analysis of individual node dynamics

In this chapter, metrics useful in the evaluation of the dynamics of single nodes in a dynamic network are explored, particularly focusing on the Entropy Rate (ER) measure associated with system complexity, thus with non-regularity and unpredictability of the node dynamics (Sect. 3.1), as well as on its complementary measure, the Information Storage (IS), which quantifies regularity and predictability of the process dynamics (Sect. 3.2). Specifically, this latter is evaluated through time-resolved estimation approaches that result in a description of the information carried by the process at any specific time step.

Let us consider the system $\mathcal{Y}$ representing a single node of a dynamic network as the red one in the network represented in Fig. 3.1 and the stationary stochastic process Y describing the states of the system over time, i.e., $Y = \{Y_n\}$ where $n \in \mathbb{Z}$ is the time counter. We indicate with Y_n the scalar random variable representing the current state of Y, with $Y_{n-1:n-m} = [Y_{n-1}, \ldots, Y_{n-m}]$ the m-dimensional vector variable sampling Y over the past m lags, and with $Y_{<n} = \lim_{m\to\infty} Y_{n-1:n-m}$ the infinite-dimensional variable representative of its whole past history (Packard et al. (1980); Takens (2006)).

3.1. Conditional entropy as a measure of complexity

The *Kolmogorov-Sinai (KS) entropy* was introduced to describe the dynamical evolution of the information carried by the system quantifying the average rate at which this information is generated (Sinai (1959); Kolmogorov (1985)). It is formally defined as the *entropy rate*

$$H_{KS} = \lim_{n\to\infty} \frac{1}{n} H(Y_n, Y_{<n}), \tag{3.1}$$

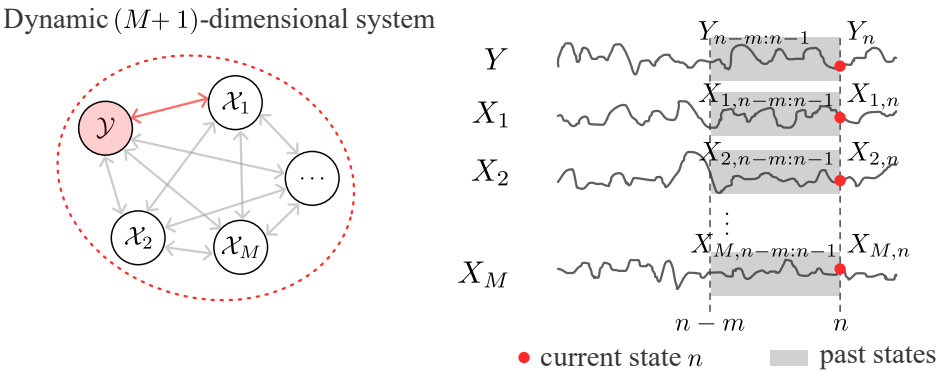

Figure 3.1: Graphical representation of a $(M+1)$-dimensional system formed by the random process $\mathcal{Y}$ and the vector random process $\boldsymbol{\mathcal{X}}$ constituted by a sequence of random variables temporally ordered is used to perform dynamic analysis by looking at the current and the past states of the processes. It is used to investigate static network at level of the individual system (colored node), of the link involving couples of systems (highlighted arrow), and of groups of systems or whole network (dotted line).

where $H(Y_n, Y_{<n})$ is the joint entropy of the states of the process Y considered up to time n. According to this definition, the average amount of information gained by the system tends towards zero if the information carried by the system does not increase with time. Under the hypothesis of stationarity for the process Y, the entropy rate metric is related to that of conditional entropy, indeed it was observed that the KS quantity asymptotically converges to the value asymptotically associated with the information carried by the present state Y_n of the process that cannot be inferred from its past states $Y_{<n}$ (Cover (1999)), i.e.,

$$\lim_{n\to\infty} \frac{1}{n} H(Y_n, Y_{<n}) = H(Y_n|Y_{<n}). \tag{3.2}$$

The value obtained by the limit on the right side of Eq. 3.2 is not expected to change over time, allowing to estimate the entropy rate term as the conditional entropy $H(Y_n|Y_{<n})$ – also when working with finite length data.

Considering the stationary process Y, the Shannon entropy of its current state $H(Y_n)$ – represented by the blue circle in the Venn diagram depicted in Fig. 3.2 – does not depend on the time n and is a static quantity that measures the information carried by the system at each time step (Lizier (2012a)). To gain insight into the dynamical evolution of the system, it is necessary to quantify the conditional entropy $H(Y_n|Y_{<n})$ between the present state Y_n and the past states $Y_{<n}$ of the process that quantifies the information carried by the current state of the process when its past dynamics are known (Lizier (2012a)) – represented by the yellow area in Fig. 3.2. This measure is obtained as the difference between the entropy jointly associated to the current and past states of the process $H(Y_n, Y_{<n})$ and that associated only to its

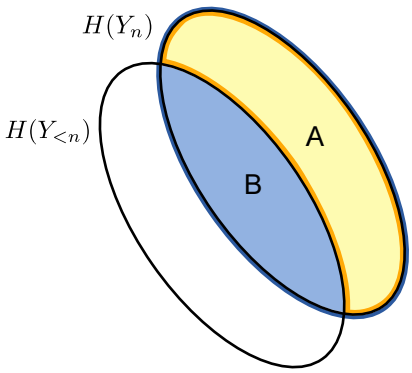

Figure 3.2: Venn diagram representing entropy and conditional entropy for a stochastic process Y. Taking the areas of the two circles as the entropy of the current state Y_n (left curve given by the union of A and B with blue contour) and of its past states $H_{<n}$ (right curve), the entropy rate of Y H_Y is represented by the area of A with yellow contour. The figure was modified from Pinto et al. (2024).

past states $H(Y_{<n})$, i.e.,

$$H_Y = H(Y_n|Y_{<n}) = H(Y_n, Y_{<n}) - H(Y_{<n}). \tag{3.3}$$

As a consequence of this definition, the complexity of the system $\mathcal{Y}$ results directly related to the predictability of the process Y: if the system presents a high conditional entropy H_Y, it is characterized by unpredictable and non-deterministic interdependencies and can be generically considered as complex (Azami et al. (2023)).

3.1.1. *Entropy rate estimation approaches*

To compute the entropy rate of a stationary dynamic process Y starting from a realization represented by the time series $y = \{y_i\}, i = 1, \ldots, N$, with N the number of available samples, it is necessary to assume Y as an ergodic Markov process of order m, for which the infinite-length past history $Y_{<n}$ is approximated by a collection of the observations over time (rather than across realizations) of m-lagged past states, i.e., $Y_{<n} \approx Y_{n-1:n-m}$. Under this assumption, the ER of the process Y can be obtained as the conditional entropy of Y_n when $Y_{n-1:n-m}$ is known, i.e.,

$$\hat{H}_Y = \hat{H}(Y_n, Y_{n-1:n-m}) - \hat{H}(Y_{n-1:n-m}) = -\mathbb{E}\left[\log \frac{\hat{p}(y_n, y_{n-1:n-m})}{\hat{p}(y_{n-1:n-m})}\right], \tag{3.4}$$

with $\hat{p}(\cdot)$ being the probability estimated from the time series y.

In the following, the estimation strategies detailed in Sect. 2.3 are used to compute the entropy rate of the stationary dynamic process Y. The related implementing codes are collected in the *univariate Information Decomposition (unID)* MATLAB-toolbox freely shared on GitHub.

Linear parametric estimator

Let us consider a linear parametric representation of the stationary zero-mean Gaussian process Y provided by the autoregressive (AR) model of order p, i.e., $Y_n = Y_{n-1:n-p}\boldsymbol{A} + U_n$, with $\boldsymbol{A} = \left[a_1, \ldots, a_p\right]^\top$ being the p-dimensional coefficient vector collecting a_k, for $k \in \{1, \ldots, p\}$, relating the present Y_n with the past of the process at lag k Y_{n-k}, and U_n a white Gaussian noise with zero mean and variance σ_U^2 representing the prediction error. The linear estimate of the entropy rate ER_{lin} is obtained as:

$$\hat{H}_Y = \frac{1}{2} \ln \left(2\pi e \hat{\sigma}_U^2\right), \tag{3.5}$$

where $\hat{\sigma}_U^2$ is the estimated variance of the prediction error obtained after quantifying the AR model using the OLS method. Specifically, to identify the AR model from the time series y, the OLS strategy described in Sect. 2.3.1 is particularized as $\hat{\boldsymbol{A}} = (\boldsymbol{Y}^{k\top}\boldsymbol{Y}^k)^{-1}\boldsymbol{Y}^{k\top}\boldsymbol{y}$, being $\boldsymbol{y} = [y_{k+1}, \ldots, y_N]^\top$ and $\boldsymbol{Y}^k = [y_1, \ldots, y_{N-k}]^\top$. Then, the prediction error U_n is estimated as $\hat{U} = \boldsymbol{y} - \boldsymbol{Y}^k\hat{\boldsymbol{A}}$. The use of the linear regression allows to define relations between statistical moments of the investigated process through the model coefficients, e.g., it has been demonstrated how the variance of the prediction error coincides with the partial variance of Y_n given $Y_{n-1:n-p}$, i.e., $\hat{\sigma}_U^2 = \hat{\sigma}^2_{Y_n|Y_{n-1:n-p}}$. Moreover, other relations (that will be useful in the following) link the autocorrelation of the process assessed at different time lags, i.e., $\boldsymbol{\Sigma}_{Y_{n-1:n-p},Y_n} = \boldsymbol{\Sigma}_{Y_{n-1:n-p}}\boldsymbol{A}$ and $\sigma_{Y_n}^2 = \boldsymbol{A}^\top\boldsymbol{\Sigma}_{Y_{n-1:n-p},Y_n} + \sigma_U^2$, where $\boldsymbol{\Sigma}_{Y_{n-1:n-p}} = \mathbb{E}[Y^\top_{n-1:n-p}\, Y_{n-1:n-p}]$ and $\boldsymbol{\Sigma}_{Y_{n-1:n-p},Y_n} = \mathbb{E}[Y^\top_{n-1:n-p}\, Y_n]$. The latter formulations are generalized by means of the Yule-Walker (YW) equations which express the correlation of the process at a generic lag k as $r_Y(k) = \sum_{l=1}^{p} a_{Y,k} r_Y(k-l) + \delta_{k0}\sigma_U^2$, where $r_Y(k) = \mathbb{E}\left[Y_n\, Y_{n-k}\right]$ represents the autocorrelation of the process at the lag k, and δ_{k0} is the Kronecher product (Walker (1931)). The YW equations can be solved through appropriate algorithms (e.g., Levinson Durbin recursion or discrete time Lyapunov equation) to find the correlations from the AR parameters.

Different model selection strategies, such as the Akaike Information Criterion (AIC) (Akaike (1974)), the Bayesian Information Criterion (BIC) (Schwarz (1978)), or the Minimum Description Length (MDL) approach (Rissanen (1978)), can be used to estimate the optimal order p of the AR model. These criteria help to achieve a balance between accurately representing the dynamics of the process Y and avoiding underfitting – where the model fails to capture the full dynamics – or overfitting – where the model captures both the process dynamics and noise. AIC and BIC criteria differ in the cost function which has to be minimized to obtain the optimal order of the model and consequently on the way these penalize the model complexity. Specifically, AIC focuses more on the predictive power of the model and on obtaining an accurate prediction of future unobserved data. It generally uses complex, higher-order models that tend to overfit process dynamics, especially when

working with longer time series. Conversely, BIC tends to identify a more conservative fit, considering only the observed data, resulting in lower-order models. The MDL strategy is designed to select the most effective descriptive model by reducing the overall length of the description, which encompasses both the model and the data. BIC and MDL approaches often result in the same optimal model order: it has been demonstrated that the two approaches are equivalent for Gaussian problems (Rissanen (1978)).

The parametric data representation ensures high data efficiency, allowing accurate estimation of entropy measures even from relatively short time series. More reliable estimates, however, are obtained when the time series length N is much larger than m. Its robustness to noisy data is supported by the OLS approach used to fit the regression model (Gibson et al. (2000)). Moreover, this framework enables the exploration of oscillatory dynamics by analyzing information content within specific frequency bands (Geweke (1982); Chicharro (2011)). Nevertheless, the method relies on the assumption of Gaussianity, which, although reasonable in many applications (at least in a first approximation), may cause the estimator to miss important nonlinear structures in the data (Barnett et al. (2009)). Additionally, it has been observed that this estimator does not work properly in nonstationary conditions: slow trends superimposed on Gaussian data can distort the distribution, creating bimodal dynamics, while spike artifacts can alter data variability and disrupt linear relationships between samples, rendering the linear parametric approach infeasible (Xiong et al. (2017)).

The linear parametric approach has a computational complexity of $O(N)$, which – as will be shown – is the lowest among the ER estimation methods investigated (Barà et al. (2024c)). It is important to note how the embedding size m – which corresponds to the model order p in the linear parametric approach – does not affect the computational complexity.

Nearest-neighbor estimator

By considering the KSG formulation of the nearest-neighbor strategy, the nonlinear model-free entropy rate estimate ER_{knn} can be obtained looking at the neighbor samples in the highest-dimensional space $\{Y_n\, Y_{n-1:n-m}\}$ and using the same range search in the lower-dimensional space $Y_{n-1:n-m}$. Specifically, the formula in the following is used:

$$\hat{H}_Y = -\psi(k) + \frac{1}{N-m}\sum_{n=1}^{N-m}\left(\ln \epsilon_{n,k} + \psi(N_{Y_{n-1:n-m}}+1)\right), \tag{3.6}$$

where $\psi(\cdot)$ is the digamma function, $\epsilon_{n,k}$ the maximum norm distance of $(y_{n-1:n-m}, y_n)$ to its k^{th} neighbor in the $(m+1)$-dimensional space, and $N_{Y_{n-1:n-m}}$ the number of samples whose distance from $y_{n-1:n-m}$ is lower than $\epsilon_{n,k}/2$ in the m-

dimensional space.

The two estimation parameters of the nearest-neighbor approach are the embedding dimension m, which has to be set to find a trade-off between the accuracy of the reconstruction of the process history and the curse of dimensionality, and the number of neighbor samples k used to evaluate the probability distribution, which has to be set to find a trade-off between the estimation variance and bias (Xiong et al. (2017)). Indeed, even if – as already evidenced in Sect. 2.4 – the nearest-neighbor approach is the most efficient non-parametric strategy in estimating information quantities in high-dimensional spaces, the entropy rate estimate becomes less reliable when increasing the embedding dimension m due to the curse of dimensionality. For data-driven estimation approaches, some strategies have been developed to reconstruct the most descriptive past space reconstruction characterized by the embedding dimension m and the time delay τ, representative of the temporal distance between equally spanned lagged samples as to satisfy the Takens's theorem (Takens (1981)). Approaches as the box-counting method (Falconer (1990)), the correlation dimension method (Grassberger and Procaccia (1983)), and the false nearest-neighbor method (Kennel et al. (1992)) test the invariance of different geometrical properties of the data at varying the embedding dimension m as to find its optimal value, while other strategies, such as the average mutual information method (Fraser and Swinney (1986)), the correlation sum method (Grassberger and Procaccia (1983)), and the phase space expansion method (Buzug and Pfister (1992)) can be used to identify the optimal τ. An alternative strategy that allows the selection of the most informative past samples of a process, not accounting for continuously or equally spanned lags, is the non-uniform embedding technique (Huke and Broomhead (2007)). This approach involves identifying past samples that are informative about the current state of the process and iteratively selecting those that provide the greatest contribution. This process continues until a stopping criterion is met, typically defined by a significant statistical improvement in the information content when additional past samples are included. On the other hand, regarding the setting of the parameter k indicative of the nearest-neighbor samples used to define the searching range, it usually remains quite arbitrary as a satisfactory search for the optimal k value that appropriately capture the dynamics of the process (mentioned in Sect. 2.4) can be computationally expensive and time consuming.

The nearest-neighbor strategy exhibits the highest computational complexity among the ER estimation approaches discussed, with $O(N^2 \log(N))$ (Barà et al. (2024c)). Similar to the embedding dimension m in the linear parametric approach, the influence of the nearest-neighbor parameter k can be neglected when considering asymptotic complexity, although it can practically cause considerable variations in computation time.

Binning-based estimator

The binning estimate of the conditional entropy ER_{bin} is simply obtained as the difference of the two estimated entropy terms related to the discrete vector variable representing the process dynamics up to time n and $n-1$, i.e., $\hat{H}(Y_n, Y_{n-1:n-m})$ and $\hat{H}(Y_{n-1:n-m})$.

As detailed in Sect. 2.3.3, the number of bins b used to discretize a continuous-valued time series determines the resolution at which the process dynamics are represented and has a strong impact on the accuracy of the resulting estimates. This parameter is typically fixed to 6 when ER is estimated on time series of 300 samples (usually employed for short-term physiological variability analysis), while if b is equal to 2 a binarization of the process dynamics is performed (Azami et al. (2023)). Nevertheless, as highlighted in Sect. 2.4, both the number of bins and the embedding dimension have a significant impact on the size of the symbolic alphabet. Therefore, it is recommended to maintain b^{m+1} smaller than the time series length N (Faes and Porta (2014); Barà et al. (2024c)). To enhance the performance of this estimator when working with a limited number of samples, some approaches have been proposed, such as the Corrected Conditional Entropy (CCE) (Porta et al. (1998)). Unlike traditional approaches, CCE does not fix the embedding dimension m a priori; instead, it identifies the most informative pattern length, effectively discarding decreases in entropy rate caused by low-complexity dynamics or short-length data. Additionally, as discussed for the nearest-neighbor approach, non-uniform embedding methods can be employed to mitigate the curse of dimensionality by limiting the dimensionality of the investigated space to selected past samples that capture only the most relevant information.

In addition to the simplicity of the algorithm, the discrete estimation approach based on the binning strategy is also computationally efficient, with a complexity of $O(N \log(N))$ (Barà et al. (2024c)).

Permutation-based estimator

Starting from the embedding vector representing the process dynamics up to time n and $n-1$, i.e., $[Y_n, Y_{n-1:n-m}]$ and $[Y_{n-1:n-m}]$, the rank-ordering procedure is applied to obtain their discrete representation. Analogously to the binning approach, the entropy estimates of these vectors are then subtracted to compute the permutation-based entropy rate measure ER_{perm}. Notably, this estimation strategy differs from the more commonly used permutation-based approach in the literature, which evaluates entropy rate by analyzing the regularity with which ordinal patterns of dimension m follow one another (Unakafov and Keller (2014)).

Regarding the sole estimating parameter of this approach, i.e., the embedding dimension m, larger values allow for a more detailed representation of the process

dynamics. However, it is recommended to limit the size of the alphabet used for estimating conditional entropy, i.e., $(m+1)!$, to be smaller than the length N of the time series (Faes and Porta (2014); Kugiumtzis (2013); Barà et al. (2024c)). Moreover, when using the permutation-based estimation approach, it is possible to leverage non-uniform embedding techniques specifically developed for this purpose (Tao et al. (2018)).

The computational complexity of the permutation-based estimation strategy is the same of the binning-based one, i.e., $O(N\log(N))$ (Barà et al. (2024c)).

3.1.2. *Validation on stationary autoregressive and mixed nonlinear deterministic/linear stochastic dynamics processes*

The simulation studies presented in Barà et al. (2024c), which investigate the behavior of different ER estimation approaches on two dynamic systems – a linear stochastic process and a mixed system combining nonlinear deterministic and linear stochastic dynamics – are reported here. Specifically, the performance of the different estimators was investigated by varying both the level of complexity and the length of the time series representing system realizations. Moreover, the analyses were firstly performed by varying the embedding dimension m (or equivalently the model order p for the linear approach) in the range $[2,3,4,6]$ and keeping constant the other estimation parameters (i.e., $k=10$ for the nearest-neighbor approach and $b=4$ for binning-based one), and then fixing the parameter m (or p for ER_{lin}) to 3 and varying the number of neighbors in the range $k=[5,10,15,30]$ for estimating ER_{knn} and the number of bins in the range $b=[2,4,6,8]$ for estimating ER_{bin}.

Stationary autoregressive process

A linear regression model was used to simulate a linear stochastic process Y characterized by an oscillatory dynamic with frequency $f=0.25$ Hz and amplitude proportional to the modulus ρ of the complex conjugate poles describing the process in the complex-plane. Specifically, a third-order AR model was employed (Xiong et al. (2017)):

$$Y_n=\sum_{j=1}^{3}a_jY_{n-j}+U_n, \tag{3.7}$$

with a_j, $j\in\{1,\dots,3\}$, being the linear regression coefficient and U_n a zero-mean and unit-variance white Gaussian noise. The amplitude of the stochastic oscillation determines the regularity of the AR process, thus the complexity of the system dynamics: the regularity of the process increases as the value of ρ increases, revealing fully unpredictable dynamics for $\rho=0$ and highly predictable dynamics for values of ρ close to 1. Working with a linear parametric model, ER theoretical values can be obtained from the true coefficients of the AR model making possible the com-

parison with the estimated values, thus evaluating the feasibility of the estimation strategies (Faes et al. (2015c)). Nevertheless, it is important to highlight that these theoretical values cannot be used as reference for estimates obtained through approaches based on symbolization strategies; in these cases a corrective term related to the discrete representation of the space should be considered (Cover (1999); Faes and Porta (2014); Santamaría-Bonfil et al. (2016)).

In a first validation setting, one-hundred realizations of the process were generated for values of ρ ranging from 0 to 0.9 with a step of 0.1 to evaluate the behavior of the estimates by varying the regularity of the process; in this case, representative time series of 300-sample length were used. Fig. 3.3 shows that all estimation approaches reveal the expected decrease in the entropy rate term as the parameter ρ increases, with the exception of the discrete approaches for some estimation parameters setting. We observe that both ER_{lin} and ER_{knn} trends agree with the theoretical ones for all possible values of m and k (panels (a) and (b)), even if a slight increase in the estimation bias is found for the nearest-neighbor approach by increasing the value of both estimation parameters. In contrast, discretization-based approaches fail in same cases, unrevealing the complexity decrease when the alphabet dimension became larger than the length N of the analyzed time series, i.e., when $b = 4$ and $m \geq 4$ or $b \geq 6$ and $m = 3$ for the binning strategy (for which the alphabet size is greater than 1024 and 1296, respectively; panel (c)) and when $m = 6$ for the permutation strategy (for which the alphabet size is 5040; panel (d)).

Similar conclusions on the feasibility of the estimators in capturing variations in the magnitude of the system complexity can be obtained by looking at Fig. 3.4, where the percentage variations for the entropy rate measures at varying the parameter ρ between pairs of consecutive values taken in the set $[0, 0.3, 0.5, 0.7, 0.8, 0.9]$ are reported, together with the statistical significance assessment of such variations through a paired Student's t-test. All estimation approaches are indeed able to detect significant changes in the complexity of the process, except for the lowest variation obtained varying the value of ρ from 0 to 0.3. Notably, the values obtained with the linear and nearest-neighbor estimators behave more similarly to the true theoretical values than the discretization-based approaches as these are differential entropy metrics.

A second simulation setting was used to investigate the influence of the time series length N on the reliability of the entropy rate estimates. Fig. 3.5 shows the entropy rate values obtained with the different estimation approaches after fixing the amplitude of the stochastic oscillation to $\rho = 0.8$ and varying the values of N in the range $[50, 100, 200, 300, 500, 700, 1000]$. For all estimation approaches, the entropy rate values stabilize and present lower variance as the parameter N increases, and the rate of convergence of these values is faster when the embedding dimension is equal or lower the one imposed by the simulated setting, i.e., $m = 3$, while

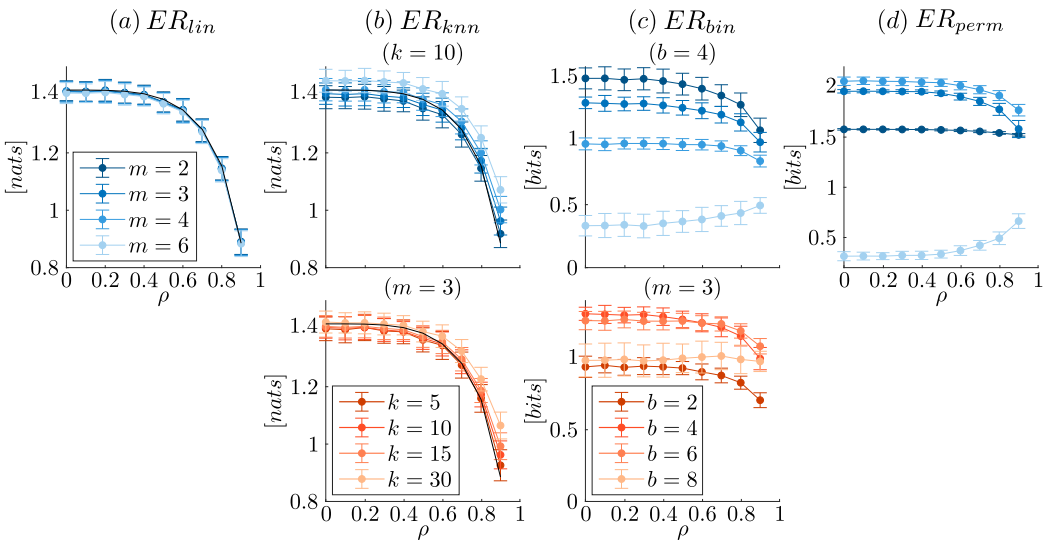

Figure 3.3: Error plots (mean ± std) depicting the distributions of the entropy rate estimates over one-hundred 300-sample realizations of a stationary AR process characterized by a stochastic oscillation with fixed frequency $f = 0.25$ Hz and variable amplitude ρ. Performance of linear (panel (a)), nearest-neighbor (panel (b)), binning-based (panel (c)), and permutation-based (panel (d)) estimation strategies are reported by varying the embedding dimension m (top row) and the estimator-specific parameters (bottom row), together with theoretical values for the continuous estimators (black line). The figure was modified from Barà et al. (2024c).

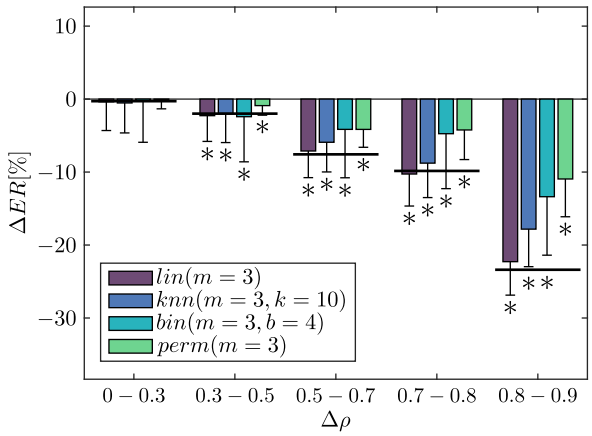

Figure 3.4: Errorbar plots depicting the percentage variation (mean ± std over one-hundred 300-sample realizations) of the entropy rate computed for an AR process with oscillatory dynamics at fixed frequency $f = 0.25$ Hz by increasing the value of the amplitude ρ between consecutive values in the range $[0, 0.3, 0.5, 0.7, 0.8, 0.9]$ as indicated on the x-axis. The estimation parameters are set to $m = 3$ for all the estimation approaches, $k = 10$ for the nearest-neighbor and $b = 3$ for the binning-based. The horizontal black lines represent the true theoretical percentage variation of the conditional entropy measure, while asterisk denotes for each estimation approach a statistically significant difference between the distributions of the entropy rate obtained for the selected values of ρ (paired Student's t-test, $p < 0.05$). The figure was modified from Barà et al. (2024c).

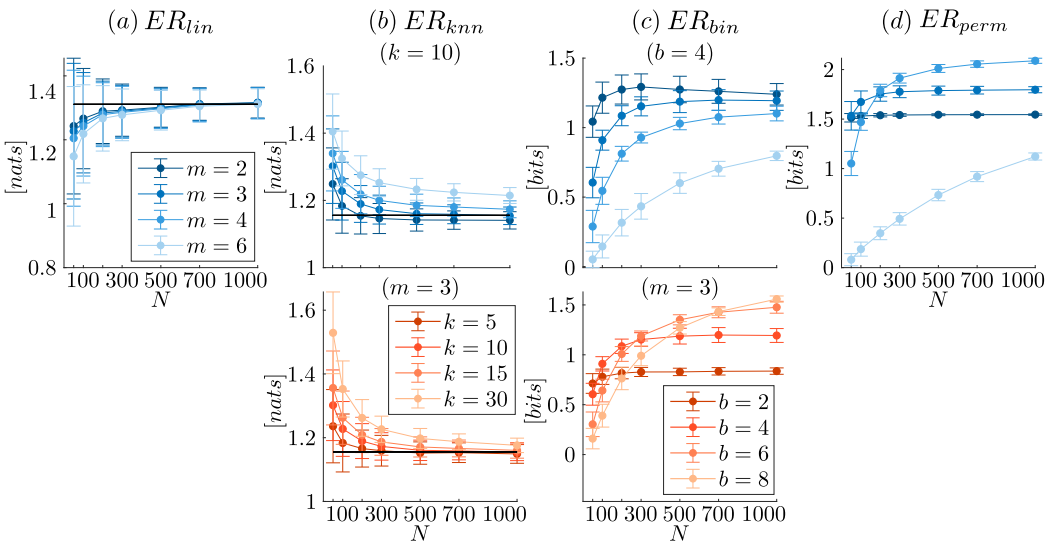

Figure 3.5: Error plots (mean ± std) depicting the distributions of the entropy rate estimates over one-hundred realizations of a stationary AR process characterized by a stochastic oscillation with fixed frequency $f = 0.25$ Hz and amplitude $\rho = 0.8$ by varying the length N of the time series. Performance of linear (panel (a)), nearest-neighbor (panel (b)), binning-based (panel (c)), and permutation-based (panel (d)) estimation strategies are reported by varying the embedding dimension m (top row) and the estimator-specific parameters (bottom row), together with theoretical values for the continuous estimators (black line). The figure was modified from Barà et al. (2024c).

decreases at increasing m. Moreover, while both ER_{lin} and ER_{knn} estimates tend towards the theoretical value at increasing N (panels (a) and (b)), the convergence value for the discretization-based approaches strongly depends on the estimation parameters (panels (c) and (d)).

Mixed nonlinear deterministic and linear stochastic dynamics process

A combination of nonlinear deterministic and linear stochastic dynamics was used to test the ability of the entropy rate estimators to capture variations in the randomness of the system. The logistic map function describing evolutionary population phenomena was used to simulate a chaotic deterministic process (May (1976)), while the Iterative Amplitude Adjusted Fourier Transform (IAAFT) technique, preserving spectrum and linear correlation, was used to generate a linear stochastic process (Schreiber and Schmitz (1996)). Specifically, the nonlinear finite-difference equation

$$X_n = cX_{n-1}(1 - X_{n-1}) \tag{3.8}$$

was used to generate the chaotic temporal evolution of a logistic process by imposing $c = 3.9$, while its surrogate obtained by using the IAAFT technique employed to have a stochastic process Z. These two processes were convexly combined by using

a parameter λ regulating the prevalence of the two opposite dynamics, i.e.,

$$Y_n = \lambda X_n + (1 - \lambda) Z_n. \tag{3.9}$$

Accordingly, as the value of λ increases, the system shifts from purely linear stochastic ($\lambda = 0$) to nonlinear deterministic ($\lambda = 1$) dynamics.

One-hundred 300-sample realizations of the mixed process were generated by varying the parameter λ from 0 to 1 with a step of 0.1 and the estimated entropy rate values reported in Fig. 3.6. It is observed how the estimated values are almost constant up to $\lambda = 0.5$ and decrease as the parameter λ increases, reflecting how high levels of stochasticity result in highly complex dynamics and how complexity decreases as the deterministic component of the system becomes dominant. The only exception is the linear approach (panel (*a*)): the surrogate technique preserves the linear temporal correlation of the process without altering the complexity of the linear dynamics, thus maintaining a constant ER_{lin} at varying λ. Furthermore, similar observations to those from the previous simulation can be made regarding the influence of estimation parameter settings. Specifically, the discrete approaches become infeasible when the alphabet size exceeds the number of available samples (panels (*c*) and (*d*)). Nevertheless, in this scenario, the lowest embedding dimension (i.e., $m = 2$) is still sufficient to capture the expected entropy rate trends, as the simulated process involves primarily one-lag dynamics.

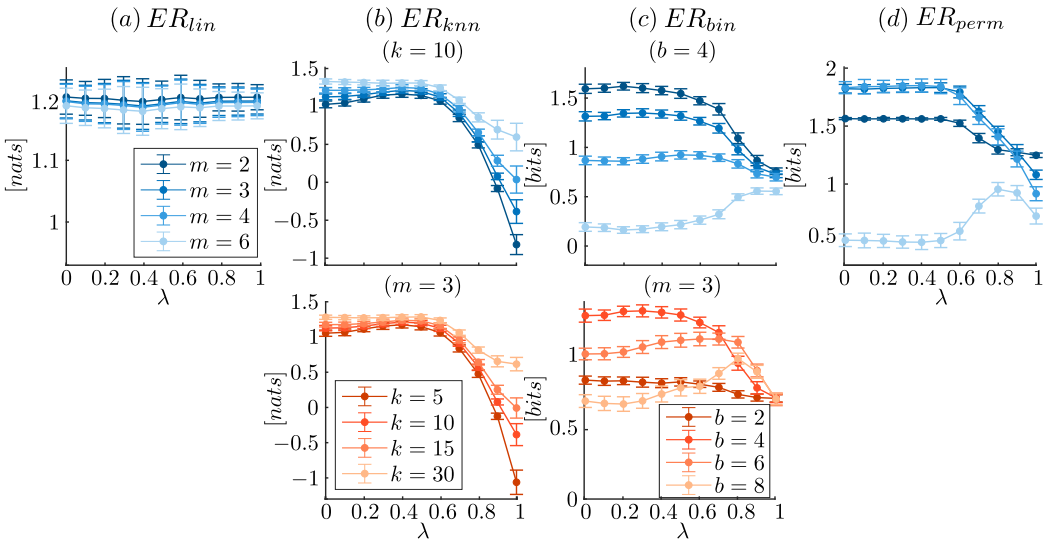

Figure 3.6: Error plots (mean ± std) depicting the distributions of the entropy rate estimates over one-hundred 300-sample realizations of a mixed nonlinear deterministic and linear stochastic process at varying the parameter λ. Performance of linear (panel (*a*)), nearest-neighbor (panel (*b*)), binning-based (panel (*c*)), and permutation-based (panel (*d*)) estimation strategies are reported by varying the embedding dimension m (top row) and the estimator-specific parameters (bottom row). The figure was modified from Barà et al. (2024c).

Looking at the percentage variations of the entropy rate measures at varying the

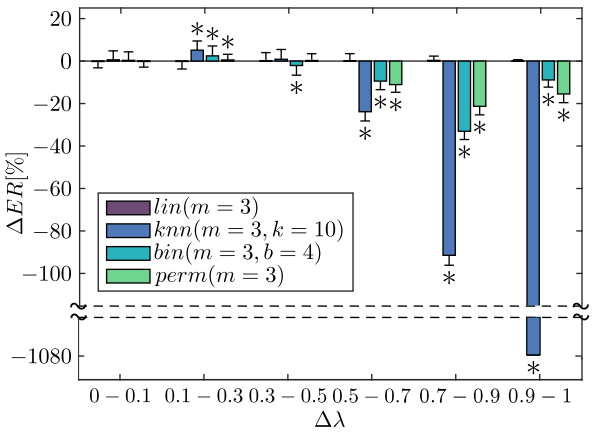

Figure 3.7: Errorbar plots depicting the percentage variation (mean ± std over one-hundred 300-sample realizations) of the entropy rate computed for a mixed nonlinear deterministic and linear stochastic process by increasing the value of the parameter λ between consecutive values in the range $[0, 0.1, 0.3, 0.5, 0.7, 0.9, 1]$ as indicated on the x-axis. The estimation parameters are set to $m = 3$ for all the estimation approaches, $k = 10$ for the nearest-neighbor and $b = 3$ for the binning-based. The asterisk denotes for each estimation approach a statistically significant difference between the distributions of the entropy rate obtained for the selected values of λ (paired Student's t-test, $p < 0.05$). The figure was modified from Barà et al. (2024c).

parameter λ between pairs of consecutive values in the set $[0, 0.1, 0.3, 0.5, 0.7, 0.9, 1]$ and at the statistical significance assessment of such variations reported in Fig. 3.7, significant decreases are observed for all the estimator when λ is higher than 0.5, except for the linear approach. The nearest-neighbor strategy appears to be the most sensitive in revealing complexity changes; the prominent percentage variation observed in Fig. 3.7 for ER_{knn} is related to the negative values computed when $\lambda = 1$. Slight significant complexity variations are also observed with the binning approach for values of λ lower than 0.5 (even with higher p-values).

Fig. 3.8 depicts the trends of the estimated entropy rate measures at varying the length N of the realizations of a process in a balanced condition of deterministic linearity and stochastic nonlinearity, i.e., for $\lambda = 0.5$. Similarly to the results achieved for the AR process, the estimated quantities tend to converge faster using smaller values of the embedding parameter m and the convergence value depends also on b for the binning approach (panel (c)).

3.2. Local estimation of conditional entropy and information storage

Another important measure providing information on the dynamics generated by a stochastic process is the *information storage* (Lizier (2012a); Faes et al. (2016b)). This is defined as the information content of the past of a stationary process that can be used to predict its present, and is expressed in terms of the MI between the current

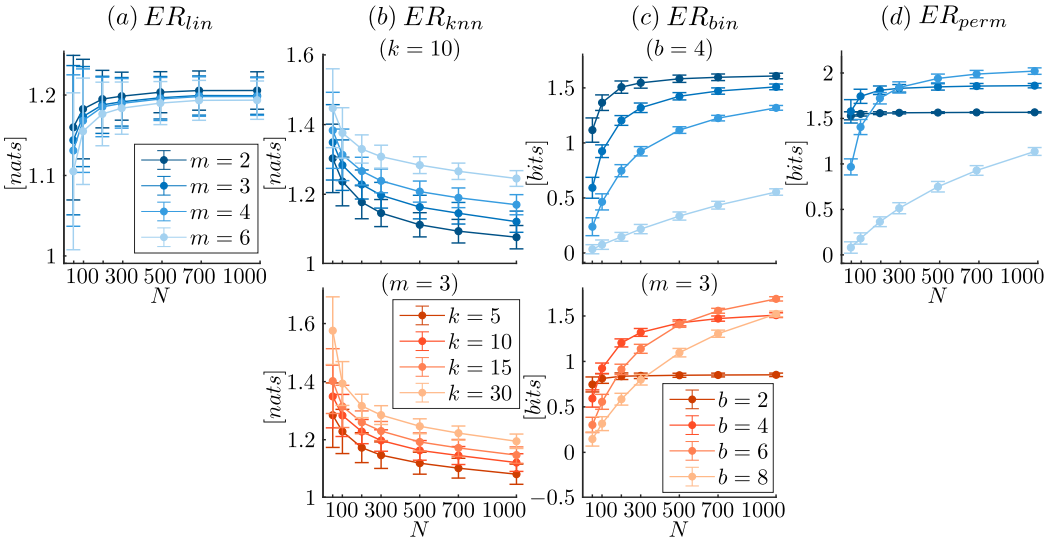

Figure 3.8: Error plots (mean ± std) depicting the distributions of the entropy rate estimates over one-hundred realizations of a mixed nonlinear deterministic and linear stochastic process with parameter $\lambda = 0.5$ by varying the length N of the time series. Performance of linear (panel (*a*)), nearest-neighbor (panel (*b*)), binning-based (panel (*c*)), and permutation-based (panel (*d*)) estimation strategies are reported by varying the embedding dimension m (top row) and the estimator-specific parameters (bottom row). The figure was modified from Barà et al. (2024c).

state of the process Y_n and its past states $Y_{<n}$ (Lizier (2012a); Xiong et al. (2017)), i.e.,

$$S_Y = I(Y_n; Y_{<n}) = \mathbb{E}\left[\log \frac{p(y_n, y_{<n})}{p(y_n)p(y_{<n})}\right]. \tag{3.10}$$

IS quantifies the average uncertainty about the state of the process that could be resolved from the knowledge of its past states – represented by the blue area of the Venn diagram in Fig. 3.2.

As defined in Eq. 3.10, IS provides a global index which accounts for the whole temporal evolution of the process, rather than time-resolved information about the process dynamics. However, the latter is useful in the investigation of complex dynamics presenting transient behavior. This limitation can be addressed by using *local measures* of information dynamics (Lizier (2012a, 2014); Stramaglia et al. (2021); Antonacci et al. (2025a)). Preserving the assumption of stationarity, this approach looks at the probability distributions of variables representing the present and past states of the processes computed at any specific time step n. Accordingly, Eq. 3.10 can be expressed as the statistical average of a local measure that quantifies the amount of stored information used by the process at each specific n, i.e., $S_Y = \mathbb{E}[i(y_n; y_{<n})]$, with $i(y_n; y_{<n})$ defined as (Lizier, 2014):

$$s_{y_n} = i(y_n; y_{<n}) = \log \frac{p(y_n, y_{<n})}{p(y_n)p(y_{<n})}. \tag{3.11}$$

Contrarily to the global measure, that is always positive and bounded above by the entropy of the current state of the system, the local IS is not bounded and can assume negative values (Lizier (2012a,b)). Positive values arise when knowledge of the past state $y_{<n}$ increases the probability of observing the current state y_n, whereas negative values occur when the past state is misinformative, reducing the predictability of the present state.

3.2.1. *Local information storage estimation approaches*

Considering the process Y as a stationary ergodic Markov process of order m, the global and local IS measures can be computed starting from a single realization of the process Y, available in the form of finite-length time series $y = \{y_i\}$, $i = 1, \dots, N$. Specifically, the local IS measure is estimated as:

$$\hat{s}_{y_n} = \log \frac{\hat{p}(y_n, y_{n-1:n-m})}{\hat{p}(y_n)\hat{p}(y_{n-1:n-m})}, \tag{3.12}$$

with $\hat{p}(\cdot)$ being the estimate of the joint and marginal probabilities, while the global IS is obtained as the temporal average of the local IS, i.e.,

$$\hat{S}_Y = \frac{1}{N-m} \sum_{n=m+1}^{N} \hat{s}_{y_n}. \tag{3.13}$$

In the following, the continuous estimation strategies detailed in Sect. 2.3, i.e., the linear parametric and nearest-neighbor approaches, are used to evaluate the local IS measure and its global counterpart for a stationary dynamic process Y. The implementing codes are collected in the *local univariate Information Decomposition* (*local-unID*) MATLAB-toolbox freely shared on GitHub.

Linear parametric estimator

Assuming a joint Gaussian distribution for the variables representing the present and the past states of the observed process, the probability densities involved in the definition of the IS can be written starting from Eq. 2.7 as follows:

$$\hat{p}(y_n) = \frac{1}{\sqrt{2\pi\sigma_Y^2}} e^{-\frac{1}{2}\frac{y_n^2}{\sigma_Y^2}}, \tag{3.14a}$$

$$\hat{p}(y_{n-1:n-m}) = \frac{1}{\sqrt{(2\pi)^m |\Sigma_{Y^m}|}} e^{-\frac{1}{2} y_{n-1:n-m} \Sigma_{Y^m}^{-1} y_{n-1:n-m}^\top}, \tag{3.14b}$$

$$\hat{p}(y_n, y_{n-1:n-m}) = \frac{1}{\sqrt{(2\pi)^{m+1} |\Sigma_{Y^{m+1}}|}} e^{-\frac{1}{2} [y_n \; y_{n-1:n-m}] \Sigma_{Y^{m+1}}^{-1} [y_n \; y_{n-1:n-m}]^\top}, \tag{3.14c}$$

where $\sigma_Y^2 = \mathbb{E}[Y_n^2]$ is the variance of Y_n, $\Sigma_{Y^m} = \mathbb{E}[Y_{n-1:n-m}^\top \, Y_{n-1:n-m}]$ is the covariance matrix of $Y_{n-1:n-m}$, and $\Sigma_{Y^{m+1}} = \mathbb{E}\left[[Y_n \, Y_{n-1:n-m}]^\top \, [Y_n \, Y_{n-1:n-m}]\right]$ is the joint covariance matrix of Y_n and $Y_{n-1:n-m}$. Replacing these terms in Eq. 3.12, the explicit formulation of the local IS is_{lin} for Gaussian processes is obtained Barà et al. (2023c); Antonacci et al. (2025a):

$$\hat{s}_{y_n} = \frac{1}{2}\log\frac{\sigma_Y^2|\Sigma_{Y^m}|}{|\Sigma_{Y^{m+1}}|} + \frac{1}{2}\left(\frac{y_n^2}{\sigma_Y^2} + y_{n-1:n-m}\Sigma_{Y^m}^{-1}y_{n-1:n-m}^\top - [y_n \, y_{n-1:n-m}]\,\Sigma_{Y^{m+1}}^{-1}\,[y_n \, y_{n-1:n-m}]^\top\right). \tag{3.15}$$

It can be observed that the first term of Eq. 3.15 corresponds to the global IS estimate IS_{lin}, i.e.,

$$\hat{S}_Y = \frac{1}{2}\log\frac{\sigma_Y^2|\Sigma_{Y^m}|}{|\Sigma_{Y^{m+1}}|}, \tag{3.16}$$

while the second term changes at any time step n and has a zero average value (Stramaglia et al. (2021)).

The estimation procedure of the local and global IS is related to the computation of the correlation matrices between the variables representing the present and the past states of the process starting from its linear modeling via YW equations (Faes et al. (2015c); Stramaglia et al. (2021)). Indeed, once obtained the autocorrelation of the process for each lag $k \in \{1, \ldots, p\}$, with p the order of the AR model used to describe the process dynamics, the YW equations can be iterated to obtain the autocorrelation matrices up to the desired lag m, and their proper arrangement is used to derive the covariances σ_Y^2, Σ_{Y^m}, and $\Sigma_{Y^{m+1}}$ needed to compute local and global IS. A detailed description of the computational procedure needed to obtain the local linear IS is reported in Barà et al. (2023c).

Nearest-neighbor estimator

Using the KSG nearest-neighbor approach, a nonlinear model-free estimate of local and global IS measures for the process Y can be obtained by performing a neighbor search in the highest-dimensional space composed of both current and past states of the process $\{Y_n : Y_{n-1:n-m}\}$ and then using the computing distances in the lower dimensional spaces Y_n and $Y_{n-1:n-m}$. Specifically, the formula in Eq. 2.12 is first adapted to compute the information content of $(y_n, y_{n-1:n-m})$ (Barà et al. (2023c)), i.e.,

$$\hat{h}(y_n, y_{n-1:n-m}) = \ln(N - m - 1) - \psi(k) + \ln c_{m+1,L} + (m+1)\ln\epsilon_{n,k}, \tag{3.17}$$

with $\epsilon_{n,k}$ being twice the distance from $[y_n \, y_{n-1:n-m}]$ to its k^{th} neighbor, used to compute the information content in the lower-dimensional spaces via range searches,

i.e.,

$$\hat{h}(y_{n-1:n-m}) = \ln(N-m-1) - \psi(N_{Y_{n-1:n-m}}+1) + \ln c_{m+1,L} + m \log \epsilon_{n,k}, \tag{3.18a}$$

$$\hat{h}(y_n) = \ln(N-m-1) - \psi(N_{y_n}+1) + \ln c_{m+1,L} + \ln \epsilon_{n,k}, \tag{3.18b}$$

with $N_{Y_{n-1:n-m}}$ and N_{Y_n} being the number of realizations of $Y_{n-1:n-m}$ and Y_n whose distance from $y_{n-1:n-m}$ and y_n is lower than $\epsilon_{n,k}/2$. Combining the terms in Eqs. 3.17 and 3.18, obtained by considering the maximum norm distance to find neighbors (i.e., $c_{m+1,L} = 0$), the local IS model-free estimate is_{knn} is computed as:

$$\begin{aligned} \hat{s}_{y_n} &= \hat{h}(y_n) + \hat{h}(y_{n-1:n-m}) - \hat{h}(y_n, y_{n-1:n-m}) = \\ &= \ln(N-m-1) + \psi(k) - \psi(N_{Y_{n-1:n-m}}+1) - \psi(N_{Y_n}+1), \end{aligned} \tag{3.19}$$

while the global measure IS_{knn} is estimated by combining Eqs. 3.13 and 3.19, resulting in:

$$\hat{S}_Y = \ln(N-m-1) + \psi(k) - \frac{1}{N-m} \sum_{n=m+1}^{N} \left(\psi(N_{Y_{n-1:n-m}}+1) + \psi(N_{Y_n}+1) \right). \tag{3.20}$$

3.2.2. *Validation on time-varying stochastic autoregressive and noisy deterministic processes*

In this section, we present simulation studies specifically designed to assess the feasibility of the estimation strategies described above for the local evaluation of process predictability. To this end, time-varying (TV) processes, representative of systems exhibiting transient changes over time and characterized by nonstationary dynamics, are considered. Specifically, TV processes exhibiting both linear and nonlinear dynamics were generated, and their regularity was assessed using local IS. In particular, the simulation settings proposed in Antonacci et al. (2023), based on linear dynamics with time-varying statistical properties, were reproduced. Additionally, a noisy logistic map with a time-varying level of superimposed noise and varying degrees of chaotic behavior was considered. In designing these simulations, special care was taken to ensure the global stationarity of the generated signals: although their statistical properties vary over time, the presence of repetitive alternating patterns allows the processes to be treated as globally stationary.

Time-varying AR process

Let us consider a TV-AR process defined as $Y_n = a_{1,n} Y_{n-1} + U_n$, where $a_{1,n}$ is the coupling strength between the current and the past of the process Y at lag 1 and U_n denotes a zero-mean Gaussian noise with variance $\sigma^2_{U,n}$. The parameter $a_{1,n}$ governs the information stored in the system at each time instant n, such that higher val-

ues correspond to greater information retention and, consequently, increased predictability of the system dynamics at that instant. To investigate the effects of varying system parameters, three independent realizations of the process, each comprising 60000 samples, were generated, incorporating distinct temporal profiles of the AR coefficient $a_{1,n}$ and noise variance $\sigma^2_{U,n}$ waveforms. Specifically, as shown in Fig. 3.9 (*a*), in the first setting the noise variance $\sigma^2_{U,n}$ was fixed to 0.8 and $a_{1,n}$ varied according to a periodic square waveform alternating between 0.3 and 0.9 with a duty cycle of 50% (panel (*.1*)), in the second setting the AR coefficient $a_{1,n}$ was kept constant and $\sigma^2_{U,n}$ varied following the aforementioned squared waveform (panel (*.2*)), while in the third setting both $a_{1,n}$ and $\sigma^2_{U,n}$ were varied with the same periodic squared wave (panel (*.3*)). Local IS was evaluated in the three scenarios using the linear approach, by fixing the model order p to 1, and the nearest-neighbor approach, by fixing the embedding dimension m to 1 and the number of neighbors k to 10. The parameters p and m, related to the embedding representation of the system dynamics, were set according to the theoretical order of the investigated TV-AR process, while the value of k was chosen based on previously reported results in the literature.

Fig. 3.9 reports the theoretical and estimated trends of local IS computed with both the linear parametric (panels (*b.*)) and the nonlinear model-free (panels (*c.*)) approaches for the three simulated settings (panels (*.1*), (*.2*), and (*.3*)). Theoretical values show that the time-resolved IS is dependent on the modification of the coupling strength $a_{1,n}$ and not on the innovation term $\sigma^2_{U,n}$. Indeed, when only the variance of the innovation term oscillates, as in the second setting, the local IS remains constant assuming a value of 0.51 at each time step, while in the other cases it follows a squared waveform reflecting $a_{1,n}$ variations. This behavior can be explained by looking at Eq. (3.16): local IS is defined as the ratio between the process variance σ^2_Y and the innovation variance $\sigma^2_{U,n} = \frac{|\Sigma_{Ym+1}|}{|\Sigma_{Ym}|}$, that in the second case change following the same waveform. The local measures computed with both estimation approaches show how this quantity is sensitive to both internal and unpredictable dynamics (panels (*b.*) and (*c.*)). Specifically, when the modifications are associated with the coupling strength – as in the first and third settings – both mean and variance of the IS measures show a modulation that overall follows that of $a_{1,n}$, while, when the modification is associated only with the innovation variance – as in the second setting – just the variance of the time-resolved IS measures follows the modulation profile. In summary, the mean of the local IS reflects the predictable component of the system's internal dynamics, as quantified by the theoretical time-varying IS, whereas its variance captures the unpredictable dynamics, as characterized by the innovation variance. Notably, the temporal fluctuations of the local IS profile do not simply mirror changes in the innovation variance over time; rather, they reflect the combined influence of both the innovation variance and the coupling strength,

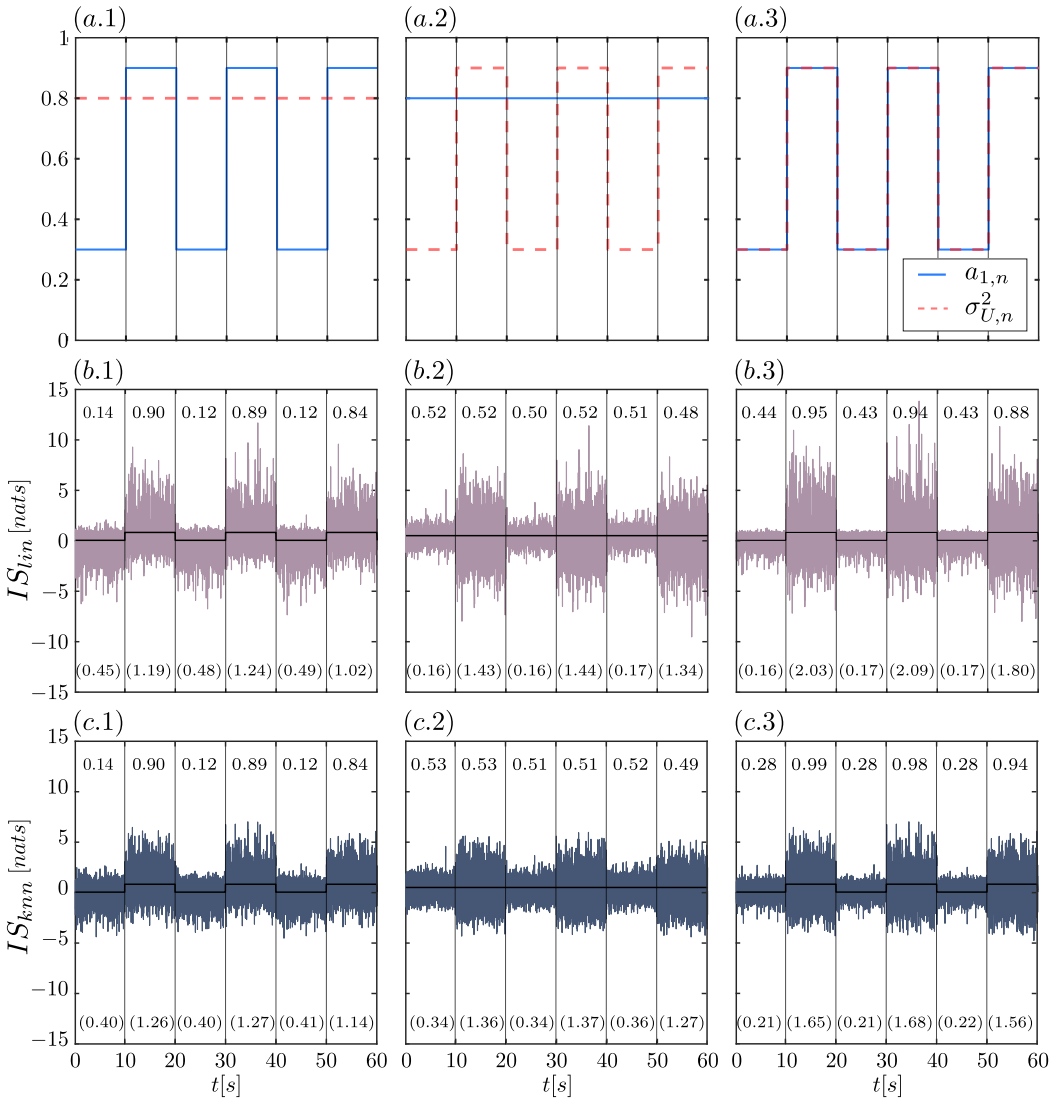

Figure 3.9: Settings of the simulated time-varying AR processes (panels (*a.*)) characterized in terms of the evolution over time of the AR coefficient $a_{1,n}$ (bluish continuous line) and the noise variance $\sigma^2_{U,n}$ (pinkish dashed line), i.e., $\sigma^2_{U,n} = 0.8$ and squared waveform for $a_{1,n}$ (panels (*.1*)), $a_{1,n} = 0.8$ and squared waveform for $\sigma^2_{U,n}$ (panels (*.2*)), and squared waveform for both $a_{1,n}$ and $\sigma^2_{U,n}$ (panels (*.3*)). Estimated and theoretical values (black lines) of local IS evaluated by using linear parametric (panels (*b.*)) and nearest-neighbor (panels (*c.*)) methods; mean and standard deviation of the estimated values of IS in each time window, delimited by vertical lines, are reported on the top and on the bottom (in brackets) of the figures, respectively.

highlighting the interplay between these two factors. Furthermore, it is noteworthy that negative values of the local information storage predominantly arise when the stochastic perturbations drive the system in a direction opposing that imposed by the coupling between Y_n and Y_{n-1}. In such cases, knowledge of the past state provides misleading information regarding the current state, resulting in a locally detrimental contribution to predictability. Conversely, large positive values occur when the effects of the noise and the coupling strength act coherently in the same direction, thereby enhancing the predictive relationship between past and present

states.

Time-varying noisy logistic map

A nonlinear process was generated by adding uniformly distributed noise to the deterministic dynamics described in Eq. 3.8. Specifically, the properties of the process were modulated by varying the chaotic growth rate, governed by the parameter c, and the amount of superimposed noise, expressed as a percentage s of the variance of the original deterministic signal. These parameters were varied according to the repetitive patterns illustrated in Fig. 3.10 (*a*). In particular, the parameter c was alternated within the range $[3.7, 3.8, 3.9]$, while s was set to values in $[0.3, 0.6]$. A process with a total length of $N = 180000$ samples was generated, with parameter changes occurring every 1500 samples. For illustrative purposes, a representative segment of 9000 samples of the generated process is shown in Fig. 3.10 (*b*). As for the TV-AR process, local IS was estimated using both linear parametric and nearest-neighbor approaches. As before, the linear method was implemented by fixing a model order $p = 1$, while the nearest-neighbor one was applied with an embedding dimension $m = 1$ and a number of neighbors $k = 10$.

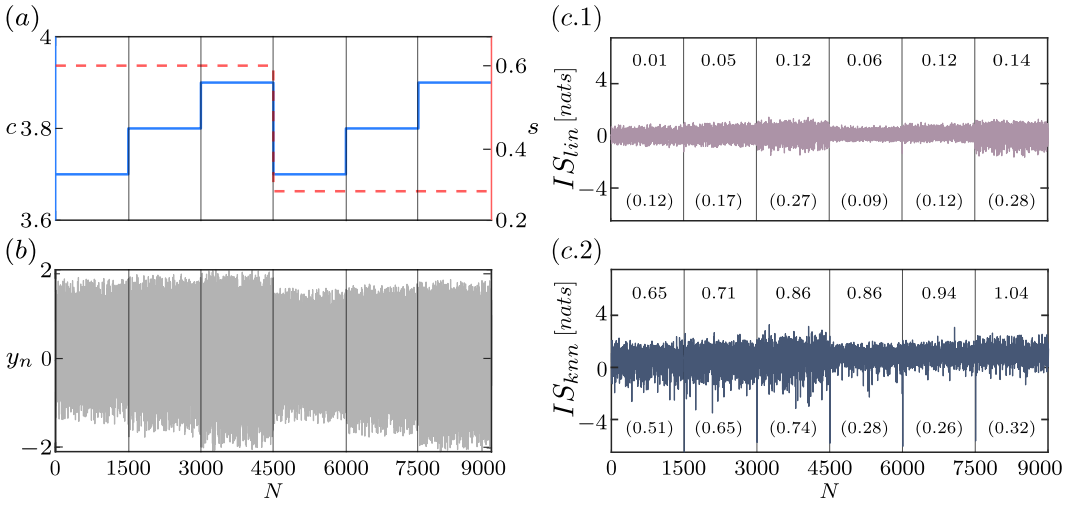

Figure 3.10: Setting parameters of the noisy time-varying coupled logistic maps for the first 9000 samples in terms of chaos level c (bluish continuous line) and variance of the superimposed noise s (pinkish dashed line) (panel (*a*)) and generated signal (panel (*b*)). Estimated local IS obtained with the linear parametric (panel (*c.1*)) and the nearest neighbor (panel (*c.2*)) strategies; mean and standard deviation of the estimated values of IS in each time window, delimited by vertical lines, are reported on the top and on the bottom (in brackets) of the figures, respectively.

Fig. 3.10(*c*) reports a portion of the local IS time series obtained by using the two estimation approaches, while Fig. 3.11 reports the distributions of the mean and standard deviation of local IS computed over segments of 1500 samples. Specifically, the segments were grouped according to the values of the parameters c (panels (*a*)) and s (panels (*b*)). While increasing the chaotic parameter c, both estimation

approaches consistently show an increase in the mean IS. This behavior reflects the strengthening of the deterministic component of the dynamics for higher values of c, which results in enhanced regularity and, consequently, greater predictability as quantified by IS. Conversely, the variability of the local IS increases with c only when the linear estimator is used, while remaining relatively stable when using the nearest-neighbor strategy. Looking at the modulation of the noise parameter s, both estimators reveal a decrease in the mean IS and an increase in its standard deviation as the amount of noise increases. A higher noise level progressively disrupts the deterministic structure of the logistic dynamics, thereby reducing predictability and increasing fluctuations in local IS. These findings are consistent with those obtained for the TV-AR process, while also indicating a greater sensitivity of IS variability to noise when estimated using the nearest-neighbor approach. This behavior may be attributed to the nonlinear nature of the investigated process, which can be more effectively captured by nonparametric estimation methods.

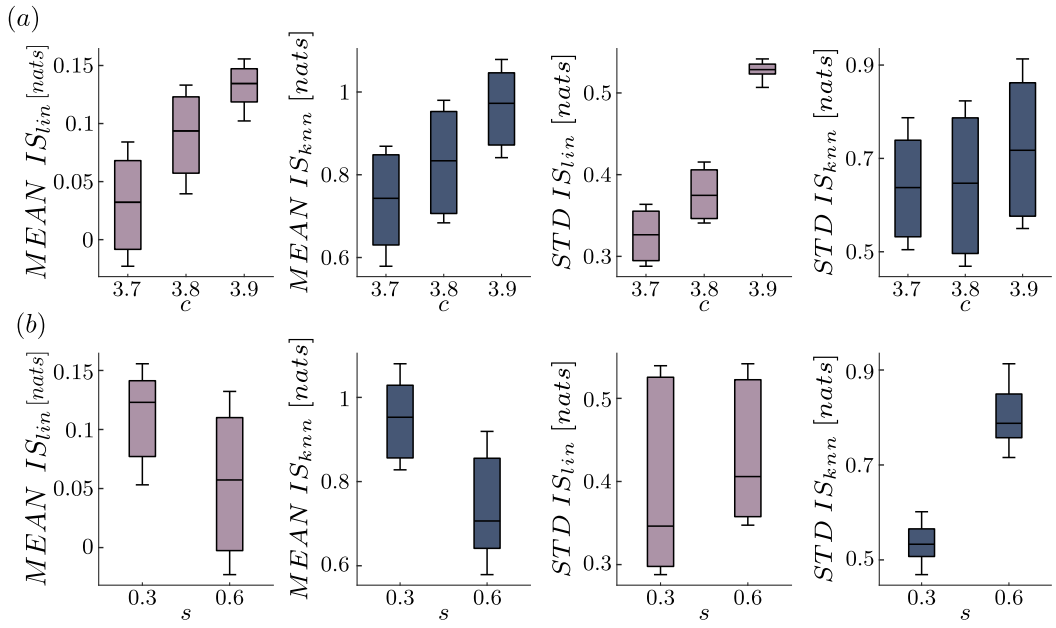

Figure 3.11: Boxplot distributions of local IS estimated with both linear parametric (*lin*) and nearest-neighbor (*knn*) approaches and representative of the mean (MEAN) and standard deviation (STD) when accounting for the intervals characterized by different levels of chaos (panel (*a*)), i.e., $c \in \{3.7, 3.8, 3.9\}$, and superimposed noise (panel (*b*)), i.e., $s \in \{0.3, 0.6\}$.

3.3. Overview and conclusions of chapter 3

This chapter investigates individual nodes within a network by analyzing the complexity of their dynamics. As discussed in Sect. 1.1, complexity is a broad concept that can be associated with several signal characteristics. Accordingly, a range of methodologies have been proposed to characterize complex systems (Valente et al., 2018), including fractal dimension (Theiler, 1990), Lyapunov exponent (Wolf et al.,

1985) and Lempel–Ziv complexity (Lempel and Ziv, 2003), which capture properties such as self-similarity, emergent dynamics, and system numerosity. Stochastic representations of complex dynamics are particularly relevant, as they relate complexity to non-regularity and unpredictability (Foote, 2007). In this context, we implemented information-theoretic measures such as the entropy rate and the complementary measure of information storage, which have been widely used to quantify the complexity of stationary stochastic processes (Lizier, 2012b; Faes and Porta, 2014). Specifically, ER quantifies the average rate at which a system generates new information, whereas IS evaluates the amount of information in the present that can be explained by past dynamics. Consequently, complex and less predictable dynamics are typically associated with higher ER and lower IS values.

The implementation of these measures relies on the assumption of stationarity. However, this requirement can be weakened when the objective is to investigate temporal modulations of the complexity of systems. In such cases, local nonstationarity becomes the focus of the analysis. In this context, it is important to emphasize that the notion of stationarity is inherently scale-dependent as it depends on the temporal resolution at which the dynamics of the processes are observed. In particular, processes exhibiting repetitive patterns may still be regarded as stationary when considered over sufficiently large time scales, despite displaying nonstationary behavior locally. Standard global information-theoretic measures are unable to provide time-resolved information about the process dynamics, which is however essential for studying systems exhibiting transient or multi-scale behavior. As discussed in Sect. 3.2, this limitation can be addressed through local approaches that preserve the overall stationarity assumption while evaluating the probability distributions of variables that represent the present and past states of processes at specific time instants (Lizier, 2012b). In particular, local measures can assume positive or negative values, indicating whether past states provide informative or misinformative contributions to the present state. Furthermore, their temporal average coincides with the corresponding global measure (Lizier, 2012b). An alternative framework for time-resolved analysis is the time-varying approach, which relaxes the stationarity assumption by estimating the system dynamics at each time instant using data from short preceding windows. Within the linear parametric framework, this approach is typically implemented through the recursive estimation of least squares of TV-AR models (Antonacci et al. (2023)). Local and time-varying methods provide complementary insights into system behavior. In Antonacci et al. (2025a), it was shown that variations in local entropy measures – both in terms of mean and variance – reflect the surprise associated with state transitions, capturing both predictable and unpredictable aspects of system dynamics (Wibral et al. (2014a); Stramaglia et al. (2021); Barà et al. (2023c)). In contrast, variations in time-varying entropy measures primarily reflect abrupt changes in the internal dynamics of the

system and are therefore related mainly to predictable components (Antonacci et al. (2023)).

The ability of ER and IS measures to track complexity modulation was demonstrated in Sects. 3.1.2 and 3.2.2 across systems of different nature. In particular, reductions in system complexity – associated with increases in the coupling coefficient of AR processes or with altered chaotic regimes in coupled logistic maps – resulted in decreased ER values. Conversely, IS increased with higher regression coefficients in linear systems and with altered chaotic dynamics in nonlinear deterministic systems. Although local IS effectively captures temporal variations in predictability, these trends are primarily reflected in the mean IS values computed over segments with homogeneous dynamics. Additional insights can be obtained from the variability of the local measure within these segments, as fluctuations in local IS reflect stochastic and less predictable components of the underlying process dynamics.

Findings reported in Sect. 3.1.2 demonstrated how selecting an appropriate estimation method and parameter configuration is a nontrivial task and strongly depends on the characteristics of the analyzed system. Linear parametric estimators are widely used for complexity analysis but are primarily suited for Gaussian processes and exhibit limited ability to capture nonlinear dynamics (Xiong et al., 2017; Barrett et al., 2010). This limitation is evident in systems with deterministic dynamics, where the linear estimator failed to detect complexity reductions associated with nonlinear behavior (Fig. 3.6 (panel (*a*)), and Fig. 3.7), and did not adequately capture the increased unpredictability induced by superimposed noise, which was not reflected in the variability of local IS (Fig. 3.11 (panel (*b*)). Despite these limitations, the linear parametric approach remains relatively robust to short data lengths, providing reliable estimates even for limited time series (Fig. 3.5 (panel (*a*))). Moreover, in the case of AR processes, it can be naturally extended to the frequency domain, enabling spectral characterization of process dynamics, thus to investigate the distribution of information across frequency bands (Geweke, 1982).

To overcome the limitations of parametric models, several model-free approaches have been proposed to move beyond the simple linear representation provided by parametric methods, enabling the direct quantification of probability distributions from data. Among these, the nearest-neighbor estimator demonstrates strong performance for non-Gaussian processes (Xiong et al., 2017; Lombardi and Pant, 2016). Consistently, our results show that this estimator effectively captures complexity changes in both simulated linear dynamics (Figs. 3.3 and 3.5 (panels (*b*))) and mixed linear-chaotic dynamics (Figs. 3.6 and 3.8 (panels (*b*))). Specifically, in the case of the AR dynamics, ER_{knn} closely follows the theoretical measure and reproduces the statistically significant variations identified by the linear estimator (Fig. 3.4). Although the method may exhibit bias due to the dimensionality

of the embedding space used for neighbor search, it provides stable ER estimates across different embedding dimensions m and numbers of neighbors k (Fig. 3.3 (panels (b))). Additionally, the bias associated with the time series length N is negligible compared with discretization-based model-free approaches (Fig. 3.5) (Faes and Porta, 2014).

Among discretization-based methods, the binning strategy is the most widely used (Porta et al., 1998, 2007a; Takahashi et al., 2012; Tobaldini et al., 2013). However, our results indicate that this approach is poorly suited for detecting subtle variations in system complexity. This limitation likely arises from the excessive coarse-graining introduced by quantization, which becomes unavoidable when analyzing short time series due to the curse of dimensionality (Faes and Porta (2014)). Permutation-based approaches, in contrast, require fewer patterns for a given embedding dimension and are therefore more efficient in characterizing process dynamics (Kugiumtzis (2013); Barà et al. (2024c)). Nevertheless, despite this method overall effectively identifies relevant changes in stochastic systems, in simulations involving mixed stochastic and deterministic dynamics it reveals reduced sensitivity to subtle nonlinear variations (Fig. 3.6 (panel (d)) and Fig. 3.7), primarily because amplitude information is disregarded (Cuesta Frau et al. (2019)).

Finally, computational complexity is an important factor when selecting an estimation approach. Although the computational costs reported in Sect. 3.1.1 depend on the specific implementation and computing environment, it is generally recognized that linear parametric and discretization-based methods are computationally less demanding than nearest-neighbor estimators. Consequently, significant efforts have been devoted to developing more efficient nearest-neighbor algorithms, given their superior ability to capture nonlinear complexity (Arya et al. (1998); Merkwirth et al. (2000); Samet (2007)).

The proposed simulation settings enables the investigation of the feasibility of ER and IS measures under relatively simple and well-established dynamics, as those of the stochastic AR and deterministic chaotic systems. These models provide suitable settings for deriving general insights on the ability of these measures to characterize process unpredictability and regularity, as well as for identifying appropriate and feasible estimation settings. Nevertheless, further validation studies should be conducted using models that more realistically reproduce physiological dynamics. For instance, in the context of cardiac electrical activity, the probabilistic point-process model proposed by Barbieri et al. (2005) and deterministic integral pulse frequency modulation models, such as that introduced by Candia-Rivera et al. (2021), could be employed to generate heartbeat dynamics, while the more physiologically realistic model described in Castiglioni et al. (2025) may be used to simulate the generation of cardiac action potentials. In addition, alternative approaches based on multiplicative cascades could be exploited to generate complex dynamics reproduc-

ing the multifractal properties of heartbeat dynamics (Lin, 2003). Data generated by using the latter class of models should be investigated across multiple time scales, thereby requiring longer recordings and providing an appropriate framework for assessing the feasibility of the multiscale extensions of the proposed metrics.

In conclusion, the validation studies presented in this chapter suggest that the linear parametric approach remains the most efficient and reliable method for complexity estimation, at least when there are no significant deviations from the assumption of Gaussianity of data. Among the model-free strategies, the nearest neighbor estimators provides particularly robust performance in both linear and nonlinear settings. Their robustness and stability with respect to parameter choices explain their widespread adoption despite higher computational costs. Among discretization-based estimation methods, the permutation approaches offer a simple and effective strategy for assessing system complexity when appropriate embedding parameters are selected. With regard to the possibility of obtaining a time-resolved evaluation of system dynamics, the use of local estimation approaches has been shown to be effective in detecting the presence of local transient nonstationarities in system exhibiting repetitive dynamical patterns, thus an overall stationary characterization.

Chapter 4

Pairwise analysis of link dynamics

This chapter first introduces the Mutual Information Rate (MIR) metric and its decomposition strategies. These approaches quantify the information exchanged over time between two coupled systems, capturing both individual systems dynamics and their mutual causal influences (Sect. 4.1). Subsequently, the Predictive Information (PrI) measure is presented to assess the uncertainty in the current state of a process that can be resolved through knowledge of the past states of the entire system (Sect. 4.2). Finally, methodologies for investigating the dynamics of individual links within a multivariate network framework are discussed (Sect. 4.3).

Let us consider a link within the dynamic network in Fig. 3.1 comprising the nodes representing the systems $\mathcal{Y}$ and $\mathcal{X}_j$, with $j = 1, \dots, M$. The latter can be characterized as similarly done for the system $\mathcal{Y}$ in Chapter 3. Specifically, it is possible to refer to a stationary stochastic process X_j which describes the states of the system over time, i.e., $X_j = \{X_{j,n}\}$ with n the time counter, by considering $X_{j,n}$ as the scalar random variable representing the current state of $X_{j,n}$ and $X_{j,n-1:n-m} = [X_{j,n-1} \dots X_{j,n-m}]$ as the vector random variable representing the past states of the process X_j over the past m lags. Also in this case, the entire past history of the process is represented by the infinite-dimensional variable $X_{j,<n} = \lim_{m\to\infty} X_{j,n-1:n-m}$.

4.1. Mutual Information Rate and its decomposition terms

The *mutual information rate* is a well-defined measure assessing the dynamic coupling between a pair of time series quantifying the information exchanged over time by the two coupled systems. By considering the stationary and ergodic stochastic processes Y and X_j, MIR is defined as the limit of the rate at which the MI between

the two processes increases over time (Duncan, 1970), i.e.,

$$I_{X_j;Y} = \lim_{n\to\infty} \frac{1}{n} I(X_{j,<n}; Y_{<n}). \tag{4.1}$$

Although MIR is formally defined for infinite-dimensional variables, its reliable estimation in practical applications is made possible by decomposing it into information-theoretic quantities such as conditional entropy and conditional mutual information (Chicharro, 2011).

Accordingly, the first decomposition strategy expresses MIR in terms of the dynamical complexity of the individual processes and of the joint process, by exploiting the ER measure defined in Eq. 3.3. Specifically, MIR is obtained as the difference between the sum the ERs of the two individual processes, $H_{X_j} = H(X_{j,n}|X_{j,<n})$ and $H_Y = H(Y_n|Y_{<n})$ – represented by the areas contoured in azure and yellow in the Venn diagram of Fig. 4.1, respectively – and their joint ER, $H_{X_j,Y} = H(X_{j,n}, Y_n|X_{j,<n}, Y_{<n})$ – instead represented by the area contoured in red. Formally, this relationship can be written as:

$$I_{X_j;Y} = H_{X_j} + H_Y - H_{X_j,Y}, \tag{4.2}$$

resulting in the area with the purple contour in the Venn diagram.

On the other hand, the second decomposition strategy emphasizes the causal relationships between the two coupled processes by introducing the asymmetric directional measure of *Transfer Entropy* (TE), which quantifies the dynamic flow of information from one process to another (Vicente et al., 2011). In addition, a symmetric measure of instantaneous interaction is considered, capturing the information exchanged between the two processes at zero-lag. This measure is also interpreted as a measure of *Instantaneous Causality* (IC) (Chicharro, 2011). Formally, TE is defined as the conditional mutual information between the current state of one of the processes, i.e., Y or X_j, and the past states of the other process, i.e., X_j or Y, conditioned to the past of the former, i.e.,

$$T_{X_j\to Y} = I(Y_n; X_{j,<n}|Y_{<n}) = H(Y_n|Y_{<n}) - H(Y_n|X_{j,<n}, Y_{<n}), \tag{4.3a}$$

$$T_{Y\to X_j} = I(X_{j,n}; Y_{<n}|X_{j,<n}) = H(X_{j,n}|X_{j,<n}) - H(X_{j,n}|X_{j,<n}, Y_{<n}). \tag{4.3b}$$

These terms – represented by the orange and blue areas in the Venn diagram shown in Fig. 4.1, respectively – quantify the portion of uncertainty associated with the present state of the first process that is resolved by the knowledge of the past of the second process, beyond what is already explained by the self-dynamics of the former. Similarly, the instantaneous causality term – represented by the green area in Fig. 4.1 – is formally expressed as the conditional mutual information between

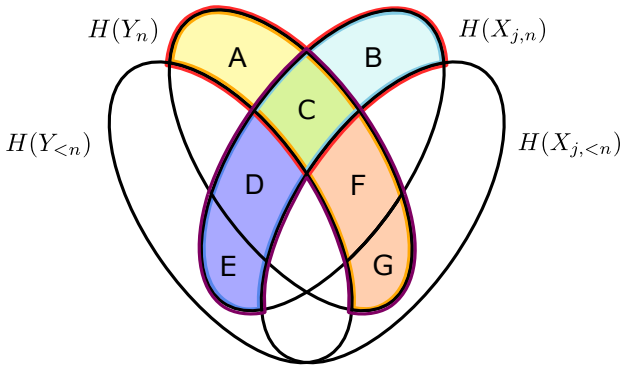

Figure 4.1: Venn diagram representing the MIR decomposition terms for two stochastic processes X_j and Y. Taking the areas of the four circles as the entropy of the current state (upper curves) and of the past states (lower curves) of X_j (right) and Y (left), it is possible to observe that: the entropy rate of X_j (H_{X_j}) is the union of B, C, D, and E (area with azure contour); the entropy rate of Y (H_Y) is the union of A, C, F, and G (area with yellow contour); the joint entropy rate of X_j and Y ($H_{X_j,Y}$) is the union of A, B, and C (area with red contour); the transfer entropy from X_j to Y ($T_{X_j \to Y}$) is the union of F and G (area in orange); the transfer entropy from Y to X_j ($T_{Y \to X_j}$) is the union of D and E (area in blue); the instantaneous causality between X_j and Y ($I_{X_j \cdot Y}$) is the portion in C (area in green); and the MIR ($I_{X_j;Y}$) is the union of C, D, E, F, and G (area with purple contour). The figure was modified from Barà et al. (2023b).

the current states of the two processes conditioned on their own past states, i.e.,

$$I_{X_j \cdot Y} = I(Y_n; X_{j,n} | Y_{<n}, X_{j,<n}) = H(Y_n | Y_{<n}, X_{j,<n}) - H(Y_n | Y_{<n}, X_{j,n}, X_{j,<n}). \tag{4.4}$$

This term quantifies the portion of uncertainty about the current state of one process that can be resolved by knowledge of the current state of the other process, beyond what is already explained by their past histories.
Considering the quantities defined in Eqs. 4.3 and 4.4, MIR can be expressed as the sum of the two directional transfer entropies, $T_{X_j \to Y} = I(Y_n; X_{j,<n} | Y_{<n})$ and $T_{Y \to X_j} = I(X_{j,n}; Y_{<n} | X_{j,<n})$, and the instantaneous information shared between X_j and Y at zero-lag, $I_{X_j \cdot Y} = I(X_{j,n}; Y_n | X_{j,<n}; Y_{<n})$, i.e.,

$$I_{X_j;Y} = T_{X_j \to Y} + T_{Y \to X_j} + I_{X_j \cdot Y} \tag{4.5}$$

which again corresponds to the region enclosed in the purple contour in the Venn diagram shown in Fig. 4.1.

The mathematical derivations leading to the two aforementioned decompositions, starting from the definition of ER for an ergodic stochastic process given in Eq. 3.1, can be found in the supplementary material of Mijatovic et al. (2021).

4.1.1. Mutual information rate estimation strategies

Let us consider the N-length time series $y = \{y_i\}$ and $x_j = \{x_{j,i}\}$, $i = 1, \ldots, N$, representing the stationary dynamical processes Y and X_j, respectively. To evaluate MIR and its decomposition measures, it is necessary to assume that the histories of the two processes can be approximated by a finite number of past observations. Accordingly, both Y and X_j are modeled as m-order ergodic Markov processes, such that $Y_{<n} \approx Y_{n-1:n-m}$ and $X_{j,<n} \approx X_{j,n-1:n-m}$. Under this assumption, the quantities appearing in Eqs. 4.2 and 4.5 can be computed as combination of the ER terms into which each of the decomposition measures can be further decomposed.

Specifically, MIR and its decomposition measures can be estimated using continuous approaches based on linear parametric models or nonlinear nearest-neighbor strategies, as well as discrete methods relying on binning or permutation techniques. The implementation of these estimators is available in the *Mutual Information Rate* (*MIR*) MATLAB-toolbox available on GitHub.

Linear parametric estimator

Assuming that the bivariate process $\boldsymbol{S} = \{Y, X_j\}$ has a joint Gaussian distribution, the bivariate AR (2AR) model can be used to relate the dynamics of the current state of the whole process to its past states, i.e.,

$$\boldsymbol{S}_n = \sum_{k=1}^{p} \boldsymbol{A}_k \boldsymbol{S}_{n-k} + \boldsymbol{U}_n, \tag{4.6}$$

where p is the order of the 2AR model, $\boldsymbol{S}_n = [Y_n \;\; X_{j,n}]^\top$ includes the current state of the joint process, $\boldsymbol{A}_k$ is a 2×2 coefficient matrix relating the present and the past states of the two processes at lag k, and $\boldsymbol{U}_n$ is a bivariate process formed by two white and uncorrelated zero-mean Gaussian noises with covariance matrix $\Sigma_{\boldsymbol{U}} = \mathbb{B}[\boldsymbol{U}_n \, \boldsymbol{U}_n^\top] = \begin{bmatrix} \sigma^2_{U_Y} & \sigma^2_{U_Y X_j} \\ \sigma^2_{U_{X_j Y}} & \sigma^2_{U_{X_j}} \end{bmatrix}$. Moreover, the restricted AR models predicting the current state of the single processesfrom their own past states can be identified to describe the dynamics of the processes Y and X_j. These can be written as follows:

$$Y_n = \sum_{k=1}^{\infty} b_{YY,k} Y_{n-k} + W_{Y,n}, \tag{4.7a}$$

$$X_{j,n} = \sum_{k=1}^{\infty} b_{X_j X_j,k} X_{j,n-k} + W_{X_j,n}, \tag{4.7b}$$

where $b_{YY,k}$ and $b_{X_j X_j,k}$ are the AR coefficients of the processes Y_n and $X_{j,n}$ at lag k, respectively, and $W_{Y,n}$ and $W_{X_j,n}$ are two white Gaussian noises with variance $\sigma^2_{W_Y}$ and $\sigma^2_{W_{X_j}}$, respectively.

By exploiting the linear parametric formulation of the ER measure in Eq. 3.5, the following estimators can be derived for MIR and its decomposition terms (Pinto et al., 2025):

$$\hat{H}_{X_j} = \frac{1}{2} \ln \left(2\pi e \hat{\sigma}^2_{W_{X_j}} \right), \tag{4.8a}$$

$$\hat{H}_Y = \frac{1}{2} \ln \left(2\pi e \hat{\sigma}^2_{W_Y} \right), \tag{4.8b}$$

$$\hat{H}_{X_j,Y} = \frac{1}{2} \ln \left((2\pi e)^2 |\hat{\Sigma}_{\boldsymbol{U}}| \right), \tag{4.8c}$$

$$\hat{T}_{X_j \to Y} = \frac{1}{2} \ln \frac{\hat{\sigma}^2_{W_Y}}{\hat{\sigma}^2_{U_Y}}, \tag{4.8d}$$

$$\hat{T}_{Y \to X_j} = \frac{1}{2} \ln \frac{\hat{\sigma}^2_{W_{X_j}}}{\hat{\sigma}^2_{U_{X_j}}}, \tag{4.8e}$$

$$\hat{I}_{X_j \cdot Y} = \frac{1}{2} \ln \frac{\hat{\sigma}^2_{U_{X_j}} \hat{\sigma}^2_{U_Y}}{|\hat{\Sigma}_U|}, \tag{4.8f}$$

$$\hat{I}_{X_j ; Y} = \frac{1}{2} \ln \frac{\hat{\sigma}^2_{W_{X_j}} \hat{\sigma}^2_{W_Y}}{|\hat{\Sigma}_{\boldsymbol{U}}|}. \tag{4.8g}$$

To compute the variance of the prediction errors appearing in the equations above, both full and restricted AR models must be identified. After determining the optimal order p using one of the approaches mentioned in Sect. 3.1.1 or fixed to a given value, the full 2AR model can be estimated using the OLS method. In contrast, the restricted models are theoretically of infinite order, making their identification challenging when dealing with finite-length data. A common approximation is to truncate the restricted models to the same order as the full model, providing a compromise between estimation bias and variance, although this limits the reliability of the estimates (Stokes and Purdon, 2017). To address this limitation, alternative approaches estimate the parameters of the restricted models directly from the full 2AR model. Notable methods include state-space (SS) modeling (Barnett and Seth, 2015; Solo, 2016) and approaches based on solving the YW equations using the autocovariance and cross-covariance matrices of the bivariate process (Barnett and Seth, 2014). The SS approach relies on a discrete linear model formulated through first-order difference equations, which relate the current and past states of the bivariate process via an unobserved state vector (Antonacci et al., 2020). Conversely, as discussed in Sect. 3.1.1, the YW-based approach computes the autocovariance matrices of the bivariate process up to a lag $q > p$ and reorganizes their elements to determine the variances and covariances required for computing the information dynamics. A complete derivation of these quantities for a bivariate process is provided in (Faes et al., 2015c).

Nearest-neighbor estimator

By exploiting the KSG nearest-neighbor approach, nonlinear and non-parametric estimates of the quantities decomposing MIR can be obtained. In this framework, the neighbor search is performed in the joint space of both current and past states of the two processes, i.e., $\{Y_n\ Y_{n-1:n-m}\ X_{j,n}\ X_{j,n-1:n-m}\}$, and the number of points falling within the same distance in the observed lower-dimensional subspaces is counted. Accordingly, the following formulations for the MIR decomposition terms are derived (Pinto et al., 2025):

$$\hat{H}_{X_j} = \frac{1}{N-m}\sum_{n=1}^{N-m}(\ln \epsilon_{n,k} + \psi(N_{X_{j,n-1:n-m}}+1) - \psi(N_{X_{j,n}X_{j,n-1:n-m}}+1)), \tag{4.9a}$$

$$\hat{H}_{Y} = \frac{1}{N-m}\sum_{n=1}^{N-m}(\ln \epsilon_{n,k} + \psi(N_{Y_{n-1:n-m}}+1) - \psi(N_{Y_nY_{n-1:n-m}}+1)), \tag{4.9b}$$

$$\hat{H}_{X_j,Y} = -\psi(k) + \frac{1}{N-m}\sum_{n=1}^{N-m}(2\ln \epsilon_{n,k} + \psi(N_{X_{j,n-1:n-m}Y_{n-1:n-m}}+1)), \tag{4.9c}$$

$$\begin{aligned}\hat{T}_{X_j\to Y} = \frac{1}{N-m}\sum_{n=1}^{N-m}&(\psi(N_{Y_nX_{j,n-1:n-m}Y_{n-1:n-m}}+1) - \psi(N_{X_{j,n-1:n-m}Y_{n-1:n-m}}+1)\\ &- \psi(N_{Y_nY_{n-1:n-m}}+1) + \psi(N_{Y_{n-1:n-m}}+1)),\end{aligned} \tag{4.9d}$$

$$\begin{aligned}\hat{T}_{Y\to X_j} = \frac{1}{N-m}\sum_{n=1}^{N-m}&(\psi(N_{X_{j,n}X_{j,n-1:n-m}Y_{n-1:n-m}}+1) - \psi(N_{X_{j,n-1:n-m}Y_{n-1:n-m}}+1)\\ &- \psi(N_{X_{j,n}X_{j,n-1:n-m}}+1) + \psi(N_{X_{j,n-1:n-m}}+1)),\end{aligned} \tag{4.9e}$$

$$\begin{aligned}\hat{I}_{X_j\cdot Y} = \psi(k) + \frac{1}{N-m}\sum_{n=1}^{N-m}&(\psi(N_{X_{j,n-1:n-m}Y_{n-1:n-m}}+1)\\ &- \psi(N_{X_{j,n}X_{j,n-1:n-m}Y_{n-1:n-m}}+1) - \psi(N_{Y_nX_{j,n-1:n-m}Y_{n-1:n-m}}+1)),\end{aligned} \tag{4.9f}$$

$$\begin{aligned}\hat{I}_{X_j;Y} = \psi(k) + \frac{1}{N-m}\sum_{n=1}^{N-m}&(\psi(N_{Y_{n-1:n-m}}+1) + \psi(N_{X_{j,n-1:n-m}}+1)\\ &- \psi(N_{X_{j,n}X_{j,n-1:n-m}}+1) - \psi(N_{Y_nY_{n-1:n-m}}+1) - \psi(N_{X_{j,n-1:n-m}Y_{n-1:n-m}}+1)),\end{aligned} \tag{4.9g}$$

with $\psi(\cdot)$ being the digamma function, N the number of available realizations of the variables, and k the number of neighbors counted for the samples in the highest-dimensional space reaching the maximum distance $\epsilon_{n,k}/2$. $N_{Y_{n-1:n-m}}$ and $N_{X_{j,n-1:n-m}}$ indicate the number of samples within a distance of $\epsilon_{n,k}/2$ from the samples in the spaces accounting for the past states of the processes Y and X_j, respectively, while $N_{Y_nY_{n-1:n-m}}$ and $N_{X_{j,n}X_{j,n-1:n-m}}$ those related to spaces accounting for both current and past states of the same processes. Moreover, $N_{X_{j,n-1:n-m}Y_{n-1:n-m}}$ is used to indicate the number of samples counted within the same range in the space visiting the past of both processes, and $N_{Y_nX_{j,n-1:n-m}Y_{n-1:n-m}}$ and $N_{X_{j,n}X_{j,n-1:n-m}Y_{n-1:n-m}}$ those in the space visiting, apart from the past of both processes, also the current states of the processes

Y and X_j, respectively.

Discrete estimation approaches

Discrete estimation approaches based on binning and permutation strategies can be readily applied within the MIR framework. In both cases, the computation reduces to evaluating the entropy terms, which are then combined to obtain the decomposition measures. In the binning-based approach, the continuous variables representing the current and past states of the processes are first quantized to obtain discrete random variables. The entropy terms are then computed using the frequentistic approach, as described in Sect. 2.3.3. In contrast, the permutation-based approach constructs discrete variables by evaluating the rank ordering of samples within the observations of the current and past states of the analyzed processes Y and X_j, as detailed in Sect. 2.3.4.

Specifically, the variables $X_{j,n-1:n-m}$ and $[X_{j,n}X_{j,n-1:n-m}]$, as well as $Y_{j,n-1:n-m}$ and $[Y_{j,n}Y_{j,n-1:n-m}]$ are considered for estimating the individual entropy rate terms $\hat{H}_{X_j}$ and $\hat{H}_Y$, respectively; while the joint variables $[X_{j,n}Y_nX_{j,n-1:n-m}Y_{j,n-1:n-m}]$ and $[X_{j,n-1:n-m}Y_{j,n-1:n-m}]$ are evaluated to evaluate the joint entropy term $\hat{H}_{X_j,Y}$. Moreover, the entropy of the variables $[Y_nX_{j,n-1:n-m}Y_{j,n-1:n-m}]$ and $[X_{j,n}X_{j,n-1:n-m}Y_{j,n-1:n-m}]$ has to be estimated to compute the causality terms $\hat{T}_{X_j\to Y}$, $\hat{T}_{Y\to X_j}$, and $\hat{I}_{X_j\cdot Y}$. As discussed in Sect. 2.4, a crucial aspect in applying discretization-based approaches is the selection of the estimation parameters, namely the memory length m of the processes and the number of quantization levels b used in the binning approach. Given the challenges associated with estimating entropy terms for high-dimensional variables, the empirical rule mentioned above requires that the alphabet size of the highest-dimensional variable $[X_{j,n}Y_nX_{j,n-1:n-m}Y_{j,n-1:n-m}]$ – that is equal to b^{2m+2} in the case of binning approach and $((m+1)!)^2$ in the case of the permutation approach – remains lower than or equal to N (Barà et al., 2023b).

4.1.2. *Validation on bivariate autoregressive and chaotic processes*

The analytical framework for the computation of MIR was validated through different simulation settings designed to characterize coupling and causal relationships in a bivariate system. In particular, two simulation studies from Pinto et al. (2025) are reported to assess the behavior of continuous-valued estimators, while the simulation presented in Barà et al. (2023b) is used to evaluate the performance of discretization-based approaches.

Bidirectionally coupled VAR process

Let us consider a linear bidirectionally coupled bivariate second-order VAR process characterized by fixed self-dependency effects of both processes and modulated

causal interactions (Faes et al., 2015c):

$$\begin{aligned} X_n &= -0.5X_{n-2} + \beta_{Y\to X} Y_{n-1} + U_{X,n}, \\ Y_n &= -0.5Y_{n-2} + \beta_{X\to Y} X_{n-1} + U_{Y,n}, \end{aligned} \tag{4.10}$$

where $U_{X,n}$ and $U_{Y,n}$ denote independent Gaussian white noise processes with zero mean and unit variance, and the parameters $\beta_{Y\to X}$ and $\beta_{X\to Y}$ ranging from 0 to 1 with a step of 0.1 represent the strength of the causal interactions from Y to X and *vice versa*, respectively. For each combination of the two causal parameters, one-hundred realizations of 500 samples were generated.

The MIR measures were computed by fixing the model order to $p = 2$ for the linear estimation approach, and by using an embedding dimension $m = 2$ with $k = 10$ neighbors for the nonlinear nearest-neighbor method. The parameters p and m were set according to the theoretical order of the investigated process, while the number of neighbor k by looking at the previous literature on the estimation approach. The statistical significance of each decomposition term was assessed by generating one-hundred pairs of surrogate data for each simulation setting, following the procedures described in Sect. A.2.1 for H_X and H_Y and in Sect. A.2.2 for $I_{X;Y}$, $H_{X,Y}$, $T_{X\to Y}$, $T_{Y\to X}$, and $I_{X\cdot Y}$. Specifically, a significance level of $\alpha = 0.5$ was fixed.

Fig. 4.2 shows the results of MIR and its decomposition terms computed using both linear parametric (panel (*a*)) and nearest-neighbor (panel (*b*)) estimation strategies showing a high degree of similarity between the two approaches. Both methods reveal increasing values of $I_{X;Y}$ in the same direction of both coupling parameters with non significant values only for very low $\beta_{X\to Y}$ and $\beta_{Y\to X}$ values. This trend mainly results from an increasing regularity of the process X when the coupling strength $\beta_{Y\to X}$ increases and the dynamics of Y are not dependent on those of X, and from an increasing complexity of X for strong bidirectional coupled dynamics, visible in terms of H_X modulations. The same behavior is also shown by the complexity of the process Y, represented by H_Y. Moreover, looking at the trends of $H_{X,Y}$, it is possible to observe how the overall system dynamic is complex when the two processes are mainly mutually independent, i.e., when there is no strong unidirectional or bidirectional coupling. In terms of causality, the expected increase in $T_{X\to Y}$ is observed with the increase in $\beta_{X\to Y}$, independently of the value of $\beta_{Y\to X}$, with a statistically non significant causality for low values of $\beta_{X\to Y}$; the same trend is observed in the opposite direction when considering $T_{Y\to X}$. Moreover, due to the absence of a modeled instantaneous effect between the two processes, the values of $I_{X\cdot Y}$ are close to zero and are not statistically significant for all possible values of both $\beta_{X\to Y}$ and $\beta_{Y\to X}$.

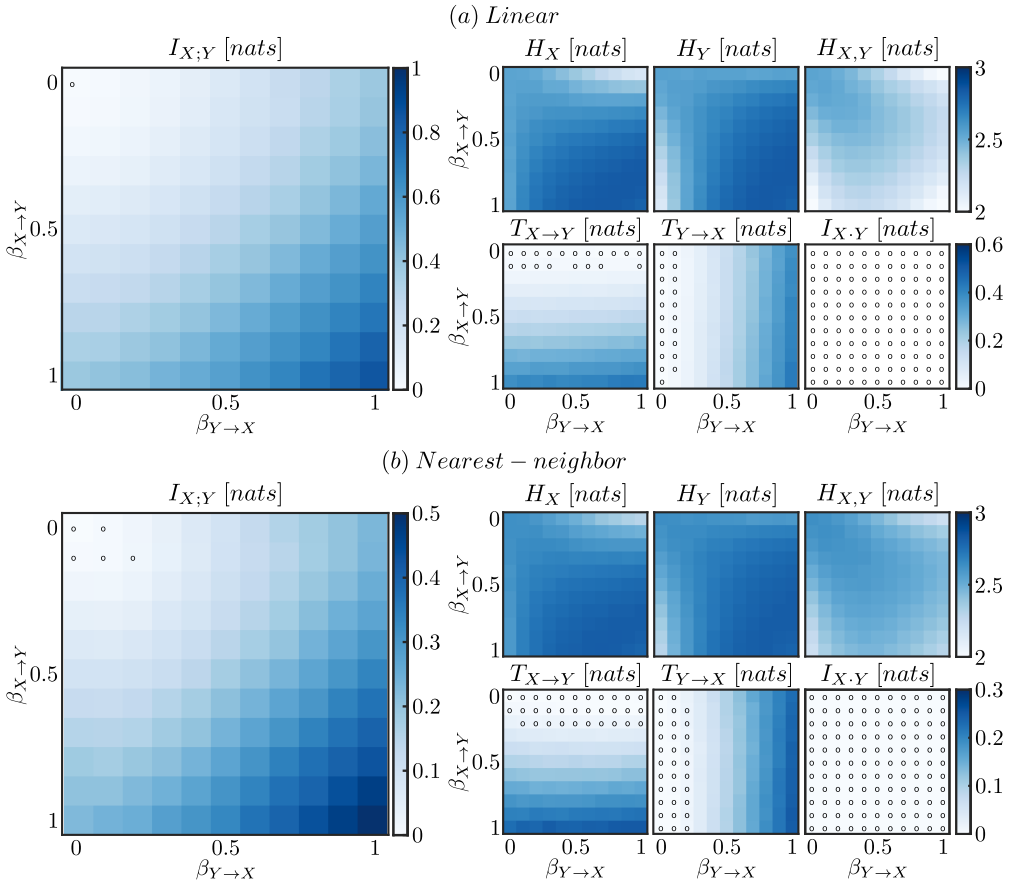

Figure 4.2: Heatmaps of the mean values over one-hundred realizations of the MIR and its decomposition measures computed through linear (panel (*a*)) and nearest-neighbor (panel (*b*)) estimation approaches on bidirectionally coupled linear VAR process at varying the coupling strength from X to Y and from Y to X represented by the parameters $\beta_{X\to Y}$ and $\beta_{Y\to X}$, respectively. Black empty circles indicate combinations of parameters where less than 40% of realizations are significant. The figure was modified from Pinto et al. (2025).

Coupled logistic maps

In this section, the bivariate system proposed by Sugihara et al. (2012), widely studied for coupling and causal relationships, is considered. The system consists of two coupled logistic maps, whose chaotic behavior and bidirectional coupling strengths are parametrically controlled as follows:

$$\begin{aligned} X_n &= X_{n-1}(r_x - r_x X_{n-1} - \beta_{Y\to X} Y_{n-1}), \\ Y_n &= Y_{n-1}(r_y - r_y Y_{n-1} - \beta_{X\to Y} X_{n-1}), \end{aligned} \tag{4.11}$$

where r_x and r_y denote the growth rates of X and Y, respectively, and $\beta_{Y\to X}$ and $\beta_{X\to Y}$ represent the coupling strength from Y to X and *vice versa*. One-hundred realizations of the system were generated by varying both initial conditions and parameters r_x and r_y to ensure the system chaotic behavior. Specifically, 500-point long time series were considered for subsequent analysis after removing transient dynamics.

The MIR measures were evaluated by using the optimal model order estimated through the AIC criterion for the linear estimation approach and by fixing a dimension of embedding $m = 3$ and a number of neighbors $k = 10$ for the nearest-neighbor method. In this case, the parameter m was set according with the average of the optimal values of p. Also in this case, the statistical significance of each decomposition term was assessed by generating one-hundred pairs of surrogate data for each simulation setting, following the procedure described in Appendix as done for the previous simulation, by fixing a significance level of $\alpha = 0.5$.

Fig. 4.3 depicts the results of MIR and its decomposition terms computed on the coupled logistic maps using both linear parametric (panel (*a*)) and nearest-neighbor (panel (*b*)) estimation approaches, highlighting greater feasibility for the results obtained via the nonlinear model-free strategy. Indeed, even if an increase of MIR $I_{X;Y}$ is observed with the parametric approach when both $\beta_{X\to Y}$ and $\beta_{Y\to X}$ increase, the entropy rate terms show low and non clearly distributed values with the coupling parameters, and also the causality terms report higher values of $T_{X\to Y}$ and $T_{Y\to X}$ as $\beta_{X\to Y}$ and $\beta_{Y\to X}$ increase, respectively, statistically significant just for high values of the coupling parameters. On the other hand, the nearest-neighbor approach highlights low values of the entropy rate terms when the corresponding coupling parameter is lower than 0.25 and a more evident increase of the causality terms with $\beta_{X\to Y}$ and $\beta_{Y\to X}$ with higher significance. As expected, the instantaneous causality is not revealed by both estimation approaches.

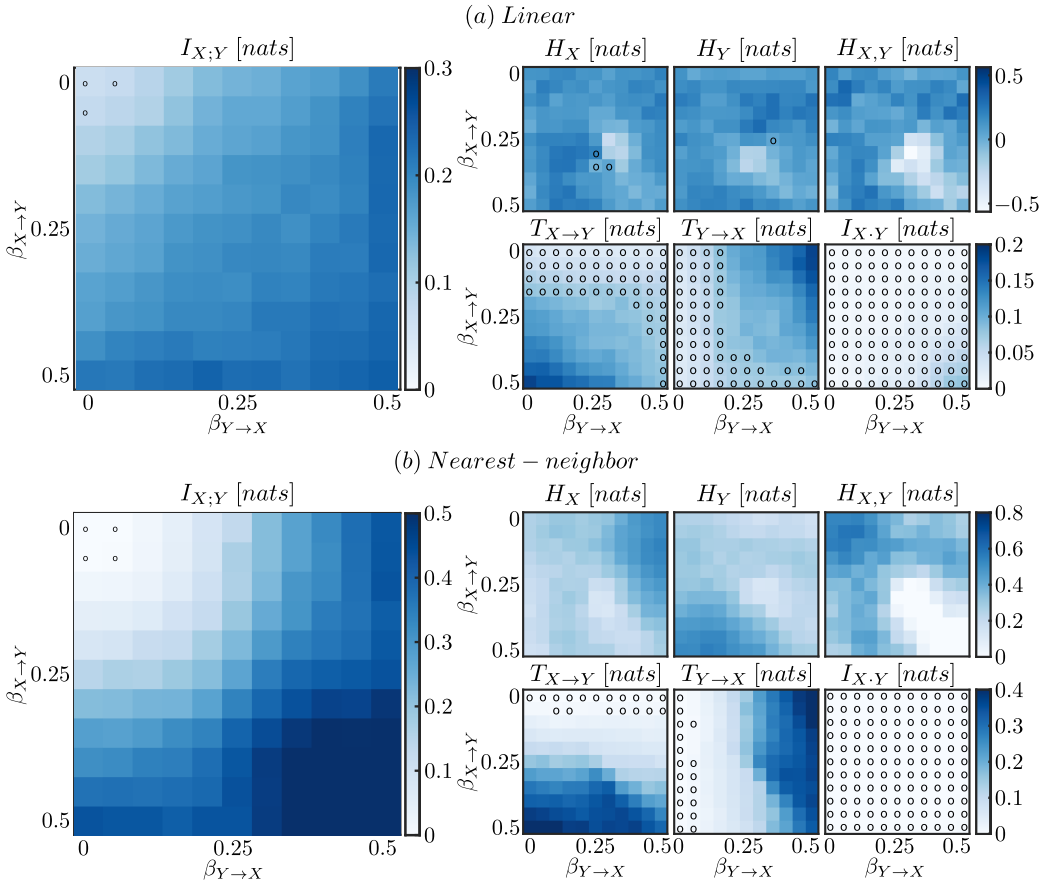

Figure 4.3: Heatmaps of the mean values over one-hundred realizations of the MIR and its decomposition measures computed through linear (panel (*a*)) and nearest-neighbor (panel (*b*)) estimation approaches on two coupled logistic maps at varying the coupling strength from X to Y and from Y to X represented by the parameters $\beta_{X\to Y}$ and $\beta_{Y\to X}$, respectively. Black empty circles indicate combinations of parameters where less than 40% of realizations are significant. The figure was modified from Pinto et al. (2025).

Coupled non-identical Hènon maps

A nonlinear chaotic system composed of two coupled non-identical Hènon maps is defined as follows (Faes et al., 2008b; Wiesenfeldt et al., 2001):

$$\begin{aligned} X_n &= 1.4 - X_{n-1}^2 + 0.3X_{n-2} + c_2(X_{n-1}^2 - Y_{n-1}^2), \\ Y_n &= 1.4 - Y_{n-1}^2 + 0.1Y_{n-2} + c_1(Y_{n-1}^2 - X_{n-1}^2), \end{aligned} \tag{4.12}$$

with c_1 and c_2 being the constants determining the strength of coupling in the directions from X to Y and from Y to X, respectively. Specifically, a weak coupling was determined from Y to X by fixing the parameter c_2 to 0.05, while that in the opposite direction was varied by shifting the parameter c_1 from 0 to 0.3 in steps of 0.05. One-hundred realizations of the process were generated for each value of c_1, herein referred to as c, by randomly varying the initial conditions (equally for the two systems). Time series of 300-points length were considered for the analysis after the initial transient responses were discarded.

The framework of MIR was investigated by employing different parameter settings. Specifically, as regards the binning approach, the discretization parameters were fixed to $b = 2$ and $m = 3$, $b = 3$ and $m = 2$, and $b = 4$ and $m = 1$ as to deal with a maximum of 256, 729, and 256 quantization levels, respectively. On the other hand, regarding the permutation approach, the embedding dimension was fixed to $m = 2$, $m = 3$, and $m = 4$ so as to work with ordinal patterns of maximum alphabets of size equal to 36, 576, and 14400. Also in this case, the statistical significance of each decomposition term was assessed by generating one-hundred pairs of surrogate data for each simulation setting, following the procedure described in Sects. A.2.1 and A.2.2 of the Appendix with a significance level of $\alpha = 0.05$.

Fig. 4.4 depicts mean and standard deviation of the estimated MIR values and of the other information terms computed over one-hundred realizations of the investigated system at varying the coupling strength from X to Y – represented by the parameter c – together with their statistical significance according to surrogate data analysis. In general, MIR $I_{X;Y}$ increases with the parameter c, capturing a larger exchange of information between the two processes. This trend is reflected by the rise in transfer entropy from X to Y and the rise in the instantaneous term $I_{X\cdot Y}$. Despite the absence of zero-lag interactions in the Hènon maps, the increase of this term is indicative of the high degree of synchronization observed in the dynamics when the two systems are strongly coupled. Furthermore, as expected, $T_{Y\to X}$ is relatively constant, given the independence of X from Y with respect to c. Conversely, the entropy rate terms show an increase in H_Y and a decrease in $H_{X,Y}$ with c, while H_X remains overall unaltered. These trends are indicative of an increasing complexity of Y and a decreasing complexity of the joint process, resulting from an increased dependence of Y on both X and its own past history (the latter is indeed related to the depen-

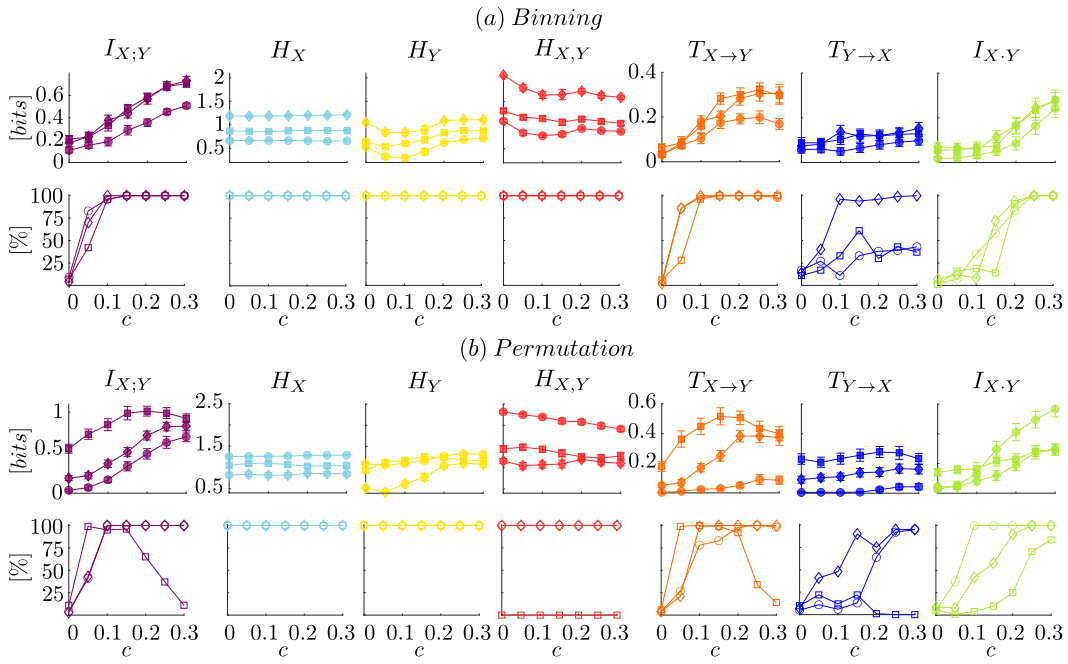

Figure 4.4: Errorbar plots depicting estimated values over one-hundred realization (top row) and plot of significance results (bottom row) for the MIR and its decomposition measures computed on bidirectionally coupled non-identical Hènon systems with fixed coupling strength from Y to X and modulated coupling from X to Y controlled by the parameter c through the binning-based (panel (a)) and the permutation-based (panel (b)) approaches. Results are shown for different combinations of the estimation parameters: $b = 2$ and $m = 3$ (circles), $b = 3$ and $m = 2$ (squares), and $b = 4$ and $m = 1$ (diamonds) for the binning; $m = 2$ (circles), $m = 3$ (diamonds), and $m = 4$ (squares) for the permutation. The figure was modified from Barà et al. (2023b).

dence of X on the past of Y). The percentage significance trends demonstrate a high degree of consistency with the average values, while concurrently exhibiting variations according to the various parameter settings. Specifically, with regard to the binning approach (panel (a)), the setting $b = 2$ and $m = 3$ yields lower values for all estimated metrics. This is due to the use of only two bins for the discretization of the amplitude of the series, which results in a significant loss of information. Similarly, the setting $b = 3$ and $m = 2$ leads lower significance due to the use of an alphabet size that exceeds the length of the series. Similarly, for the permutation approach (panel (b)), metrics computed with $m = 4$ exhibit reduced significance, whereas those computed with $m = 2$ fail to fully capture the system dynamics and changes in coupling strength due to the limited memory length.

4.2. Predictive Information framework

When the objective is to determine whether one system exerts a directional influence on another, it is necessary to distinguish between a *target* process and a *driver* process. Instead of merely assessing statistical dependence between the two systems,

the focus is on quantifying how much the past behavior of the driver contributes to predicting the current state of the target. In this context, the *predictive information* measure captures the uncertainty associated with the current state of a target process Y_n that can be resolved by the knowledge of the history of the entire system $[Y_{<n}, X_{j,<n}]$ (Chicharro et al., 2012; Faes et al., 2015c). Formally, this measure is defined as the mutual information between the current state of the target process and the past states of both target and driver, i.e.,

$$P_Y = I(Y_n; Y_{<n}, X_{j,<n}) = H(Y_n) - H(Y_n|Y_{<n}, X_{j,<n}). \tag{4.13}$$

To separate the statistical contribution of each system, PrI can be decomposed by using the chain rule for mutual information. In this manner, it can be expressed as the sum of distinct components reflecting different aspects of information dynamics (Faes et al., 2015c):

$$P_Y = S_Y + T_{X_j \to Y}, \tag{4.14a}$$

$$P_Y = C_{X_j \to Y} + S_{Y|X_j}. \tag{4.14b}$$

These alternative decompositions distinguish two components associated with the intrinsic dynamics of the target process Y – namely the *self-entropy* S_Y (SE), also referred to as information storage, and the *conditional self-entropy* $S_{Y|X_j}$ (cSE) – and two quantities related to the directed influence of the driver process on the target – the *transfer entropy* $T_{X_j \to Y}$ and the *cross-entropy* $C_{X_j \to Y}$ (CrossEn). While SE and TE have already been defined in Sects. 3.16 and 4.3, respectively, the remaining measures are defined as follows.

The cSE quantifies the portion of information in the present state of the target that is predictable from its own past beyond what is explained by the driver's past. Formally, it is defined as the conditional mutual information between the current state of the target Y_n and its past $Y_{<n}$ given the past of the driver $X_{j,<n}$ (Faes et al., 2015c), i.e.,

$$S_{Y|X_j} = I(Y_n; Y_{<n}|X_{j,<n}) = H(Y_n|X_{j,<n}) - H(Y_n|Y_{<n}, X_{j,<n}). \tag{4.15}$$

In the Venn diagram in Fig. 4.5, cSE is represented by the pink area.

Conversely, CrossEn measures the cross-predictability of the target from the driver, capturing asymmetric coupling between the two processes. It is defined as the mutual information between the current state of the target Y_n and the past state of the driver $X_{j,<n}$ (Faes et al., 2015c; Porta et al., 2023), i.e.,

$$C_{X_j \to Y} = I(Y_n; X_{j,<n}) = H(Y_n) - H(Y_n|X_{j,<n}), \tag{4.16}$$

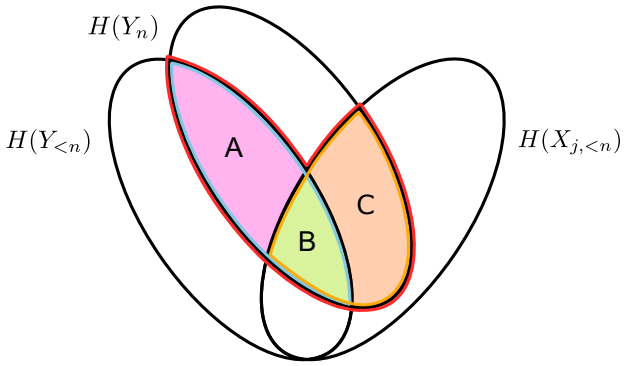

Figure 4.5: Venn diagram representing the PrI decomposition terms for two stochastic processes X_j and Y. Taking the areas of the three circles as the entropy of the current state of the (upper curve) and of the past states (lower curves) of X_j (right) and Y (left), it is possible to observe that: the self-entropy of Y (S_Y) is the union of A and B (area with azure contour); the transfer entropy from X_j to Y ($T_{X_j \to Y}$) is the portion E (area in orange); the cross entropy from X_j to Y ($C_{X_j \to Y}$) is the union of B and C (area with yellow contour); the conditional self-entropy of Y given X_j ($S_{Y|X_j}$) is the portion in A (area in pink); and the PrI (P_Y) is the union of A, B, and C (area with red contour).

In the Venn diagram in Fig. 4.5, cSE is represented by the area with the yellow contour.

Referring to Fig. 4.5, S_Y and $T_{X_j \to Y}$ measures are respectively represented by the area with the azure contour and the area in orange, while P_Y by the area with the red contour.

4.2.1. *Predictive information estimation strategies*

Let us consider the N-length time series $y = \{y_i\}$ and $x_j = \{x_{j,i}\}$, $i = 1, \ldots, N$, representative of the stationary target and driver dynamic processes, respectively. As in the case of MIR estimation, the computation of the information terms decomposing PrI requires assuming that both the target and driver processes are ergodic Markov processes, so that their past history can be approximated by a finite number of previous observations. Accordingly, the past states of the two processes are represented by $Y_{n-1:n-m}$ and $X_{j,n-1:n-m}$, where m denotes the order of the Markov processes.

In the following, the formulas for estimating the quantities involved in the PrI framework are derived for the estimation strategies considered so far. Also in this case, MATLAB codes for the computation of PrI quantities are collected in the *Predictive Information* (PrI) toolbox available on GitHub.

Linear parametric approach

Assuming that the bivariate process $\boldsymbol{S} = [Y, X_j]$ has a joint Gaussian distribution, the auto- and cross- regressive (ARX) model can be used to relate the dynamics of

the current state of the target process to the past state of both target and source processes, i.e.,

$$Y_n = \sum_{k=1}^{p} \boldsymbol{A}_k \boldsymbol{S}_{n-k} + U_n, \tag{4.17}$$

where p is the order of the ARX model, $\boldsymbol{A}_k$ is a 2×2 coefficient matrix relating the present and the past states of the two processes at lag k, and U_n is a white and uncorrelated zero-mean Gaussian noise process with variance σ_U^2. Moreover, the restricted auto- and cross- (X) regressive models describing the current dynamics of the target process from the past states of the target itself and of the source process, respectively, have to be identified:

$$Y_n = \sum_{k=1}^{\infty} b_{YY,k} Y_{n-k} + W_{Y,n}, \tag{4.18a}$$

$$Y_n = \sum_{k=1}^{\infty} b_{YX_j,k} X_{j,n-k} + W_{X_j,n}, \tag{4.18b}$$

with $b_{YY,k}$ and $b_{YX_j,k}$ being the AR and X coefficients at lag k, respectively, and $W_{Y,n}$ and $W_{X_j,n}$ two white Gaussian noises with variance $\sigma^2_{W_Y}$ and $\sigma^2_{W_{X_j}}$, respectively.

As discussed for the MIR decomposition framework, once the order of the full ARX model has been identified (or fixed), the model parameters can be estimated using the OLS method. The corresponding restricted AR and X models can instead be derived either through SS modeling or by solving the YW equations.

Subsequently, the variance of the target variable σ_Y^2, together with the variances of the residuals obtained from the different models, are used to compute the measures within the PrI framework, as reported below (Faes et al., 2015c):

$$\hat{S}_Y = \frac{1}{2} \ln \frac{\sigma_Y^2}{\sigma^2_{W_Y}}, \tag{4.19a}$$

$$\hat{T}_{X_j \to Y} = \frac{1}{2} \ln \frac{\sigma^2_{W_Y}}{\sigma_U^2}, \tag{4.19b}$$

$$\hat{C}_{X_j \to Y} = \frac{1}{2} \ln \frac{\sigma_Y^2}{\sigma^2_{W_{X_j}}}, \tag{4.19c}$$

$$\hat{S}_{Y|X_j} = \frac{1}{2} \ln \frac{\sigma^2_{W_{X_j}}}{\sigma_U^2}, \tag{4.19d}$$

$$\hat{P}_Y = \frac{1}{2} \ln \frac{\sigma_Y^2}{\sigma_U^2}. \tag{4.19e}$$

Nearest-neighbor approach

By adopting the well-established KSG nearest-neighbor estimation strategy, the search space used to compute the PrI measure – and, consequently, its decomposition terms – consists of the joint space formed by the current and past states of the target process together with the past states of the driver process, i.e., $\{Y_n\ Y_{n-1:n-m}\ X_{j,n-1:n-m}\}$. After identifying the k-nearest neighbors in this highest-dimensional space, the corresponding lower-dimensional subspaces are considered to count the number of samples falling within the same range (i.e., within the distance determined in the highest-dimensional space). Specifically, the following formulations are obtained:

$$\hat{S}_Y = \psi(N) + \frac{1}{N-m}\sum_{n=1}^{N-m}(\psi(N_{Y_nY_{n-1:n-m}}+1) - \psi(N_{Y_n}+1) - \psi(N_{Y_{n-1:n-m}}+1)), \tag{4.20a}$$

$$\hat{T}_{X_j\to Y} = \psi(k) + \frac{1}{N-m}\sum_{n=1}^{N-m}(\psi(N_{Y_{n-1:n-m}}+1) - \psi(N_{Y_nY_{n-1:n-m}}+1) - \psi(N_{X_{j,n-1:n-m}Y_{n-1:n-m}}+1)), \tag{4.20b}$$

$$\hat{S}_{Y|X_j} = \psi(k) + \frac{1}{N-m}\sum_{n=1}^{N-m}(\psi(N_{X_{j,n-1:n-m}}+1) - \psi(N_{Y_nX_{j,n-1:n-m}}+1) - \psi(N_{X_{j,n-1:n-m}Y_{n-1:n-m}}+1)), \tag{4.20c}$$

$$\hat{C}_{X_j\to Y} = \psi(N) + \frac{1}{N-m}\sum_{n=1}^{N-m}(\psi(N_{Y_nX_{j,n-1:n-m}}+1) - \psi(N_{X_{j,n-1:n-m}}+1) - \psi(N_{Y_n}+1)), \tag{4.20d}$$

$$\hat{P}_Y = \psi(k) + \psi(N) - \frac{1}{N-m}\sum_{n=1}^{N-m}(\psi(N_{X_{j,n-1:n-m}Y_{n-1:n-m}}+1) + \psi(N_{Y_n}+1)), \tag{4.20e}$$

$$\tag{4.20f}$$

where $\psi(\cdot)$ is the digamma function and N is the number of available realizations of the variable, k the number of neighbors considered in the highest-dimensional space, and $\epsilon_{n,k}/2$ the maximum distance between the sample and the k^{th} neighbor. The terms $N_{Y_{n-1:n-m}}$ and $N_{X_{j,n-1:n-m}}$ denote the number of samples within a distance of $\epsilon_{n,k}/2$ from the reference sample in the spaces associated with the past states of the processes Y and X_j. Similarly, $N_{X_{j,n-1:n-m}Y_{n-1:n-m}}$ indicates the number of neighbors in the projected space associated to the past states of both processes, $N_{X_{j,n-1:n-m}}$ and $N_{Y_{n-1:n-m}}$ in the spaces associated to the past state of the driver and target processes, respectively, and N_{Y_n} in the space associated to the current state of the target process.

Discrete estimation approaches

Among the discrete estimation approaches discussed in this thesis, the binning-based method can be used to obtain a model-free estimation of PrI and its decomposition terms, in an analogous manner as that used for the other investigated measures. Specifically, after discretizing the continuous-valued target and driver variables using the quantization procedure described in Sect. 2.3.3, the relevant entropy terms are computed via a frequency-based approach and combined to obtain the measures of interest. To satisfy the empirical rule adopted to set the estimation parameters and mitigate the curse of dimensionality – thereby ensuring feasible estimation within the PrI framework – the alphabet size, given by b^{2m+1}, must not exceed the number of available samples N.

In contrast, the permutation-based approach cannot be applied within the investigate analytical framework, as it does not allow for the estimation of entropy for scalar variables (e.g., the entropy of the current state of the target), which is required to compute PrI and its decomposition terms.

4.3. Multivariate analysis of pairwise link dynamics

As shown in Fig. 3.1, the link between the dynamical target system $\mathcal{Y}$ and a generic driver system $\mathcal{X}_j$ is embedded within a larger network. From this perspective, the multivariate nature of the complex systems should be accounted for even when investigating the dynamics of a single link, in order to taken into account the indirect influence of the other nodes in the network on coupling and causality interactions between the investigated pairs of processes. In this context, the PrI decomposition reported in Eqs. 4.14 can be extended to isolate the contributions of the driver to the target by removing the influence of the remaining network. This is achieved using partial measures that, by conditioning on all network nodes except those involved in the link, aim to isolate the direct interaction between the two investigated nodes (Faes et al., 2016b). Among these measures, the *Conditional Transfer Entropy* (CTE) is widely used, as it determines whether the interaction between two dynamical processes is direct or mediated by other nodes in the network (Vakorin et al., 2009).

Let us define a vector process $\boldsymbol{X}_{\setminus j}$, incorporating the $M-1$ source processes excluding X_j. Denoting by $\boldsymbol{X}_{\setminus j,n}$ and $\boldsymbol{X}_{\setminus j,<n}$ the random variables describing its current and past states, respectively, the CTE is defined as the mutual information between the current state of the target process and the past states of the driver process, conditioned on the past states of both Y and $\boldsymbol{X}_{\setminus j}$ (Vakorin et al., 2009), i.e.,

$$T_{X_j \to Y|\boldsymbol{X}_{\setminus j}} = I(Y_n; X_{j,<n}|Y_{<n}, \boldsymbol{X}_{\setminus j,<n}). \tag{4.21}$$

This measure enables the disambiguation of indirect or direct links between X_j

and Y, capturing the information uniquely associated with the direct path from driver to target. Network configurations in which intermediate nodes form chain pathways or act as common drivers influencing both processes can produce spurious causal detections when using standard TE. In contrast, CTE vanishes in the absence of a direct causal influence, even if information flows indirectly through the network, whereas TE may remain greater than zero. Nevertheless, it is important to highlight how even CTE can detect spurious direct links between two nodes when conditioning on a common child. Indeed, in this case, even if TE is equal to zero, CTE may be greater then zero.

4.3.1. Conditional transfer estimation strategies

As similarly done for the target and driver processes Y and X_j, the $M-1$ processes collected in $\boldsymbol{X}_{\setminus j}$ could be treated as ergodic Markov processes to enable estimation of the CTE measure. Accordingly, the current state of this vector process is denoted as $\boldsymbol{X}_{\setminus j,n}$ and its history is approximated using a finite number m of past states, i.e., $\boldsymbol{X}_{\setminus j,<n} \approx \boldsymbol{X}_{\setminus j,n-1:n-m}$, where m is the order of the process.

MATLAB codes and functions for estimating the CTE measure using both linear parametric and nearest-neighbor approaches are provided in the *direct causal transfer entropy* toolbox, freely available on GitHub.

Linear parametric estimation approach

Assuming that the oscillatory activity of the network nodes can be described by linear Gaussian stationary processes, an AR model can be employed to represent the dynamic interactions among the $M+1$ processes in $\boldsymbol{S} = [Y, X_j, \boldsymbol{X}_{\setminus j}]$ in determining the target process Y, i.e.,

$$Y_n = \sum_{k=1}^{p} \boldsymbol{A}_k \boldsymbol{S}_{n-k} + U_n, \tag{4.22}$$

where p is the order of the AR model, $\boldsymbol{S}_{n-k}$ is the $(M+1)$-dimensional vector collecting the past state of all processes at lag k, $\boldsymbol{A}_k$ is the $1 \times (M+1)$-dimensional matrix of the model coefficients relating the present of the target with the past of the processes at lag k, and U_n is a zero-mean white noise vector, uncorrelated with $\boldsymbol{S}_{n-k}$, $k = 1, \ldots, p$, with variance σ_U^2.

To compute the CTE term from X_j to Y conditioned on $\boldsymbol{X}_{\setminus j}$, a restricted linear model is also considered, where the dynamics of the target process Y are described by its own past states and the past states of the conditioning processes. Specifically, defining a process $\tilde{\boldsymbol{S}} = [Y\ \boldsymbol{X}_{\setminus j}]$, the restricted linear model can be expressed as:

$$Y_n = \sum_{k=1}^{\infty} \boldsymbol{B}_k \tilde{\boldsymbol{S}}_{n-k} + W_n, \tag{4.23}$$

where $\tilde{\boldsymbol{S}}_{n-k}$ is the M-dimensional vector collecting the past state of the process $\tilde{\boldsymbol{S}}$ at lag k, $\boldsymbol{B}_k$ is the $(1 \times M)$-dimensional matrix of the model coefficients relating the present state of the target with the past of the process $\tilde{\boldsymbol{S}}$ at lag k, and W_n is a vector collecting the present states of the zero-mean white noise, uncorrelated with $\tilde{\boldsymbol{S}}_{n-k}$, with variance σ_W^2.

Once the models in Eqs. 4.22 and 4.23 are identified, the CTE measure can be compute through the following formula (Schiatti et al., 2015):

$$\hat{T}_{X_j \to Y | \boldsymbol{X}_{\setminus j}} = \frac{1}{2} \ln \frac{\sigma_W^2}{\sigma_U^2}. \tag{4.24}$$

Nearest-neighbor estimation approach

By exploiting the decomposition of CMI into entropy terms, the CTE can be expressed as a combination of four entropy contributions. In the KSG nearest-neighbor framework, the maximum norm distance between each sample in the highest-dimensional space $[Y_n, Y_{n-1:n-m}, X_{j,n-1:n-m}, \boldsymbol{X}_{\setminus j,n-1:n-m}]$ and its k^{th} nearest neighbor, denoted as $\epsilon_{n,k}/2$, is first evaluated. The same range distance is then projected onto the explored lower-dimensional subspaces to count the neighbors falling within that radius for each realization. Proceeding in this manner, the nearest-neighbor estimator of the conditional transfer entropy is obtained as (Faes et al., 2015a):

$$\begin{aligned} \hat{T}_{X_j \to Y | \boldsymbol{X}_{\setminus j}} = \psi(k) + \frac{1}{N-m} \sum_{n=1}^{N-m} (\psi(N_{Y_{n-1:n-m} \boldsymbol{X}_{\setminus j,n-m}} + 1) \\ - \psi(N_{Y_n Y_{n-1:n-m} \boldsymbol{X}_{\setminus j,n-1:n-m}} + 1) - \psi(N_{Y_{n-1:n-m} X_{j,n-1:n-m} \boldsymbol{X}_{\setminus j,n-1:n-m}} + 1)), \end{aligned} \tag{4.25}$$

where $\psi(\cdot)$ is the digamma function, while $N_{Y_{n-1:n-m} \boldsymbol{X}_{\setminus j,n-m}}$, $N_{Y_n Y_{n-1:n-m} \boldsymbol{X}_{\setminus j,n-1:n-m}}$, and $N_{Y_{n-1:n-m} X_{j,n-1:n-m} \boldsymbol{X}_{\setminus j,n-1:n-m}}$ represent the number of samples counted within a distance smaller than $\epsilon_{n-k}/2$ in the respective projected spaces $[Y_{n-1:n-m}, \boldsymbol{X}_{\setminus j,n-1:n-m}]$, $[Y_n, Y_{n-1:n-m}, \boldsymbol{X}_{\setminus j,n-1:n-m}]$ and $[Y_{n-1:n-m}, X_{j,n-1:n-m}, \boldsymbol{X}_{\setminus j,n-1:n-m}]$.

4.4. Overview and conclusions of chapter 4

A variety of approaches have been proposed to characterize the statistical structure and interactions between coupled dynamic processes using bivariate time series. Classical methods include state-space interdependence measures (Rulkov et al., 1995; Arnhold et al., 1999) and correlation-based analyses (Li et al., 2009; Bashan et al., 2012). These approaches typically encode direct causal relationships under the assumption of acyclic dependencies and explicitly neglecting the role of temporal dynamics. In contrast, dynamic causal modeling (Friston et al., 2003) and Wiener–Granger causality (Wiener, 1956; Bressler and Seth, 2011), associated with

statistical causal modeling (Valdes-Sosa et al., 2011), explicitly incorporate temporal structure and allow the analysis of reciprocal (i.e., cyclic) causal interactions. A more flexible framework is provided by information dynamics (Lizier, 2012a), which encompasses statistical causal modeling approaches and has been widely applied to the study of interdependent systems across diverse domains. This chapter focused on two information-theoretic bivariate frameworks grounded in distinct perspectives on dynamical coupling: the mutual information rate and the predictive information. MIR is a non-directional measure quantifying the symmetric exchange of information between two processes, capturing statistical dependence without imposing assumptions about causal directionality or interaction strength (Faes et al., 2012a). In contrast, PrI is a directional measure that quantifies how the dynamics of one process – the driver – influence another – the target (Faes et al., 2015c). Considering these complementary perspectives enables a more comprehensive characterization of coupled dynamics. Moreover, their respective decomposition schemes separate interaction effects from the intrinsic dynamics of each process.

As discussed in Sect. 4.1, MIR admits two equivalent decompositions: it can be expressed as the sum of the individual entropy rates of the two processes minus their joint entropy rate, or as the sum of the bidirectional transfer entropies plus the zero-lag instantaneous shared information (Barà et al., 2023b). These representations provide complementary insights. The former highlights the overall complexity of the coupled system, whereas the latter emphasizes directional dynamical interactions, encompassing both lagged and instantaneous effects. While complexity and unpredictability were previously examined in Sect. 3.1 in the context of individual process dynamics – here extended to the joint bivariate setting – the present chapter explicitly introduces the concept of causality. TE is widely used due to its sensitivity to directional, linear, and nonlinear dependencies and its close relationship with Wiener–Granger causality (Wiener, 1956; Granger, 1963). It quantifies the causal influence by the temporal precedence of the driver and the provision of unique information about the target's future states. Simulation studies reported in Sect. 4.1.2 confirm that TE increases with the parameters governing causal strength in bidirectional coupled VAR processes, logistic maps and coupled Hènon maps. Moreover, as observed in this latter setting, MIR decompositions allow the detection of instantaneous causality, revealing effects of strong synchronization even in the absence of explicit zero-lag interactions (Fig. 4.4).

Within the PrI framework described in Sect. 4.2, TE captures only a fraction of the information conveyed from the past of the bivariate system to the current state of the target. Complete characterization requires accounting for the target's intrinsic dynamics via SE, which quantify the the information in the target's past that predicts its current state (see Sect. 3.11). An alternative decomposition involves cSE and CrossEn, which distinguish intrinsic target dynamics from directed driver-

target interactions. SE reflects predictive information in the target's past, irrespective of origin, and is positive when external causal influences enhance predictability. In contrast, cSE conditions on the driver's past, isolating genuine self-dependencies, being thus related to the concept of Granger autonomy defined for Gaussian processes (Seth (2010); Sparacino et al. (2024)). Similarly, CrossEn captures the total information about the target from the driver, but may include contributions from intrinsic dynamics or reverse interactions; only TE isolates purely directed transfer, being strictly positive only when causal influence exists (Faes et al., 2015c).

Reliable estimation of MIR and PrI requires decomposing these measures into tractable information-theoretic terms, indeed, being MIR defined over infinite-dimensional past histories, cannot be estimated from short stationary realizations. Early work focused on specific stochastic processes, including continuous-time point processes (Mijatovic et al., 2021) and discrete-time linear Gaussian processes (Pernice et al., 2022c), where relationships between entropy rate, prediction error variance (Barrett et al., 2010), and Granger causality (Barnett et al., 2009) enable practical computation. Moreover, in this context, long-memory effects can be addressed using YW equations (Faes et al., 2015c) or state-space models (Faes et al., 2022). Only recently, more general model-free approaches – including nearest-neighbor and discretization estimators – relaxing distributional or interaction assumptions have been combined with the MIR framework (Barà et al., 2023b; Pinto et al., 2025). In this case, the use of finite-dimensional past histories allows feasible estimation from finite-length time series, as similarly done for the estimation of the entropy rate metrics.

Simulation results reported in Sect. 4.1.2 confirm previous findings regarding estimation strategies. Both linear and nearest-neighbor estimators effectively capture the dynamics of linear VAR processes (see Fig. 4.2), whereas linear estimators fail to detect variations in nonlinear dynamics and weakly recover causal effects in coupled logistic maps (see Fig. 4.3). In the case of the discrete estimation applied on the coupled Hénon maps (Fig. 4.4), parameter selection is critical due to the rapid growth of alphabet size when embedding two processes jointly. For the binning approach, extreme parameter choices lead to information loss or insufficient memory capture, whereas an intermediate setting ($b = 3$, $m = 2$) balances amplitude resolution and temporal dynamics. For the permutation approach, increasing m improves memory but introduces bias due to the exponential growth of ordinal patterns. While PrI avoids some of MIR's estimation challenges, its decomposition into simpler components facilitates its practical computation. Even if no validation studies have been reported in this thesis for assessing the different estimation approaches, general conclusions on the comparison of the explored estimation strategies remain valid.

An import aspect in the quantification of asymmetric coupling and causality

concerns the inclusion of possible instantaneous (zero-lag) effects of the driver on the target. Incorporating zero-lag effects into TE and CrossEn – defined as in Eqs. 4.3 and 4.16 – leads to define the extended measures $iT_{X_j \to Y} = I(Y_n; X_{j,n}, X_{j,<n} | Y_{<n})$ and $iC_{X_j \to Y} = I(Y_n; X_{j,n}, X_{j,<n})$. From a theoretical perspective, $iT_{X_j \to Y}$ is equivalent to the sum of the lagged TE $T_{X_j \to Y}$ and the instantaneous information term $I_{X_j \cdot Y}$ appearing in the MIR decomposition (Eq. 4.5). Nevertheless, this equivalence does not necessarily hold in practical estimation as the overall estimation bias depends on the number of entropy terms involved and on the manner in which they are combined. This issue is particularly relevant for nearest-neighbor estimators, for which the bias is also influenced by the dimensionality of the searching space. In this context, it is important to note that the estimation formulas reported in Eqs. 4.9d and 4.20b, corresponding to TE computation within the MIR and PrI frameworks, respectively, differ in their structure and dimensional embedding, potentially leading to distinct results.

As discussed in Sect. 4.3, in multivariate networks, pairwise interactions may be confounded by indirect effects through other nodes. Conditional Transfer Entropy addresses this by conditioning on all other nodes, isolating direct information transfer. Even if no validation settings have been shown for assessing CTE computational feasibility, at this point it is well-known that the high-dimensionality in multivariate settings increases the estimation challenges, particularly for model-free estimators. In this regard, recent advances in data-efficient estimation procedures – especially those based on non-uniform embedding strategies – have enabled more reliable estimation of direct causal measures from short multivariate time series (Vlachos and Kugiumtzis, 2010; Faes et al., 2011; Runge et al., 2012; Faes et al., 2013b). Nevertheless, future validation studies should be conducted to assess the capability of isolating direct effects depending on estimator and data length, as well as to assess the sensitivity to spurious effects due to common child effects.

In conclusion, this chapter has shown that MIR and PrI provide a distinct and complementary characterizations of separate interactions, and that their decomposition into fundamental information-theoretic quantities enables a deeper investigation of system complexity, coupling, and causality. Parametric estimators are reliable and computationally efficient for short time series, crucial in multivariate contexts, while model-free approaches offer broader generality but are more sensitive to parameter selection and the curse of dimensionality. Careful consideration of estimation strategy, data length, and system dimensionality is therefore essential for robust and interpretable results.

Chapter 5

High-order investigation of group dynamics

After providing an overview of the main analytical frameworks devoted to the investigation of multivariate systems and based on the concepts of synergy and redundancy (Sect. 5.1), this chapter focuses on the Partial Information Decomposition (PID) framework (Sect. 5.2), which has recently been widely exploited in the literature. In particular, both aspects related to the mathematical definition of the decomposed measures and issues concerning their practical estimation are addressed.

As mentioned in Chapter 2, the investigation of behaviors related to the interaction of more than two parts of a network reported in this thesis is mainly restricted to the analysis of static multivariate networks. Accordingly, variables representing the $(d+1)$-dimensional system depicted in Fig. 3.1 are considered.

5.1. Overview on multivariate analytical frameworks

To characterize the nontrivial interplays within network systems, measures are required that can capture High-Order Interactions (HOIs), whereby groups of nodes in the system may carry information that is not present in any pair of nodes (Battiston et al., 2020). Indeed, networks often exhibit collective behaviors across multiple hierarchical levels, reflecting interactions that involve more than two nodes (Anderson, 1972; Berge, 1984). Core concepts in the analysis of HOIs are those of redundant and synergistic information. *Redundant information* arises when multiple (more than two) nodes convey the same information, whereas *synergistic information* corresponds to information that is jointly provided by multiple nodes and that cannot be obtained from pairs of nodes. Accordingly, the former represents duplicated information shared across multiple nodes, while the latter represents an emergent information arising from their joint interaction.

Despite the longstanding recognition of such groupwise interactions, systematic analyses of HOIs have only recently gained popularity in the study of complex network, also thanks to development of two distinct lines of inquiry. The first concerns the study of the structure of group interactions, with emphasis on the detection of the rules governing the causal evolution of the system – referred to as *high-order mechanisms* (HOMs) (Malizia et al., 2024). The second focuses on the statistical assessment of patterns of activity that can be explained when considering the system as a whole but not when any of its parts is taken separately – referred to as *high-order behaviors* (HOBs) (Rosas et al. (2019); Faes et al. (2022)). Mechanisms and behaviors provide complementary, yet closely related, perspectives on the description of high-order phenomena, whose interplay is far from trivial (Rosas et al. (2022); Robiglio et al. (2025); Barà et al. (2026a)).

Recently, metrics grounded in the framework of information theory have been proposed to investigate HOBs, aiming to capture redundant and synergistic modes of interaction within groups of random variables or processes. Nevertheless, the definitions of synergy and redundancy reported above are not mathematically rigorous and do not refer to uniquely defined information quantities; as a result, a variety of measures and analytical frameworks have been developed to investigate multivariate interactions, none of which is inherently incorrect but rather offers a different perspective on the quantification of HOIs (Timme et al., 2014).

The most popular measures of synergy and redundancy are based on the concept of *Interaction Information* (II). This quantity extends the MI measure by assessing the information gained about one variable by observing the others. Originally defined for systems composed of three variables, II compares the information that one variable shares with two other variables when the latter are considered individually or jointly (McGill, 1954):

$$II(W_1; W_2; W_3) = I(W_1; W_2) + I(W_1; W_3) - I(W_1; W_2, W_3). \tag{5.1}$$

This measure has recently been generalized to quantify interactions among an arbitrary number of random variables through the *O-Information* (OI) (Rosas et al., 2019). Considering the d-dimensional subnetwork represented by the vector random variable $\boldsymbol{W} = [W_1, \dots, W_d]$, OI is defined as a combination of entropy terms computed over subsets of $\boldsymbol{W}$, i.e.,

$$\Omega(\boldsymbol{W}) = (d-2)H(\boldsymbol{W}) + \sum_{j=1}^{d} \left(H(W_j - H(\boldsymbol{W}_{\setminus j}))\right), \tag{5.2}$$

where $\boldsymbol{W}_{\setminus j} = \boldsymbol{W} \setminus W_j$ denotes the subset of variables obtained removing W_j from $\boldsymbol{W}$. Both II and OI assume positive values when redundancy exerts a predominant influence on the interactions among the variables, and negative values when synergy

is dominant (McGill, 1954; Rosas et al., 2019).

Also related to the II measure is the multivariate information metric implementing the concept of *whole-minus-sum* (WMS) (Anastassiou, 2007). By considering one variable of the network as the target variable – represented here by V – and the other as source variables – represented here by $\boldsymbol{W}$ – a measure can be defined that quantifies the difference between the mutual information obtained when the sources are considered jointly to predict the target and the sum of the mutual information values obtained when each source is considered individually (Barà et al., 2026a):

$$\Delta_{\mathrm{MI}} = I(V;\boldsymbol{W}) - \sum_{j=1}^{d} I(V;W_j). \tag{5.3}$$

This quantity assumes positive values when the information provided jointly by all sources about the target exceeds the sum of the information provided individually, thus indicating a predominance of synergistic interactions. Conversely, it assumes negative values when redundant interactions dominate.

The Δ_{MI} measure differs from the aforementioned II and OI quantities because it adopts a directional perspective when investigating HOIs. Specifically, it highlights the redundant and synergistic informative contributions of a group of variables towards a single variable taken as the target. Contrarily, II and OI are symmetric measures that do not assign any preferential role to any variable in the system. Nevertheless, all these metrics quantify the balance between high- and low-order statistical dependencies within the interactions of the investigated network. As such, they do not allow synergistic and redundant information contributions to be assessed separately, since these are conflated into a single quantity that may therefore mask the presence of HOIs.

To disentangle these two contributions, the framework of Partial Information Decomposition – introduced in the next section – has been extensively explored in the literature and represents one of the main analytical approaches investigated during my research activity, with particular emphasis on the estimation of its associated metrics (Barà et al., 2025a).

5.2. Partial Information Decomposition

Partial Information Decomposition has been widely explored to capture high-order dependencies among multiple source variables sharing information with a target (Williams and Beer, 2010). This analytical framework distinguishes among terms representative of the *unique* information exclusively available from each source, the *redundant* information obtained from two or more different sources, and the *synergistic* information that emerges only when multiple sources are considered jointly.

By considering the variable V as target and the variables collected in $\boldsymbol{W}$ as sources, the PID problem can be compactly formulated by expressing the MI between target and sources as:

$$I(V;\boldsymbol{W}) = \sum_{j=1}^{d} U(V;W_j) + R(V;\boldsymbol{W}) + S(V;\boldsymbol{W}), \tag{5.4}$$

where $U(V;W_j)$, $R(V;\boldsymbol{W})$, and $S(V;\boldsymbol{W})$ respectively denote the unique information shared by V exclusively with the j^{th} source, the redundant information simultaneously shared by all sources with V, and the synergistic information that emerges only when all sources are jointly observed.

The original formulation of the PID involves all and only the terms appearing in Eq. 5.4 only when two source variables are considered (case $d = 2$). Indeed, more generally, this framework decomposes the information shared between target and source variables into *Partial Information* (PI) terms, which represent the information exclusively associated with a specific source or combinations of sources. Accordingly, $I(V;\boldsymbol{W})$ is decomposed as:

$$I(V;\boldsymbol{W}) = \sum_{\alpha\in\mathcal{A}} I_\delta(V;W_\alpha), \tag{5.5}$$

where, being $\mathcal{A}$ the collection of all subsets of sources such that no source is a superset of any other, $I_\delta(V;W_\alpha)$ indicates the information exclusively related to each specific atom α corresponding to a given collection of sources, and $W_\alpha \subset \boldsymbol{W}$ contains the variables indexed by α.

To explore how the target shares information with the sources, it is necessary to employ mathematical lattice structures, such as the redundancy lattices shown in Fig. 5.1. These structures organize specific sources (or collections of them) according to the information they provide about the target variable. In the case of the *redundancy lattice*, atoms that provide at least as much redundant information as those below are placed higher in the structure (Williams and Beer, 2010). In the simplest case of three variables – one target and two sources – the lattice consists of the four PI atoms depicted in Fig. 5.1 (panel (*a.1*)), i.e., $\mathcal{A} = \{\{1\}\{2\}, \{1\}, \{2\}, \{12\}\}$. Using the common notation in which redundant information is denoted by sources in separate brackets and synergistic information by sources in the same brackets, each atom of the lattice represents a specific contribution of the PID, i.e., $R(V;\boldsymbol{W}) = I_\delta(V;W_{\{1\}\{2\}})$, $U(V;W_1) = I_\delta(V;W_{\{1\}})$, $U(V;W_2) = I_\delta(V;W_{\{2\}})$, and $S(V;\boldsymbol{W}) = I_\delta(V;W_{\{12\}})$ (see Fig. 5.1 (panel *a.2*))). The structural complexity of the redundancy lattice increases rapidly with the dimensionality of the system. Specifically, the number of atoms grows super-exponentially with the number of sources, following the Dedekind numbers – i.e., the sequence of monotonic Boolean functions – minus two (Gutknecht et al., 2021). For example, the number of PID atoms $l = |\mathcal{A}|$ is 18 when $d = 3$ and 166 when $d = 4$. In the case of four variables – one target and three sources – the eigh-

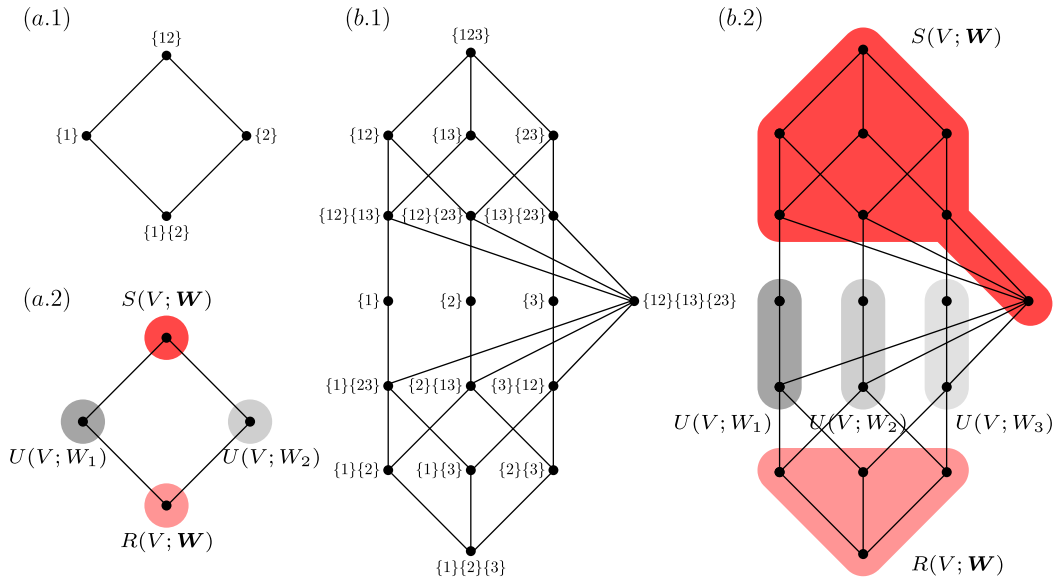

Figure 5.1: Redundancy lattices representing the PI atoms ordering (panels *.1*) and the PID components definition (panels *.2*) for the PID with two sources (panels *a.*) and for the PID with three sources (panels *b.*). The figure was modified from Barà et al. (2025a).

teen PI atoms are ordered as shown in Fig. 5.1 (*b.1*). Accordingly, the redundant information provided by the three sources is represented by the lowest atom (i.e., {1}{2}{3}), while the information redundantly associated to combinations of pairs of single sources (i.e., {1}{2}, {1}{3} and {2}{3}), of single sources and couples of them (i.e., {1}{23}, {2}{13} and {3}{12}), and of couples of sources (i.e., {12}{13}, {12}{23}, {13}{23} and {12}{13}{23}) are associated to nodes placed in higher positions in the lattice. PI atoms representing the information provided individually by the sources (i.e., {1}, {2} and {3}) are also present, while atoms attributed to synergistic combinations of sources (i.e., {12}, {13}, {23} and {123}) are placed in the highest positions of the lattice. At this point, it is clear that, to relate the PID problem to the formulation in Eq. 5.4 when working with more than two sources, it is necessary to apply a *coarse-graining approach*. This merges several atoms and sums the corresponding partial information terms, $I_\delta(V;W_\alpha)$, to obtain single information values for each of the unique, synergistic, and redundant components (Rosas et al., 2020). As illustrated in Fig. 5.1 (panel (*b.2*)) in the case of three source variables, by exploiting one of the possible grouping strategies – specifically, the first-order coarse-grained approach – the PID components are obtained by summing the PI of the collected atoms in $\mathcal{R} = \{\{1\}\{2\}\{3\}, \{1\}\{2\}, \{1\}\{3\}, \{2\}\{3\}\}$ for the redundancy term $R(V;\boldsymbol{W})$, in $\mathcal{S} = \{\{12\}\{13\}\{23\}, \{12\}\{13\}, \{12\}\{23\}, \{13\}\{23\}, \{12\}, \{13\}, \{23\}, \{123\}\}$ for the synergistic term $S(V;\boldsymbol{W})$, and in $\mathcal{U}_1 = \{\{1\}, \{1\}\{23\}\}$, $\mathcal{U}_2 = \{\{2\}, \{2\}\{13\}\}$, $\mathcal{U}_3 = \{\{3\}, \{3\}\{12\}\}$ for the unique information $U(V;W_1)$, $U(V;W_2)$ and $U(V;W_3)$, respectively.

Once the lattice structure is determined, the PID problem is solved by comput-

ing the PI associated to each atom $\alpha \in \mathcal{A}$. However, this problem cannot be determined unequivocally only using the traditional measures of Shannon's information theory, i.e., entropy and MI terms, as the number l of PI atoms to be computed is greater than the MI quantities that can be computed between the target and the d sources (both individually and grouped), i.e., $l > 2^d - 1$. To solve the PID problem, it is therefore necessary to formally specify one of the type of the information content appearing in the decomposition (Gutknecht et al., 2025). For instance, the so-called *redundancy function* $I_\cap(V; W_\alpha)$ can be define to generalize the MI over the lattice structure setting the connections between PI atoms. Considering that the redundant information associated to each of the atoms is given by the sum of the PI quantities attributed to the atoms below in the structure, i.e., $I_\cap(V; W_\alpha) = \sum_{\beta \preceq \alpha} I_\delta(V; W_\beta)$, with β representing the atoms that precede α in the lattice structure, the PI of each atom α can be can be recursively computed by using the Möbius inversion, i.e.,

$$I_\delta(V; W_\alpha) = I_\cap(V; W_\alpha) - \sum_{\beta \prec \alpha} I_\delta(V; W_\beta). \tag{5.6}$$

It is noteworthy that, as described above, the PID problem is generally solved by defining a redundancy function (Williams and Beer, 2010; Harder et al., 2013; Barrett, 2015; Ince, 2017). However, alternative approaches have been proposed that define synergistic or unique contributions directly and utilize atom orderings different from those established by the redundancy lattice described here (Griffith, 2014; Bertschinger et al., 2014).

5.2.1. Redundancy measures

Several works in the field have focused on quantifying redundancy by proposing various axiomatic definitions that differ based on their underlying operational principles (Liardi et al., 2026) (e.g., decision-theoretic (Pakman et al., 2021), game-theoretic (Bertschinger et al., 2014; Ince, 2017), or information-theoretic (Mäki-Marttunen et al., 2013)), the nature of the variables involved (i.e., continuous (Barrett, 2015; Pakman et al., 2021; Ehrlich et al., 2024) or discrete (Williams and Beer, 2010; Bertschinger et al., 2014; Ince, 2017)), and the assumptions made regarding their distribution (e.g., Gaussian (Barrett, 2015)).

As proposed in the seminal work of PID by Williams and Beer (2010), a measure quantifying redundant information should satisfy the axioms of (Williams, 2011):

i *symmetry*, according to which a redundancy term is invariant with the ordering of the sources;

ii *self-redundancy*, according to which the redundancy attributed to a specific source (or group of sources) equals the its MI with the target variable;

iii *monotonicity*, according to which redundancy does not increase when adding sources;

iv *non-negativity*, according to which redundancy measures are always positive.

Nevertheless, other works argued these axioms as not sufficient in defining a proper redundancy measure, and looked at additional properties like that of *identity*, which accounts for the possibility that sources share with the target not only the "same amount" of information but also the "same information content" (Harder et al., 2013; Bertschinger et al., 2014), *strong symmetry*, for which redundancy should be a symmetric measure that does not vary when changing the role of sources and target variables (Bertschinger et al., 2014), or *additivity*, for which, considering two independent systems, the redundancy term attributed to the combined system should be given by the sum of the redundancy terms of the single systems (Bertschinger et al., 2014).

Considering a discrete system where the target variable takes values in the discrete alphabet $A_V = \{1, \dots, Q_V\}$ and the source variables take values in the discrete alphabet $A_{W_j} = \{1, \dots, Q_{W_j}\}$, the pioneer definition of redundancy given by Williams and Beer is based on the definition of a *specific information* measure quantifying the information shared by the sources with a particular observation of the target variable $I(V = v; W_s)$. Specifically, the information brought redundantly to the target by the sources associated to the atom α is defined as the minimal information provided by any of these sources to each specific outcome v of the target (Williams and Beer, 2010):

$$I_\cap(V; W_\alpha) = \sum_{v \in A_V} p(V = v) \min_{s \in \alpha} I(V = v; W_s), \tag{5.7}$$

where $I(V = v; W_s)$ is denoted as the specific MI. This measure looks at the amount of information shared by the sources with the target ensuring that the redundant contribution is the minimum between the information that the sources shared with the target, but it does not take care of the information content itself. Looking at the minimum of specific MI terms, the $I_\cap(V; W_\alpha)$ defined in Eq. 5.7 does not guarantee that the selected information is the same for the two sources, i.e., that it represents the redundant contribution of the sources.

Starting from this definition, several works have proposed alternative redundancy measures aimed at addressing the limitations of the original Williams and Beer definition, particularly its tendency to overestimate redundant information. Among these, the approaches of Harder (Harder et al., 2013) and Bertschinger (Bertschinger et al., 2014) are based on a geometric definition of shared information, while others focus on the pointwise common change in surprisal (Ince, 2017) or on the concept of shared exclusion of probability densities (Makkeh et al., 2021). In this

context, it is evident that a univocal definition of the redundancy measure is still lacking, and that the PID framework remains an unresolved and debated research problem (Liardi et al., 2026).

5.2.2. *Estimation strategies*

Closely related to the definition of redundancy is the selection of the estimation strategies that can be used to quantify the PID quantities. As already evidenced, the original formulation of redundancy reported in Eq. 5.7 – as also the redundancy definition from Bertschinger et al. (2014) – cannot be employed when working with systems not entirely represented by discrete variables. Accordingly, to properly apply this definition to entirely continuous systems, the nature of the describing variables should be transformed, and thus the data should be processed through quantization procedures, reducing the resolution of the data and affecting the information content. The first formulation of PID for continuous source and target variables was that of Barrett (Barrett, 2015). While conceptually straightforward, it was shown that the associated redundancy measure tends to be overestimated (Rosas et al., 2016). Other notable formulations working with continuous variables are the already mentioned definition of Ince (2017), based on the concept of pointwise common change in surprisal, and of the one of Ehrlich et al. (2024), that adapts the nearest-neighbor estimation strategy to the definition of redundancy based on the idea of shared exclusion of probability densities of Makkeh (Makkeh et al., 2021). These latter are based on local measures of shared information, consequently the resulting redundancy terms can take negative values, not respecting the non-negativity axiom and posing problems of interpretability. Other formulations, such as that reported in the work of Schick-Poland et al. (2021), can be applied for resolving mixed variable problems for systems represented by discrete target and continuous source variables. Based on the Makkeh's redundancy definition and using local MI measures, this approach guarantees some desirable properties for a redundancy measure, e.g., localizability and differentiability, but implies negative decomposition terms. In Barà et al. (2025a), we recently introduced an alternative approach based on the original definition of redundancy – thus ensuring the non-negativity of the PI atoms – relying on the nearest-neighbor estimation strategy.

Notwithstanding the awareness of the issues associated with the Williams and Beer redundancy definition, the following sections focus on this formulation. Indeed, it is evident that none of the proposed alternative redundancy definitions (nor any of the other approaches outlined in literature) are entirely free of limitations. Moreover, the Williams and Beer definition can be more easily extended to settings in which not only discrete variables are considered. This potentiality rises from the possibility of expressing the specific information term – representing the information shared by W_s with a specific outcome v of the target variable V – as

the KL divergence between $p(w_s|v)$ and $p(w_s)$, i.e., the probability densities of W_s when considering, for the variable V, a specific outcome v or all possible outcomes, respectively. Accordingly, the $I(V = v; W_s)$ quantity can be expressed as:

$$\begin{aligned} I(V = v; W_s) &= H_{W_s|v}(W_s) - H_{W_s|v}(W_s|v) \\ &= \mathbb{E}_{p_{w_s|v}}\left[\log \frac{1}{p(w_s)}\right] - \mathbb{E}_{p_{w_s|v}}\left[\log \frac{1}{p(w_s|v)}\right], \end{aligned} \tag{5.8}$$

where $H_{W_s|v}(W_s)$ represents the cross-entropy of the unconditioned density $p(w_s)$ with respect to the conditional density $p(w_s|v)$ and $H_{W_s|v}(W_s|v)$ represents the entropy of $p(w_s|v)$.

Mathematical details on how this formula can be exploited when working with discrete random variables (Williams and Beer, 2010), with continuous Gaussian variables (Barrett, 2015), and with continuous sources and discrete target (Barà et al., 2025a) are reported below. MATLAB codes for solving the PID problem in these settings are collected in the *model-free Partial Information Decomposition* (mfPID) toolbox available on GitHub.

Fully discrete estimation approach

When working with discrete target and source variables, i.e., such that V assumes possible outcomes in the discrete alphabet $A_V = \{1, \dots, Q_V\}$ and a generic source variable W_s in the discrete alphabet $A_{W_s} = \{1, \dots, Q_{W_s}\}$, the specific information shared by W_s and the outcome v of V can be expressed as:

$$I(V = v; W_s) = \sum_{w_s \in W_s} \frac{p(v, w_s)}{p(v)} \log_2 \frac{p(v, w_s)}{p(v)p(w_s)}, \tag{5.9}$$

where the marginal probabilities of specific values of W_s and Y, i.e., $p(v)$ and $p(w_s)$, and their joint probabilities, i.e., $p(v, w_s)$, are estimated through the frequentistic approach. As done when working with discrete variables, the entropy measures are usually computed using the log operator in base 2 and expressed in bits.

Fully continuous estimation approach

Let us consider a target variable V taking values in the continuous domain $\mathcal{D}_V \subseteq \mathbb{R}$ and a vector source variable $\boldsymbol{W} = \{W_1, \dots, W_d\}$ taking values in the continuous domain $\mathcal{D}_{\boldsymbol{W}} \subseteq \mathbb{R}^d$. Assuming that V and $\boldsymbol{W}$ are jointly multivariate Gaussian, it has been demonstrated that the redundancy function in Eq. 5.7 reduces to the minimum of the MI terms computed between the target and each of the sources (individually or jointly) collected in the atom α. Accordingly, in the so-called *Minimal Mutual*

Information PID (MMI-PID), the redundancy measure is expressed as (Barrett, 2015):

$$I_{\cap}(V; W_{\alpha}) = \min_{s \in \alpha} I\left(V; W_s\right). \tag{5.10}$$

In the case of gaussinity, exploiting the tight connection between information measures and linear regression that holds for zero-mean joint Gaussian variables (Barrett et al., 2010), the MI terms in Eq. 5.10 can be computed from the variance of the residuals obtained when using regression models that describe the target variable V from the sources in s (scalar or vectorial), i.e., $V = W_s A + U$. Specifically, as seen in Eq. 2.10, the MI term $I\left(V; W_s\right)$ is obtained as:

$$\hat{I}\left(V; W_s\right) = \frac{1}{2} \ln \left(\frac{\sigma_V^2}{\sigma_U^2} \right), \tag{5.11}$$

with σ_V^2 the variance of the target variable, and σ_U^2 the variance of the prediction error.

This straightforward strategy further worsens the problem of redundancy overestimation associated with the definition proposed by Williams and Beer. Considering the simple case of two source variables, it is easy to verify that, when the other PID quantities are computed recursively, zero unique information is assigned to the source providing the least information about the target, and that synergy corresponds to the additional information contributed by the weaker source when the stronger source is already known (Barrett, 2015).

Mixed estimation approach

When working with discrete target variable V and d continuous source variables $\boldsymbol{W} = \{W_1, \ldots, W_d\}$, respectively taking values in the discrete alphabet $\mathcal{A}_V = \{1, \ldots, Q_V\}$ and in the continuous domain $\mathcal{D}_{\boldsymbol{W}} \subseteq \mathbb{R}^d$, the specific MI in Eq. 5.8 can be straightforwardly generalized as:

$$I(V = v; W_s) = \int_{w_s \in D_{W_s}} p(w_s|v) \ln \frac{p(w_s|v)}{p(w_s)} \mathrm{d}w_s. \tag{5.12}$$

In this case, the natural logarithm is employed to measure information.

The implemented mixed estimation approach relies on estimation strategy proposed by Ross (2014), thus defining the search space by considering how the observations of the source variables are associated with specific outcomes of the target. As mentioned in Sect. 2.3.5, this approach enables to disentangle the information shared among variables of different nature, including both discrete and continuous variables. In particular, the discreteness of the target variable is exploited to define the spaces within which neighbors are searched. This formulation effectively trans-

forms the problem of estimating MI quantities between discrete and continuous variables into a purely continuous setting, thereby improving computational feasibility and comparability with estimators designed for continuous variables. Specifically, the KSG estimation strategy was employed to reduce the estimation bias arising from the combination of entropy terms computed using a different number of observations and exploited to derive *specific* and *global* probabilities, i.e., $p(w_s|v)$ and $p(w_s)$. Indeed, although the dimensionality of the searching space remains unchanged (e.g., while computing $H_{W_1|v}(W_1)$ and $H_{W_1|v}(W_1|v)$), the combination of cross-entropy and entropy estimates produces effects analogous to those observed when estimating entropy terms based on neighbor searches in spaces of different dimensionalities (Kraskov et al., 2004) . Furthermore, the proposed estimator accounts for the fact that solving the PID implies computing specific MIs involving different number of source variables (e.g., for the case of two sources, $I(V = v; W_1, W_2)$, $I(V = v; W_1)$ and $I(V = v; W_2)$). Accordingly, there is the need to apply the KSG strategy also in a more standard view to accounts for the entropy terms to be computed in spaces of different dimension. Indeed, when working with d source variables, the application of the PID framework consists in the computation of the MI terms for the individual d sources and for any possible combination for each each of the Q_V outcomes of the target.

Following the estimation strategy described above and illustrated in Fig. 5.2, the specific MI between a specific outcome of the target variable v and all sources $\boldsymbol{W}$ can be expressed as:

$$\hat{I}(V = v; \boldsymbol{W}) = \psi(N) - \psi(N_v) + \psi(k) - \frac{1}{N_v} \sum_{\{\boldsymbol{w}^v\}} \psi(m_{\boldsymbol{W}} + 1), \tag{5.13}$$

where $\psi(\cdot)$ is the digamma function, N is the total number of samples, N_v the number of samples associated to the outcome $\{V = v\}$, $m_{\boldsymbol{W}}$ is the number of observations of $\boldsymbol{W}$ found at distance smaller than $\epsilon_{i,k}/2$ from the observation $\boldsymbol{w}^v$, with d_v being the distance between $\boldsymbol{w}^v$ and its k^{th} nearest neighbor, and $\boldsymbol{w}^v$ is indicative of the observations of $\boldsymbol{W}$ associated with the specific outcome $\{V = v\}$. Applying again the KSG strategy, the specific MI can be estimated for a generic subset of source variables, $W_s \subset \boldsymbol{W}$, performing range searches within the range of distances d_v determined in the highest-dimensional spaces:

$$\hat{I}(V = v; W_s) = \psi(N) - \psi(N_v) + \frac{1}{N_v} \sum_{\{w_s^v\}} \left(\psi(m_{W_s}^v + 1) - \psi(m_{W_s} + 1)\right), \tag{5.14}$$

where m_{W_s} and $m_{w_s}^v$ are the number of observations of W_s counted at distances smaller than $\epsilon_v/2$ from w_s, respectively considering all the samples or only the samples associated with $\{V = v\}$, and $\{w_s^v\}$ represents all observations of W_s associated with $\{V = v\}$. The complete derivations of the terms necessary to compute all PID

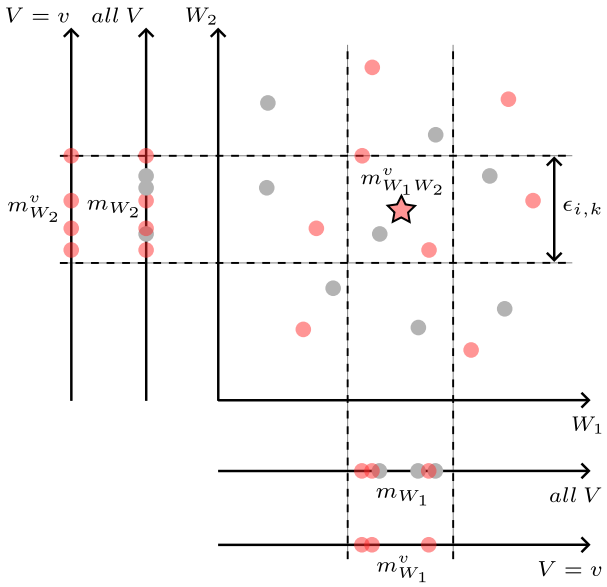

Figure 5.2: Schematic representation of the nearest-neighbor estimation of the specific MI measure for a binary target variable V and two continuous sources W_1 and W_2. The estimation proceeds by computing the Chebyshev distance between each reference sample $\boldsymbol{w}^v$ (star symbol) and its k^{th} neighbor (here, $k = 2$) counted among the samples with $V = v$ (red circles), and then counting the number of samples falling within this distance in the two-dimensional space ($m_{W_1W_2} = 3$) and in the projected one-dimensional spaces considering all samples ($m_{W_1} = 6, m_{W_2} = 7$) or only the samples for which $\{V = v\}$ ($m^v_{W_1} = 3, m^v_{W_2} = 4$). The figure was modified from Barà et al. (2025a).

terms for $d = 2$ and $d = 3$ sources are reported in the supplementary material of Barà et al. (2025a).

5.2.3. *Validation on boolean logic gates*

In this section, the simulation studies proposed in Barà et al. (2025a) to validate the estimation strategy for systems with a discrete target and continuous source variables are reported. Moreover, a comparison with the original formulation, working with fully discrete variables, is provided. The feasibility of the Barrett approach is not assessed in this thesis, as it is not directly comparable with the other investigated approaches and has already been thoroughly explored in Barrett (2015).

Let us consider three independent uniformly distributed continuous variables, $W_1 \sim \mathcal{U}(a,b)$, $W_2 \sim \mathcal{U}(c,d)$ and $W_3 \sim \mathcal{U}(e,f)$, with $a = e = -b = -f = -0.5$, d in the range $[0.05 : 0.1 : 0.95]$, and $c = d - 1$. Three different Boolean logic-gates have been simulated: (i) the logic-gate of XOR with two sources (XOR2) as $V = \Theta(W_1 \cdot W_2)$, (ii) the logic-gate AND considering two sources (AND2) as $V = \Theta(W_1) \cdot \Theta(W_2)$, and (iii) the logic-gate AND considering three sources (AND3) as $V = \Theta(W_1) \cdot \Theta(W_2) \cdot \Theta(W_3)$, with the Heaviside function $\Theta(x) = 1$ if $x \geq 0$ and $\Theta(x) = 0$ if $x < 0$. The probabilities of the three sources of being positive or negative are theoretically known and,

exploiting their statistical independence, also the joint probabilities can be derived as reported in tables 5.1, 5.2 and 5.3. From these quantities, all the marginal probabilities needed for the computation of the theoretical values of the PID measures are obtained.

The estimation strategies were applied over one-hundred 300-point realizations of the variables. Specifically, the mixed approach was used by fixing a number of neighbor $k = 5$, while the fully discrete approach was used by firstly applying an uniform discretization of the source variables using a number of levels $b = 6$. The statistical significance of the computed metrics was assessed by using a properly developed surrogate data analysis approach based on the application of random shuffling procedure on the target variable (see Sect. A.2.5 in the Appendix). Specifically, the statistical significance of the PI terms computed for specific outcomes of the target $I_\delta(V = v; W_\alpha)$ was evaluated by using a significance threshold defined as the $100\left(1 - \frac{0.05}{Q_V \cdot m}\right)^{th}$ percentile of the distribution obtained by computing the same metric on multiple surrogate data. Then, a PI term was considered significant if at least one of the Q_V specific terms was significant. Moreover, in the case of multiple sources – thus when using coarse-graining strategy – PID terms are deemed as significant if at least one of the PI terms contributing to their computation is significant.

Depicted in both Fig. 5.3 and 5.4, the theoretical trend of the MI reveals constant

XOR2			
W_1	W_2	$p(V=1,\boldsymbol{W})$	$p(V=0,\boldsymbol{W})$
< 0	< 0	$(b-1)(d-1)$	0
≥ 0	< 0	0	$-b(d-1)$
< 0	≥ 0	0	$-(b-1)d$
≥ 0	≥ 0	bd	0

Table 5.1: Theoretical values of the joint probability of the target and source variables for the logic XOR2 as function of the parameters b and d.

AND2			
W_1	W_2	$p(V=1,\boldsymbol{W})$	$p(V=0,\boldsymbol{W})$
< 0	< 0	0	$(b-1)(d-1)$
≥ 0	< 0	0	$-b(d-1)$
< 0	≥ 0	0	$-(b-1)d$
≥ 0	≥ 0	bd	0

Table 5.2: Theoretical values of the joint probability of the target and source variables for the logic AND2 as function of the parameters b and d.

AND3				
W_1	W_2	W_3	$p(V=1,\boldsymbol{W})$	$p(V=0,\boldsymbol{W})$
< 0	< 0	< 0	0	$-(b-1)(d-1)(f-1)$
< 0	< 0	≥ 0	0	$(b-1)(d-1)f$
< 0	≥ 0	< 0	0	$(b-1)d(f-1)$
< 0	≥ 0	≥ 0	0	$b(d-1)(f-1)$
≥ 0	< 0	< 0	0	$-(b-1)df$
≥ 0	< 0	≥ 0	0	$-b(d-1)f$
≥ 0	≥ 0	< 0	0	$-bd(f-1)$
≥ 0	≥ 0	≥ 0	bdf	0

Table 5.3: Theoretical values of the joint probability of the target and source variables for the logic AND3 as function of the parameters b, d and f.

values for the XOR gate and increasing values with d for the AND gates (Timme et al., 2014). Specifically, it is observed how the XOR gate yields exclusive synergy when X_1 and X_2 are positive or negative with the same probability ($d = 0.5$) – in this case, both sources must be known to determine the output of the gate – while it yields exclusive unique contribution from X_1 when X_2 are only negative ($d = 0$) or only positive ($d = 1$), thus becoming irrelevant. In the AND gates, the target is deterministic if $d = 0$, but increasing d the sources share more information with Y. This information is both redundant and synergistic, with synergy prevailing over redundancy, and is completed by unique contributions from X_2 for $d < 0.5$ and from X_1 (and also X_3 for the case of three sources) for $d > 0.5$.

In Fig. 5.3, the trends of the PID terms estimated using the mixed estimation strategy reveal how the computed measures reliably follow the true values of each measure, though exhibiting a bias that is more evident for the terms involving samples counted in higher dimensional spaces (i.e., the overall MI and the synergy). In the supplementary material of Barà et al. (2025a), the effect of the negative bias influencing the nearest-neighbor strategy has been explored on the mixed estimator of the PID framework. Specifically, it has been shown that the estimation bias is larger for higher-dimensional systems, and increases with a reduction of the length N of the data and an increase of the number k of neighbors searched, while the standard deviation increases at decreasing N and is rather stable at varying k. In this regard, it is interesting to note the absence of data points in the plot for low value of d for the AND logic-gates. In this case, the estimation of the PID terms is not feasible as the target variable, exhibiting imbalanced values across the possible outcomes, does not have sufficient points to count neighbors. This is highly possible for short data length or when using a high number of neighbors.

Fig. 5.4 reports the trends of the PID terms estimated using discretized variables. Overall, the estimated quantities follow the theoretical values for all terms of the decomposition, and the surrogate data analysis also show trends similar to those obtained using the mixed estimation approach. Nevertheless, as thoroughly discussed in Barà et al. (2025a), the use of the discretization approach requires manipulating the data, thereby "compromising" the original information conveyed by the continuous values of the source variables. This effect is reflected in an overall higher percentage bias in these estimates compare to those obtained with the mixed estimation approach, particularly when working with a limited number of quantization levels. Conversely, while the estimation variance is generally higher when only a limited number of quantization levels is considered, it is also strongly influenced by the number of the samples and their balance across the groups defined by the target output (Barà et al., 2024c). Furthermore, it has been observed that the amount of shared information may depend on the nature of the investigated system, for instance by the correlation between the variables (Papana and Kugiumtzis,

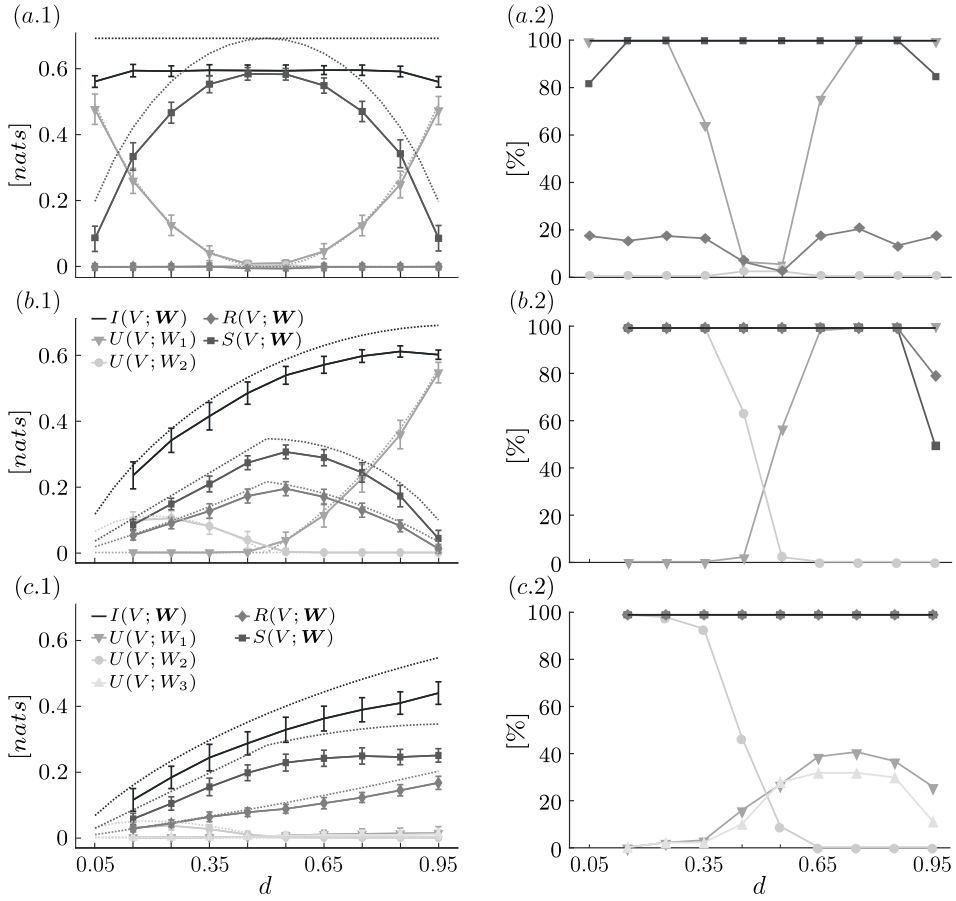

Figure 5.3: Theoretical values (dotted lines) and estimated distributions (solid lines, MEAN ± STD over 100 simulations) of the PID measures (panel *.1*) and percentage of realizations for which PID measures are statistically significant according to surrogate data analysis (panel *.2*) for the XOR2 (panel *a.*), AND2 (panel *b.*) and AND3 (panel *c.*) obtained through the mixed estimation approach by fixing $k = 5$ and $N = 300$. The figure was modified from Barà et al. (2025a).

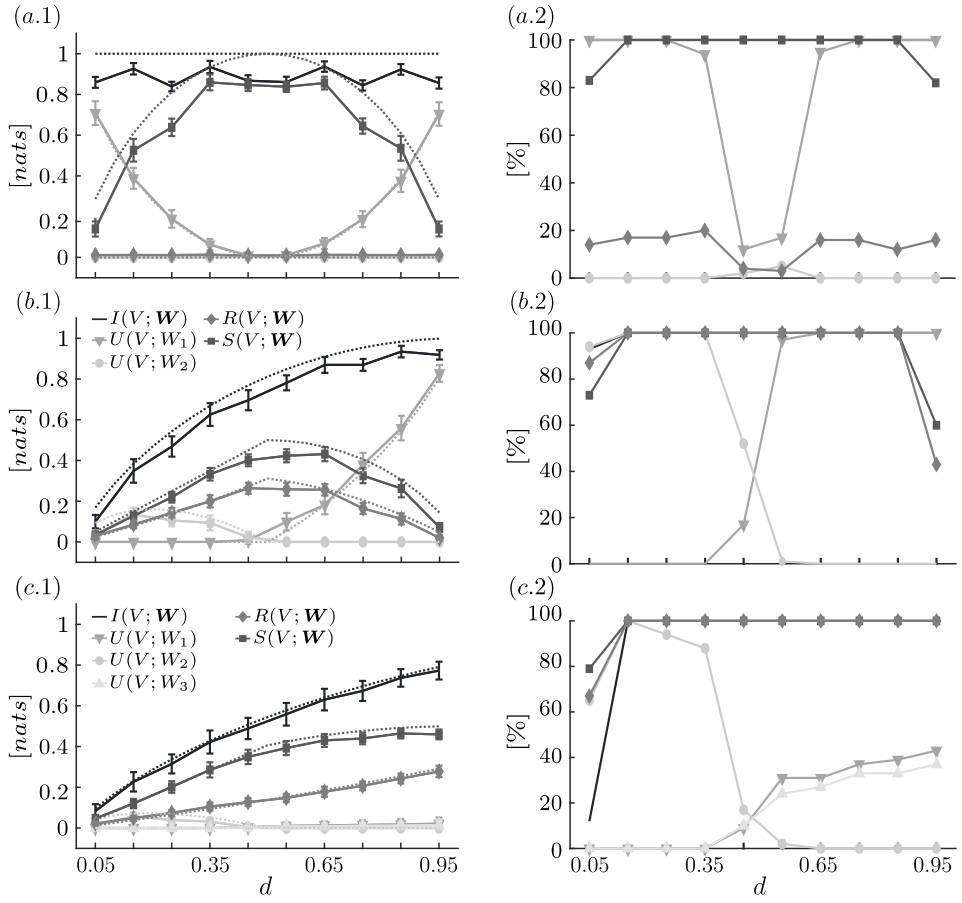

Figure 5.4: Theoretical values (dotted lines) and estimated distributions (solid lines, mean ± std. dev. over 100 simulations) of the PID measures (panel *.1*) and percentage of realizations for which PID measures are statistically significant according to surrogate data analysis (panel *.2*) for the XOR2 (panel *a.*), AND2 (panel *b.*) and AND3 (panel *c.*) obtained through the discrete estimation approach by fixing $b = 6$ and $N = 300$. The figure was modified from Barà et al. (2025a).

2009), that in the proposed simulation settings is governed by the parameter d.

5.3. Overview and conclusions of chapter 5

Standard network descriptions of complex systems typically focus on the investigation of pairwise interactions between units. However, it is widely acknowledged that a comprehensive understanding of these systems requires moving beyond simplistic approaches that consider networks only in terms of nodes and their pairwise links, toward frameworks that incorporate HOIs among more than two nodes (Battiston et al., 2020). In this context, the key concepts of synergistic and redundant interactions among multiple units of a system have emerged.

In Sect. 5.1, an overview of some of these metrics used to investigate the presence of multivariate interactions is provided. Specifically, the measures of II defined for three variables (McGill, 1954) and its extended version, the O-information (Rosas et al., 2019), as well as the Δ_{MI} term based on the concept of whole-minus-sum

(Anastassiou, 2007), are described. While the former measures account for the symmetry of the investigated network, the latter focuses on the information shared by one of the variables in the network – the target – with the remaining variables, thus providing an asymmetric view of the system. Despite this difference, all these quantities look at the balance between the redundant and synergistic contributions of the information shared within the investigated network. Consequently, these measures are not able to fully characterize the high-order behaviors of networks in which both redundant and synergistic interactions coexist, as these two contributions may mask each other. This limitation is well recognized in literature and recent research on network systems has sought to overcome it by developing analytical frameworks that are able to separately account for the two high-order contributions to multivariate information (Bertschinger et al., 2014; Ince, 2017; Gutknecht et al., 2021).

Most of these approaches are based on the framework of PID introduced by Williams and Beer (2010). As described in Sect. 5.2, PID allows to characterize how a target variable shares information with multiple source variables, yielding PI terms that describe the exclusive contributions of individual sources or combination of sources to the target. Nevertheless, as discussed, this analytical framework presents several inherent limitations that restrict its unambiguous employment in different contexts. First, the PID framework cannot be fully defined using only the classical measures of the information theory, thus requiring the introduction of axioms that the terms of the decomposition should be satisfied and that are not universally accepted. The resulting decomposition strongly depends on the measure used to solve the PID problem (Gutknecht et al., 2021) – in our case, the redundancy term – and on the properties that this inducing measure is required to satisfy (Bertschinger et al., 2012). As highlighted in Sect. 5.2.1, the original definition of redundancy, as well as all the definitions directly derived from it – such as the MMI-PID proposed by Barrett (2015) – satisfy properties of symmetry, self-redundancy, monotonicity, and non-negativity, but are known to overestimate redundancy (in particular, the MMI-PID provides an upper bound of the effective information redundantly shared within the system (Rosas et al., 2016)). Indeed, since these formulations do not satisfy the identity property, they quantify the minimal amount of information shared by any source with the target, without ensuring that this information corresponds to the same information content, thus conflating the concepts of content and amount of information (Bertschinger et al., 2014). To overcome this limitation, less conservative definitions of redundancy have been proposed as those based on the pointwise evaluation of the system behavior introduced by Ince (2017), Makkeh et al. (2021), and Ehrlich et al. (2024). However, these redundancy measures may yield negative atoms, complicating the straightforward interpretation of the resulting information quantities. Consequently, according to the most recent literature, the definition of a robust operationalization of PID that simultaneously ensures computational feasi-

bility and interpretability remains an open problem.

As highlighted in this chapter, an aspect closely related to the definition of the redundancy function concerns the estimation approach used to compute the PID terms. Although the redundancy function proposed by Williams and Beer was originally defined for discrete variables, it can be relatively easily generalized to variables of different nature. In Barrett (2015), it has been mathematically demonstrated that the MMI-PID developed for continuous joint multivariate Gaussian variables coincides with the original formulation proposed by Williams and Beer, as well as with other PID schemes introduced by Harder et al. (2013) and Bertschinger et al. (2014). More recently, this redundancy function has been extended to the case in which the system is characterized by both discrete and continuous variables (Barà et al., 2025a). The development of PID schemes for mixed-variable settings – where the target is discrete and the sources are continuous – is highly desired in several applications. For example, in machine learning, such formulations are relevant in feature selection problems, where the class label is represented in a discrete form while features are continuous (Coelho et al., 2016). Similarly, in computational physiology and neuroscience, discrete stimuli are often conveyed, e.g., by the nervous system, generating continuous-valued responses (Borst and Theunissen, 1999). The proposed approach combines the estimation strategy proposed by Ross (2014) for computing MI terms between discrete and continuous variables with the projection strategy adopted by the KSG nearest-neighbor estimation method (Kraskov et al., 2004). This combination allows feasible estimates of Williams and Beer redundancy function, and consequently of all the PI terms describing the information shared within the system. The estimation approach was validated on different Boolean logic-gates for which the true PI values can be analytical computed. As shown in Fig. 5.3, the estimated quantities closely follow the theoretical values of the unique, synergistic, and redundant contributions of the sources to the target variable. This behavior is also observed for the corse-grained terms computed in the three-source AND3 setting. Furthermore, the percentage of significance of the estimates reflects the trends of the computed quantities, demonstrating the computational feasibility of this strategy for estimating PID in mixed-variable settings.

In conclusion, this chapter highlights recent and significant advances in the tools of multivariate analysis, with particular emphasis on the PID framework. Enabling the disambiguation of high-order redundant and synergistic interaction arising among multiple system components, this analytical framework allows for investigating the coexistence of different high-order effects, thereby underscoring its relevance for investigating complex networks. However, it is noteworthy to further highlight a limitation already discussed in Sect. 2.5: the groupwise analysis presented here is restricted to static network systems due to the severe curse of dimensionality associated with increasing system size. Accordingly, the analyzed multi-

variate time series have been treated as realizations of random processes assumed to be stationary and memoryless, and the OI and PID can be employed as tools to decompose the information shared instantaneously among the processes. However, this assumption is rarely satisfied when investigating real-world scenario, as empirical data often exhibit temporal correlation. To overcome this limitation, recent developments have extended these frameworks to the dynamic domain through the introduction of the *O-Information Rate* (OIR) and the development of the *Partial Information Rate Decomposition* (PIRD). The former generalizes the MIR computed for bivariate processes, following the same rationale whereby the OI extends the MI between random variables (Faes et al., 2022), while the latter extends the framework of PID to the analysis of dynamic systems (Faes et al., 2025). Both OIR and PIRD have been extensively studied in systems modeled as jointly multivariate Gaussian processes and are typically estimated via linear parametric approaches. Indeed, as previously highlighted, although these parametric approaches restrict the analysis to linear dynamics, they enable the spectral characterization of the investigated processes and mitigate dimensionality issues. Contrarily, to the best of our knowledge, these methods have not been thoroughly explored using model-free approaches, and a comprehensive feasibility assessment is still lacking.

Part III

Applications on physiological data

Chapter 6

Physiological and methodological grounds

This chapter serves as an introduction to the Part III of the thesis, providing an overview of the complex regulatory mechanisms behind physiological dynamics. Specifically, the physiological dynamics and control mechanisms explored in the thesis through the information-theoretic measures and frameworks reported in the previous part are described, emphasizing those related to cardiovascular and cardiorespiratory dynamics, as well as to brain-heart interactions (Sect. 6.1). Then, the strategies used to extract and represent relevant information from physiological signals as time series is provided (Sect. 6.2). Finally, a detailed description of the datasets employed throughout the thesis is reported (Sect. 6.3).

6.1. Overview of the investigated physiological control mechanisms

Physiological system dynamics exhibit an *intrinsic variability* arising from the complex regulatory mechanisms sustaining the homeostatic body state. These fluctuations are not random but reflect the continuous adaptation of biological processes operating across multiple temporal and spatial scales, thus providing crucial insights into the organism functioning. Within the framework of Network Physiology, the dynamics of any single organ cannot be fully understood in isolation; rather, they emerge from the interdependent activity of multiple systems, whose intrinsic fluctuations influence and are influenced by one another (Bashan et al., 2012; Ivanov and Bartsch, 2014; Bartsch et al., 2015).

Such interactions may occur through *direct anatomical pathways*, including neural pathways, vascular connections, or mechanical interactions, as well as through *indirect functional influences*, mediated by shared regulatory drivers, cascading physiological responses, or environmental perturbations. This networked organization enables the complex patterns of synchronization, phase coupling, and information

transfer across organs, which collectively maintain adaptive homeostasis.

Consequently, providing a complete yet concise description of the regulatory dynamics governing resting physiological states – and their modulation under physiological or pathological conditions – is challenging. The following subsections, however, aim to highlight the key dynamic interactions and variability patterns that are mainly investigated in this thesis.

6.1.1. Cardiovascular and cardiorespiratory dynamics

Heartbeat activity exhibits high variability – commonly referred to as *heart rate variability* (HRV) – largely reflecting *autonomic nervous system* (ANS) control of the sinoatrial node. Sympathetic activation increases heart rate (HR) and reduces its variability, whereas parasympathetic modulation decreases HR and enhances its variability. At rest, both branches are tonically active, with parasympathetic dominance; under stress, sympathetic activity prevails (Shaffer et al., 2014; Elstad et al., 2018). This variability depends on age and sex (Shaffer et al., 2014) and is often reduced in pathological conditions such as nervous system disorders (Gorman and Sloan, 2000), diabetes (Benichou et al., 2018), arterial hypertension (Pagani and Lucini, 2001), and myocardial infarction (Buccelletti et al., 2009).

Respiration activity strongly influences cardiac heartbeat dynamics. Central respiratory drives – exerting a direct communication between respiratory and cardiomotor centers via vagal nerve activity – and the lung inflation reflex – mechanically influencing the sinoatrial node activity – overall result in the *respiratory sinus arrhythmia* (RSA) mechanism, for which there is an increase of HR during inspiration and a decrease during expiration (Berntson et al., 1993; Grossman et al., 2004; Elstad et al., 2018). Although cardiorespiratory coupling is often considered unidirectional, evidence suggests that heartbeats can influence respiration, contributing to synchronization mechanisms (Rosenblum et al., 1998). One example is *cardioventilatory coupling*, in which ventilation and heartbeats become synchronized in whole number ratios and maintain a fixed temporal relation with inspiration onset (Galletly and Larsen, 1998; Dick et al., 2014). Causal mechanisms of these coupling include the cardiac-triggered inspiration via haemodynamic afferents and the baroreflex-mediated autonomic effects. Another phenomenon is the *cardio-respiratory phase synchronization* (CRPS), for which cardiac events align with specific phases of the respiratory cycle, producing phase locking rather than amplitude modulation as in RSA (Bartsch et al., 2012).

As regards the cardiovascular regulation, this is coordinated by a brainstem center that integrates inputs from proprioceptors, chemoreceptors, and cardiac mechanoreceptors with signals from the cerebral cortex and limbic system (Shaffer et al., 2014). Among the referred mechanoceptors dynamics, it is necessary to

account for the influence of the arterial pressure dynamics on HR through the well-known *baroreflex mechanism* (Piepoli et al., 1997; Di Rienzo et al., 2001; Parati et al., 2004; Porta et al., 2012). Baroreceptors located in heart chambers, vena cavae, carotid sinuses, and aortic arch detect stretch and mediate a negative feedback control: increased pressure enhances vagal activity and reduces sympathetic output, lowering HR and blood pressure. Several works highlight the strong relevance of this regulatory mechanisms in response to postural changes as in the case of an orthostatic challenge. Indeed, this condition is associated with a venous pooling of the blood in the lower portion of the body, a consequent decrease of cardiac filling, cardiac output and stroke volume (Burton et al., 2004), that in turn determines a drop of arterial blood pressure sensed by baroreceptors (Berntson et al., 1994; Cooke et al., 1999). Finally, as mentioned, this results in a vagal inhibition and sympathetic activation directed to the heart and vessels.

Arterial blood pressure also exhibits spontaneous beat-to-beat fluctuations, influenced by respiration and sympathetic activity (Oleksakova et al., 2023), commonly referred to as *blood pressure variability* (BPV). The respiratory effects arise from intrathoracic pressure changes that alter venous return and blood pressure independently of HR (Janssen et al., 1995). Nevertheless, blood pressure variability is also affected by feedforward effects of HR, likely mediated by *Windkessel* (Belz, 1995) and *Frank–Starling* (Sequeira and van der Velden, 2015) mechanisms. Studies suggest a pathway in which HR primarily affects DAP, which in turn influences SAP, explaining substantial information flow from HR to systolic pressure at rest (Svacinova et al., 2015; Javorka et al., 2017). Variability in arterial compliance may also contribute to ABP dynamics, particularly with aging or pathology (O'Rourke, 1990; Lantelme et al., 2002). Beat-to-beat SAP modulation can arise from stroke volume (SV) changes transmitted through respiratory and venous blood pool dynamics (Ursino and Magosso, 2003; Mukkamala et al., 2003). Peripheral vascular resistance (PVR), driven by vasomotion in small arteries, further contributes to mean arterial pressure variability by influencing diastolic decay and venous return (Elstad et al., 2011).

Recent studies highlight the importance of arterial compliance (AC) in cardiovascular and cardiorespiratory regulation (Svec et al. (2021); Sparacino et al. (2024); Barà et al. (2026b)). Sympathetic control of vascular tone in large arteries may act as an unobserved confounder in interactions involving AC (Sugawara et al., 2012). ABP significantly modulates pulse wave velocity (PWV), often used as a surrogate of AC (Tan et al., 2016; David and Javorka, 2021), suggesting a causal influence from arterial pressure to compliance. Moreover, it has been observed that the relationship between arterial pressure and compliance can also be affected by sympathetic activity and cardiac contractility within the baroreflex pathway (Krohova et al., 2020). Heart rate fluctuations may influence compliance independently of ANS activity

and variability of ABP (Cunha et al., 1997; Lantelme et al., 2002; Tan et al., 2016). Indeed, increased HR shortens the cardiac cycle and reduces arterial recoil time, promoting vascular stiffening due to viscous and inertial wall properties (Armentano et al., 1995; Lantelme et al., 2002). Finally, also respiratory variability may modulate arterial compliance. Indeed, changes in intrathoracic pressure and lung volume during spontaneous breathing can alter atrial filling, preload, and transmural arterial pressure (Shekerdemian and Bohn, 1999). These effects can modify SV and arterial wall mechanical properties directly influencing arterial stiffness and vessel compliance also in resting conditions (Pinsky, 1990; Innes et al., 1993).

6.1.2. Brain-heart interaction

Recent advances in the physiological understanding of brain–heart interactions have demonstrated the presence of bidirectional communication between these two organs (Candia-Rivera et al., 2025). Beyond the efferent regulation of cardiac rhythm exerted by ANS, previously discussed in Sect. 6.1.1 (Azzalini et al., 2019; Shaffer and Ginsberg, 2017; Taggart, 2013), cardiac interbeat activity can also influence neural dynamics through ascending pathways (Cameron, 2009; Greco et al., 2019; Catrambone et al., 2021). In this context, it is noteworthy that the majority of fibers within the vagus nerve are afferent and that cardiovascular afferents transmit signals to the brain more extensively than with the other organs (Cameron, 2001). Moreover, several studies suggest how heart timing enables the optimization of numerous neural processes related to homeostatic and allostatic regulation (Candia-Rivera, 2022).

In addition to the sympathetic and parasympathetic branches of the ANS, several physiological pathways participate in brain-heart communication. These include baroreceptors (due to the aforementioned regulatory mechanisms), cardiac neurons embedded within the myocardial wall, cutaneous receptors, and the *Intrinsic Cardiac Nervous System* (ICNS) (Park and Blanke, 2019; Khalsa et al., 2009; McCraty and Schafer, 2016). The ICNS constitutes a brain-like structure – including ganglia, neurotransmitters, proteins, and cells – located inside the heart and able to integrate signals from the ANS and all sensory systems related to cardiovascular activity. Information processed within this network is transmitted to the central nervous system via the vagus nerve and spinal pathways, reaching the nucleus tractus solitarii (NTS) and subsequently projecting to higher cortical regions (Azzalini et al., 2019; Chen et al., 2021).

Functional neuroimaging studies identified several cortical areas involved in processing visceral cardiovascular signals, including ventro-medial prefrontal cortex (vmPFC), insular cortex, and anterior cingulate cortex (ACC) (Azzalini et al., 2019; Wong et al., 2007; Babo-Rebelo et al., 2016). These cortical regions partially overlap with the two major brain structures implicated in brain-heart interactions,

i.e., the *Central Autonomic Network* (CAN) and the *Default Mode Network* (DMN) (Candia-Rivera, 2022). The CAN comprises interconnected brainstem and cortical structures responsible for integrating autonomic and cognitive regulation through complex feedforward and feedback loops linking central neural activity with peripheral autonomic outputs (Riganello et al., 2018). In contrast, the DMN consists of brain regions that exhibit higher intrinsic activity during resting-state conditions compared with task-related states (Buckner et al., 2008; Fox and Raichle, 2007; Martinez-Gutierrez et al., 2022). Within this network, the vmPFC has the role of integrating sensory information received from both the internal body – interoceptive – and the external environment – exteroceptive – and of trasmitting them to hypothalamus and amygdala, thus playing a key role in the link between sensory processing, visceral-motor regulation, and behavioral control (Raichle, 2015).

6.2. Extracting time series from physiological signals

When investigating physiological dynamics through signals acquired from the human body, it is necessary to extract the signal features that convey the information of interest. The methods employed for feature extraction depend on the nature of the acquired signals – such as electrical, mechanical, or optical – as well as, and more importantly, on their temporal resolution. As discussed in the introductory chapter of this thesis, particular attention is devoted to the study of dynamical physiological mechanisms. For this reason, the analysis typically relies on physiological time series, defined as sequences of consecutive values describing the temporal modulation of specific signal characteristics (e.g., amplitude, time intervals, or other derived measures). Moreover, when investigating interactions between different organ systems, it is necessary to ensure the comparability of the extracted time series, particularly in terms of temporal resolution. This requirement becomes especially relevant when the signals originate from physiological systems characterized by markedly different dynamics, such as the heart and the brain or the heart and the respiratory system.

With regard to the investigation of cardiovascular and cardiorespiratory dynamics described in Sect. 6.1.1, beat-to-beat time series are generally extracted from ECG, ABP, Breath, and impedance cardiography (ICG) signals. Specifically, the R peak of the ECG waveform – representing the onset of each cardiac cycle – was used in our analyses as the primary fiducial point for the temporal alignment of all signals. Indeed, based on the occurrence of the R peaks, the remaining fiducial points of the other signals were identified to extract beat-to-beat time series. As graphically shown in Fig. 6.1, the n^{th} interbeat interval (RR) is defined as the time distance between the n^{th} and the $(n+1)^{th}$ R peaks of the ECG (i.e., RR_n), generally identified by using the Pan–Tompkins algorithm (Pan and Tompkins, 2007). This quantity reflects

the heart period and therefore is directly related to the heart rate (HR), computed as $HR_n = \frac{60}{RR_n}$, where HR is expressed in beats per minute (bpm). Accordingly, the n^{th} systolic arterial pressure (SAP) value (i.e., SAP_n) is measured as the maximum of the ABP signal inside RR_n and the n^{th} diastolic arterial pressure (DAP) value (i.e., DAP_n) as the minimum of ABP between the occurrences of SAP_n and SAP_{n+1}, whereas mean arterial pressure (MAP) is calculated as the average pressure value obtained by integrating the ABP signals between the occurrences of DAP_{n-1} and DAP_n. Moreover, a surrogate of the interbeat interval time series can be extracted from the ABP signal, namely the pulse pressure (PP) interval. Specifically, the n^{th} pulse interval (i.e., PP_n) is measured as the time distance between the maxima of the arterial pressure waveform within the n^{th} and $(n+1)^{th}$ heartbeats. As can be observed, the respiratory signal presents a slower modulation compared with the cardiac activity. Therefore, to obtain a respiratory-related measure with the same beat-to-beat resolution, the n^{th} respiration amplitude (RESP) value (i.e., $RESP_n$) is extracted sampling the Breath signal at the occurrence of the n^{th} R peak of the ECG. Less investigated cardiovascular parameters can be derived from the first mathematical derivative of the ICG, i.e., the dZ/dt waveform. In particular, by exploiting the Bernstein and Sramek formula (Bernstein, 1986), the stroke volume is estimated by exploiting its proportionality to the maximal systolic ejection speed (dZ/dt^{max}) and the duration of the ejection phase (Left Ventricular Ejection Time, LVET) evaluated in the same beat as the temporal difference between the opening (B point of dZ/dt) and closing (X point of dZ/dt) of the aortic valve. The n^{th} cardiac output (CO) value (i.e., CO_n) is also computed as the ratio between SV_n and RR_{n-1} (Bernstein, 1986; Krohova et al., 2022). These quantities are required to compute AC. In particular, the PVR for each heartbeat (i.e., PVR_n) is computed as the ratio of MAP_n and CO_n, assuming a negligible venous pressure at the right atrium, and then the AC value is derived from the estimation of the time constant τ, which represents the rate of the peripheral ABP decay during the diastolic phase, and exploiting the well-known relationship between τ, AC and PVR based on the two-element Windkessel model, i.e., $AC_n = \tau_n / PVR_n$ (David and Javorka, 2021).

Regarding the investigation of brain-heart interactions described in Sect. 6.1.2, EEG and ECG signals are commonly employed, as they allow the rapid dynamics of both physiological brain and heart systems to be investigated (Valenza et al., 2016). However, these two signals exhibit markedly different temporal dynamics, with EEG characterized by much faster oscillatory activity than the heart rate. Standard approaches for exploring the interplay between cardiac activity and cortical processes from these signals include the analysis of heartbeat-evoked potential (HEP) (Schandry et al., 1986) and the correlation between time series representing ECG-derived features – such as HRV – and the spectral dynamics of EEG oscillations. In the latter case, as for other mentioned physiological dynamics, it is necessary to ex-

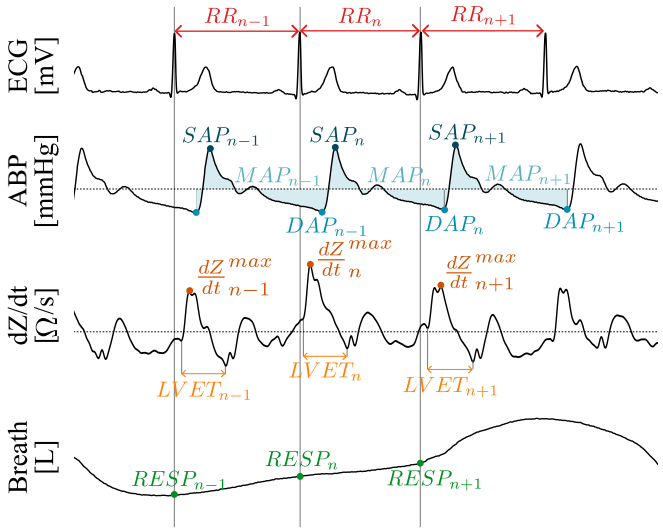

Figure 6.1: Physiological signals (electrocardiogram, ECG; arterial blood pressure, ABP; impedance cardiography, dZ/dt; respiration signal, Breath) and corresponding extracted time series (interbeat interval, RR; systolic arterial pressure, SAP; diastolic arterial pressure, DAP; mean arterial pressure, MAP; respiration amplitude, RESP; left ventricular ejection time, LVET); arterial compliance (AC) is computed exploiting parameters extracted from dZ/dt and ABP waveforms. The figure modified from Barà et al. (2026b).

tract time series with comparable temporal resolution. From this perspective, recent studies have shown that the neuro-autonomic feedback mechanisms linking brain and heart vary across temporal scales and physiological states, highlighting that both coupling and internal brain–heart dynamics are time-scale dependent (Vergara et al., 2025b). In particular, analyses conducted at the cardiac cycle time scale are able to capture heartbeat-related neural responses (Bashan et al., 2012; Schulz et al., 2016), while analyses performed at longer time scales enable the investigation of broader oscillatory dynamics, such as those characterizing different sleep stages (Faes et al., 2014b, 2015b). The application on brain-heart interactions reported in this thesis (Sect. 7.4) does not rely on the extraction of beat-to-beat time series. Instead, the analysis focuses primarily on the dynamics of brain activity, while cardiac activity is used only marginally to evaluate brain responses within specific temporal windows aligned with cardiac events.

An important aspect in the extraction of physiological time series from acquired data concerns both their length and the way temporal relationships are represented, as these factors directly affect the applicability of information-theoretic tools and the interpretation of the results. In clinical practice, 24-hour recordings – commonly referred to as long-term analysis – are considered the "gold standard" for investigating a wide range of physiological responses. In the context of cardiovascular regulation, such extended recordings enable the characterization of slower temporal fluctuations, including circadian rhythms and the influence of multiple external

stimuli (Shaffer and Ginsberg (2017); Cohen and Taylor (2002)). Nevertheless, short-term (ST) measurements – typically based on 5-minute recordings and, in the case of beat-to-beat time series, corresponding to approximately 300 data points – are more widely adopted in both practical applications and research, as they are sufficient to capture most of the physiological regulatory mechanisms described in Sect. 6.1.

Moreover, closely related to these aspects is the possibility of including instantaneous interactions when evaluating causal dynamics. Since causal inference typically assumes that the causes precede their effects, the attribution of the zero-lag interactions depends on how the time series are constructed. Specifically, these instantaneous effects can be visually attributed to one direction rather than the other by inspecting the temporal sequence of the extracted relevant physiological indices in the underlying signals. For example, in the case of cardiovascular and cardiorespiratory time series depicted in Fig. 6.1, zero-lag effects are attributed along the following directions: $RESP_n \rightarrow RR_n$, $RESP_n \rightarrow SAP_n$, $RESP_n \rightarrow DAP_n$, $RESP_n \rightarrow MAP_n$, $RESP_n \rightarrow AC_n$, $SAP_n \rightarrow RR_n$, $RR_n \rightarrow MAP_n$, $SAP_n \rightarrow MAP_n$, $SAP_n \rightarrow DAP_n$, $RR_n \rightarrow DAP_n$, $RR_n \rightarrow AC_n$, $SAP_n \rightarrow AC_n$, $MAP_n \rightarrow AC_n$, and $DAP_n \rightarrow AC_n$ (Barà et al., 2026b).

6.3. Explored databases

This section provides a detailed description of the physiological datasets analyzed in the following chapters. Most of the databases, from Database A to Database D, include recordings representative of cardiovascular and cardiorespiratory dynamics acquired on young healthy subjects during resting conditions, in presence of physiological stressors (e.g., postural changes or mental arithmetic), or under controlled conditions (e.g., paced breathing). While these datasets refer to healthy individuals, Database E, Database F, and Database G were collected from subjects affected by sleep apnea, myocardial infarction, and heart failure, respectively. EEG recordings from healthy subjects during rest are also accounted for in Database H and Database I. Finally, Database L contains gene expression data from breast cancer tissues.

Database A

This database has been collected to have insights on the response of young healthy subjects to the autonomic modulation, as well as to the mechanical influence of ventilatory activity on both cardiac and ventilatory dynamics, during both spontaneous and paced breathing at different respiratory frequencies. More details on the experimental protocol approved by the ethical committee of the "L. Sacco" Hospital (Milan, Italy) and of the Department of Technologies for Health, University of Milan (Italy), can be found in Porta et al. (2011a) and Cairo et al. (2023).

ECG signals (lead II), noninvasive ABP (Finapres 2300, Ohmeda, Englewood,

CO), and respiratory flow traces via nasal thermistor (Marazza, Monza, Italy) were collected from 19 healthy subjects (8 males; age range 27-35 years). Signals were acquired with a sampling frequency of 300 Hz and synchronized through a 12-bit analog-to-digital board (National Instruments, Austin, TX, United States. The acquisition protocol consisted of four sessions: a spontaneous breathing (SB) state, during which subjects were to lie in a supine resting position and breathe spontaneously, followed by randomly ordered paced breathing experimental phases, during which subjects were forced to breathe at three different rates, i.e., 10, 15, and 20 breaths/min (CB10, CB15, and CB20, respectively). Subjects were trained to follow a metronome providing, together with verbal commands given by the experimenter, indications on the initial times of the inspiratory and expiratory phases. The inspiratory-to-expiratory ratio was set to a traditional 1:2 (De Maria et al., 2021). Each of the protocol phases lasted 10 minutes and subjects were not allowed to talk for the entire duration of the protocol.

From the acquired signals, interbeat intervals (RR), systolic arterial pressure (SAP), and respiratory amplitude (RESP) time series were synchronously extracted. Specifically, sequences of 256 consecutive samples starting from about 2 minutes from the start of each of the protocol phases were employed for the analysis reported in Sects. 7.1 and 8.1.

This database has been used in Faes et al. (2022); Pernice et al. (2022a,b); Barà et al. (2023b, 2024c).

Database B

In this section, an historical database employed to investigate cardiovascular and cardiorespiratory dynamics in resting state and in presence of physiological stressors, both physical and mental, and presenting several physiological signals is detailed. Approved by the Ethical Committee of the Jessenius Faculty of Medicine, Comenius University, Martin, Slovakia, the study protocol is described with higher level of detail in (Javorka et al., 2017, 2018).

The study was conducted on a cohort of 127 young healthy subjects (52 males; age 18.6 ± 3.3 years). The experimental protocol consisting of recording cardiovascular signals for 15 minutes in resting supine position (REST1), for 8 minutes after eliciting orthostatic stress by performing the head-up tilt (HUT) maneuver tilting the motor-driven bed where the subjects lie of 45 degrees, and for 6 minutes during long mental arithmetic (MA) during which subjects were asked to sum three digits in the least possible time and to indicate if the resulting number is even or odd. Furthermore, an additional resting state phase was conducted for a duration of 10 minutes between the HUT and MA phases (REST2) with the objective of restoring baseline physiological parameters before proceeding to the mental effort. Specifi-

cally, the ECG signal was recorded by using a horizontal bipolar thoracic lead (CardioFax ECG-9620, NihonKohden, Tokyo, Japan), the ABP waveform acquired from the finger – with the subsequent brachial arterial blood pressure reconstruction – by the photoplethysmographic volume-clamp method (Finometer Pro, FMS Netherlands), and the respiratory volume trace collected through the respiratory inductance plethysmography method (RespiTrace, NIMS, Miami Beach, FL, USA) using both thoracic and abdominal impedance belts. Moreover, the ICG was acquired (CardioScreen 2000, Medis, Germany) , thus enabling continuous beat-to-beat non-invasive monitoring of several indices characterizing myocardial performance and hemodynamics. All the signals were synchronously acquired at a sampling frequency of 1 kHz.

For each subject, different 300 point-long physiological time series were extracted for each of the acquisition phases by discarding the transition effects related to the physiological changes due to the shift from one phase to another. Specifically, these were extracted starting from about 8 minutes after the beginning of the measurement for REST1, about 3 minutes after the position change from supine to tilt for HUT, about 3 minutes after the beginning of the supine recovery for REST2, and about 2 minutes from the beginning of the arithmetic test for MA.

This database has been used in Barà et al. (2022a,b); Volpes et al. (2022a,b); Sparacino et al. (2022); Barà et al. (2023a); Pinto et al. (2023); Barà et al. (2024a,b); Sparacino et al. (2024); Barà et al. (2025a); Antonacci et al. (2025b); Ontivero-Ortega et al. (2025b); Barà et al. (2026b,a, 2025c); Sparacino et al. (2025d); Iovino et al. (2025); Sparacino et al. (2025b); Iovino et al. (2026).

Different versions of the database are used in this thesis, differing for the numerosity of the investigated cohort and the considered signals, due to both the continuation of the acquisition procedures during years and the difficulty of having good quality and continuous time series for some physiological parameter.

Version 1 - From the data acquired on the whole cohort, interbeats intervals (RR) and pulse pressure interval (PP) time series were extracted, together with the time series representative of the respiratory amplitude signal (RESP), and the three components of the arterial pressure dynamics (SAP, DAP, and MAP). This version is used in Sects. 9.1, 9.3, and 12.2.

Version 2 - Interbeats intervals (RR), systolic arterial pressure (SAP), and respiratory amplitude (RESP) time series were extracted from data acquired on 61 subjects (24 males; age 17.5 ± 2.4 years). This version in used in Sects. 7.2, 8.3, and 9.2.

Version 3 - Interbeats intervals (RR), mean arterial pressure (MAP), respiratory amplitude (RESP), and arterial compliance (AC) time series extracted from 39 young healthy subjects (17 males, median age 18.7 years) are used in Sect. 8.5.

Database C

Employed in Sect. 8.1 to investigate cardiovascular dynamics in response to the postural stress, this database has been acquired at the Cardiology Division of the Santa Chiara Hospital of Trento, Trento, Italy. Details on data acquisition protocol and population are reported in Nollo et al. (2005).

Surface electrocardiographic (lead II) and continuous arterial pressure signal acquired via the finger volume-clamp method (Finapres, Ohm-eda 2300; Englewood, CO) were acquired from 15 young healthy subjects (8 males; age 25 ± 3 years) with a sampling frequency of 1 kHz. After 15 minutes of stabilization, subjects were monitored for 10 minutes in a resting supine position (REST) and for 10 minutes in the 60 degree upright position (HUT) reached after a passive head-up tilt maneuver.

Finally, interbeats interval (RR) and systolic arterial pressure (SAP) beat-to-beat time series were extracted from the acquired data, cleaned up from artifacts, windowed to 300 points, and detrended to fulfill stationarity criteria.

This database has been used in Barà et al. (2023b); Mijatovic et al. (2023).

Database D

The Healthy Young POLes (HYPOL) dataset includes recordings from 278 healthy young Polish adults (129 males; age 23.8 ± 2.6 years). Participants underwent a comprehensive clinical screening to exclude cardiovascular and systemic pathologies.

Signals were recorded in the supine resting position using a bipolar chest-lead ECG and noninvasive finger ABP (Portapres 2 or Finapres Nova, FMS, Netherlands). The electrocardiographic signal was sampled at either 1600 Hz or 2048 Hz, while the arterial blood pressure waveform at 100–200 Hz, depending on the hardware. The electrocardiographic signal was sampled at either 1600 Hz or 2048 Hz, while the arterial blood pressure waveform was acquired at 100–200 Hz, depending on the hardware configuration. Analog-to-digital conversion was performed using Porti 5 or Porti 17 systems (TMSI, The Netherlands). Recordings lasted up to 45 minutes, and approximately 30 minutes of high-quality data were selected for each subject.

From the acquired signals, beat-to-beat time series of interbeats interval (RR), systolic arterial pressure (SAP), and diastolic arterial pressure (DAP) were extracted. For each subject, 300-sample segments were analyzed after discarding the first 60 beats.

An application of this database is reported in Sect. 12.1. Further details regarding the experimental protocol and ethical approval can be found in Guzik et al. (2023).

This database has been used in Iovino et al. (2024a); Ontivero-Ortega et al.

(2025b).

Database E

A respiratory signal from a 49-year-old male with a diagnosis of sleep apnea was acquired. Acquired via a nasal thermistor at a sampling frequency of 250 Hz, the signal was down-sampled to 2 Hz using an averaging procedure over a window of 0.08 seconds to obtain the RESP time series, and then a segment of 40 minutes (i.e., 1200 samples) over around six hours of sleep was selected. The signal investigated in Sect. 7.3 was acquired at the sleep laboratory of Boston's Beth Israel Hospital and is available online on Physionet (Goldberger et al., 2000).

This database has been used in Antonacci et al. (2025a); Pinto et al. (2025).

Database F

This section describes part of the data collected within a multicenter randomized clinical trial conducted to assess the efficacy of lisinopril, transdermal glyceryl trinitrate, and their combination in improving survival and ventricular function after acute myocardial infarction (AMI), known as the GISSI-3 study (Del Greco et al., 1998).

It includes data acquired from (i) 19 young healthy subjects (10 males; age 25.0 ± 2.6 years), (ii) 12 old healthy subjects (3 males; age 63.1 ± 8.3 years), and (iii) 35 post-AMI subjects (31 males; age 58.5 ± 10.2 years) examined 10±3 days after the event. Eight patients from the post-AMI group were treated with β-blockers discontinued two half-lives before the recordings, while all healthy subjects were normotensive and without previous disease states. One-lead electrocardiographic signal (Siemens Mingograph) and arterial blood pressure waveform by a photoplethysmographic Finapres device (Ohmeda 2300; Englewood, CO) were synchronously acquired at a sampling frequency of 1 kHz. After a period of 15 minutes in a resting supine condition (REST), the subjects underwent 10 minutes of passive head-up tilt at 60 degree (HUT).

The acquired signals were high-pass filtered using a zero-phase AR filter to remove slow trends and then, interbeats interval (RR) and systolic arterial pressure (SAP) time series with a length of 300 samples selected for each subject and experimental condition to obtain visually artifact-free and stationary windows.
Further details on experimental protocol and data acquisition are reported in Nollo et al. (2002); Faes et al. (2019a). These data have been used in Sect. 8.2.

This database has been used in Cimignolo et al. (2025a,b).

Database G

The physiological signals described here are part of the database used in Radovanović et al. (2021), which includes patients with heart failure characterized by reduced left ventricular ejection fraction (LVEF < 35%) and provides information related to the implantation of a cardiac resynchronization therapy (CRT) device. The study was conducted at the Pacemaker Center of the University Clinical Center of Serbia and was approved by the Ethics Committee of the Faculty of Medicine, University of Belgrade. Analyses performed on this database are reported in Sect. 8.4.

Specifically, 29 heart failure patients were divided into three groups: (i) 14 patients with sinus rhythm (HFSin), (ii) 11 patients with a number of extrasystole lower than 6 (HFVES1), and (iii) 14 patients with more than 6 extrasystole (HFVES2). Measurements were performed immediately before device implantation (baseline) and approximately 9 months after CRT device implantation (follow-up). After follow-up, patients were divided into two groups, i.e., responders (N = 25) and non-responders (N = 14), in relation to their response to CRT. This distinction was assessed according to changes in certain echocardiographic and clinical parameters, e.g., increasing of at least 5% and improving of at least one class category in the New York Heart Association functional classification.

For each of the acquisition phases, electrocardiographic and respiratory signals were acquired for 20 minutes with patients lying in supine position and spontaneously breathing. Specifically, ECG was acquired using an ECG 100C electrocardiogram amplifier module, while the ventilatory activity in terms of bdominal expansion and contraction was measured via an RSP 100C respiratory pneumogram amplifier module with TSD 201 transducer attached to the belt. The Biopac MP100 system and AcqKnowledge 3.9.1 software (BIOPAC System, Inc., Santa Barbara, CA, USA) were used to synchronously acquired the two signals by using a sampling frequency of 1 kHz.

Starting from the acquired signals, physiological time series were obtained. Specifically, interbeat intervals (RR) time series were extracted by using the Pick Peaks tool from OriginPro 8.6 (OriginLab Corporation, Northampton, MA, USA) and the respiratory amplitude (RESP) time series from the detected ECG peaks. In the case of extrasystole patients, the time coordinate of the peak from extrasystole was used was R peak coordinate. Moreover, given that the RR and respiration samples obtained in this way were not equally positioned, an equidistant resampling of both series was carried out using the mean RR value of each individual as resampling interval, by using a linear interpolation between two corresponding adjacent existing samples (Kapidžić et al., 2014). In this way, the resampling frequency was different for each subject (range 0.8–1.5 Hz) and the final RR and RESP time series result in a different numbers of samples according to the individual resampling fre-

quency. Details on time series differences for the different investigation groups are reported in the original paper.

This database has been used in Platiša et al. (2023).

Database H

This section describes the database employed in Sect. 7.4 to investigate brain–heart interactions. The acquisition protocol was carried out at the "Institute for Advanced Biomedical Technologies – ITAB" of the "G. d'Annunzio" University of Chieti-Pescara. Further details are provided in Zaccaro et al. (2022).

EEG and ECG signals were synchronously acquired from 20 healthy subjects (6 males; age 28.88 ± 4.78 years) during a resting-state condition, in which participants were instructed to remain seated with eyes open. EEG recordings were obtained using a gel-based BrainAmp system (BrainCap MR, Brain Vision, LLC) equipped with 64 electrodes positioned according to the international extended 10–20 system. The midfrontal electrode served as reference, and the inion electrode was used as ground. ECG traces were recorded using a single-lead system (BIOPAC Systems, Inc.). All signals were synchronously sampled at 2 kHz.

This database has been used in Antonacci et al. (2022); Barà et al. (2023c); Antonacci et al. (2023); Vergara et al. (2023, 2025c,a).

Database I

This database includes electroencephalographic signals recorded from 21 young healthy subjects (10 males; age range 22–39 years) with normal vision and no history of neurological or psychiatric disorders.

19 EEG channels were recorded using the 10-20 standard system for electrode positioning, with Fpz and Oz electrodes set as reference and ground electrodes, respectively (Micromed Brain Quick System, Treviso, Italy). The acquired data were then digitized with a sampling rate of 256 Hz and 16-bit resolution. Participants were instructed to lie down and assume a relaxed state in a dark room free from electrical and acoustic interference. Then, brain neural signals were acquired for 40 seconds with both eyes closed (EC) and eyes open (EO).

Further detailed in Faes et al. (2016a), this database was employed in Sect. 12.4.

This database has been used in Barà et al. (2025b).

Database L

This dataset, obtained from the Marginal Contribution Feature Importance (MCI) framework (Catav et al., 2021), is derived from The Cancer Genome Atlas – Breast Invasive Carcinoma (RCGA-BRCA) RNA sequencing dataset, which contains gene

expression measurements from breast cancer tissues (Tomczak et al., 2015). It comprises 572 samples characterized by the expression levels of 50 genes and spans four molecular breast cancer subtypes: 304 Luminal A (LumA), 114 Luminal B (LumB), 105 Basal-like, and 49 HER2-enriched. The database is publicly available on GitHub and was employed in Sect. 12.3.

This database has been used in Lazic et al. (2026).

6.4. Overview and conclusions of chapter 6

This chapter provides the background necessary for the appropriate application of the information-theoretic measures introduced in the previous part to physiological dynamics, as well as for the correct interpretation of the results shown in the current part of the thesis in light of physiological regulatory and control mechanisms. The objective is thus to bridge physiological concepts with the methodological framework of information theory.

Focusing mainly on cardiovascular and cardiorespiratory dynamics, Sect. 6.1 describes the regulatory mechanisms underlying the intrinsic variability of cardiac activity, arterial pressure, and respiratory dynamics, emphasizing their interconnections within a complex physiological network. The potential of information-theoretic metrics lies in their ability to exploit the variability of the investigated dynamics and to capture network interactions, thus distinguishing them from conventional approaches operating in the time or frequency domains. These aspects have already been introduced in the thesis in relation to the concepts of physiological complexity and network physiology. Information-theoretic measures, grounded on the concept of entropy, investigate physiological dynamics by quantifying the information conveyed by temporal variations in the observed time series and, as previously discussed, such variability characterizes healthy physiological behavior, whereas dysfunction in regulatory mechanisms typically leads to a reduction in this variability (Pincus, 1994; Romero-Ortuño et al., 2021). Additionally, within the framework of network physiology, these tools enable the investigation of how variability in one physiological subsystem relates to that in another, either through coupling mechanisms or via directed (causal) interactions, as well as to that of multiple physiological subsystems, thus revealing emergent collective dynamics (Ivanov, 2021). Accordingly, the mentioned information-theoretic measures are used throughout the current part of the thesis to hierarchically evaluate physiological dynamics related to individual body districts (Chapter 7), pairs of physiological systems (Chapter 8), and subgroups of systems within a wider network (Chapter 9).

As highlighted in Sect. 6.2, investigating physiological dynamics from signals acquired from multiple body districts requires careful consideration of how signals features are extracted from the signals, temporal alignment and consistency in the

resolution of the extracted features, so as to enable meaningful comparison and integration of information across different physiological sources. Moreover, another critical point relates to the number of observations of these features. For instance, as previously mentioned, short-term cardiovascular and cardiorespiratory dynamics are typically investigated through beat-to-beat time series of approximately 300 samples, thus supporting the suitability of the databases described in Sect. 6.3 (from Database A to Database G). In the context of HRV analysis, ST recordings allow for the assessment of the balance between sympathetic and parasympathetic activity, as well as the associated regulatory mechanisms involving respiration, baroreflex control, and vascular tone, which jointly contribute to short-term cardiovascular dynamics (Shaffer and Ginsberg, 2017; Malpas, 2002; Schulz et al., 2013). Similarly, short-term BPV reflects the complex interaction between extrinsic environmental influences and intrinsic cardiovascular regulatory processes (Parati et al., 1997, 1998; Pernice et al., 2019). Recent studies have investigated the feasibility of HRV and BPV analysis using ultra-short-term (UST) recordings, thus employing physiological recordings shorter than 5 minutes (Castaldo et al., 2019; Kim et al., 2021; Pecchia et al., 2018; Shaffer et al., 2016). The ability of such recordings to resolve slow cardiovascular oscillations is inherently limited (Shaffer et al., 2016; Camm et al., 1996). Specifically, it has been suggested that recordings of at least 2 minutes are required to capture low-frequency dynamics (0.04–0.15 Hz), whereas recordings of approximately 1 minute may suffice for high-frequency dynamics (0.15–0.4 Hz). Finally, another relevant aspect concerns the selection of the most appropriate time series for investigating specific physiological dynamics. From a single signal, multiple time series can be extracted, each reflecting different dynamics of the complex regulatory mechanisms. For examples, ABP signals can yield SAP, DAP, and MAP time series and, while BPV has traditionally been assessed via systolic or diastolic arterial pressure, recent studies support the use of MAP as a robust measure (Krohova et al., 2022).

Finally, it is important to note that, while the pipeline for extracting cardiovascular and cardiorespiratory time series is well established in the literature, the investigation of other physiological dynamics mentioned in the chapter, such as brain dynamics, involves less standardized time series extraction approaches. It has been demonstrated how the interpretation of brain dynamics and brain–body interactions, as investigated through information-theoretic approaches, is significantly influenced by the method employed for time series extraction. Furthermore, the outcomes are contingent on the characterisation of the phenomena under investigation across a range of temporal scales (Vergara et al., 2025c).

Chapter 7

Univariate analysis of physiological signals

In this chapter, different applicative examples of the univariate dynamic measures defined in Chapter 3 are shown to demonstrate their applicability over a variety of physiological time series. Specifically, complexity of cardiorespiratory (Sect. 7.1) and cardiovascular (Sect. 7.2) dynamics are investigated in response to a controlled breathing protocol and to the head-up tilt maneuver. Moreover, local respiratory dynamics during sleep apnea events (Sect. 7.3) and the modulation of the electroencephalographic dynamics with the different phases of the cardiac cycle (Sect. 7.4) are evaluated.

7.1. Cardiac and breathing dynamics complexity during spontaneous and controlled breathing

In this section, the analyses conducted in Barà et al. (2024c) for investigating the modulation of physiological complexity with different physiological states are reported. Specifically, different entropy rate estimation approaches have been applied to explore short-term cardiorespiratory dynamics by investigating RR and SAP time series collected in Database A during spontaneous (SB) and controlled breathing at different respiratory rates (CB10, CB15, and CB20).

Data preprocessing - Time series were preprocessed by using a high-pass AR filter (zero phase and cut-off frequency of 0.0156 Hz) and by removing and interpolating the outlier samples (i.e., samples differing more than three standard deviation from the mean value). Moreover, all time series were normalized to zero mean and unit variance.

Data and statistical analysis - The ER estimation strategies delineated in Sect. 3.1.1 were applied to both RR and RESP time series, with the estimation parameters

set based on the results of the simulation studies reported in Sect. 3.1.2 and in accordance with the most prevalent choice in the extant literature. Specifically, the BIC criterion was employed to define the optimal order of the AR model used to linearly describe the dynamics of the two processes by fixing a maximum model order of 10. Moreover, the embedding dimension m was fixed to 2 for the nearest-neighbor and binning approaches, and to 4 for the permutation-based method. The estimation parameter k was fixed at 10 for the nearest-neighbor strategy, while the number of quantization levels b to 6 for the binning approach.

The hypothesis of Gaussianity was tested through the Kolmogorov-Smirnov test, thus parametric statistical tests were used to assess statistical differences among the distributions of ER obtained among the different phases of the breathing protocol. Specifically, the ANOVA test of variance was performed followed by a post-hoc paired Student's t-test between the SB condition and each of the controlled breathing stages by applying the Bonferroni correction for multiple comparisons ($n = 3$). All statistical tests were performed with a significance level of 5%.
Furthermore, the statistical significance of each estimated value was evaluated for each subject and condition by using the surrogate data analysis approach detailed in Sect. A.2.1 of the Appendix. Specifically, one-hundred surrogate data were generated for each time series by using a significance level of $\alpha = 0.5$.

Results and discussion - Fig. 7.1 reports how all methods reveal a decrease of the entropy rate of RR during CB10 and CB15 compared to SB, as well as similar values during CB20 (panels (*.1*)). This trend is always statistically significant for the slowest paced breathing rate, i.e., CB10, being instead not significant for CB15 using the binning estimation strategy (panel (*c.1*)). This decrease is indicative of a reduction of the cardiac system complexity and an increased regularity that can be related to a strengthening of specific regulatory mechanisms. Specifically, the result can be related to the RSA mechanism, which is responsible for the modulation of the cardiac dynamics by breathing activity (Berntson et al., 1993) and that has been demonstrated to be enhanced during forced ventilation at lower respiratory rates (Tzeng et al., 2003) Moreover, the same trend is reported for the ER measures evaluated on the RESP time series (panels (*.2*)), with a statistically significant decrease during CB10 with all estimators and during CB15 with the linear and the permutation ones (panels (*a.2*) and (*d.2*)). This finding can be related to the respiratory stroke volume synchronization mechanism which induces changes in respiratory dynamics analogous to those of the heartbeats (Elstad et al., 2018).

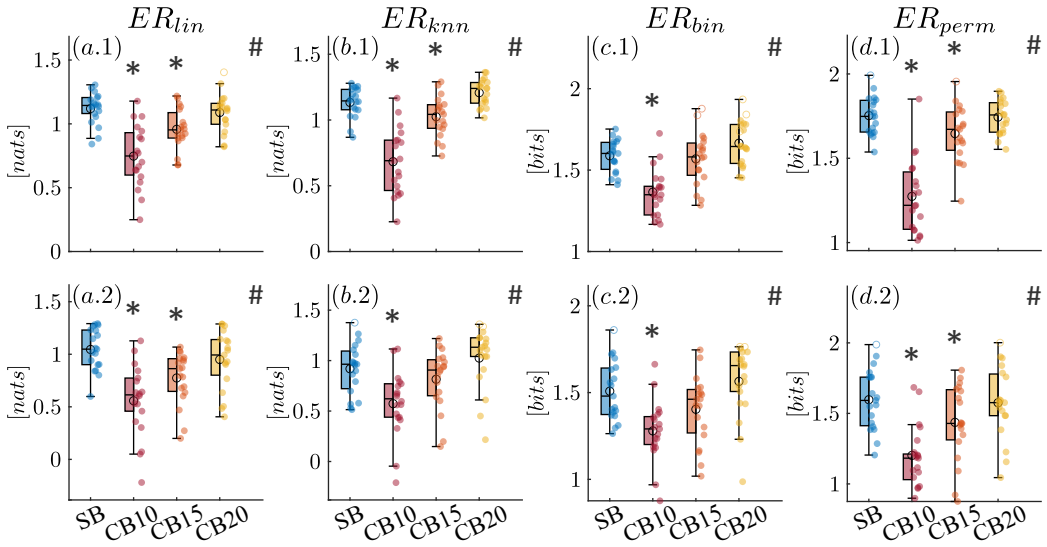

Figure 7.1: Boxplot distributions and individual values of the ER computed for the RR (panels (.1)) and RESP (panels (.2)) time series during spontaneous (SB) and controlled breathing at 10, 15, and 20 breaths/minute (CB10, CB15, and CB20) with (panels (*a*)) linear, (panels (*b*)) nearest-neighbor, (panels (*c*)) binning, and (panels (*d*)) permutation approaches. In each panel, empty circles correspond to values deemed as statistically non-significant using surrogate data analysis; black open circles refer to the sample mean of each distribution. Statistical tests: #, $p < 0.05$, ANOVA test; *, $p < 0.05/3$ CB10/CB15/CB20 vs. SB, paired Student's *t*-test with Bonferroni correction. The figure was modified from Barà et al. (2024c).

7.2. Ultra-short term analysis of cardiac and vascular dynamics complexity during postural and mental stress

Heart rate variability and blood pressure variability are usually investigated through ST measurements, which exploit ECG and ABP recordings of at least 5 minutes, corresponding to beat-to-beat physiological time series of about 300 samples. Recent research is focused on using reduced time series length to assess if the use of UST analysis is able to capture physiological insights about cardiovascular variability. In this section, the comparison between ST and UST measures computed on heart period and systolic arterial pressure dynamics performed in Volpes et al. (2022a) is discussed. Specifically, RR and SAP time series collected in Database B - *version 2* during all the four phases of the acquisition protocol (REST1, HUT, REST2, and MA) were investigated.

Data preprocessing - In order to perform UST analyses, the 300-length time series were progressively shortened. Specifically, the time series length was reduced of 60 samples each step, till reaching time series of 60 samples. Thus, the resulting UST time series were composed of 240, 180, 120, and 60 samples, selected starting from the beginning of the whole time series.

Data and statistical analysis - After normalizing RR and SAP time series to

zero mean and unit variance, the linear parametric and nearest-neighbor estimation strategies were applied to compute the ER measures related to each subject and condition. The number of neighbor k was fixed to 10 for the nearest-neighbor approach, while the history of the two processes was approximated to $m = 2$ past lags for both estimation strategies.

After the assessment of the normality distribution of the ER values computed on the cohort of subjects for each condition and time series (for all the considered lengths) via the Kolmogorov–Smirnov test, the paired parametric Student's t-test was used to perform a pairwise comparisons between the resting states and the two stress conditions, as well as between ST and UST distributions. Specifically, by imposing a significance threshold of 0.05, the first resting phase was compared with the orthostatic stress state (HUT vs. REST1), while the second resting phase with the mental stress state (MA vs. REST2). Moreover, the same threshold was used to assess the statistical differences between the ER distributions obtained by using time series with the length of 300 samples and each of the shortened ones.
The effect size of the differences between the distributions obtained for different protocol phases was also evaluated for the ST and UST analysis to avoid possible misleading influences of the sample size on the results of the statistical tests and to quantify to what extent the strength of the distribution modification changes using shortened data (Fritz et al., 2012). Specifically, the Cohen's d measure, obtained as the difference between the means of the two compared distributions divided by the pooled standard deviation, was used; the effect size d was deemed as small for values lower than 0.2, medium for values between 0.2 and 0.5, and large for values larger than 0.8 (Cohen, 2013).
Finally, a correlation analysis was performed to evaluate the strength of the linear relationship between each of the UST distributions and the ST distribution as to quantify their agreement when reducing the length of the time series. In accordance to (Shaffer et al., 2016, 2020), we set a threshold of $r^2 = 0.81$ for the squared Pearson correlation coefficient over which a strong agreement between the indices derived from UST and ST analysis was acknowledged.

Results and discussion - Fig. 7.2 shows a decrease of the entropy rate of the RR time series when shifting from resting condition to orthostatic or mental arithmetic stress states computed with both linear and nearest-neighbor estimators. Specifically, this variation is statistically significant for both estimators and for both ST and all UST analyses in the case of the postural stress (panels (*.1*)), while only with the linear estimator by using time series with a duration of at least 120 samples in the case of mental stress (panel (*a.2*)). It can be observed that ER values tend to increase when decreasing the length N of the time series, particularly for the nonlinear estimator. As evidenced by the statistical comparison between ST and UST distributions, the *knn* approach highlights significant difference starting from $N = 240$ in-

dependently from the experimental conditions (panels (*b.*)), while the *lin* approach starting from $N = 120$ and $N = 240$ for the HUT and MA, respectively (panels (*a.*)). The Cohen's d values reveal higher effect size for the linear approach, even reporting high and medium effect size during HUT and MA, respectively, independently from the estimation strategy. Finally, the squared correlation coefficient decreases with N still showing a high degree of correlation for all conditions and estimators till $N = 120$.

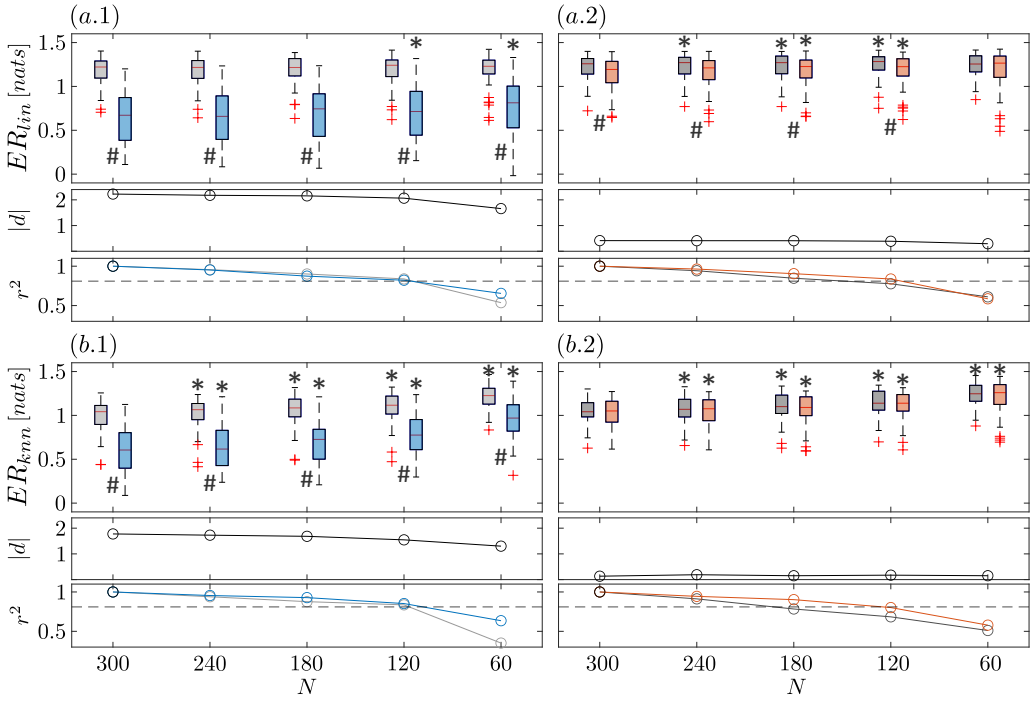

Figure 7.2: Boxplot distributions (top subplots) of ST and UST indices of ER calculated on RR time series using linear (panels (*a.*)) and nearest-neighbor (panels (*b.*)) estimation approaches during REST1 (light gray) and HUT (light blue) (panels (*.1*)), and during REST2 (dark gray) and MA (red) (panels (*.2*)) phases. Statistical tests: #, $p < 0.05$ HUT vs. REST1 or MA vs. REST2, Student's t-test; *, $p < 0.05$ ST vs. UST, Student's t-test. Cohen's d in absolute value (central subplots) evaluated between each stress condition and the previous rest phase for all the considered time series lengths. Squared Pearson correlation coefficient (bottom subplots) computed between each UST distribution and the correspondent ST reference, with a threshold of $r^2 = 0.81$ indicated by a dotted gray line. The figure was taken from Volpes et al. (2022a).

Fig. 7.3 reveals a decrease of the ER terms for the SAP time series from REST1 to HUT and, conversely, an increase from REST2 to MA. Nevertheless, while the difference between resting state and mental stress is statistically significant for both ST and all UST analysis (panels (*.2*)), the shift from resting state to orthostatic stress leads to significant differences only with the linear estimator for $N \geq 120$ (panel (*a.1*)). Also in this case, the ER estimates increase with a decrease of N, revealing statistically significant difference already for $N = 240$ when compared with $N = 300$, with the exception of the linear estimator when evaluating ER values in REST1 and

HUT, that reveal significant differences only for $N \geq 120$ and $N \geq 180$, respectively (panel (*a.1*)). The effect size is always medium-low and overall decreases in absolute value when N decreases. The squared correlation coefficient decreases with the length of the time series, still reporting values higher than the threshold for $N \geq 180$ for all experimental conditions and estimators.

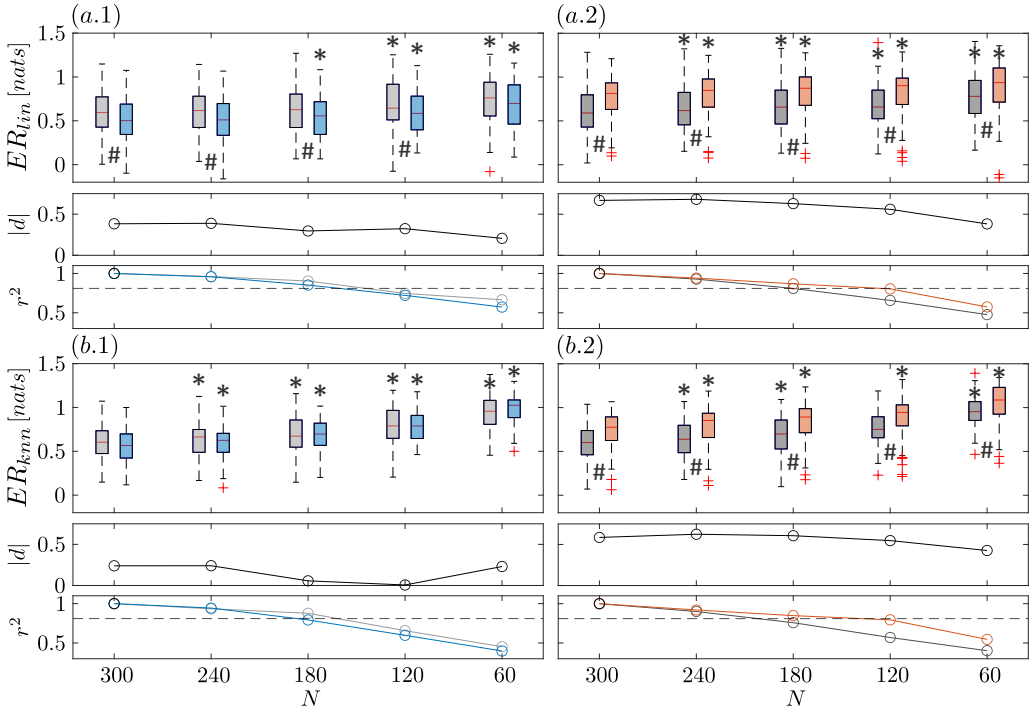

Figure 7.3: Boxplot distributions (top subplots) of ST and UST indices of ER calculated on SAP time series using linear (panels (*a.*)) and nearest-neighbor (panels (*b.*)) estimation approaches during REST1 (light gray) and HUT (light blue) (panels (*.1*)), and during REST2 (dark gray) and MA (red) (panels (*.2*)) phases. Statistical tests: #, $p < 0.05$ HUT vs. REST1 or MA vs. REST2, Student's t-test; *, $p < 0.05$ ST vs. UST, Student's t-test. Cohen's d in absolute value (central subplots) evaluated between each stress condition and the previous rest phase for all the considered time series lengths. Squared Pearson correlation coefficient (bottom subplots) computed between each UST distribution and the correspondent ST reference, with a threshold of $r^2 = 0.81$ indicated by a dotted gray line. The figure was taken from Volpes et al. (2022a).

The results of these investigations demonstrate a decrease in the complexity of cardiac dynamics in response to both postural and mental stress. These findings support the well-known shift in autonomic balance, characterized by sympathetic activation and vagal withdrawal during these challenges (Cooke et al., 1999). This alteration has been indeed associated with the regularization of cardiac interbeat dynamics at the frequency of Mayer waves, as already evidenced in the works of Porta et al. (2007b); Javorka et al. (2018); Pernice et al. (2019), and that results in a decreasing complexity of such dynamics. Conversely, less evident and opposite trends are observed for the complexity of arterial pressure dynamics with stressors of different nature. The decreasing trend of SAP complexity during tilt can be at-

tributed to the synchronization of peripheral vascular activity and blood pressure fluctuations due to sympathetic activation (Baselli et al., 2005). On the other hand, the increasing complexity in response to mental stress can be associated with complex patterns of vascular resistance, also indicative of a larger involvement of the upper brain centers in the sympathetic activation response, as discussed by Fauvel et al. (2000) and Javorka et al. (2018).

We found that both estimators have the capacity to distinguish orthostatic and mental stress states, even with a higher efficacy of the linear strategy when using UST analysis. Linear ER measures have been shown to reveal differences between rest and stress conditions using time series of 120 samples (in some cases also 60 samples). However, the correlation analysis demonstrated a strong agreement across the results obtained via UST and ST analysis for RR when N is greater than 120 and for SAP when N is greater than 180. Furthermore, as emphasized by the effect size, a diminished discriminatory ability among stress and rest states is observed when reducing the length of the time series. This finding may be attributed to the loss of information associated with slower physiological dynamics, which are less likely to be captured in shorter recordings. However, a non-negligible contribution may also arise from physiological nonstationarity within the 300-beat time series, resulting from varying levels of orthostatic stress during the HUT phase, as well as from both fatigue and adaptation responses occurring during the MA phase. Further analysis should therefore consider the use of shorter moving windows shifting across the entire duration of the recordings. This would serve to mitigate the effects of nonstationarity and enable a more reliable assessment of the impact of the time series length on the characterization of cardiovascular dynamics.

7.3. Case report: respiratory dynamics during sleep apneas through local predictability measures

Sleep apnea events are characterized by the occurrence of repetitive and alternated transitions of the respiratory dynamics from relatively stable breathing periods to apneic episodes, during which no respiratory activity is detected. The transient nature of this phenomenon makes approaches suitable for the temporal observation of evolving dynamics appropriate for its investigation. In this section, the local IS measure estimated through both continuous linear and nonlinear estimation strategies is applied on the respiratory signal detailed in Database E acquired on a subject suffering of sleep apnea. In Fig. 7.4 (*a*), the investigated RESP time series is depicted and the apnea intervals, characterized by the absence of the respiratory oscillations, highlighted in gray. These findings are partly retrieved by Antonacci et al. (2025a), where a comparison between linear local and time-varying IS metrics was performed. This study is a case report, investigating data from a single subject,

with the aim of illustrating the behavior of the local IS approach. Therefore, it does not delve into the details of the sleep apnea event phenomenology.

Data and statistical analysis - The local IS was evaluated on the RESP time series by using both linear parametric and nearest-neighbor approaches. Specifically, IS_{lin} was obtained by using a model order $p = 7$ for defining the AR model describing time series dynamics; this was estimated according to the MDL criterion by fixing the maximum order to 20. IS_{knn} was indeed computed using an embedding dimension m of 3 and fixing the number of neighbor k to 10. The distributions of the mean (MEAN) and variance (VAR) of the local IS series obtained during the 14 apneas intervals (A) and the 15 breathing intervals (B) are compared by means of a non-parametric Wilcoxon signed rank test for unpaired data with a significance threshold α of 0.05.

Results and discussion - Fig. 7.4 shows how the IS profiles computed with both the linear (panel (*b*)) and nearest-neighbor (panel (*c*)) estimation approaches clearly distinguish respiratory and apnea windows, revealing higher variability during breathing activity and almost absence of variability during apneic episodes. This result is indicative of stronger predictable dynamics of the respiratory signal during non-apneic periods due to reduced respiratory oscillatory activity (Stramaglia et al., 2021). This finding is statistically confirmed in Fig. 7.5, where significant differences are observed when comparing the variance of the IS evaluated in windows corresponding to the two different respiratory conditions (panel (*b*)).

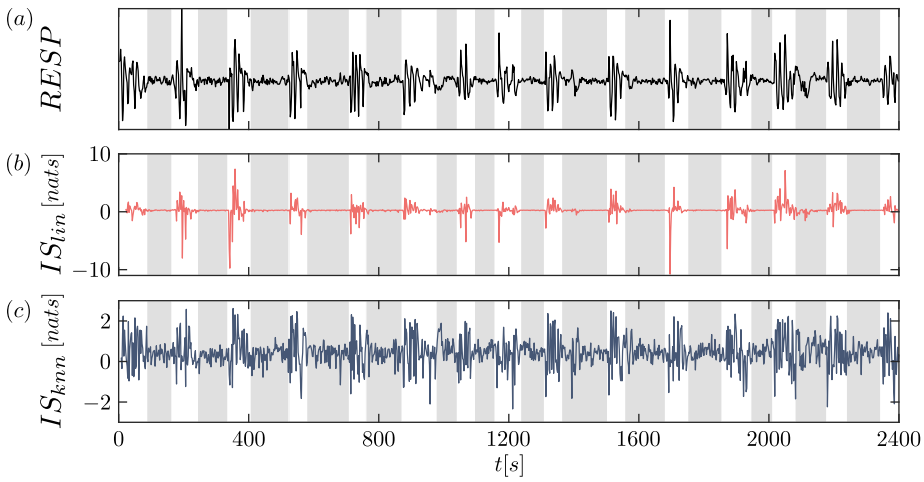

Figure 7.4: Respiratory time series (RESP) measured for a subject suffering of sleep apneas (panel (*a*)); not-breathing intervals are evidenced with gray windows. Temporal profiles of the local information storage estimated through linear parametric (panel (*b*)) and nearest-neighbor (panel (*c*)) estimation approaches. The figure was partly adapted from Antonacci et al. (2025a).

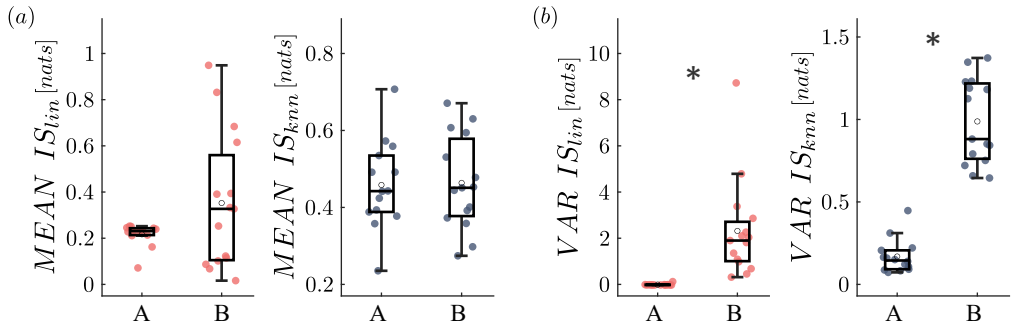

Figure 7.5: Boxplot distributions and individual values of local IS estimated with both linear parametric (*lin*) and nearest-neighbor (*knn*) approaches and representative of the mean (MEAN, panels (*a*)) and variance (VAR, panels (*b*)) in apneic (A) and breathing (B) epochs. Statistical test: *, $p < 0.05$ A vs. B, non-paired Wilcoxon signed rank. The figure was partly adapted from Antonacci et al. (2025a).

7.4. Local predictability analysis of heartbeat-evoked cortical responses

Local measures of regularity can be applied to assess how the predictability of the brain signals varies in relation to the simultaneously recorded cardiac activity, and therefore to investigate how these two processes overlap in generating physiological events such as the cortical processing of the heartbeat. Specifically, electroencephalographic and electrocardiographic signals from Database H have been employed. This analysis was conducted in Barà et al. (2023c) and the main results are here reported.

Data preprocessing - EEG signals were band-pass filtered with a Hamming window FIR filter with cut-off frequencies of 0.5 and 40 Hz, while artifacts and noise due to movements or incorrect contact of electrodes with skin were manually removed and spherically interpolated. Moreover, Independent Component Analysis (ICA) was employed (fastICA algorithm) to limit the influence of artifacts and other physiological activities on EEG signals. Finally, EEG signals were down-sampled to 128 Hz and re-referenced to the average of all channels. As regards the ECG traces, a modified version of the Pan–Tompkins algorithm was applied for each subject to identify the R peaks, and the T and P waves extracted using an appositely developed threshold-based peaks detection algorithm. Due to the presence of artifacts, subsequent analyses were performed on 18 subjects.

Data and statistical analysis - For each subject, the global and local IS were computed on all EEG traces using both linear parametric and continuous model-free estimation strategies. Specifically, a model order $p = 5$ was fixed for the AR model necessary for linear estimation, while an embedding dimension $m = 5$ and a number of neighbor $k = 10$ were set for the nearest-neighbor estimation approach.

Based on EEG and ECG signals synchronization, the local IS was analyzed sep-

arately in different phases of the cardiac cycle. Specifically, as shown in Fig. 7.6 (*a*, top), three different intervals were defined by segmenting the cardiac intervals as follows: the first interval I_1 starts at the R peak of the ECG signal and ends 80 ms after the peak of the T wave, the second interval I_2 starts at the end of the first interval and ends 40 ms before the peak of the P wave of the next cardiac cycle, and the third interval I_3 covers the rest of the cardiac cycle until the R peak of the next cardiac cycle. These intervals have been defined to take into account the influence of the Cardiac Field Artifact (CFA) on brain signals (Dirlich et al., 1997). The electrical activity generated by the heart can be detected on the whole body surface, including the scalp. CFA affects the amplitude of the EEG signals in different magnitudes according to the spatial distribution on the scalp, depending on the proximity of the electrodes to the heart, and with time, depending on the phase of the cardiac cycle. Specifically, previous research highlighted how the interval I_1 is the most affected by the CFA being more evident between the QRS complex and the T wave, while the interval I_2 presents a negligible influence Dirlich et al. (1997). Accordingly, the local IS evaluated on 300-heartbeat were segmented in these three intervals, as shown for a representative subject in Fig. 7.6 (*a*, center and bottom). For each subject and electrode, the mean (MEAN) and the standard deviation (STD) of the local IS measures were computed within the whole cardiac cycle and each of the three intervals, thus obtaining 300 values of local IS mean and standard deviation.

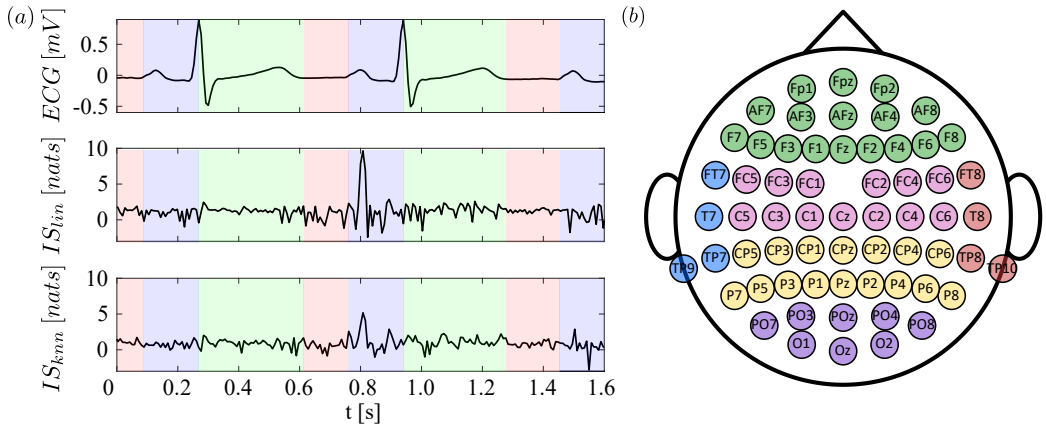

Figure 7.6: ECG signal fragment for a representative subject (top) and corresponding local IS time series obtained by linear (middle) and nearest-neighbor (bottom) estimators, depicting the three time intervals obtained through segmentation of the cardiac cycle (I_1 in green, I_2 in red, and I_3 in purple) (panel (*a*)). Schematic representation of the placement of the EEG electrodes, evidencing the clustering of electrodes according to six scalp regions: frontal in green, central in magenta, parietal in yellow, occipital in blue, right-temporal in red and left-temporal in cyan (panel (*b*)). The figure is adapted from Barà et al. (2023c).

Finally, spatial variations across the scalp were analyzed across the six regions according to the electrode locations reported in Fig. 7.6 (*b*), i.e., frontal (F) in green, central (C) in pink, parietal (P) in yellow, occipital (O) in purple, right temporal (Tr)

in red, and left-temporal (Tl) in azure. Specifically, for each subject and interval, values of local IS MEAN and STD were determined for each region taking the average of the values referred to all electrodes belonging to that region. A statistical comparison between pairs of regions was performed using the paired Student's t-test with Bonferroni correction for multiple comparisons ($n = 15$). Moreover, the effect size was evaluated to assess the magnitude of the differences observed among regions by using the Cohen's d measure already described in Sect. 7.2.

Results and discussion - Fig. 7.7 shows that the distributions over the scalp of the average values of the IS evaluated during the whole cardiac cycle and also in the three defined intervals are very similar with both estimation strategies (panels (a)). Contrarily, the distributions of the standard deviation values exhibit different patterns during the cardiac cycle showing a decreasing trend going from the first to the third interval, with highest values if evaluated globally (panels (b). Results evidence that the nonlinear estimator leads to values of the local IS and of its variability lower

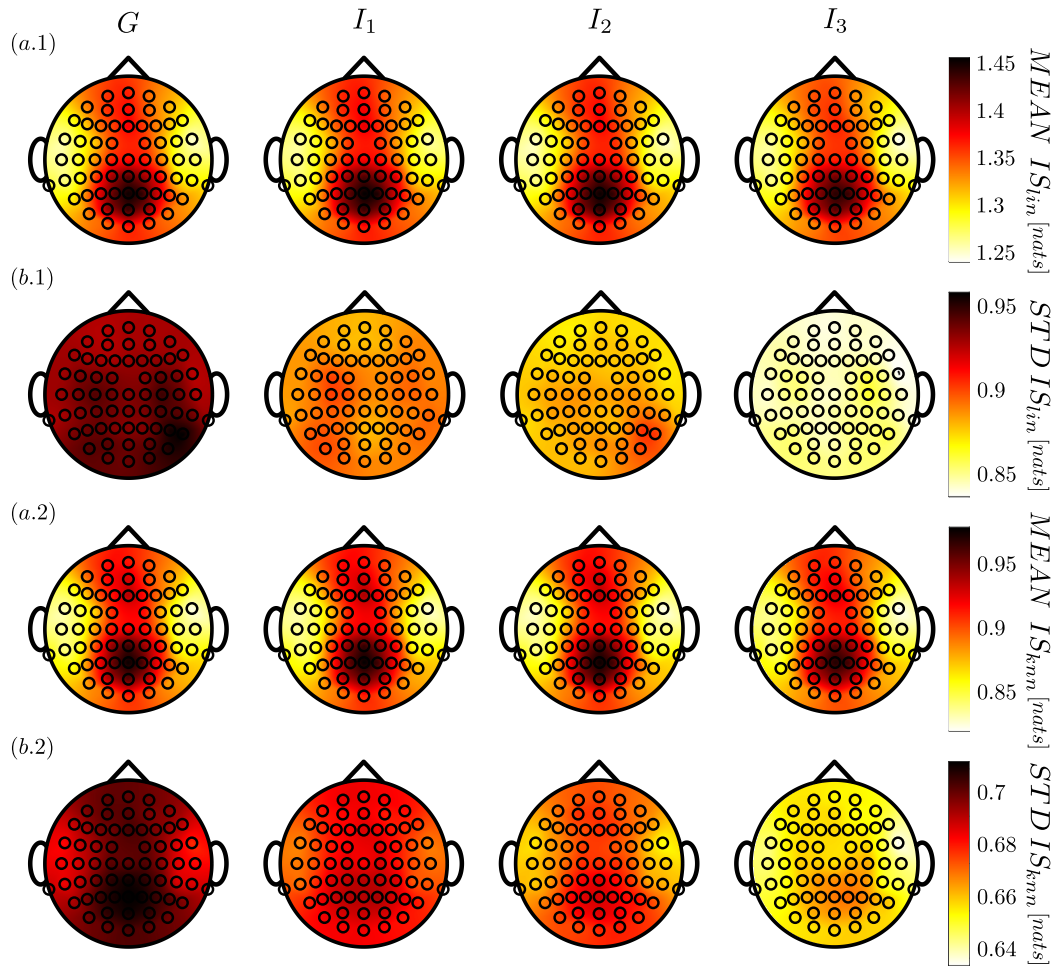

Figure 7.7: Distribution over the scalp of the average values across all subjects of the mean (MEAN, panels (a.)) and standard deviation (STD, panels (b.) of the global IS (G) and of the local IS computed in the different intervals (I_1, I_2, and I_3) evaluated through the linear (panels (.1)) and nearest-neighbor (.2) estimation approaches. The figure is adapted from Barà et al. (2023c).

than those obtained with the linear estimator, while maintaining the same patterns in terms of spatial distributions over the scalp and the same modifications across intervals.

Spatial differences of MEAN and STD IS values over the scalp are reported in Figs. 7.8 and 7.9. Specifically, the higher average values in both parietal and occipital regions if compared with the temporal ones, reported in Fig. 7.7 (*a*), are statistically assessed in Fig. 7.8; both estimators reveal significant lower values in the temporal regions than in the other areas (even if with a lower number of statistically significant differences in I_3). Furthermore, the effect size analysis demonstrates that the most significant differences are observed in the parietal and occipital regions, with average Cohen's d values among the three intervals of 1.05 and 1.02 for linear and 0.83 and 0.78 for nearest-neighbor strategies, when comparing parietal and occipital regions with temporal, respectively. In contrast, the relatively homogeneous distribution of SD values across the scalp is corroborated by the linear estimator, which does not detect statistically significant differences among regions (Fig. 7.9 (panels (*a*)). The nearest-neighbor method also provides clear evidence of this, albeit with a higher number of statistically significant differences, particularly between the parietal and left temporal regions (Fig. 7.9 (panels *b*)).

The present study has demonstrated that, in general, there is an increase in the regularity of neural rest activity in parietal and occipital regions, suggesting the

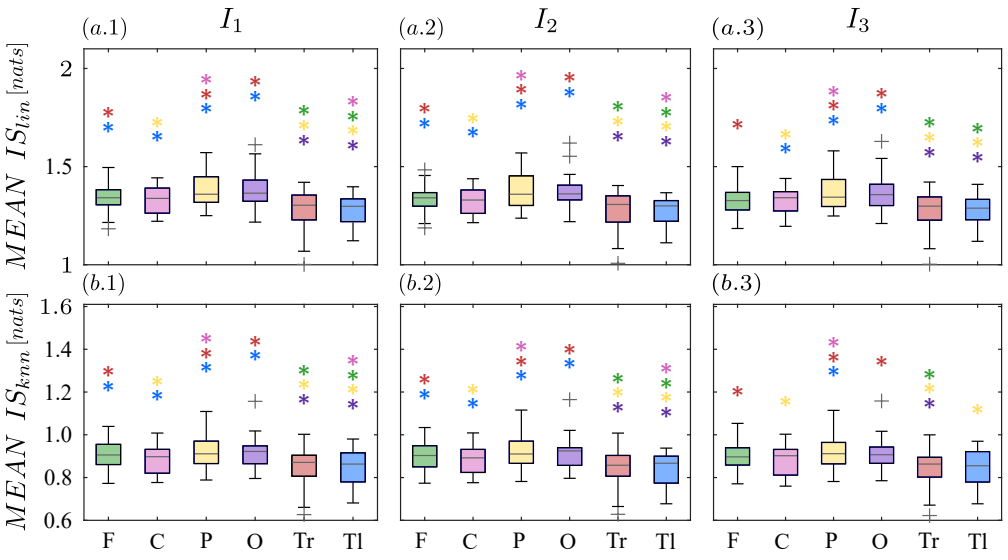

Figure 7.8: Boxplots of the mean of the local IS computed in each of the three intervals (I_1, I_2, and I_3) using both the linear (panels (*a.*)) and nearest-neighbor (panels (*b.*)) estimator for the six regions of the scalp (frontal in green, parietal in pink, parietal in yellow, occipital in purple, temporal right in red, and temporal left in azure). Statistical test: * of correspondet color, $p < 0.05/15$ between two regions, paired Student's t test with Bonferroni correction. The figure is adapted from Barà et al. (2023c).

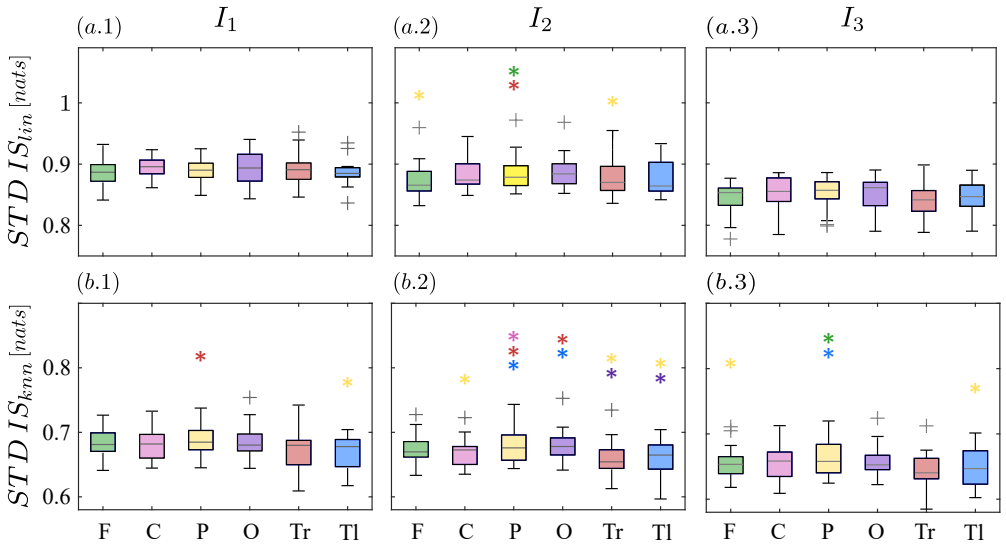

Figure 7.9: Boxplots of the standard deviation of the local IS computed in each of the three intervals (I_1, I_2, and I_3) using both the linear (panels (*a.*)) and nearest-neighbor (panels (*b.*)) estimator for the six regions of the scalp (frontal in green, parietal in pink, parietal in yellow, occipital in purple, temporal right in red, and temporal left in azure). Statistical test: * of correspondet color, $p < 0.05/15$ between two regions, paired Student's t test with Bonferroni correction. The figure is adapted from Barà et al. (2023c).

occurrence of a prevalent neural rhythm even in the absence of specific tasks. This result may be related to the augmented EEG power in the alpha and beta bands in brain areas associated with the DMN activity, that as found in Fox and Raichle (2007) is mainly referable to the parietal and occipital regions of the scalp. Another explanation may be the restriction of the neural response to the heartbeat to the parietal region, as observed in Dirlich et al. (1997). The congruence of the findings achieved with global and local metrics across the different intervals indicates that the regulatory mechanisms governing neural rhythms remain consistent throughout the cardiac cycle. However, it is important to note that different considerations can be made in light of the variability in the regularity of brain activity. As time elapses from the occurrence of the cardiac stimulus, recognized in the R peak of the ECG, the effect of the trigger activity gradually diminishes until the subsequent occurrence of a stimulus. Therefore, this study suggests that variability in EEG regularity is crucial to understanding the mechanisms of brain-heart communication.

7.5. Overview and conclusions of chapter 7

This chapter highlights the relevance and utility of investigating the dynamics of physiological network systems at the level of individual nodes using the measures introduced in Chapter 3. The applications here presented demonstrate the effectiveness of ER and IS measures in capturing variations in physiological dynamic com-

plexity and regularity. In particular, a decrease in ER and a corresponding increase in IS values are expected when physiological dynamics are dominated by specific control mechanisms that promote more regular and synchronized activity across organ systems. In this context, several previous studies have shown that these entropy measures can detect reductions in complexity associated with the performance of specific tasks, such as postural changes including tilting or standing (Javorka et al., 2008; Porta et al., 2017b; Castiglioni et al., 2023), as well as with diminished cooperation among physiological systems, for instance as a consequence of aging (Takahashi et al., 2012; Porta et al., 2014; Jia et al., 2017) or in presence of pathological conditions (Pincus, 1994; Romero-Ortuño et al., 2021). Such reductions have been reported in patients affected by cardiac (Chen et al., 2017), immune (Trunkvalterova et al., 2008), behavioral (Tobaldini et al., 2013), neurological, and psychiatric disorders (Hornero et al., 2006; Fernández et al., 2009; Méndez et al., 2012). Moreover, given the inherently time-varying nature of physiological processes, local entropy measures have been widely adopted to characterize transient changes in the regularity of physiological dynamics. This approach was supported by studies reporting task-related modulations of brain activity in cats during visual stimulation (Wibral et al., 2014b) and altered neural dynamics in humans with autism spectrum disorders (Gómez et al., 2014).

The findings presented here are consistent with expectations derived from both local (i.e., time-resolved) and global (i.e., averaged across time under the hypotheses of stationarity and ergodicity) information measures. A reduction in the ER of cardiac activity was observed during controlled breathing (Sect. 7.1), attributable to the strengthening of the RSA mechanism, particularly at slower breathing rates (Berntson et al., 1993; Tzeng et al., 2003). A comparable decrease in ER was also detected in response to orthostatic and mental stressors (Sect. 7.2), reflecting increased sympathetic activation and the concomitant withdrawal of parasympathetic modulation (Baselli et al., 2005). Similarly, reduced ER values were observed in respiratory dynamics during slow, controlled breathing (Sect. 7.1), which can be attributed to the enhanced synchronization between ventilatory activity and cardiac function (Elstad et al., 2018). Furthermore, arterial pressure dynamics under orthostatic stress exhibited lower ER values (Sect. 7.2), consistent with the predominance of sympathetic activity in this condition (Baselli et al., 2005).

In contrast, higher IS values were associated with increased regularization of brain dynamics in parieto-occipital regions during resting conditions (Sect. 7.4), likely reflecting enhanced activity of the DMN in the alpha and beta frequency bands (Fox and Raichle, 2007). Nevertheless, in agreement with previous empirical findings and simulation studies, local information measures appear to provide deeper insight into time-varying physiological dynamics when their variability is considered rather than their mean value (Lizier (2012b); Stramaglia et al. (2021); An-

tonacci et al. (2025a)). In particular, the variance of local IS measures computed from ventilatory dynamics proved effective in discriminating between breathing and apneic epochs, while the standard deviation of local IS measures evaluated on brain activity across the cardiac cycle yielded more informative results than the corresponding averaged measures (Sect. 7.3). Overall, these findings further support the relevance of the variability of local information measures for characterizing interactions among physiological systems and distinguishing their behavior during transitions between different functional states, in line with previous observations (Stramaglia et al., 2021).

By comparing different estimation approaches, the results presented in Sect. 7.1 demonstrate that when the estimation parameters properly account for the characteristics of physiological dynamics and effectively mitigate the curse of dimensionality, strong regulatory mechanisms can be consistently identified regardless of the estimator employed. Accordingly, robust mechanisms – such as those coordinating cardiac and respiratory dynamics during very slow, controlled breathing – are reliably detected by all estimators. In contrast, more weakly synchronized dynamics, such as those observed during breathing at a rate of 15 breaths/minute, are detected only by the linear estimator and the permutation-based method for respiratory dynamics, and additionally by the nearest-neighbor approach for cardiac dynamics. Notably, the predominance of linear dynamics exhibited by the RSA mechanism under slow-breathing conditions (Morales et al., 2021) contributes to the superior performance of the linear estimator and the permutation-based approach in discriminating variations in physiological complexity. These findings highlight the effectiveness of ER measures in capturing significant changes associated with parasympathetic activity. Moreover, an increasing body of literature has investigated the ability of complexity measures to characterize dynamics related to sympathetic activity (Porta et al., 2002; Javorka et al., 2018). This issue is further examined in Sect. 7.2, which focuses on cardiovascular complexity responses to physical and mental stressors. In this context, although concordant changes in linear parametric and nearest-neighbor estimates are observed for both RR and SAP dynamics under the two stress conditions, discrepancies in statistical significance may be attributed to estimation bias inherent to the methods employed (Faes et al., 2015a).

The growing adoption of wearable biomedical devices in smart healthcare has stimulated interest in the use of shorter physiological recordings, motivated by reduced computational and storage demands and by the need for timely extraction of clinically relevant indicators (Chen et al., 2019; Dias and Paulo Silva Cunha, 2018; Kakria et al., 2015; Kos and Umek, 2018). Previous investigations of predictability and complexity measures derived from UST recordings (Castaldo et al., 2019; Shaffer et al., 2016) are largely consistent with the results presented in Sect. 7.2, indicating that recordings of at least 2–3 minutes should be considered to ensure re-

liable estimation. Although variations in cardiovascular complexity could still be assessed using shorter time series (e.g., 60 samples), the resulting estimates exhibited reduced correlation with ST reference values. Within this framework, the comparison between a more reliable but computationally demanding model-free estimator and a linear model-based approach suggests that the latter represents a viable alternative for detecting changes in physiological conditions. This suitability arises from its substantial reduction in computational cost, albeit at the expense of losing information related to nonlinear cardiovascular dynamics. Indeed, the combined use of UST recordings and computationally efficient linear entropy estimators has proven advantageous for the integration of such measures into wearable devices aimed at real-time cardiovascular monitoring. Nonetheless, as highlighted by preliminary studies (Lee et al., 2022), further investigation into discretization-based estimation approaches for UST analysis is warranted. Although careful selection of estimation parameters is required to mitigate the curse of dimensionality – an issue exacerbated when dealing with UST recordings – the permutation-based approach offers practical advantages. Specifically, it can be executed concurrently with signal acquisition, just postponing probability distribution estimation at the end of the recording. This strategy enhances real-time performance while reducing the overall computational time.

Chapter 8

Pairwise analysis of physiological dynamics

This chapter collects the findings of different studies applying the coupling and causality measures detailed in Chapter 4 on coupled physiological systems, with particular attention to the exploration of cardiovascular and cardiorespiratory interactions during controlled breathing (Sect. 8.1), postural changes (Sects. 8.1, 8.2, 8.3, and 8.5) or mental stress conditions (Sect. 8.3). Though the majority of these analyses are conducted on cohorts of young, healthy subjects, findings from studies focused on the alteration of these physiological interactions in elderly people (Sect. 8.2), after myocardial infarction (Sect. 8.2), and in heart failure patients undergoing rehabilitative therapy (Sect. 8.4) are also reported.

8.1. Mutual Information Rate decomposition in cardiorespiratory and cardiovascular systems

Applying MIR and its decomposition strategies in assessing short-therm physiological interactions allows to disentangle complex dynamics involving individual organ systems or their causal interplay. Specifically, in this section, the results achieved in Barà et al. (2023b) by applying the MIR framework with discretization estimation strategies on both cardiorespiratory and cardiovascular interactions are reported. Specifically, cardiorespiratory dynamics were investigated exploiting RR and RESP time series from Database A collected during spontaneous (SB) and controlled breathing (CB10, CB15, and CB20), while cardiovascular dynamics by using RR and SAP time series collected in Database C at rest (REST) and during postural stress (HUT).

Data and statistical analysis - MIR decomposition measures were computed by means of the two discretization-based strategies focused on this thesis for pairs

of time series representative of cardiorespiratory dynamics, by considering $X = RR$ and $Y = RESP$, and cardiovascular dynamics, by considering $X = RR$ and $Y = SAP$. Specifically, accounting for the empirical rule reported in the previous chapters, the discretization parameters were set to $b = 4$ and $m = 1$ for the binning approach, and $m = 3$ for the permutation approach. Moreover, the statistical significance of each of the estimated information measures was assessed by using surrogate data analysis approaches described in Appendix. Specifically, the strategy described in Sect. A.2.1 was applied for the univariate measures of entropy rate, while the one described in Sect. A.2.2 for all the other measures, all with a significance level of $\alpha = 0.05$.

Statistical differences among protocol phases were tested in both databases by using parametric tests; the normality of the distributions was indeed assessed for all measures and both databases through the one-sample Kolmogorov–Smirnov test. As regards the analysis of the cardiorespiratory interactions, a one-way analysis of variance (ANOVA) was applied, followed by a post-hoc paired Student's t-test to assess differences between each of the controlled breathing conditions and the spontaneous one, i.e., SB vs. CB10, SB vs. CB15, SB vs. CB20; the Bonferroni correction for multiple comparisons was also performed ($n = 3$). On the other hand, as regards cardiovascular analyses, the paired Student's t-test was carried out between supine and tilt positions. All statistical tests were performed at a 5% significance level. Finally, to further assess changes related to the experimental conditions, the effect size index was evaluated by computing the Cohen's d value described in Sect. 7.2.

Results and discussion - Fig. 8.1 depicts the distributions of the information measures decomposing the MIR computed for RR and RESP time series in the controlled breathing protocol by using binning (panel (*a*)) and permutation (panel (*b*)) estimation strategies. Looking at the MIR measure, the ANOVA test highlights significant variations across the protocol phases with both estimation approaches, with a lower p-value in the case of binning ($< 10^{-5}$ vs. 0.0141); also the post-hoc paired tests evidence significantly higher values during paced breathing at 10 and 15 breaths/minute than during spontaneous breathing with also a large effect size ($d > 0.8$). Moreover, the estimates obtained via the binning approach are significant for a larger number of subjects, although the permutation strategy returns higher values. Entropy rate terms evidence not significant higher complexity for cardiac dynamics with controlled breathing and quite stable values for the respiratory dynamics with the binning approach; the joint entropy rate $H_{RR,RESP}$ shows a significant decrease during CB10 and a significant increase during CB20 compared to SB. Contrarily, the results obtained with the permutation approach reveal significantly lower complexity for cardiorespiratory dynamics during CB10 and CB15, as well as comparable or even higher values during CB20. As already observed in Sect. 7.1, the lower complexity of the cardiorespiratory dynamics with controlled breathing at CB10 and CB15 can be related to the strengthening of the RSA mechanism with

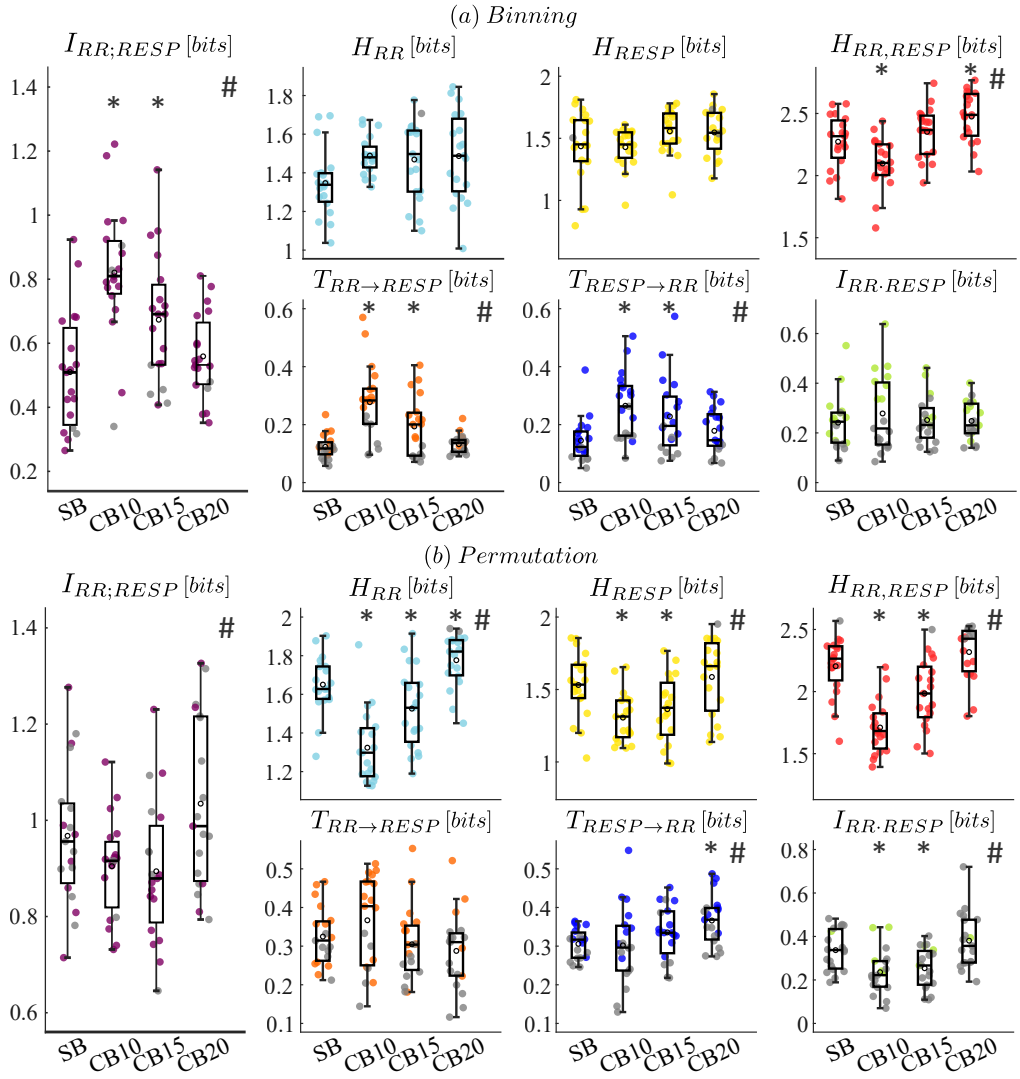

Figure 8.1: Boxplot distributions and individual values of MIR and its decomposition terms computed on RR and RESP time series during spontaneous breathing (SB) and controlled breathing at 10, 15, and 20 breaths/minute (CB10, CB15, and CB20) using the binning (panel (*a*)) and the permutation (panel (*b*)) approaches. In each panel, colored and gray circles correspond to values deemed, respectively, as statistically significant and non-significant using surrogate data analysis; black open circles refer to the sample mean of each distribution. Statistical tests: #, $p < 0.05$, ANOVA; *, $p < 0.05/3$ SB vs. CB10/CB15/CB20, paired Student's *t*-test with Bonferroni correction. The figure was modified from Barà et al. (2023b).

slow breathing activity (Berntson et al., 1993; Tzeng et al., 2003; Song and Lehrer, 2003), as well as to the presence of cardio-ventilatory coupling and stroke volume synchronization mechanisms, that elicit in similar changes in both cardiac and respiratory dynamics (Elstad et al., 2018). The lack of consistency for the two estimation approaches and the inability of the binning-based strategy to observe a complexity modulation at different breathing rates is related to the limited description of the physiological dynamics both in amplitude and past lags. The different past lengths considered for the two estimation approaches are also relevant in determining the difference in the trends of the causality measures. Specifically, while the binning approach reveals an increase in the information transferred from RR and RESP and *viceversa* with CB10 and CB15 compared to SB, with quite constant values across conditions for instantaneous causality, the permutation approach shows more stable values, with statistically significant higher values during CB20 for $T_{RESP \to RR}$ and statistically significant lower values during CB10 and CB15 for $I_{RR \cdot RESP}$, even if with barely significant values. The causal interactions highlighted by the permutation approach are more consistent with those observed on the same dataset by using the nearest-neighbor estimator (Faes et al., 2015c) and are in agreement with the physiological hypothesis that significant physiological changes do not occur during supine paced breathing (Saul et al., 1989).

Fig. 8.2 depicts the distributions of the information measures decomposing the MIR computed for RR and SAP time series during the postural stress protocol by using binning (panel (*a*)) and permutation (panel (*b*)) estimation strategies. No statistically significant differences are revealed between supine rest and postural stress states considering the MIR distributions obtained with both estimation strategies. Moreover, the estimated values exhibit an opposite modulation with the postural change highlighting a trend toward higher values for the binning approach and toward lower values for the permutation approach. Both estimation approaches reveal a decrease of cardiac and cardiovascular dynamics with the orthostatic stress, while vascular dynamics exhibit stable entropy rate. These results are in agreement with the analysis showed in Sect. 7.2 and with the well-known tilt-induced activation of the sympathetic nervous system, which simplifies cardiac dynamics (Porta et al., 2007b; Javorka et al., 2018; Faes et al., 2019a). Looking at the causality measures, an increase of the information transferred from SAP to RR is detected with both estimation strategies, together with a decrease of the instantaneous term (barely significant values are observed with the permutation approach). Contrarily, a decrease of the information transferred from RR to SAP is revealed only by the permutation approach. The findings are in agreement with the presence of a balanced interaction within the cardiovascular closed-loop along the two directions in the supine rest. These interactions shift towards a predominance of baroreflex feedback from SAP to RR with tilting, accompanied by a weakening of the mechanical

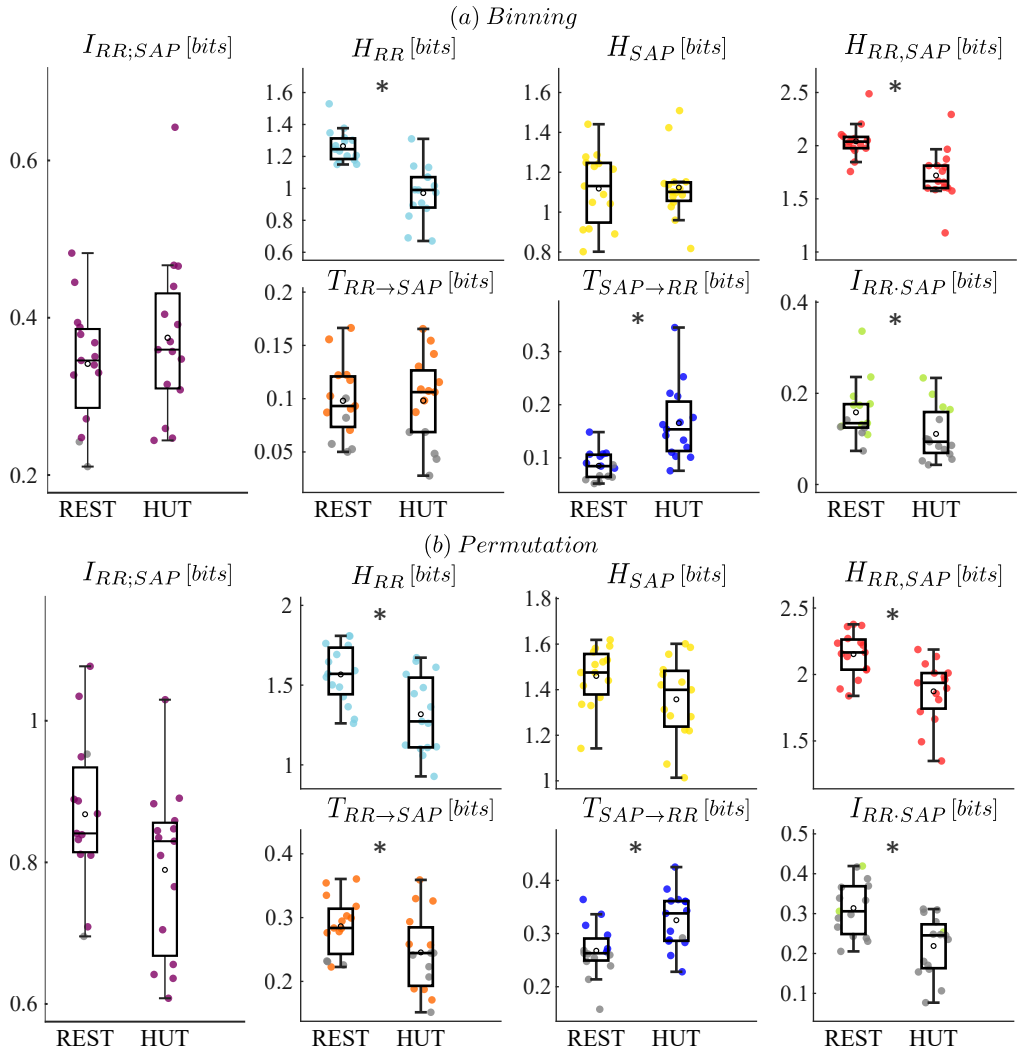

Figure 8.2: Boxplot distributions and individual values of MIR and its decomposition terms computed on RR and SAP time series during supine rest (REST) and head-up tilt maneuver (HUT) using the binning (panel (*a*)) and the permutation (panel (*b*)) approaches. In each panel, colored and gray circles correspond to values deemed, respectively, as statistically significant and non-significant using surrogate data analysis; black open circles refer to the sample mean of each distribution. Statistical test: *, $p < 0.05$ REST vs. HUT, paired Student's *t*-test. The figure was modified from Barà et al. (2023b).

feedforward from RR to SAP. This is observed just by the permutation approach, probably due to greater consideration of past dynamics (Mullen et al., 1997; Nollo et al., 2005).

8.2. Testing coupling and nonlinearities in cardiovascular dynamics during postural stress

The analyses of cardiovascular interactions reported in Cimignolo et al. (2025b) and extended in Cimignolo et al. (2025a) performed on physiological data collected in Database F are here reported. The MIR and the terms of its decomposition into complexity and causality measures were applied on RR and SAP time series to explore the response to orthostatic postural stress in healthy young subjects, but also in healthy old subjects and in patients affected by acute myocardial infarction. The combined use of the nonlinear nearest-neighbor estimation strategy and of surrogate data analysis approach allows to investigate the role on nonlinearities in cardiovascular regulatory activities and in their adaptation with aging and the presence of cardiac pathology.

Data and statistical analysis - The analytical framework of MIR was applied on RR and SAP time series to evaluate complexity of cardiac and vascular dynamics, as well as causal and coupling cardiovascular interactions. The two individual ER measures and the joint one were computed, together with the TE measures in the two directions. Specifically, following the reasoning in Sect. 6.4, the instantaneous term was associated with the causal direction $SAP \rightarrow RR$. The joint evaluation of instantaneous and lagged effects has been demonstrated to provide a more realistic and complete description of the dynamics underlying baroreflex responses (Faes et al., 2015c). According to previous studies on cardiovascular dynamics (Barà et al., 2023b), all decomposition metrics were estimated using the nearest-neighbor approach with $k = 10$ and $m = 3$.

The computed measures were statistically tested for both significance and nonlinearities. As discussed in the Appendix, different surrogate data analysis approaches were employed depending on the properties under investigation. For each of the measures and the relative data generation approach, one-hundred surrogate time series were obtained and the significance level fixed to $\alpha = 0.05$. For each group, a comparison between REST and HUT conditions was performed by using the non-parametric Wilcoxon signed-rank test for paired data. Moreover, a χ-squared test was applied to assess whether the proportion of significant measures or significant nonlinearities differs across conditions. Finally, the Kruskal-Wallis test followed by a post-hoc Wilcoxon rank-sum test for unpaired data with Bonferroni correction ($n = 3$) was applied to perform a between-group comparison for the two separate conditions. A significance threshold of 0.05 was fixed for all statistical anal-

ysis.

Results and discussion - Fig. 8.3 depicts for each of decomposition terms of the coupling measure of MIR the values computed by means of the nearest-neighbor strategy and the results of the surrogate data analysis for testing nonlinearities.

No significant variations with postural stress are evidenced in terms of global coupling for both young and post-AMI patients, while a statistically significant increase is observed in old subjects. Moreover, a weaker cardiovascular coupling is observed in both old and post-AMI subjects at REST, which is confirmed only for the post-AMI group during HUT (panel (*a*), top). While the significance of MIR is around 100% for all groups and conditions, the level of nonlinearities detected for young healthy people during HUT is significantly lower than REST (panel (*a*), bottom). These results overall suggest the preservation of the cardiovascular functional balance in response to the investigated postural stress state in young healthy subjects and the strong activation of the sympathetic ANS branch evidenced by the significant linearization of the dynamics (Porta et al., 2006). Accordingly, the difference highlighted for old subjects already at REST and the absent modulation of nonlinearities for the post-AMI group indicate an impairment of the cardiovascular dynamics with these physio-pathological alterations.

Regarding the modulation of the complexity measures, both cardiac and vascular dynamics present a decrease of ER with orthostatic stress for young healthy subjects, as well as significantly higher values for both old and post-AMI subjects during HUT if compared with young subjects (panels (*b*),(*c*), top). Moreover, significantly higher ER values are detected for the post-AMI group compared to the old subjects at REST (panel (*c*), top). A significant decrease of nonlinearities for old subjects is detected with HUT (panel (*b*), bottom). The modulation of the complexity of the overall cardiovascular dynamics reflects that of the two separate systems, presenting the same statistical difference observed for the cardiac system, apart from that regarding nonlinearities (panel (*d*)). Both individual and joint ER terms result significant for almost 100% of subjects for all conditions and groups. The complexity reduction observed with HUT for the young group is consistent with previous studies (Faes et al., 2011; Kamiya et al., 2014; Valente et al., 2018; Faes et al., 2019a), providing evidence of the well-known shift of the sympatho-vagal balance towards sympathetic activation and the reduced baroreceptor loading in response to the orthostatic stress. Also findings achieved on the old group are sustained by previous studies (Carrington and White, 2002; Dani et al., 2022). Specifically, the increased complexity of the vascular dynamics is indicative of the activation of more complex regulatory strategies in maintaining an hemodynamic stability, thus suggesting a reduced flexibility of ANS and a potential impairment of the cardiovascular compensation mechanisms (Lipsitz and Goldberger, 1992; Takahashi et al., 2012). This is also supported by the documented lower stability of systolic pressure dynamics

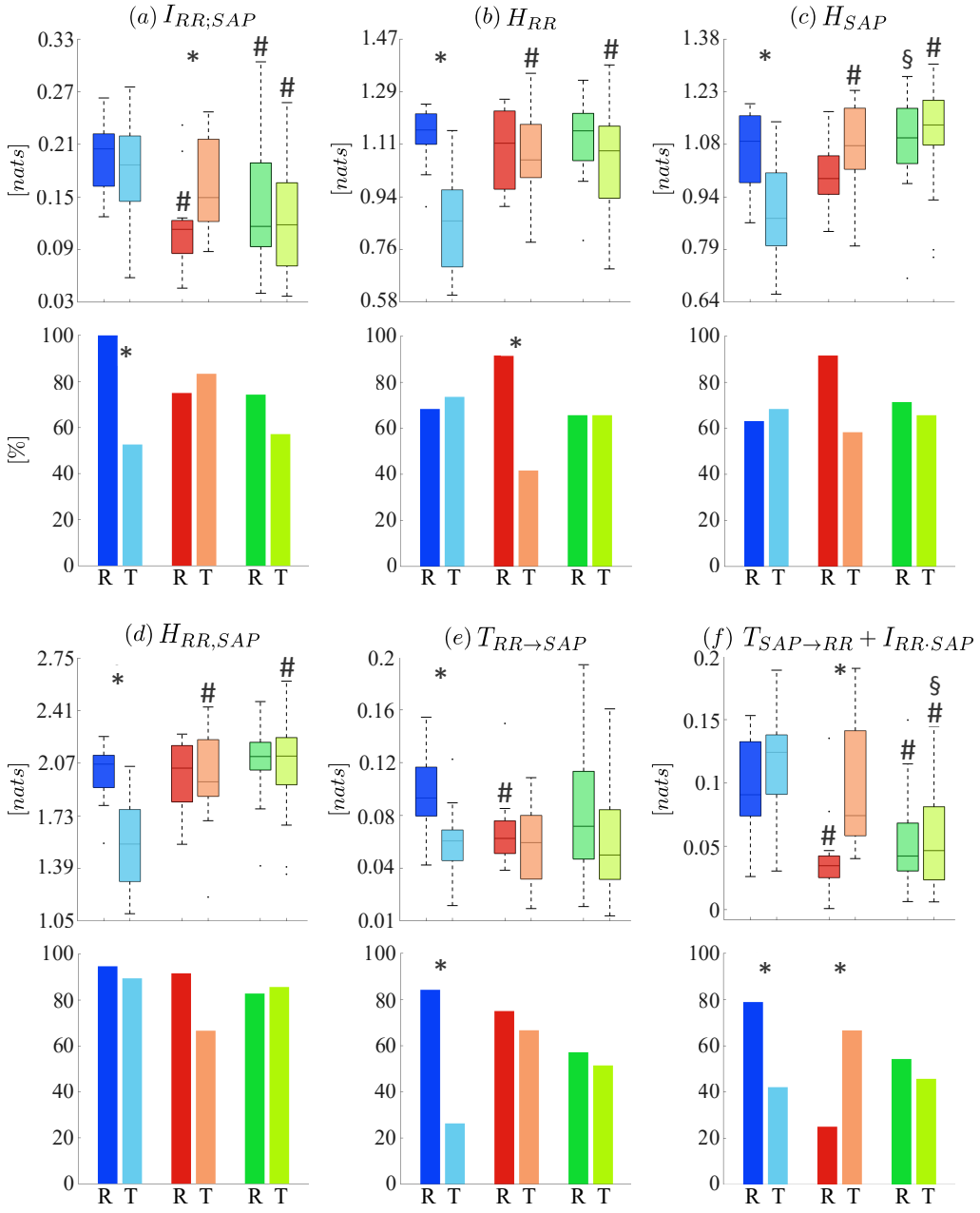

Figure 8.3: Boxplot distributions of MIR (panel (*a*)), complexity (panels (*b*), (*c*), and (*d*)), and causality (panels (*e*) and (*f*)) measures values (top panels) and percentage of subjects exhibiting nonlinear dynamics (bottom panels) computed on RR and SAP time series at rest (R) and during head-up tilt maneuver (T) in young (in bluish), old (in reddish), and post-AMI (in greenish) subjects. Statistical tests: *, $p < 0.05$ R vs. T, paired Wilcoxon signed-rank test (top panels); *, $p < 0.05$ R vs. T, χ-squared test (bottom panels); # and §, $p < 0.05/3$ young vs. old/post-AMI and old vs. post-AMI, Wilcoxon signed-rank test with Bonferroni correction. The figure was modified from Cimignolo et al. (2025a).

with advancing age due to reduced baroreflex sensitivity, a decrease in the number, density, and sensitivity of cardiac β-adrenergic receptors (Chaddha et al., 2016), as well as an increase in arterial stiffness (Svec et al., 2021). For the post-AMI subjects, complexity trends similar (even if nor significant) to those achieved for old subjects could be associated to the comparable age of the two groups and, at the same time, to the effects of the acute cardiac event, which induces an inflammatory state and oxidative stress further impairing endothelial and autonomic function, altering vascular remodeling and sympathetic innervation, also influenced by the effects of pharmacological therapies (Grieve et al., 2004; Zekios et al., 2021; Jiang et al., 2022).

The TE from RR to SAP reveals a significant decrease with HUT for young subjects both in terms of values and presence of nonlinearities, and significant lower values at REST when comparing old with young subjects (panel (*e*)). Instead, in the opposite direction, a statistically significant increase of the TE is detected with postural stress for old subjects, together with a significant decrease for old and post-AMI subjects at REST compared to young subjects and for post-AMI subjects during HUT compared to both young and old subjects (panel (*f*), top). Regarding the nonlinearity assessment, a significant decrease is observed with HUT for the young group and, contrarily, a significant increase for the old group (panel (*f*), bottom). A modulation of the percentage of significance for the causality measures is observed among REST and HUT for the three groups. Specifically, as regards the causal effect of RR on SAP, a significant increase is obtained for old subjects (33% vs. 92%) and, even if not statistically significant, for young subjects (84% vs. 95%), as well as a decrease for post-AMI subjects (62% vs. 57%). In the opposite direction, the statistical significance is attained to around 90% for all groups and conditions. These results are in agreement with the well-known physiological response to orthostatic stress, that for young healthy subjects reflects the presence of a closed-loop in cardiovascular regulation with a modulation of the sympatho-vagal balance and a strengthening of the baroreflex arm during HUT (Mullen et al., 1997; Nollo et al., 2005; Faes et al., 2008a). In old subjects, the increased causal effect of the vascular activity on heart dynamics and of the related nonlinearities reflect a less adaptive response to orthostatic stress already found in (Faes et al., 2019a). The weak dynamics observed for the post-AMI subjects and their strong linear characterization, particularly visible for the causality terms, reflect the reduced ability of the organism to respond to external stimuli and to the effect of the rehabilitation therapy (Huikuri et al., 1996; Zieman et al., 2005; Bai et al., 2008).

8.3. Comparison of linear and nonlinear directional coupling measures in cardiovascular and cardiorespiratory interactions

In this section, both linear parametric and nonlinear nearest-neighbor formulations of the bivariate causality measure of TE were applied on RR, SAP, and RESP time series collected in the Database B - *version 2* to evaluate the ability of these estimation strategies operating on continuous-valued variables to investigate the response of cardiovascular and cardiorespiratory regulatory mechanisms with postural (HUT) and mental arithmetic (MA) stress. As control condition, the REST1 phase - herein referred to as REST – was considered. The findings of this analysis were collected in a conference proceeding (Barà et al., 2023a).

Data preprocessing - Before computing the causality measures, all time series were preprocessed applying a zero phase high-pass AR filter (cutoff frequency of 0.0156 Hz). Samples differing more than three times standard deviation from the mean value were removed and interpolated. Finally, time series were normalized to zero mean and unit variance.

Data and statistical analysis - Causal interactions referred to different physiological systems were explored by using three different target-driver settings, i.e., RR as target and RESP as driver when considering the cardiorespiratory system, SAP as target and RESP as driver when considering vascular and respiratory systems, and RR as target and SAP as driver when considering the cardiovascular system. For all of these settings, the liner parametric approach was applied after identifying the optimal order of the model through the BIC strategy (considering a maximum order of 10), while the nonlinear model-free approach was applied by using a non-uniform embedding strategy (with a maximum past lag of 10 and generating one-hundred random shuffling surrogates (see Sect. A.2.5 of Appendix) to define the exit criterion) and by fixing a number of neighbor k to 10. We refer the reader to Faes et al. (2015a) for further details on the non-uniform embedding strategy.

The statistical significance of the estimated TE values was assessed for each subject, condition, and estimation approach using one-hundred surrogate data generated by using the approach described in Sect. A.2.2 by ensuring a time shift of the two series of at least 20 samples. Statistical tests were used for each estimator to compare TE measures among physiological states. Specifically, after rejecting the hypothesis of Gaussianity using the Anderson-Darling test, the non-parametric Kruskal-Wallis analysis of variance was performed followed by the post-hoc Wilcoxon signed rank test for paired data with Bonferroni correction ($n = 3$) to test differences among the distributions obtained among the three different phases of the protocol for each physiological setting. Moreover, the McNemar test for paired proportions was also carried out to determine the significance of the variations between the three conditions referring to the number of subjects showing sig-

nificant TE. Furthermore, the Pearson correlation coefficient was computed between the TE values computed through the two estimation strategies for each direction and protocol phase, testing the null hypothesis of absence of linear relation between the two TE estimates. For all statistical tests, the significance level was set at 0.05.

Results and discussion - Fig. 8.4 shows a decreased influence of the ventilatory activity on both cardiac and vascular dynamics during physical and mental stress if compared to rest (panels (*a.1*) and (*b.1*)). These trends are expected due to a reduction of the parasympathetic nervous system activity during stressors (Cooke et al., 1999; Sant'anna et al., 2003), which in turn leads a weakening of the RSA mechanism (Grossman and Taylor, 2007; Triedman and Saul, 1994), as well as to a decrease in the mechanical effect of ventilation during mental arithmetic (Faes et al., 2019a). On the other hand, an increased influence of vascular activity on the heartbeat dynamics with the head-up tilt maneuver related to the activation of the feedback mechanism in the cardiovascular closed-loop (Cooke et al., 1999) is observed (panel (*c.1*)). Moreover, the primary role of the ventilatory activity on cardiovascular variability is corroborated by the higher statistical significance of TE measures evaluated from RESP to RR (panel (*b.1*)) and from RESP to SAP (panel (*b.2*)) as already observed in literature (Schulz et al., 2013; Javorka et al., 2018).

Apart for the significant weakening of the causal effect of RESP on RR with the orthostatic stress that is detected only by the nonlinear approach, there is an agreement between the two estimators that is sustained by the results of the correlation analysis shown in Fig. 8.5. The increased correlation for $T_{RESP \to RR}$ with stressful conditions (panels (*a.2*) and (a.3)) can be related to a linearization of cardiorespiratory dynamics and to their nonlinear characterization at rest for healthy subjects due to the predominant vagal modulation (Fortrat et al., 1997; Faes et al., 2019a). Contrarily, looking at the cardiovascular dynamics, it is possible to infer the prevalence of nonlinearity during HUT (panel (*b.2*)) related to the nonlinear influence of breathing activity on cardiac baroreflex and venous return mechanisms (Porta et al., 2015). Finally, nearly constant correlation is observed for the cardiovascular mechanisms across the different phases of the protocol (panels (*c.1*)-(*c-3*)). This result can be related to the prevalence of a sympathetic dominance of SAP dynamics which is known to be overall reflected in linear dynamics (Porta et al., 2006).

8.4. Analysis of cardiorespiratory interactions in heart failure patients

In Platiša et al. (2023), cardiorespiratory dynamics variations in presence of pathological conditions characterized by different types of heart-rhythm alterations were investigated, together with the efficacy of CRT in patients with heart failure, reduced LVET, and abnormal QRS. This procedure was clinically used for more than 20 years

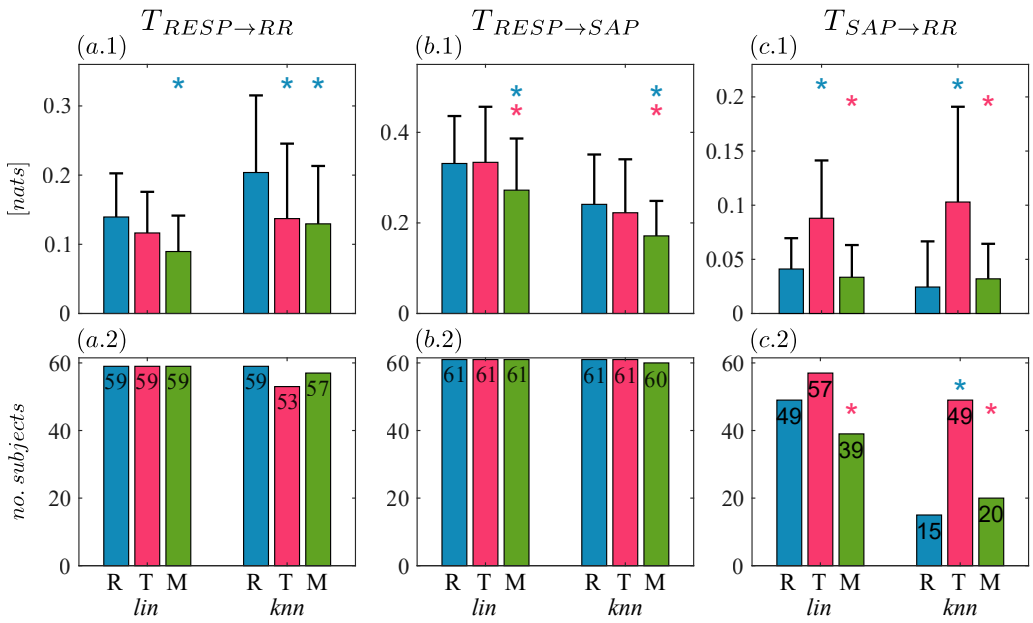

Figure 8.4: Errorbar graphs of TE computed from RESP to RR (panels (*a.*)), from RESP to SAP (panels (*b.*)), and from SAP to RR (panels (*c.*)) for all subjects during rest (R, azure), orthostatic stress (T, pink) and mental stress (M, green) states with both linear (*lin*) and nonlinear (*knn*) estimators (panels (*.1*)), and barplots representing the correspondent statistical significance in terms of number of subjects according to surrogate data analysis (panels (*.2*)). Statistical test: in panels (*.1*), * of correspondent color, $p < 0.05/3$ between phases, paired Wilcoxon test with Bonferroni correction (the results of the Kruskal-Wallis analysis are not reported in the figure, being always statistically significant); in panels (*.2*), * of correspondent color, $p < 0.05$ between phases, McNemar test. Figure taken from Barà et al. (2023a).

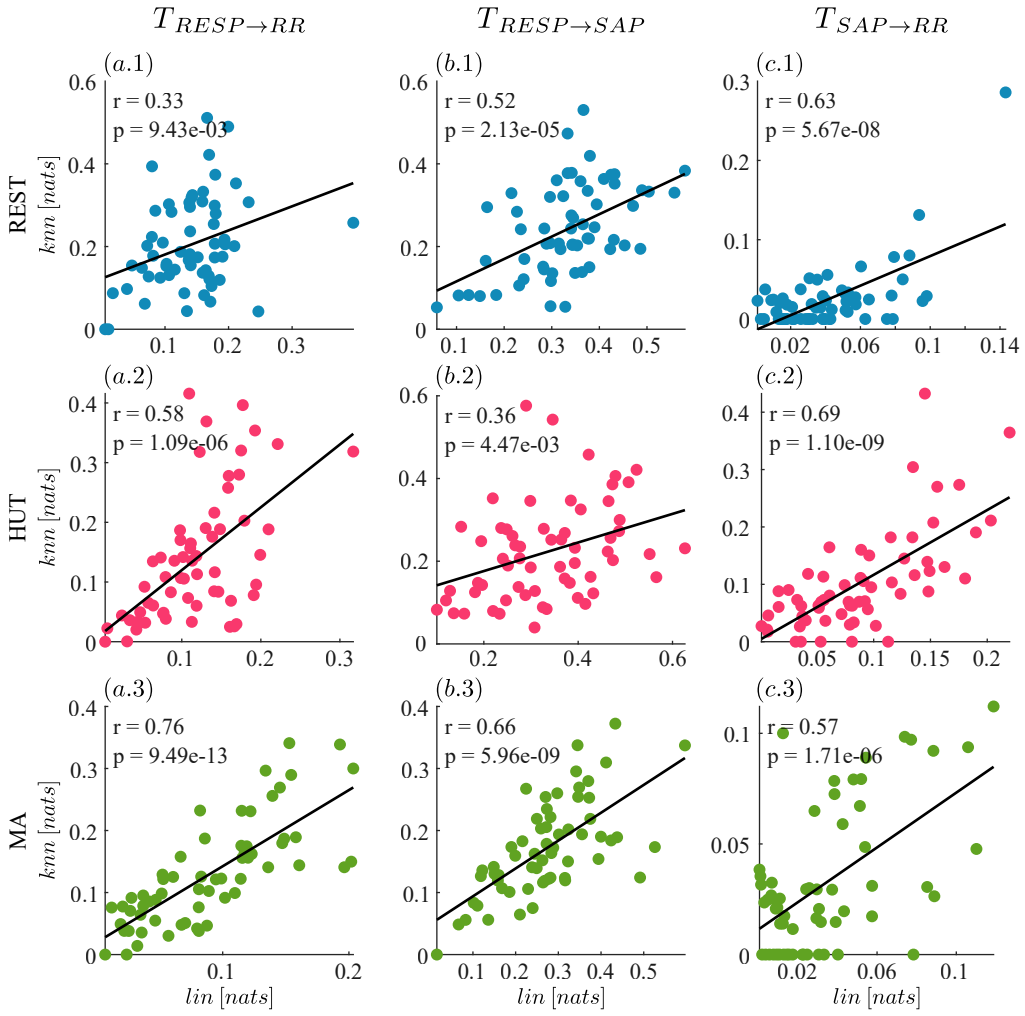

Figure 8.5: Scatterplots of pairs of linear (*lin*) and nonlinear (*knn*) estimates of TE measures computed for each subjects in a given experimental condition (REST in panels (*.1*), HUT in panels (*.2*), and MA in panels (*.3*)) from RESP to RR (panels (*a.*)), from RESP to SAP (panels (*b.*)), and from SAP to RR (panels (*c.*)). In each subplots, the solid line depicts the regression line between the two estimators, and the correlation value r as well as its significance level p are reported at the top left. Figure taken from Barà et al. (2023a).

on these patients to restore electromechanical heart synchrony, improve the cardiac pump functional capacity (Leyva et al., 2014; Dhesi et al., 2017) and remodel the β-adrenergic signaling pathways restoring the sympatho-vagal balance (Chakir et al., 2009). Nevertheless, the effect of CRT on cholinergic signaling, neurohumoral modulation, and cardio-respiratory interactions has not been fully investigated in the literature yet. Significant advancements have been made in recent years in terms of patient selection, implantation approaches, post-implantation device programming, and optimization of medical therapy. Nevertheless, one-third of patients still do not benefit as much as expected from CRT implantation (Daubert et al., 2017). From this perspective, it is important to adopt new approaches in the analysis of heart failure patients who are candidates for CRT implantation, in order to preoperatively distinguish between future responders and non-responders using parameters that have not yet been employed to define autonomic function and cardio-respiratory interactions. Accordingly, RR and RESP time series from Database G were investigated in terms of dynamical coupling between cardiac and respiratory dynamics, as measured by TE and CrossEn, in different groups (HFSin, HFVES1, and HFVES2) of CRT responders and non-responders with heart failure.

Data and statistical analysis - TE and CrossEn measures were computed along the two directions from RESP to RR and from RR to RESP to investigate the closed-loop of the cardiorespiratory interactions. Specifically, the TE measures were evaluated using both linear parametric and nearest-neighbor estimators, while the CrossEn measure was computed using only the nonlinear one. The parametric approach was applied by setting the model order p according to AIC, while the model-free approach by fixing a number of neighbors $k = 10$ and a length memory $m = 2$. Moreover, the instantaneous effect was incorporated in the measures computed in the direction from RESP to RR.

After testing normality of the obtained distribution through the Shapiro-Wilk test and since the most of the measures rejected the null hypothesis of normality, non-parametric tests were employed to assess statistically significant difference between groups and conditions. Specifically, the paired Wilcoxon signed-rank test was used to compare the two directions of interaction in both baseline and follow-up conditions for each of the group, as well as for responders and non-responders. Moreover, for each of the evaluated measures, a comparison between groups was performed in both baseline and follow-up conditions by using the Mann-Whitney U-test. For all statistical test, the threshold of significance was of 0.05.

Results and discussion - Fig. 8.6 shows the results obtained with regards the linear and nonlinear measures of TE and CrossEn computed along the two cardiorespiratory interaction directions during baseline and follow-up for all groups of patients. Higher values of TE_{lin} are observed in the direction from RESP to RR in all patients at baseline (panel (*a.1*)), but this trend is statistically significant just

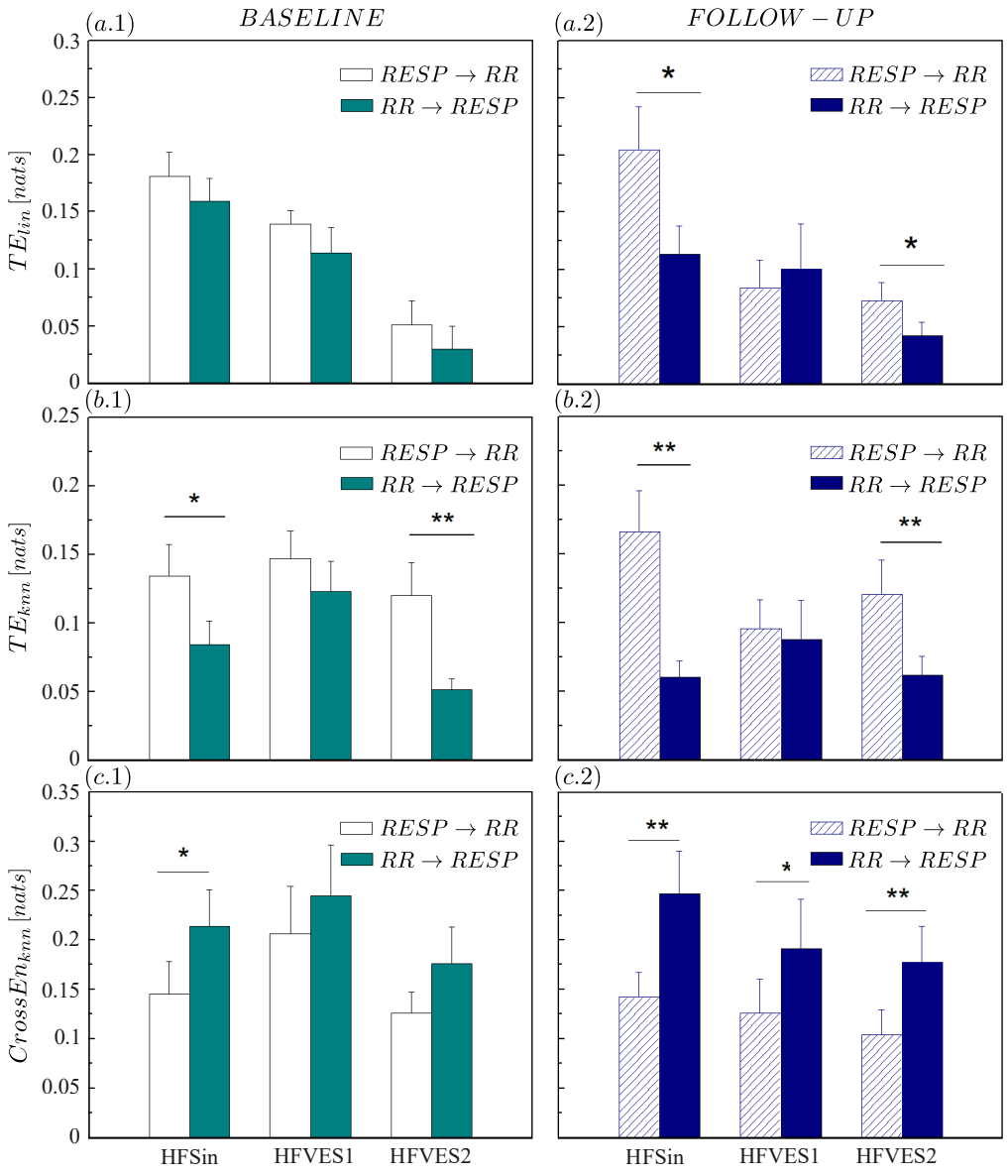

Figure 8.6: Errorbar graphs of TE computed with linear parametric (panels (*a.*)) and nearest-neighbor (panels (*b.*)) approaches and of CrossEn computed via nearest-neighbor estimator (panels (*c.*)) in both directions at baseline (panels (*.1*)) and follow up (panels (*.2*)) conditions for all investigated groups (HFSin, HFVES1, and HFVES2). Statistical test: * $p < 0.05$, ** $p < 0.01$ between directions, paired Wilcoxon signed-rank test. Figure modified from Platiša et al. (2023).

for HFSin and HFVES2 groups after CRT (panel (*a.2*)). The nonlinear estimator confirms the same significant differences in the follow-up condition (panel (*b.2*)), highlighting such difference also at baseline (panel (*b.1*)). Contrarily, higher coupling is observed in the direction from RR to RESP by using CrossEn, with statistically significant difference in HFSin at baseline (panel (*c.1*)) and for all groups (even with lower p-values for HFSin and HFVES2) after CRT (panel (*c.2*)).

In Table 8.1, the results of the comparison between groups of patients are reported for all measures and in both baseline and follow-up conditions. Lower TE_{lin} values are observed for HFVES2 compared to both HFSin and HFVES1 in both directions at baseline and just with HFSin during follow-up; in addition, a significant decrease is also found for HFVES1 compared to HFSin after CRT along the direction from RESP to RR. On the other hand, the nonlinear approach reveals significantly lower values for HFVES2 compared to HFVES1 at baseline considering the direction from RR to RESP.

The stronger influence of breathing activity on cardiac dynamics is well documented in healthy subjects due to the phenomenon of RSA (Elstad et al., 2018) and is here evidenced also in heart failure patients by using nonlinear TE estimates, thus suggesting a nonlinear characterization of the RSA mechanism (Schulz et al., 2013). Furthermore, the progressive decrease of this causal influence from sinus rhythm to the HFVES1 and HFVES2 groups during baseline just when using the linear estimator suggests that, in heart failure patients, the cardiorespiratory interactions evaluated in presence of extrasystole have a strong nonlinear component which can be captured only by using the nonlinear estimator. Furthermore, the stronger influence of respiration on heart rhythm than in the opposite direction, more evident

Table 8.1: Statistical significance of comparison between pairs of groups for bidirectional measures. The asterisks highlight significant values.

	Baseline			Follow-up		
	HFSin vs. HFVES1	HFSin vs. HFVES2	HFVES1 vs. HFVES2	HFSin vs. HFVES1	HFSin vs. HFVES2	HFVES1 vs. HFVES2
TE_{lin} $RESP \rightarrow RR$	0.432	0.001*	0.002*	0.013*	0.004*	0.751
TE_{lin} $RR \rightarrow RESP$	0.297	0.001*	0.001*	0.212	0.012*	0.527
TE_{knn} $RESP \rightarrow RR$	0.572	0.635	0.165	0.080	0.246	0.681
TE_{knn} $RR \rightarrow RESP$	0.181	0.137	0.005*	1	0.946	0.918
$CrossEn_{knn}$ $RESP \rightarrow RR$	0.258	0.131	0.123	0.440	0.781	0.758
$CrossEn_{knn}$ $RR \rightarrow RESP$	0.643	0.274	0.258	0.411	0.980	0.957

after CRT and also visible with the linear estimator, suggests that resynchronization therapy is able to restore the RSA mechanism and to activate both the linear and nonlinear components of the causal effect of RESP on RR. The opposite trends exhibited by CrossEn measures when compared to TE reflect a prevalence of the coupling in the direction from heart rate to respiratory activity amplified after CRT. The reason of this difference is likely methodological indeed, while TE quantifies the directed interactions in terms of predictability improvement, CrossEn implements the concept of cross-predictability, and is thus expected. Moreover, not significant modulations are observed for this measure between groups, suggesting that in cardiorespiratory coupling the prediction of the dynamics of one signal based solely on the history of the other is stable in time and that the presence of arrhythmia does not significantly affect it.

Fig. 8.7 depicts the results of the comparison between the two directions, as well as between baseline and follow-up conditions, for both responders and non-responders groups. For the responders group, stronger causal dynamics are observed along the direction RESP to RR at baseline using both estimators and after CRT when using the nonlinear approach (panels (*a.1-b.1*)), while a higher coupling is obtain in the opposite direction during both baseline and follow-up (panel (*c.1*)). For non-responders, the same trends are observed just after CRT (panels (*.2*)). Moreover, significantly lower values of TE_{lin} are observed from RR to RESP during follow-up than in the baseline condition (panel (*a.2*)). It is noteworthy that nonlinear causality and coupling measures are able to identify the stronger causal influence of respiration on heart dynamics, as well as the stronger coupling in the opposite direction during baseline for the responders group, suggesting these terms as possible indicators for the selection of subjects who will benefit from the device implantation. However, this conclusion should be carefully considered, given that the pre-operative difference between these parameters in the non-responders group is close to statistical significance and that these modulations are achieved in the follow-up phase.

8.5. Cardiovascular dynamic networks uncovered through direct causality measures

In Barà et al. (2026b), a first attempt to exhaustively describe a complex network of physiological cardiovascular variables was conducted by involving the beat-to-beat variability of the main cardiovascular and respiratory parameters, i.e., RR, MAP and RESP time series, and including AC. Specifically, the direct causality measure of CTE was applied on Database B - *version 3* to infer cardiovascular and cardiorespiratory physiological regulatory mechanisms in the supine resting state and in response to the homeostatic alteration due to the postural stress, i.e., REST1 (herein

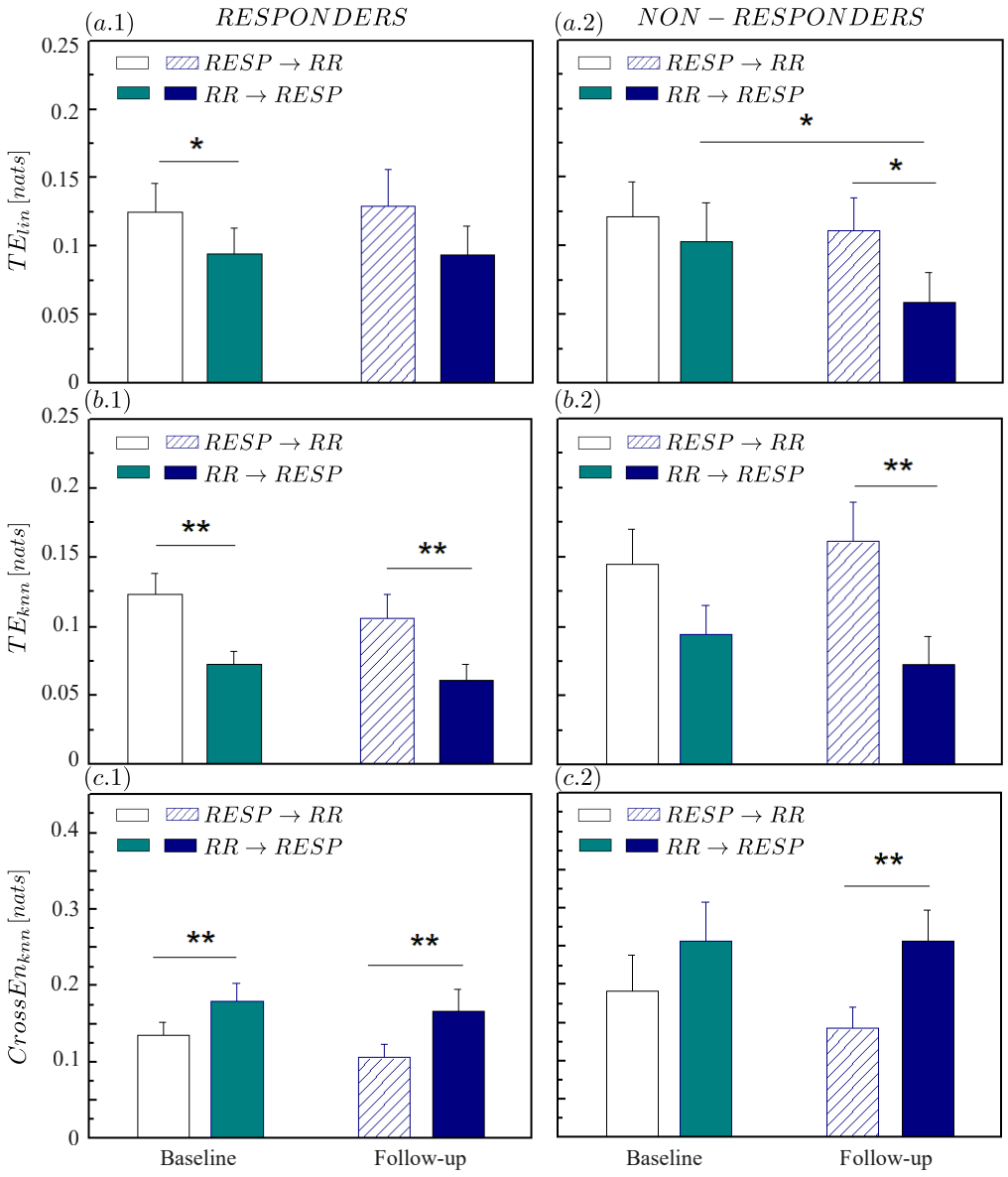

Figure 8.7: Errorbar graphs of TE computed with linear parametric (panels (*a.*)) and nearest-neighbor (panels (*b.*)) approaches and of CrossEn computed via nearest-neighbor estimator (panels (*c.*)) for both responders (panels (*.1*)) and non-responders (panels (*.2*)) during baseline and follow-up. Statistical test: * $p < 0.05$, ** $p < 0.01$ between directions, paired Wilcoxon signed-rank test; * $p < 0.05$, baseline vs. follow-up, Mann-Whitney U test. Figure modified from Platiša et al. (2023).

referred to as REST) vs. HUT. Moreover, the use of both linear and nonlinear estimation approaches allows to reason on the role of nonlinearity in the investigated physiological dynamics.

Data preprocessing - RR, MAP, RESP and AC time series were high-pass filtered through a AR filter (zero phase, cutoff frequency of 0.0156 Hz) and normalized to zero mean.

Data and statistical analysis - The CTE measure was used to quantify the causal link among RR, MAP, AC, and RESP time series constituting the four nodes of the investigated network. Specifically, the linear parametric approach was used by selecting the optimal model order for each subject and conditions according to AIC, while the nearest-neighbor approach was applied by using the non-uniform embedding strategy (maximum lag of 10 samples) and by fixing the number of neighbors $k = 10$. One-hundred realizations of surrogate data were generated with the random shuffling procedure described in Sect. A.2.5 of the Appendix to applied the non-uniform embedding strategy with a significance threshold of $\alpha = 0.05$. For both estimation approaches, instantaneous effects were accounted for. Specifically, after visually inspecting the temporal sequence of the physiological indices and considering that the cause always precedes its effect, the zero-lag effects were set along the directions RESP $\rightarrow$ RR, RESP $\rightarrow$ MAP, RESP $\rightarrow$ AC, RR $\rightarrow$ MAP, RR $\rightarrow$ AC, and MAP $\rightarrow$ AC.

Surrogate data analysis was applied to confirm the presence of the observed causality interactions through the Iterative Amplitude Adjusted Fourier Transform procedure for the linear estimates and the temporal shift of the target variable of at least 20 samples for the nonlinear estimates (see Sects. A.2.4 and A.2.2 in the 13.4 for details). Accordingly, three levels of degree of significance are accounted for in these analysis. Computing the ratio between the ratio between the number of subjects for which the measure was deemed as statistically significant over the total number of subjects, the following ranges are considered: [25 – 50]% for low significance, [50 – 75]% for medium significance, and [75 – 100]% for high significance. Considering the small size of the investigated cohort, non-parametric statistical tests were applied to evaluate the modulation of the investigated causal indices between the two phases of the experimental protocol. Specifically, the Wicoxon signed rank test for paired data was also applied on conditional causality measures evaluated for each pair of nodes using both linear and nonlinear approaches by using the Benjamini-Hochberg procedure to evaluate the false discovery rate (FDR) as to prevent error I type due to multiple comparison. A significance level of $\alpha = 0.05$ was set.

Results and discussion - Fig. 8.8 shows the inferred networks of causality interactions between cardiovascular and cardiorespiratory physiological variables at

REST and during HUT (panels (*a*, *b*)) with the aim of comparing the results achieved with the two estimation approaches, together with the results of the comparison between the two experimental conditions (panel (*c*)).

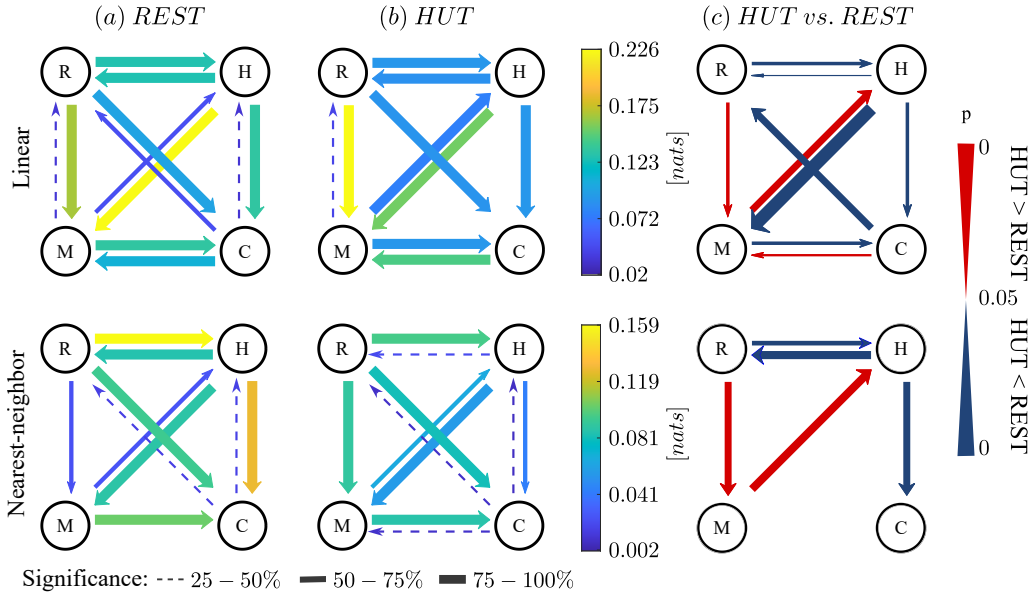

Figure 8.8: Directional networks indicating the directed causality interaction between RR (H), MAP (M), AC (C), and RESP (R) dynamics computed via the linear parametric (top row) and nearest-neighbor (bottom row) approach at REST (panel (*a*)) and during HUT (panel (*b*)), as well as their significant differences between REST and HUT (panel (*c*)). In panels (*a*) and (*b*), the width of the arrows displays results from surrogate data analysis. In panel (*c*), the results of the Wilcoxon signed rank test are reported, ($p < 0.05$), red HUT > REST, blue HUT < REST; the progressive change of the width of the arrows indicates increase/decrease of p-values in logarithmic scale. Arrows are shown only if the corresponding percentage of significance is above 50% for at least one of the two conditions. Figure taken from Barà et al. (2026b).

Cardiorespiratory dynamics are strongly detected by both approaches at both REST and HUT, with a prevalence of the respiratory activity influence on heart period at REST by using the nonlinear estimator. The causal interaction from RESP to RR significantly decreases with HUT by using both approaches, while the weakening of the causal effect in the opposite direction is more evidently observed by using the nonlinear estimator. The modified influence of the ventilatory activity on heart period dynamics reflect the well-known tilt-induced parasympathetic activity withdrawal with orthostatic stress, that in turn leads to a significant RSA weakening (Brown et al., 1993; Schmitz et al., 1995). Indeed, previous studies demonstrated a dominance of the direct central mechanism mediating RSA, thus the direct communication between respiratory and cardiomotor centres, at supine rest and a dominance of indirect peripheral mechanism, thus of ventilation-associated ABP changes transferred to heart rate, during tilt (Piepoli et al., 1997; Krohova et al., 2018). On the other hand, the decreased causal effect in the opposite direction may be associated

to a decrease of the overall complexity of cardiorespiratory interactions during with sympathetic activation (Porta et al., 2012).

Regarding cardiovascular interactions, both estimation approaches capture the causal effect of arterial pressure on heart period, with a significant increase during HUT. This is related to the significantly higher awareness of baroreflex control with tilt, due to blood redistribution and baroreceptor unloading (Sugawara et al., 2012). On the other hand, in line with previous studies (Javorka et al., 2017), the opposite link is stronger, with a significant decrease observed using the model-based approach only. This behavior may reflect the involvement of mechanisms influencing diastolic dynamics and contributing to the strength of the systolic contraction, such as changes in PVR and cardiac contractility associated with tilt-induced sympathetic activation.

Looking at causal interactions involving arterial pressure and compliance dynamics, the causal effect of MAP on AC is always captured by both approaches and in both conditions with high significance, while the opposite direction is significantly detected only by the linear estimator. In the shift from REST to HUT, an increase of the causal interaction from AC to MAP and, conversely, a decrease of the causal interaction from MAP to AC is observed using the linear approach. Even if little is known about this physiological link and its modulation with postural stress, the results on the causal effect of AC on MAP may be related to slow rhythms conveyed to the arterial system through SV modulations, that could depend on both respiratory activity and venous blood pool control (Ursino and Magosso, 2003; Mukkamala et al., 2003). Moreover, both estimation approaches show the causal effect of heart rate on arterial compliance with high significance, except for the model-free estimator during HUT, which indeed detects a decrease in this causal interaction more evidently.

The causal interaction from RESP to AC is always detected with high significance, while the opposite direction seems to play an important role only during REST, even if the values are very low; this highlights a significant decrease in the strength of this causal effect during HUT. This latter leads to speculate to a linear mechanical interaction between the arterial system and ventilation. Finally, the causal interaction from RR to MAP presents high significance with both approaches during HUT and just with the linear estimator at REST. Consequently, a strengthening of this causal effect is revealed in HUT by using both estimation approaches and is related to alterations in intrathoracic pressure, instantaneous lung volume, venous return to the heart, and cardiac output occurring with HUT, and thus to the mechanical thoracic coupling between respiration and vasculature (Draghici and Taylor, 2016).

8.6. Overview and conclusions of chapter 8

This chapter examines the application of information-dynamics frameworks widely used to investigate interactions between pairs of physiological systems, while also highlighting the importance of integrating these bivariate approaches with univariate methods – whose utility was discussed in the previous chapter – in order to achieve a more comprehensive understanding of complex physiological dynamics. Particular attention is devoted to the increasingly adopted MIR framework, which formalizes the relationship among measures of dynamic symmetric coupling, complexity, and causality, enabling a more comprehensive interpretation of the mechanisms regulating pairwise physiological dynamics. In recent years, this framework has been applied to investigate cardiovascular and cardiorespiratory dynamics (Sparacino et al. (2025c); Barà et al. (2023b); Pinto et al. (2025); Sparacino et al. (2026)), neural spike-train activity (Bernardi and Lindner, 2015; Mijatovic et al., 2021), and brain-heart interactions (Vergara et al., 2025b). Beyond complexity metrics – whose physiological significance was extensively addressed in Chapter 7 – the MIR framework enables explicit characterization of asymmetries in information flows between interacting physiological systems. The association between the TE measure involved in the MIR decomposition and the concept of causality is well established. By quantifying the information shared between the current state of a target system and the past state of a source system, while conditioning on the target's past history, TE has been widely exploited to reveal causal influences among physiological processes. Consequently, it has been used to investigate imbalances in physiological closed-loop pathways under different conditions, such as enhanced baroreflex sensitivity or RSA attenuation during orthostatic stress (Javorka et al., 2018). Similarly, TE has been applied in neurophysiological studies to infer effective connectivity during motor tasks (Vicente et al., 2011) and to quantify information flow between cortical and cerebellar networks during auditory stimulation (Wibral et al., 2011). Furthermore, TE has proven useful in identifying physiological impairments in pathological populations, including reduced pressure–flow directionality in cerebrovascular regulation after acute ischemic stroke (Gelpi et al., 2025) and alterations in brain functional organization in patients with disorders of consciousness (Mäki-Marttunen et al., 2013). Another key feature of the MIR framework is its ability to quantify the information shared between interacting processes while distinguishing between time-delayed and instantaneous interactions. This distinction is particularly relevant for physiological dynamics influenced by common driver effects or complex feedback mechanisms. Zero-lag effects may arise from non-physiological factors, such as unobserved confounders, or from fast within-beat physiologically meaningful interactions (Faes et al., 2013a). The importance of accounting for instantaneous effects has been highlighted in cardiovascular interactions, where zero-lag interdependencies contribute significantly to the baroreflex mechanism (Faes et al.,

2013a), as well as in the causal influence of respiratory activity on cardiac and vascular dynamics (Faes et al., 2012b; Nuzzi et al., 2021). Previous findings also suggest a strong association between instantaneous causality and structural brain connectivity (Alonso-Montes et al., 2015).

In this chapter, the usefulness and feasibility of the MIR framework are demonstrated through several applications. In particular, MIR reveals a clear association between strengthened cardiorespiratory coupling during slow breathing and a concomitant reduction in cardiac and respiratory complexity, together with increased bidirectional information flow between the systems (Sect. 8.1). The framework also provides deeper insight into alterations in cardiovascular dynamics that appear largely unchanged in terms of overall coupling during orthostatic challenge (Sects. 8.1 and 8.2). MIR decomposition shows that this apparent stability of the global dynamic coupling arises from internal modifications, characterized by reduced cardiac complexity and a shift in closed-loop information flow from a predominance of cardiac influence on vascular dynamics to increased baroreflex control. Moreover,distinguishing between lagged and instantaneous causal effects reveals that baroreflex enhancement is mainly associated with delayed responses, whereas analyses based on the overall information flow measured aggregating zero-lag and time-lagged components may obscure this strengthening due to opposing trends in instantaneous and lagged causality (Sect. 8.2). The applications further provide insight into the increased cardiovascular coupling observed in older individuals and the associated changes in causal dynamics and complexity, as well as into differences in cardiovascular regulatory mechanisms between healthy young subjects and post-AMI patients that may remain undetected when considering only overall coupling measures (Sect. 8.2).

Although the results reported in Sects. 8.1 and 8.2 are largely consistent with each other and with previous literature, some discrepancies emerge. These differences can be attributed to practical estimation issues, as discussed in Sect. 4.4. Model-free approaches can detect nonlinear dependencies that may not be captured by linear parametric models, but their application requires careful consideration of the Markov assumption, as well as attention in the selection of estimation parameters (Xiong et al. (2017); Pinto et al. (2025)). In discretization-based approaches, short memory lengths are often required to mitigate the curse of dimensionality, as previously highlighted for ER estimation (Barà et al., 2024c). This limitation becomes more pronounced when estimating MIR, which combines several independently estimated entropy terms. In the reported applications, the binning approach failed to detect expected variations in cardiorespiratory complexity, whereas the permutation approach showed limitations in accurately assessing causal dynamics (Sect. 8.1). These shortcomings likely reflect excessively short memory lengths in the binning method and the lack of sensitivity to amplitude information in the permutation

approach. Despite limitations in high-dimensional settings, permutation methods generally provide a more parsimonious representation of discretized patterns describing physiological dynamics (Barà et al., 2023b). This is evident when comparing the results reported in Sects. 7.1 and 8.1, where ER estimates were obtained from the same dataset in spaces of different dimensions. Pairwise analysis required shorter memory lengths and stronger coarse graining to ensure reliable estimation of higher-dimensional terms. Consequently, cardiorespiratory complexity measures failed to show modulation with breathing rate, unlike the findings from univariate analysis. In contrast to discretization-based estimators, the nearest-neighbor approach alleviates estimation bias by treating the spaces associated with the different entropy terms as projections of a common space (Kraskov et al., 2004). This strategy reduces bias effects that increase with dimensionality. However, the substantially higher data requirement associated with *knn* estimators – particularly in high-dimensional spaces – must be carefully considered. In this context, the use of non-uniform embedding strategies selecting the most informative past samples becomes even more important in bivariate analysis than in univariate one. These strategies are widely used in literature for estimation causal dynamics, for example in Faes et al. (2012b), together with enabling the identification of delay-specific causal contributions (Faes et al. (2014a); Barà et al. (2024b)). A related important factor affecting the estimation of these measures from physiological data is the available data length, an issue that becomes particularly critical when assessing coupling and causality from ultra-short time series. Although this area remains relatively underexplored, preliminary studies suggest that segments of approximately three minutes are required to reliably detect variations in cardiovascular coupling between resting supine and orthostatic stress states using linear parametric approaches (Raimondi et al., 2025a). Interestingly, analyses based on nearest-neighbor strategies indicate that reliable detection may be possible with even shorter data segments – down to about 60 samples – highlighting the relevance of nonlinearities in the investigation of this physiological interaction (Raimondi et al., 2025b).

Another aspect emerging from the applications in Sects. 8.2 and 8.3 concerns the identification of nonlinearities in physiological dynamics and the capability of simpler model-based approaches to investigate systems known to exhibit nonlinear behavior. In Sect. 8.2, integrating the MIR framework with multiple surrogate data methods was essential to ensure robust statistical validation of the significance and nonlinear nature of the estimated measures. In particular, the IAAFT method proved effective in detecting nonlinear components in the observed dynamics, confirming their physiological relevance in short-term data analysis (Schreiber and Schmitz, 2000). By contrast, Sect. 8.3 evaluated correlations between TE measures estimated using linear parametric and nearest-neighbor approaches. The results confirmed the well-known tendency toward linearization of cardiovascular

dynamics under tilt-induced sympathetic activation (Porta et al., 2006), as well as different trends in older individuals associated with altered regulatory mechanisms. Although partially contrasting with results in Sect. 8.2, these differences may arise from the inclusion of zero-lag interactions in the first analytical setting, which may emphasize nonlinear dynamics under resting conditions. The second approach provided clearer insights into nonlinearities in other subsystems, revealing linearization of causal dynamics within the cardiorespiratory system during HUT and increased nonlinearity in causal pathways from ventilatory activity to vascular dynamics – both trends consistent with previous literature (Fortrat et al., 1997; Porta et al., 2016). Nevertheless, the results reported in Sect. 8.3 show substantial agreement between model-based and model-free approaches, supporting the robustness of the findings and suggesting that, in the presence of strong physiological control mechanisms – such as those operating in healthy subjects during sympathetic activation – parametric methods may represent a reliable and computationally efficient alternative to model-free approaches.

In Sect. 8.4, the coupling measure of CrossEn and the causality TE measure were applied to investigate cardiorespiratory interactions in heart failure patients, highlighting their distinct physiological interpretations. Notably, TE and CrossEn exhibited opposite trends with respect to directionality: when one measure indicated a predominance of a direction, the other suggested the opposite. Similar findings were reported in Pernice et al. (2022a), where opposite trends were observed with varying breathing rates, underscoring the fundamentally different nature of these measures and the role of self-predictable cardiac and respiratory dynamics in shaping overall system behavior. Consistent with these observations, several studies have contrasted CrossEn and TE in the investigation of closed-loop interactions between cardiac and vascular variability, particularly regarding the balance between baroreflex-mediated feedback and mechanical feedforward pathways under postural stress. For example, Porta et al. (2011b) demonstrated the ability of CrossEn to detect the absence of baroreflex-mediated information transfer in heart transplant recipients and its gradual restoration after transplantation. Moreover, a progressive shift from circulatory mechanics to baroreflex-mediated information transfer during graded tilting procedures has been shown in healthy subjects (Faes and Porta, 2014). Beyond comparisons with causality-based measures, CrossEn has been widely applied to investigate synchronization between interacting physiological systems (Porta et al., 1999). For example, synchronization between heart period variability and ventricular repolarization variability decreases after myocardial infarction (Porta et al., 1999), and synchronization between heart period and arterial pressure variability decreases during orthostatic stress in post-infarction patients but increases in healthy subjects (Nollo et al., 2002).

The application presented in Sect. 8.5 emphasizes the importance of investigat-

ing pairwise dynamic links while explicitly accounting for their embedding within a broader physiological network. Considering additional systems participating in complex control mechanisms – thereby evaluating the partial or direct effect of one node on another – is possible through conditional causality measures (Schulz et al., 2013). The analysis concerns a four-node network including heart period, arterial pressure, respiration, and beat-to-beat arterial compliance. The relevance of conditional measures becomes evident when comparing results from Sects. 8.5 and 8.3. In both analyses, orthostatic stress was associated with reduced causal influence of ventilation on cardiac dynamics and increased influence of vascular dynamics on heart rate. However, discrepancies emerged regarding the causal effect of respiration on arterial pressure: no significant variation was observed when considering the single link, whereas a strengthening of the directional effect was detected using conditional measures. Despite differences in the variables used to represent arterial pressure variability (SAP vs. MAP), this result reflects the well-known influence of heart period on both respiratory and vascular dynamics (Rosenblum et al., 1998; Svacinova et al., 2015). Nevertheless, some potential confounding nodes remain unaccounted for in the analyzed network. Variables such as stroke volume and cardiac output – commonly used to estimate beat-to-beat arterial compliance (Svec et al., 2021) – may exert relevant influences. Similarly, sympathetic nervous activity represents a common source of oscillations affecting arterial compliance, heart rate, blood pressure, and peripheral vascular resistance, albeit with different magnitudes (Barà et al., 2026b). While the former influences could be incorporated by expanding the network, the latter represents an intrinsic limitation in physiological studies, as sympathetic neural firing cannot be directly and continuously measured despite its substantial impact on network interactions. Even more when additional variables are included, the challenges associated with high-dimensional analyses remain, particularly for model-free approaches. Strategies that may mitigate confounding effects include restricting the analysis to specific spectral bands – for instance, removing high-frequency oscillations to attenuate respiratory influence. Owing to its advantages, conditional causality has been widely applied in the study of complex physiological systems, including analyses of cardiovascular and cardiorespiratory dynamics during paced breathing (Faes et al., 2013b), cerebrovascular regulation in stroke patients (Gelpi et al., 2025), electrophysiological interactions in sleep-disordered breathing (Gu et al., 2022), and functional connectivity in epileptic patients (Papana et al., 2012). Despite its multivariate nature, CTE presents an important limitation: it does not explicitly account for high-order effects arising from complex control mechanisms. In particular, it may fail to detect redundant interactions among observed processes, leading to inferred networks that reflect mixture of direct and redundant influences (Stramaglia et al., 2024).

The applicative examples reported throughout this chapter demonstrate the use-

fulness of MIR and its decomposition measure, particularly of the transfer entropy and instantaneous causality, as well as of the conditional transfer entropy, in inferring coupling or causality networks that reflect physiological mechanisms and their alterations under both physiological and pathological conditions, provided that these measures are appropriately estimated.

Chapter 9

High-order analysis of physiological networks

This chapter presents applicative examples of the investigation of high-order behaviors in physiological dynamics by exploiting the framework of PID. Specifically, different redundancy measures and their associated estimation approaches are compared using arterial pressure time series to examine the relation among systolic, diastolic, and mean arterial pressure components (Sect. 9.1). Moreover, the mixed estimation approach is employed in a setting involving a discrete variable representing ventilatory phases and continuous source variables describing cardiovascular dynamics (Sect. 9.2). Finally, an application to cardiorespiratory dynamics is presented to highlight the potential of the PID framework in elucidating high-order dynamics arising between the current and the past states of a bivariate process when investigating pairwise interactions through the PrI decomposition framework detailed in Sect. 4.2 (Sect. 9.3).

9.1. Application of different redundancy measures on arterial pressure signals

Mean arterial pressure represents a critical hemodynamic parameter, as it reflects average arterial pressure throughout the cardiac cycle and serves as a key determinant of tissue perfusion (Papaioannou et al., 2016). Despite its clinical relevance, MAP is often estimated in routine practice using empirical formulas. In these formulations, the so-called form factor defines the percentage of pulse pressure (i.e., the difference SAP and DAP) that is added to DAP to approximate MAP. However, this form factor can vary depending on several physiological and hemodynamic conditions, which can lead to inaccuracies in MAP estimation. The investigation conducted in Sparacino et al. (2025d) explores the nontrivial relationship among MAP, SAP, and DAP through the PID framework. The study aims to quantify the

individual contributions of SAP and DAP to MAP, as well as their redundant and synergistic contributions, in shaping the beat-to-beat variability of MAP. Time series representative of the ABP components collected during the REST1 - herein referred to as REST – and HUT phases of Database B - *version 1* were used.

Data preprocessing - Prior to the analysis, all time series were preprocessed to remove slow trends using an high-pass AR filter applied in a zero-phase configuration, with a cut-off frequency of 0.0156 Hz. Subsequently, the mean value was removed from each series.

Data and statistical analysis - The PID framework was applied to a static network composed of three nodes representing the MAP, SAP, and DAP time series. Both the model-based MMI-PID – computed through a linear parametric estimation approach – and the model-free specific MI-PID – estimated using a binning-based strategy – were implemented to decomposed the MI measure evaluated between $Y = MAP$ and jointly $X_1 = SAP$ and $X_2 = DAP$, that are thus respectively considered target and source variables. In the model-free approach, continuous-valued variables were discretized through uniform quantization, fixing the number of bins to 6, as commonly adopted in short-term time series analysis.

A statistical comparison between protocol phases (REST vs. HUT) was performed for all computed metrics and for both estimation approaches. Additionally, within each condition, the significance of the differences between the two unique information terms, as well as between redundancy and synergy, was assessed. All statistical comparisons were conducted using the parametric paired Student's t-test with a significance threshold of 5%.

Results and discussion - Fig. 9.1 shows that, independently of the approach used to compute the redundancy measure, the PID framework reveals a predominance of the unique contribution of DAP in both experimental conditions (panels (*e*)). Moreover, redundancy consistently exceeds synergy (panels (*g*)). These findings corroborate the well-established empirical formula commonly used to estimate MAP, in which DAP plays a dominant role in hemodynamically stable subjects (Papaioannou et al., 2016; Jozwiak et al., 2024). They further suggest that a substantial portion of the information transferred from DAP and SAP to MAP is shared (i.e., redundant), regardless of the presence of external stressors. Considering the modulation of MI terms with postural stress, the PID analysis indicates that significant changes are confined to the redundant contribution (panels (*f*)), while neither the unique contribution of SAP nor that of DAP exhibits significant variations. This result suggests that the form factor underlying MAP estimation is likely independent of postural condition in healthy subjects, in contrast with findings obtained using traditional linear prediction models, which report a tilt-induced increase in the predictability of MAP from SAP and DAP. Furthermore, the more pronounced super-

imposed role of SAP and DAP in improving MAP predictability during postural stress – also reflected by a significant decrease in the synergistic contribution when applying the model-free approach (panel (*g*), right) – may be interpreted in light of a common-driver structure underlying the MAP–SAP–DAP relationship, whereby replicated source information is conveyed to MAP. Consistently, previous studies have highlighted the predominantly redundant nature of physiological interactions and their enhancement during tilt (Faes et al., 2022; Sparacino et al., 2025a).

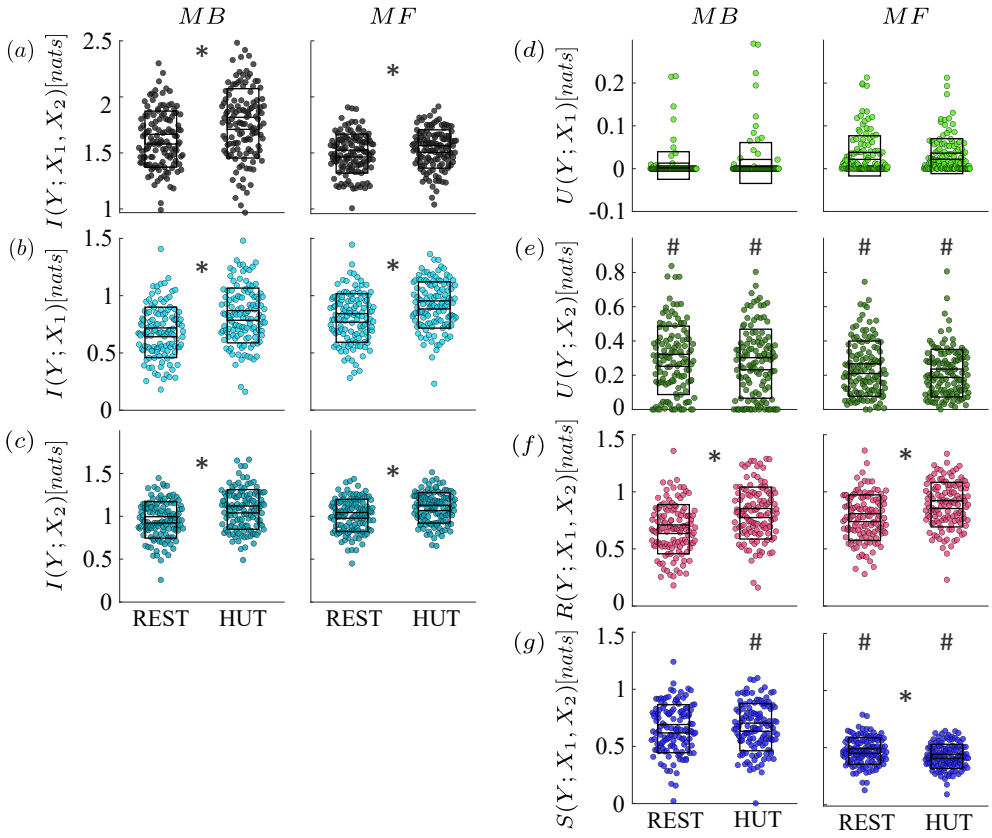

Figure 9.1: Boxplot distribution and individual values of the multivariate information $I(Y;X_1,X_2)$ (panel (*a*)) shared in a static network of vascular variables, with $Y = MAP$ the target variable, and $X_1 = SAP$ and $X_2 = DAP$ the two sources, into unique $U(Y;X_1)$, $U(Y;X_2)$ (panels (*d*, *e*)), redundant $R(Y;X_1,X_2)$ (panel (*f*)), and synergistic $S(Y;X_1,X_2)$ (panel (*g*)) contributions in the REST and HUT conditions. The redundancy function is computed following either the MMI-PID model-based (MB, left column) or the specific MI-PID model-free (MF, right column) approaches. The marginal MI shared between the target and each source, $I(Y;X_i)$, $i = 1,2$ are also shown (panels (*b*, c)). Statistical tests: *, $p < 0.05$ REST vs. HUT, paired Student's *t*-test; #, $p < 0.05$ $U(Y;X_2) > U(Y;X_1)$, $R(Y;X_1,X_2) > S(Y;X_1,X_2)$, paired Student's *t*-test. Figure modified from Sparacino et al. (2025d).

9.2. Exploring high-order dynamics between ventilatory activity phases and cardiovascular dynamics

The mixed estimation approach proposed in Barà et al. (2025a) was applied in the context of cardiovascular physiology to decompose the information shared between a binary variable representing the respiratory phase (retrieved from RESP time series) and the continuous RR and SAP time series. Data collected in Database B - *version 2* during resting (REST1, herein referred to as REST) and head-up tilt phases (HUT) were used. The results reported in Barà et al. (2024a) and in the supplementary material of Barà et al. (2025a) are summarized below.

Experimental protocol and time series extraction - To apply the proposed PID estimation approach to investigate the interplay between cardiovascular dynamics and the respiratory phase, the R time series were binarized by assigning a value of $\overline{R}_n = 0$ to the expiratory phase – identified when the current sample R_n was followed by a decrease in amplitude – and a value of $\overline{R}_n = 1$ to the inspiratory phase – identified when the current sample was followed by an increase in amplitude. In contrast, the H and S time series were retained as continuous variables and normalized to zero mean and unit variance prior to analysis.

Data and statistical analysis - The PID framework was implemented considering the current sample of the discretized respiratory time series as the target variable, $Y = \overline{R}_n$, and the cardiovascular variables as sources, defined as $X_1 = [H_n\ H_{n+1}]$ and $X_2 = [S_n\ S_{n+1}]$. In accordance with the results reported in Sect. 5.2.3, the number of neighbors was fixed to $k = 5$.

A statistical comparison between the two acquisition conditions, REST vs. HUT, was performed across subjects using a paired Student's t-test, with the significance level set at 5%. In addition, the statistical significance of each PID decomposition term was evaluated using the surrogate data analysis approach described in Sect. A.2.5 of the Appendix, generating one-hundred surrogate data and fixing a significance level of $\alpha = 0.05$.

Results and discussion - Fig. 9.2 (*a*) shows a significant decrease in $I(Y; X_1, X_2)$ during postural stress, indicating a weakening of the overall interaction between the cardiovascular and respiratory systems. The application of the PID framework provides insight into the physiological modulations underlying this behavior. In particular, the reduction in $U(Y; X_1)$ reflects a dampening of the respiratory sinus arrhythmia with postural stress (Eckberg, 2009), whereas the increase in $U(Y; X_2)$ suggests the enhancement of cyclic intrathoracic pressure changes and the baroreflex mechanism associated with ventilation (Draghici and Taylor, 2016). Although no significant variations are observed in the redundant and synergistic terms, cardiorespiratory and vasculo-respiratory interactions appear predominantly redun-

dant in both conditions. This findings is likely related to the influence of ventilatory activity on both cardiac and vascular dynamics with similar latency (Eckberg, 2009; Draghici and Taylor, 2016).

In (panel (*b*)), the information individually exchanged by heart period and systolic arterial pressure dynamics with ventilatory phases and during the specific ventilatory phases are reported. A reduction in $I(Y;X_1)$ during HUT is observed across both inspiratory and expiratory phases, whereas a significant increase in $I(Y;X_2)$ is detected exclusively during inspiration.

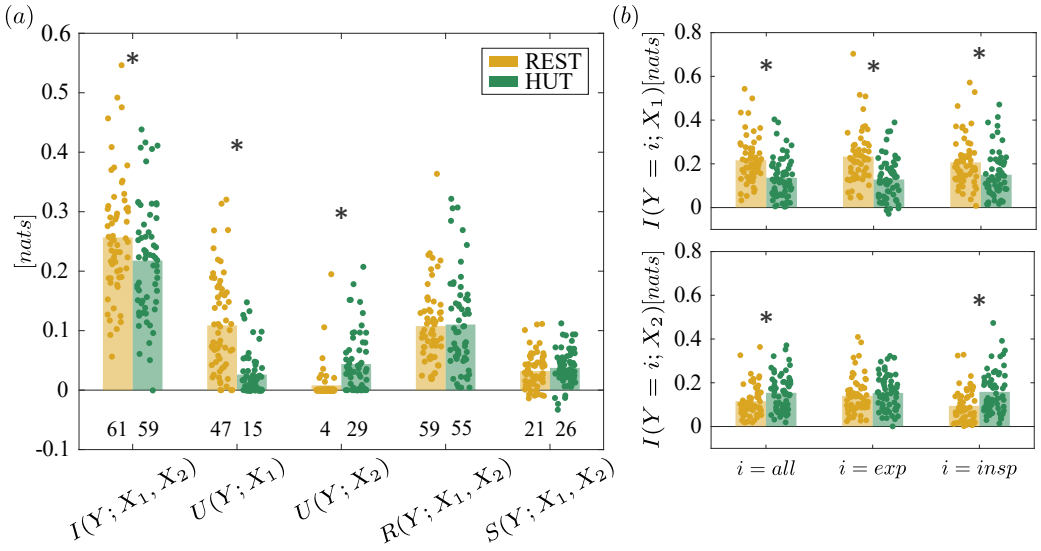

Figure 9.2: Mean and individual values of the PID terms applied to the MI between the binary target variable Y measuring inspiration/expiration phases and the continuous source variables X_1 and X_2 measuring respectively heart period and systolic arterial pressure dynamics computed in a resting state (REST) and during orthostatic stress (HUT) (panel (*a*)), and of the information exchanged by Y and each source overall and in the ventilation phases of expiration (*exp*) and inspiration (*insp*) (panel (*b*)). Statistical test: *, $p < 0.05$ REST vs. HUT, paired Student's *t*-test. The number of subjects for which each measure is statistically significant according to surrogate data analysis is shown for each PID term. Figure modified from Barà et al. (2024a) and Barà et al. (2025a).

9.3. Investigating modes of interactions within cardiorespiratory systems with physiological stressors

In this section, the PID framework is applied to decompose the Predictive Information associated with cardiorespiratory interactions. The aim is to assess the short-term regulation of heart period variability in conjunction with respiratory variability during postural and mental stress, thereby elucidating interaction mechanisms that remain concealed when considering only traditional measures derived from the PrI decomposition. As introduced in Saputo et al. (2026), the terms appearing in the decomposition of PrI can be expressed as combinations of PID atoms. Specifically,

by considering the present state of the target process, Y_n – here corresponding to the current heart period – as the PID target variable, and the past states of the target and driver processes, Y_n^- and X_n^- – corresponding in this study to the past heart period and respiratory amplitude – as the two PID sources, the four components of the PrI decomposition can be derived from appropriate combinations of the PID atoms. Without entering into the mathematical details of the derivation – for which the reader is referred to the original work – the decomposition terms can be expressed as follows: $S_Y = U(Y_n; Y_n^-) + R(Y_n; Y_n^-, X_n^-)$, $C_{X\to Y} = U(Y_n; X_n^-) + R(Y_n; Y_n^-, X_n^-)$, $T_{X\to Y} = U(Y_n; X_n^-) + S(Y_n; Y_n^-, X_n^-)$, and $S_{Y|X} = U(Y_n; Y_n^-) + S(Y_n; Y_n^-, X_n^-)$. These analyses have been conducted on the extended version of Database B. Specifically, RR and SAP time series obtained from REST1 (herein referred to as REST), HUT, and MA were investigated and the results, comprehensively integrated with those derived from the analysis of cardiovascular interactions, were reported in Saputo et al. (2026).

Data preprocessing - RR and SAP time series collected during REST, HUT, and MA phases were corrected to remove outliers beyond three standard deviations from the mean and replaced using two different interpolation algorithms, i.e., linear for isolated outliers and cubic spline for multiple successive ones. To remove the slow trends an AR high-pass filter (zero phase; cut-off frequency 0.0156 Hz) was applied to the corrected time series and the mean value was removed prior to the analysis to obtain zero-mean series.

Data and statistical analysis - The PrI measure and PID terms were computed from cardiorespiratory time series using both model-based and model-free formulations. As anticipated in the introductory paragraph, a bivariate system composed of the target process $Y = RR$ – here indicated as H – and the driver process $X = SAP$ – here indicated as S – was considered within the PrI framework. Accordingly, the current state of the heart period H_n was taken as the target variable, while the past states H_n^- and S_n^- were considered as the two source variables in the PID framework. The PID atoms were first estimated and subsequently combined to obtain the PI decomposition terms. All measures were computed for each subject and experimental condition using the continuous parametric and discrete model-free approaches described in Sect. 5.2.2. Specifically, in the former case, the order of the full model was selected according to a multivariate extension of the AIC, with a maximum scanned order of 12, and the order of the reduced models was fixed to 20, while the latter was applied using a number of quantization levels $b = 6$ and an embedding dimension $m = 1$. These parameter values were chosen to mitigate estimation bias arising from high-dimensional variables in finite-sample settings.

The statistical significance of the computed information measures was assessed using surrogate data analysis strategies based on the random shuffling of the samples of the target variable (see Sect. A.2.5 of Appendix). For the model-based

approach, a measure was deemed significant according to a significance level of $\alpha = 0.05$. For the model-free approach, the significance was first evaluated at the level of PID atoms for specific target values using a significance level of $\alpha = \frac{0.05}{4b}$ percentile. Subsequently, a PID term or PrI decomposition quantity was considered significant if at least one of its constituent specific components reached significance.

Statistical differences across physiological conditions were evaluated using parametric tests. A one-way ANOVA was first performed to assess overall differences in mean values among conditions at a 5% significance level. When appropriate, post-hoc paired Student's t-tests were conducted to compare the resting state with each stress condition. A significance level of 2.5% was adopted after applying the Bonferroni correction for multiple comparisons. Moreover, Student t-test was used to assess the statistically significant differences between redundancy and synergy across conditions with a significance level of 5%.

Results and discussion - Fig. 9.3 presents the results of the PrI decomposition obtained using both the model-based (panel (a)) and model-free (panel (b)) approaches. Both estimation strategies revealed a statistically significant increase in P_H, S_H, and $S_{H|R}$, along with a significant decrease in $T_{R\to H}$ and $C_{R\to H}$ during postural stress. Regarding the response to mental stress, a reduction in P_H is observed compared to the resting state, although this decrease reached statistical significance only with the model-free approach. This reduction was accompanied by decreases in both $T_{R\to H}$ and $C_{R\to H}$, partially counterbalanced by increases in S_H (significant only in the model-free formulation) and in $S_{H|R}$ (significant only in the model-based formulation).

Fig. 9.4 reports the results of the PID decomposition obtained using both the model-based (panel (a)) and model-free (panel (b)) approaches. In response to postural stress, the observed increase in P_H is completely attributable to a significant rise in the unique contribution $U(H_n; H_n^-)$. This increase is partially counterbalanced by a reduction in the redundant contribution when using the model-based approach and by a decrease in the synergistic contribution when using the model-free approach. Additionally, a decrease in $U(H_n; R_n^-)$ is observed, although its statistical significance is limited, particularly for the model-based estimation strategy. With regard to mental stress, a significant increase in $U(H_n; H_n^-)$ is accompanied by significant decreases in both the redundant term $R(H_n; R_n^-, H_n^-)$ and $S(H_n; R_n^-, H_n^-)$. A significant reduction in $U(H_n; R_n^-)$ is also detected when applying the model-free estimation approach.

These findings suggest that postural stress and mental stress respectively induce an increase and a decrease in the predictability of heart rate variability given its own past and the past of respiratory dynamics. According to the traditional PrI decomposition, the increase in PrI observed during postural stress can be primarily attributed to enhanced self-dynamics of the heart period, as reflected by the rise

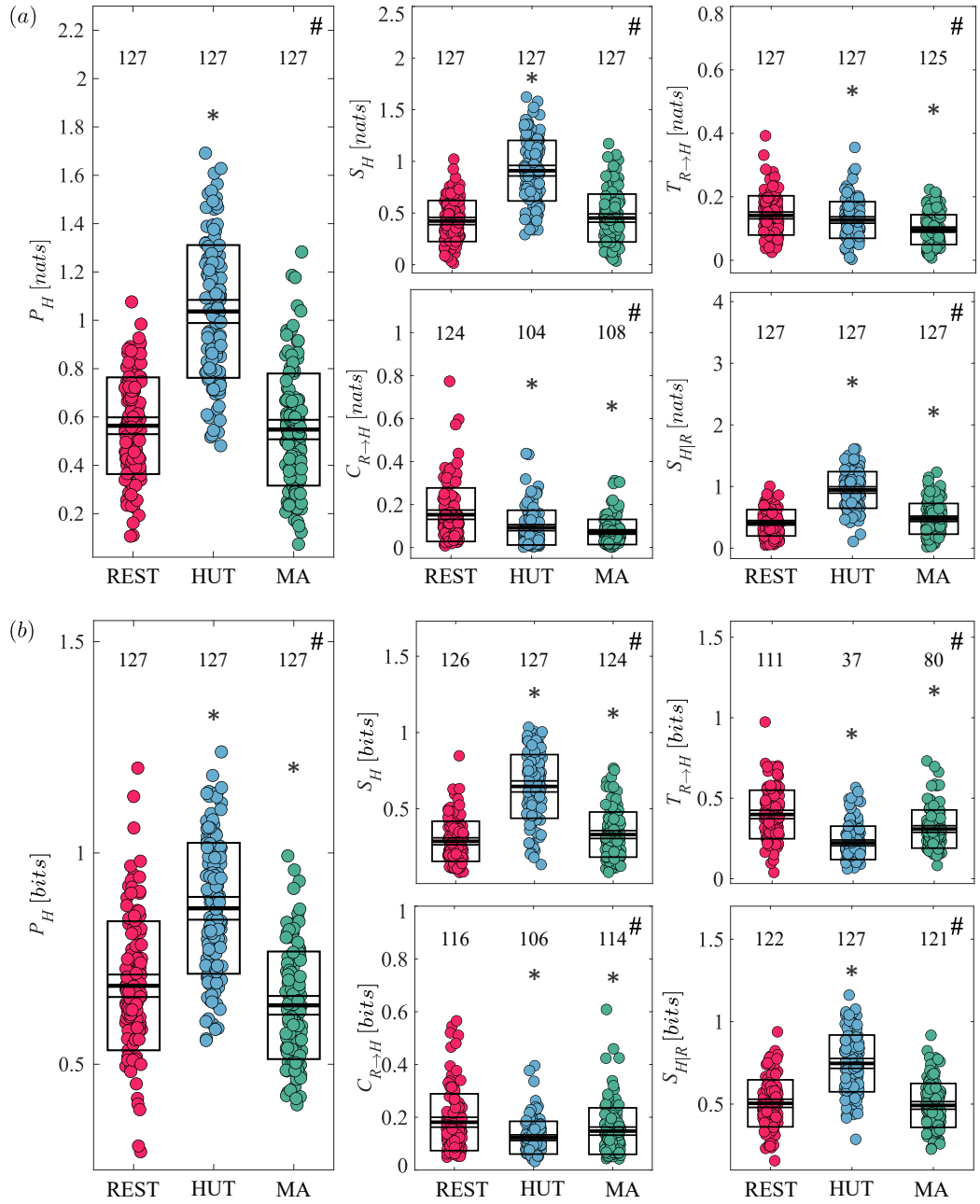

Figure 9.3: Boxplot distributions and individual values of PrI and its decomposition terms computed on cardiorespiratory interactions during supine rest (REST), head-up tilt maneuver (HUT), and mental arithmetic stress (MA) using the linear parametric approach (panel (*a*)) and the nonlinear binning approach (panel (*b*)). Values above each distribution indicate the number of subjects for which the measure was deemed as statistically significant according to surrogate data analysis. Statistical tests: #, $p < 0.05$, ANOVA; *, $p < 0.025$ REST vs. HUT/MA, Student's *t*-test. The figure was modified from Saputo et al. (2026).

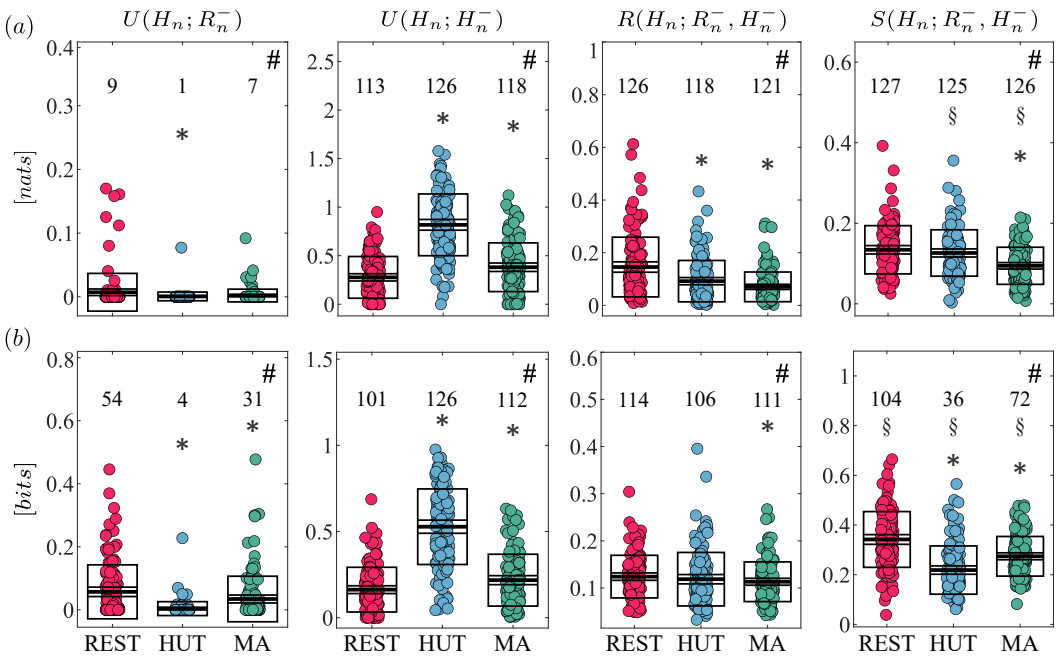

Figure 9.4: Boxplot distributions and individual values of the unique, redundant and synergistic atoms of PID decomposing the PrI measures computed on cardiorespiratory interactions during supine rest (REST), head-up tilt maneuver (HUT), and mental arithmetic stress (MA) using the linear parametric MMI-PID approach (panel (*a*)) and the specific MI approach through binning estimation strategy (panel (*b*)). Values above each distribution indicate the number of subjects for which the measure was deemed as statistically significant according to surrogate data analysis. Statistical tests: #, $p < 0.05$, ANOVA; *, $p < 0.025$ REST vs. HUT/MA, Student's *t*-test; §, $p < 0.05$ $S(H_n; R_n^-, H_n^-)$ vs. $R(H_n; R_n^-, H_n^-)$, Student's *t*-test. The figure was modified from Saputo et al. (2026).

in S_H and $S_{H|R}$. Conversely, the reduction in PrI during mental arithmetic mainly reflects modulations of coupling and causal dynamics, as indicated by decreases in $C_{R\to H}$ and $T_{R\to H}$. The PID-based decomposition of cardiorespiratory information dynamics further clarifies these mechanisms. The increased self-predictability during postural stress is driven by a stronger unique contribution of the past heart period to its present state, i.e., $U(H_n; H_n^-)$. This finding indicates that the enhanced self-dependencies of heart period dynamics are largely independent of respiration and are likely associated with low-frequency oscillatory mechanisms, such as the interplay between Mayer waves of arterial pressure and heart rhythm (DeBoer et al., 1987). In contrast, the reduced cross-predictability observed during mental stress is mainly attributable to diminished redundancy and synergy between past heart period and respiratory dynamics in determining the current heart period. The redundant and synergistic components encompass both the direct central influence of respiratory rhythms on the sinus node (Eckberg, 2009) and the reflex modulation of the sinus node mediated by arterial pressure fluctuations mechanically induced by respiration (Karemaker, 2009). Indeed, although the analysis focuses on cardiorespiratory interactions, it is not possible to fully disentangle the contribution of arterial pressure variability, which may simultaneously influence both cardiac and ventilatory dynamics. Notably, the comparison between model-free and model-based PID estimates reveals substantial agreement between the two approaches. The main discrepancy lies in the greater sensitivity of the model-free formulation in detecting the unique contribution of respiration to heart period dynamics. Moreover, the detected prevalence of synergy (over redundancy) observed when using the model-free approach indicates that heart period variability is predicted through a nontrivial interaction between the heart period and respiratory dynamics.

9.4. Overview and conclusions of chapter 9

Some applications of the analytical framework of PID described in Sect. 5.2 are reported in this chapter to highlight its capability to disentangle high-order interactions arising when considering groups of physiological variables. One of the central ideas of the Network Physiology framework is that physiological regulatory mechanisms do not operate solely through the response of individual organ systems to external stimulus, but encompass functional interactions among multiple systems (Ivanov, 2021). Moreover, physiological knowledge of human body regulation supports the complexity of these control mechanisms, which cannot be fully or correctly understood by examining only a limited set of systems or organs (see Sect. 6.1).

Within the growing literature on Network Physiology, several information-theoretic approaches have been employed to investigate interactions that extend beyond pairwise relationships between physiological systems. In particular, the dy-

namical OIR net-balance measure has been applied in different physiological contexts. For example, Faes et al. (2022) reported a hierarchical evaluation of cardiovascular and respiratory interactions during paced breathing, revealing the presence of redundant interactions between respiratory activity, heart period, and systolic arterial pressure, as well as a significant synergistic effect of respiration and systolic arterial pressure on heart period at very slow breathing rates. These findings indicate that when respiratory activity slows and overlaps with Mayer waves typically observed in SAP and HP, baroreflex and respiratory sinus arrhythmia mechanisms act independently in regulating heart rate variability. A similar hierarchical approach has been used to investigate human cortical dynamics, revealing a significant reduction in redundant interactions within the motor network during motor tasks in healthy subjects (Antonacci et al., 2024). In addition, a strengthening of synergistic interactions among resting-state networks – namely the default mode network, motor network, and executive control network – has been observed following rehabilitation therapy in ischemic stroke patients, with a particularly strong contribution from the motor network (Pirovano et al., 2023). More recently, the analytical framework of PIRD has been applied to separately quantify redundant and synergistic interactions within groups of physiological processes. For example, Sparacino et al. (2025c) reported a frequency-dependent redundant information exchange during postural stress when analyzing a network including cerebrovascular and cardiovascular processes.

All the studies mentioned above perform dynamical analyses of groupwise interactions among multiple physiological processes. Importantly, they employ linear parametric estimation approaches, which enable spectral analysis and facilitate the investigation of high-dimensional systems. As discussed previously, such analyses are generally not feasible with model-free approaches, which are often limited to static settings. Accordingly, most of the analyses reported in this chapter focus on physiological variables in order to investigate the presence of high-order static dependencies.

In Sect. 9.1, PID was applied to investigate within-beat relationships between MAP and both SAP and DAP. The unique, redundant, and synergistic contributions of SAP and DAP were analyzed to provide new insights into the hemodynamic determinants of MAP. The dominant role of DAP in shaping MAP, together with the observed increase in redundancy during postural stress, suggests a key contribution of DAP in maintaining hemodynamic stability during orthostatic challenge. Furthermore, the consistency between model-free and model-based definitions of redundancy supports the robustness of the PID framework and its applicability to cardiovascular analysis (Fig. 9.1). These findings not only deepen the understanding of the beat-to-beat MAP regulatory mechanisms, but also emphasize the importance of evaluating both independent contributions SAP and DAP and their

mutual interactions across different experimental settings and patho-physiological conditions, as to properly adapt the empirical formulas used in a lot of contexts to compute MAP from SAP and DAP. Improving the accuracy of MAP estimation is particularly relevant in clinical contexts – such as intensive care, anesthesia, and trauma management – where maintaining adequate perfusion is essential for patient monitoring and treatment.

In Sect. 9.2, high-order dynamics arising within a physiological network comprising cardiovascular and cardiorespiratory variables were investigated using the mixed PID estimation approach. Although the analysis is formally static, incorporating both the current and immediately preceding states of cardiac and arterial pressure signals in relation to the current ventilatory phase allows partial recovery of dynamical information. The results reveal that cardiac and vascular regulatory mechanisms are individually associated with respiration at rest and during postural stress, respectively. Moreover, these mechanisms jointly contribute to maintaining cardiovascular and cardiorespiratory homeostasis across inspiratory and expiratory phases, with a predominance of redundant interactions.

As highlighted in Sect. 4.4, high-order behaviors also effect dynamic interactions in a bivariate system, observing how conventional measures may fail to separate dependencies arising from directed interactions between systems or internal dependencies intrinsic to a single system. This limitation has been discussed for several metrics. For instance, SE – often interpreted as a measure of information storage – has been shown to reflect not only self-predictability but also causal influences from other processes (Wibral et al., 2014b). Similarly, TE may include information about the target that is not exclusively attributable to the driver but is instead co-localized with the target itself (James et al., 2016). Comparable considerations apply to other quantities involved in the PrI decomposition, such as CrossEn and cSE (Faes et al., 2015c). In this context, investigating high-order effects can also be informative in bivariate systems, allowing unique, redundant, and synergistic contributions underlying traditional coupling or causality measures to be disentangled. This issue was addressed in Saputo et al. (2026), where the PID framework was adopted to clarify whether a given information component is uniquely attributable to the target or source, or arises from redundant or synergistic interactions. The application reported in Sect. 9.3 shows that the increase in self-predictability observed during postural and mental stress is mainly driven by intrinsic heart period dynamics. Moreover, the information transferred from ventilatory to cardiac activity – and its modulation under stress – is largely associated with the synergistic dynamics of respiratory and cardiac processes. Beyond the results presented here, Saputo et al. (2026) also provided insights into well-established physiological mechanisms regulating cardiovascular dynamics. In particular, heart period variability was shown to be strongly influenced by redundant interactions with vascular dynamics, sup-

porting both the presence of central low-frequency oscillations transmitted from the brainstem to the sinus node (Koepchen, 1991) and the resonance mechanisms underlying short-term arterial pressure regulation through closed-loop interactions between systolic arterial pressure and heart period (DeBoer et al., 1987). These findings highlight the potential of the PID framework in pathological contexts, where the balance among unique, redundant, and synergistic information components may represent a sensitive marker of altered network coordination and impaired physiological adaptability. Nevertheless, it is important to highlight that application of model-free approaches has been made possible by the reduced dimensionality of the investigated problem, restricted to a bivariate setting (and not multivariate) and controlled by a proper choice of the embedding parameters.

Part IV

Applications to machine learning

Chapter 10

Information-theoretic foundations of machine learning

This chapter establishes a link between the information-theoretic analytical framework presented in the thesis and the ever-expanding field of machine learning, thus serving as an introduction to the Part IV of the thesis. Recent research indeed recognized the measures of information theory as potential tools for developing explainable ML strategies, particularly useful on high-dimensional physiological data (Chen et al., 2018; Haroutunian and Gharagyozyan, 2025).

After providing a ML overview and a categorization of its main approaches (Sect. 10.1), the probabilistic foundations of ML are recalled to highlight the common principles shared by the two fields (Sect. 10.2). To further clarify this connection, practical examples illustrating the applications of entropy-based measures to specific machine learning problems are presented, giving some examples of the biomedical research outcomes (Sect. 10.3).

10.1. Machine learning paradigms and feature representation

One of the main branches of artificial intelligence is *Machine Learning*, which can be broadly defined as the general capability of computational systems to imitate the complex learning processes of the human brain to learn patterns from data and develop algorithms that are able to gain insights (Bishop and Nasrabadi, 2006; Kerner et al., 2022). ML systems can be employed in a *descriptive* manner, to explain the observed phenomena, in a *predictive* manner, to predict future outcomes, and in a *prescriptive* manner, to support decision-making actions (Jeyanthi et al., 2022).

In recent years, the increasing availability of large-scale physiological data – driven by the widespread adoption of wearable and portable devices – together

with the development of advanced artificial intelligence approaches, has fostered the application of ML strategies in biomedical research. In particular, when integrated with approaches from the field of physiological computing – ranging from monitoring and analysis of physiological signals to the development of intervention and control systems – ML algorithms have demonstrated the ability to extract meaningful physiological insights and to identify physio-pathological conditions from data, highlighting their strong potential in clinical applications (Rush et al., 2019; Orphanidou, 2019; Rim et al., 2020).

ML methods are typically categorized into three main paradigms (Morales and Escalante, 2022): *supervised learning*, where labeled data are used to learn a mapping function between input variables and known outputs, as in a *classification* or *regression* tasks; *unsupervised learning*, where no labels are associated to the data and the objective is to uncover hidden structures in the data, for instance through *clustering* and *dimensionality reduction*; and *reinforcement learning*, where data are used to optimize the action of a system through interactions with an environment based on a reward mechanism, as in *control* and *decision-making* tasks.

Despite the different nature of the aforementioned paradigms, ML strategies are generally based on two key concepts: feature and label. The *features* provide a compact informative characterization of the observed system, while *labels* represent known outcomes or categories associated to data input. In the field of physiological signal analysis, features may correspond to temporal, spectral, or information-theoretic descriptors extracted from the signals, while labels to physio-pathological states or unknown values of the representative features.

ML paradigms critically depend on the quality and relevance of the features used to train learning modalities, strongly affecting performances and the generalization of the resulting ML models. From this viewpoint, considerable attention has been devoted to methods aimed at improving data representation by identifying or constructing the most informative features. Specifically, *Feature Extraction* (FE) transforms original features into a new feature set that better captures the underlying structure of the data in a lower-dimensional space, while *Feature Selection* (FS) focuses on identifying a subset of relevant features from the original set, thereby reducing redundancy and improving model interpretability. In addition, *Feature Importance* (FI) strategies provide a quantitative assessment of the contribution of each feature to the prediction task, enabling a deeper understanding of the model's decision-making process (Molnar et al., 2020). FS and FI approaches are particularly relevant in framework of *Explainable Artificial Intelligence* (XAI), which has become a key point of modern ML, especially in domains as healthcare, where interpretability, transparency, and trust are essential in automated prediction and decision-making (Gilpin et al., 2018).

10.2. Probability and information-theoretic foundations of machine learning

The effectiveness of a learning algorithm is intrinsically associated with the quality of the data employed during model training, thereby highlighting a fundamental connection between the mathematical foundations of ML and the fields of data analysis and statistics. In general, learning techniques are data-driven methodologies that integrate fundamental concepts from computer science with concepts drawn from statistics, probability theory, and optimization (Mohri et al., 2018).

The notion of probability introduced in Sect. 2.1 refers to the frequentistic occurrence of outcomes in a stochastic experiment. An alternative interpretation is provided by the Bayesian perspective, according to which probability is not contingent on the observations of a stochastic phenomena, but rather on the degree of beliefs of an experimenter regarding the uncertain events (Berge, 1984). Within this framework, probability serves as a formal tool for encoding assumptions about a phenomenon and for deriving inferences from such assumptions.

More broadly, this distinction reflects the difference between forward and inverse probability problems. *Forward probability problems* pertain generative models that describe a process assumed to generate observable data, and for which the objective is to determine the probability distribution or expected value of a quantity based on known model parameters. Contrarily, *inverse probability problems* concern the inference of generative models of a process based on the conditional probability of one or more of the unobserved data given the observed ones (MacKay, 2003). Such problems typically require the application of theorem of Bayes and are at the basis of the majority of ML methodologies. More specifically, let h denote a generic hypothesis whose probability is influenced by the observable variable V. *Bayes' theorem* expresses the posterior probability of the hypothesis given the observation, $p(h|V)$, as a function of both the prior probability of the hypothesis before observing V, $p(h)$, and the likelihood, $p(V|h)$, representing the probability of observing V under the assumption that h holds, i.e., (MacKay, 2003)

$$p(h|V) = \frac{p(V|h)p(h)}{p(V)}, \tag{10.1}$$

where $p(V)$ denotes the marginal probability of the observed data, thus of the evidence. In this formulation, both the prior distribution and the likelihood reflect assumptions about the hypothesis and are not determined on the basis of the observed data.

Given the central role of probabilistic reasoning on both data modeling and data uncertainty, the close relation between the frameworks of machine learning and information theory becomes evident. This perspective has led to the development of

Information Theoretic Learning (ITL), a framework that employs the information theory descriptors as non-parametric cost functions for the design of adaptive systems in unsupervised or supervised learning settings (Principe and Xu, 1999). ITL provides a general approach to ML tasks and can be regarded as a conceptual precursor to modern information-driven approaches in deep learning.

10.3. Applications of information-theoretic measures in machine learning

The principles of uncertainty and shared information – quantified through entropy-based measures – have profound implications in ML, particularly in algorithm optimization, uncertainty management, and the enhancement of decision-making processes. A central aspect underlying these tasks is the trade-off between bias and variance, which governs the balance between model flexibility and generalization. From this perspective, many ML problems can be interpreted and formulated as optimization of entropy-based functions (Hu, 2015). Among the most widely employed approaches, the *minimum description length* addresses this trade-off by minimizing the complexity of models while maintaining accuracy (Rissanen, 1978), while the use *maximum entropy models* exploits entropy maximization to derive probability distributions that best represent uncertainty in absence of prior knowledge (Jaynes, 1957).

A growing body of literature has emphasized the relevance of information-theoretic methods in ML (Amigó et al., 2015; Sepúlveda-Fontaine and Amigó, 2024; Haroutunian and Gharagyozyan, 2025). In the following, an overview of the principal entropy-based quantities and their main applications in ML is provided:

- *Shannon's entropy*, by quantifying the unpredictability of a random variable, is directly related to the concept of *information gain* (IG), i.e., the reduction in uncertainty resulting from new observations. Also related to the measure of conditional entropy, this measure plays a key role in optimization procedures, feature selection and extraction, and decision-making processes (Quinlan, 1986; Finnegan and Song, 2017; Marullo and Agliari, 2020). In biomedical research, IG has been widely applied in feature selection tasks, for instance in angiographic data for assessing the severity of coronary artery diseases (Ghasemi et al., 2020), in dermoscopic images analysis for early melanoma detection (Spolaôr et al., 2021), or in wearable physiological monitoring for the stress state prediction (Chouhan, 2026);
- *mutual information*, by quantifying the amount of information shared by two variables, enables the detection of dependencies and similarities among features. This property makes MI particularly effective in feature selection and unsupervised learning tasks (Peng et al., 2005; Haroutunian et al., 2024; Vergara and Estévez, 2014). When computed between input features and output

label variables, MI also provides valuable insights for predictive modeling. In biomedical applications, MI has been used for instance in feature selection for computer-aided diagnosis of acute pulmonary embolism (Tourassi et al., 2001) and for COVID-19 prediction using clinical data (Rayan et al., 2024), as well as in unsupervised approaches such as for brain structure segmentation from magnetic resonance images (Hu et al., 2024);

- *KL divergence*, by quantifying the discrepancy between two probability distributions defined on the same alphabet, can be used to measure the additional information needed to represent data using an approximated distribution instead of the true distribution. Due to its connection with convex optimization, KL divergence plays a central role in minimization and maximization problems, particularly in generative modeling and regularization strategies (Kingma and Welling, 2013; Draelos, 2019). In biomedical research, it has been applied to ML approaches ranging from feature optimization, e.g., for arrhythmia detection from ECG signals (Al-Shammary et al., 2024), to regularization strategies, e.g., for sleep stage classification from EEG data (Phan et al., 2020);
- *cross-entropy*, by quantifying the amount of information lost when using predicted probabilities instead of true probabilities, is widely employed in feature selection and classification tasks (Santosa, 2015; Wang and Zhu, 2021). In biomedical contexts, cross-entropy is commonly used to define training loss functions for classification stages, as in Spindelböck et al. (2021) for the aortic pathology detection from ICG signals and in Zhu et al. (2023) for the arrhythmia classification from ECG signals.

More recently, other information-theoretic functionals – as those based on *conditional mutual information* (Iovino et al., 2026) – have been found to be more effective in capturing the multivariate nature of ML problems and in accounting for high-order interaction among multiple features. Indeed, it has been demonstrated that, neglecting redundancy or failing to account for synergistic interactions can lead to reduced performance in both supervised and unsupervised learning approaches (Wollstadt et al., 2023; König et al., 2024).

10.4. Overview and conclusions of chapter 10

In recent decades, advancements in data acquisition and collection technologies, computational physiology, and artificial intelligence have led to an increasingly widespread adoption of ML methodologies in biomedical research (Wang et al., 2023; Zhang et al., 2023; Binson et al., 2024). As one of the most powerful frameworks for extracting knowledge from complex and high-dimensional data, ML provides effective tools for exploring physiological phenomena, thereby opening new avenues for understanding biological and physiological systems, as well as for sup-

porting diagnostic and prognostic decision-making. To ensure that the outcomes of both supervised and unsupervised approaches remain interpretable – especially when determining, characterizing, or predicting physio-pathological states – the integration of XAI strategies is essential (Jia et al., 2020; Band et al., 2023). In this context, approaches grounded on information theory offer a rigorous mathematical foundation of the data-driven modeling strategies employed to learn from data, enhancing both the transparency of ML algorithms and the interpretability of their outputs.

The primary objective of this chapter was to establish the conceptual bridge between information theory and machine learning, highlighting the fundamental principles shared by these two domains. Central to this connection is the concept of probability, whose dual interpretation allows to formulate and solve both forward and inverse probability problems by using entropy-based quantities (MacKay, 2003). Although the overview of ML here provided is very concise relatively to a widely expanded field, it underscores the relevance of integrating information-theoretic concepts into ML methodologies. In particular, the roles of key quantities as Shannon entropy, MI, Kullback-Leibler divergence, and cross-entropy have been briefly discussed in relation to ML tasks ranging from the feature preparation steps to both learning and model generation strategies (Sepúlveda-Fontaine and Amigó, 2024; Haroutunian et al., 2024), also accounting for some applications in biomedical research.

Recent studies have also highlighted the potential of information-theoretic methods in the development of scalable ML approaches capable of handling high-dimensional data, including those used in real-world healthcare applications (Chen et al., 2018; Haroutunian and Gharagyozyan, 2025). From this perspective, the adoption of tools that capture the multivariate nature of ML problems is essential for improving both the optimization and feasibility of ML strategies, as well as for achieving a more comprehensive characterization of the underlying phenomena. In particular, when evaluating the contribution of feature variables to class outputs, it is crucial to consider the presence of redundant and synergistic information among features. These aspects will be further examined in the following chapter, with a focus on feature management and analysis strategies, where recently proposed methods leveraging high-order information-theoretic frameworks for the characterization of complex systems are presented.

Chapter 11

Feature analysis strategies based on conditional Mutual Information measures and Partial Information Decomposition framework

This chapter focuses on ML strategies for feature analysis grounded in information theory. In particular, it considers approaches belonging to the class of filter methods, which assess feature relevance using statistical criteria independently of any specific learning algorithm (Guyon and Elisseeff, 2003). Compared to wrapper and embedded methods, these approaches are generally less computationally demanding, reduce the risk of overfitting, and offer greater scalability (Chandrashekar and Sahin, 2014).

After reviewing the principal approaches commonly adopted in the literature and highlighting their limitations in accounting for high-order interactions among features in determining the output variable (Sect. 11.1), the feature selection and feature importance methods recently introduced in Iovino et al. (2026) and Lazic et al. (2026) to address these issues are presented (Sects. 11.2 and 11.3, respectively). Finally, an alternative use of the PID framework, introduced in Barà et al. (2025b) and adapted to ML problems, is discussed (Sect. 11.4). Given that machine learning problems typically involve both continuous variables, representing the features of the system under investigation, and discrete variables, representing the class labels associated with observations, the adoption of mixed estimation approaches – such as that proposed in Barà et al. (2025a) – becomes essential. This aspect is addressed throughout the chapter.

Let us consider N observation of a set of M continuous features $\boldsymbol{F}$ and of a discrete variable C collecting the labels associated to each instance of $\boldsymbol{F}$ taking values in the set $A_C = 1, \ldots, N_C$. In the case of the FS tasks, the objective is to define a

subset of selected features $\boldsymbol{F}_s \subseteq \boldsymbol{F}$ of dimension $N \times M_s$, with $M_s \leq M$, preserving as much as possible information to have an accurate classification. Specifically, the aim is to measure the contribution of each feature $F_j \in \boldsymbol{F}$, with $j = 1, \ldots, M$, to predict the class variable c associated to each specific observation. On the other hand, in the case of FI tasks, the objective is to determine the importance of each feature F_j in explaining the class C, thus to assess its unique, redundant, and synergistic contributions in the context of all the other feature variables.

11.1. Information-theoretic approaches for feature analysis

Recent studies have introduced different criteria for evaluating and selecting feature subsets, including inconsistency rate, inference correlation, classification error, distance measures, and – as evidenced in the previous chapter – information-theoretic quantities (Vergara and Estévez, 2014). Among these, MI and CMI measures have emerged as widely adopted filtering criteria, often combined with heuristic strategies (Battiti, 1994; Guyon and Elisseeff, 2003; Wollstadt et al., 2023). MI-based FS methods are particularly popular due to their ability to capture dependencies between features and output variables (Lewis, 1992; Vergara and Estévez, 2014). However, these approaches fail to isolate the marginal contribution of individual features in determining class outputs (Wollstadt et al., 2023). A central challenge lies in handling redundant and synergistic information among features. When the information provided by a candidate feature is already captured by previously selected features, redundancy arises, reducing the efficiency of the selected feature set. Conversely, an exclusive focus on the individual contributions of features precludes the identification of synergistic effects arising from feature interactions, potentially contributing to the determination of the outputs of the class variable (Wollstadt et al., 2023; König et al., 2024; Ontivero-Ortega et al., 2025a).

Addressing these aspects is essential to select the most relevant features in complex and high-dimensional datasets. In this context, heuristic corrections, such as the *minimum Redundancy Maximum Relevance* (mRMR) (Peng et al., 2005), have been proposed to balance relevance and redundancy in the selection process. Nevertheless, a principled solution is provided by CMI, which quantifies the additional information provided by a candidate feature beyond what is already explained by selected features (Iovino et al., 2026). This makes CMI-based feature selection strategies particularly effective in complex datasets where high-order interactions among features may obscure meaningful contributions, being able to inherently capture synergistic contributions while discarding redundant ones (Tsimpiris et al., 2012; Wollstadt et al., 2023). Within this framework, methods such as the *Conditional Mutual Information with Nearest Neighbors* (CMINN) (Tsimpiris et al., 2012) and the *k-nearest neighbor Conditional Mutual Information method for Feature Selection* (kCMI-FS)

(Iovino et al., 2026) have been proposed. Both rely on the nearest-neighbor estimation strategy, but the former is designed for both continuous targets and features, whereas the latter accommodates discrete targets with continuous features.

Regarding FI approaches, numerous model-agnostic methods have been proposed to assess feature contributions. These range from error-based permutation importance tests (Breiman, 2001) and basic information-theoretic approaches (Vergara and Estévez, 2014), to more sophisticated techniques such as SHAP, based on evaluating the weighted average contribution of features across possible subsets (Lundberg and Lee, 2017). As for the FS approaches, these methods overall fail in isolating the marginal features contribution leading to potential misleading interpretations when the importance of a feature depends on the interactions with other features. To address high-order effects, König et al. (2024) proposed a model-agnostic approach that decomposes standalone, interaction, and dependency features components. However, this approach assumes continuous outputs, limiting its applicability to regression tasks. Building on this idea, Ontivero-Ortega et al. (2025a) extended the *Leave-One-Covariate-Out* (LOCO) method (Lei et al., 2018) – which traditionally evaluates the reduction in prediction error when a feature is included in a model – to enable the decomposition of such a reduction into unique, synergistic, and redundant feature contributions. The key innovation of this approach lies in the quantification of *High-order effects in Feature Importance* (Hi-Fi), which captures both marginal and interaction effects by analyzing changes in predictive performance under feature omission. Nevertheless, also this approach is mainly based on working with continuous variables and regression problems. To overcome this limitation, the Hi-Fi method has been recently reformulated in Lazic et al. (2026) within the information-theoretic framework using CMI, in order to decompose feature contribution into interpretable informational components and extending applicability to settings with discrete targets and continuous features.

In this context, recent advances in the PID framework have been proposed for disentangling unique, redundant, and synergistic contributions among features (Wollstadt et al., 2023; Sepúlveda-Fontaine and Amigó, 2024). In general, PID provides an indirect characterization of feature sets in determining a class variable by analyzing the distribution of high-order contributions across outputs of the class. Moreover, the fact that the number of information terms grows super-exponentially with the number of features poses significant challenges for representation and computation of high-order features effects. To address these limitations, the *state-PID* (sPID) framework was introduced in Barà et al. (2025b). This approach links redundant and synergistic interactions between pairs of features directly to the class variable and can be extended to all pairs of features in the dataset, enabling a compact and comprehensive characterization of high-order interaction modes in large feature sets. In this view, the sPID framework can be employed as the foundation

for an innovative feature importance strategy able to examine the role of features in a pair in determining a certain class.

11.2. Introduction to a novel feature selection strategy

In this section, the kCMI-FS proposed in Iovino et al. (2026) is detailed and the estimation approaches exploited in Barà et al. (2025a) adapted for the computation of the CMI terms employed by the searching algorithm. The proposed FS approach is also validated on a ground truth simulation setting that allows to evaluate both algorithm and estimation strategy feasibility.

11.2.1. Description of the feature selection algorithm

The proposed algorithm works through an iterative step-by-step forward selection. In the first iteration, the MI between each continuous feature F_j and the discrete variable C, i.e., $I(C;F_j)$, is computed and the feature exhibiting the highest MI value selected. The statistical significance of the selected feature is assessed by using surrogate data analysis under the null hypothesis of independence of the feature with the class. Accordingly, multiple surrogate data are generated by random shuffling the values of the candidate feature, destroying potential dependency with C, and MI computed for each of the generated data. A significance level of $\alpha = 0.05$ is fixed to define the significance threshold on the MI values distribution computed on surrogate and the original MI value compared to it (see Sect. A.2.5 of the Appendix). If the hypothesis is rejected, the candidate feature is added to the set of selected feature $\boldsymbol{F}_s$.

Subsequently, the algorithm proceeds with the computation of CMI between the class variable C and each of the remaining features $F_j \in \boldsymbol{F} \setminus \boldsymbol{F}_s$ conditioning on the already selected ones $\boldsymbol{F}_s$, i.e., $I(C;F_j|\boldsymbol{F}_s)$. In this case, the feature with the highest CMI is selected and its significance tested through surrogate data analysis, always with a significance level of $\alpha = 0.05$ (see Sect. A.2.5 of the Appendix). Also in this case the null hypothesis of independence between the class variable C and the selected features $\boldsymbol{F}_s$ is tested. The evaluation process is repeated iteratively, until no additional features present statistically significant MI with the class variable when conditioning on the already selected features, thus ensuring the final set $\boldsymbol{F}_s$.

11.2.2. Estimation strategy

MI and CMI terms involved in the iterative searching algorithm are practically computed by means of the mixed estimation strategy detailed in Sect. 5.2.2. Specifically, to perform the first step of the proposed FS approach, i.e., for estimating the MI terms $I(C;F_j)$, k nearest neighbors are searched for each item of the feature variable

$f_j \in F_j$ among the N_c samples associated the class c, i.e., $\{f_j^c\}$, to which the sample is associated. Denoting with d_c the distance between the specific observation f_j and its k^{th} neighbor considering the samples $\{f_j^c\}$, m_{F_j} indicates the number of samples falling within the distance d_c in the space of all possible sample $\{f_j\}$. Accordingly, the specific MI term between the outcome c of the class variable and the feature variable F_j is obtained as:

$$\hat{I}(C = c; F_j) = \psi(N) + \psi(k) - \psi(N_c) - \frac{1}{N_c} \sum_{\{f_j^c\}} \psi(m_{F_j} + 1). \tag{11.1}$$

For estimating CMI measures, the nearest neighbor search is performed in the space $\{F_j\ \boldsymbol{F}_s\}$ for each observation attributed to the class c, i.e., $\{(f_j\ \boldsymbol{f}_s)^c\}$. A number of samples $m_{F_j \boldsymbol{F}_s}$ is counted within the same range in the space considering all possible samples, while $m_{\boldsymbol{F}_s}$ and $m^c_{\boldsymbol{F}_s}$ samples are counted in the space $\boldsymbol{F}_s$ accounting for all samples or only those attributed to the class c, respectively, thus obtaining:

$$\hat{I}(C = c; F_j | \boldsymbol{F}_s) = \psi(k) + \frac{1}{N_c} \sum_{\{(f_j \boldsymbol{f}_s)^c\}} \left(\psi(m_{\boldsymbol{F}_s} + 1) - \psi(m^c_{\boldsymbol{F}_s} + 1) - \psi(m_{F_j \boldsymbol{F}_s} + 1) \right). \tag{11.2}$$

We refer to Iovino et al. (2026) for further details on the adaptation of the mixed estimation approach for the proposed FS strategy.

11.2.3. *Validation on a set of known relevant and irrelevant features*

In this section, the validation study reported in Iovino et al. (2026) is reported to assess the feasibility of the proposed FS algorithm. The reported simulation setting also allows to know theoretical values of MI and CMI involved measures, thus enabling the evaluation of the performance of the mixed approach in terms of estimation bias and variance.

Let us consider two uniformly distributed continuous variables, $W_1 \sim \mathcal{U}(a, b)$ and $W_2 \sim \mathcal{U}(c, d)$, with $a, c < 0 < b, d$, and a third normally distributed continuous variable with zero mean and variance σ^2, $W_3 \sim \mathcal{N}(0, \sigma^2)$. The three feature variables are assumed to be independent. A binary class variable is defined as the Boolean AND logic-gate, i.e., $C = \Theta(W_1) \cdot \Theta(W_2)$, with Θ the Heaviside function. A realistic classification scenario is simulated by defining three feature variables as follows: $F_1 = W_1$, $F_2 = W_2 + W_3$, and $F_3 = W_3$. Accordingly, F_1 represents a relevant feature to the class variable, F_2 a noisy combination of relevant and irrelevant features, while F_3 is a fully irrelevant feature.

The theoretical values expected from the FS process from each iteration are computed and compared with the estimates derived from 1000 realizations generated using a set of fixed parameters for the variables W_1 and W_2, i.e., $a = -1.5$, $b = 0.5$, $c = -0.5$, and $d = 0.5$, and by varying the parameter σ related to the variable W_3

from 0 to 3 with a step of 0.1. Moreover, the performance of the estimation strategy in this ML framework is assessed by using different values of the parameter $k = \{2, 5, 10, 20\}$. The procedure is repeated across 100 simulations, enabling the estimation of the confidence intervals of each measure.

Fig. 11.1 shows the results of MI and CMI measures in terms of estimation accuracy as a function of both the noise level σ and the estimation parameter k. By following the proposed selection algorithm, the first step involved the computation of the MI between the outcome of the class variable C and the one of each of the feature variables, i.e., $I(C; F_i)$, $i \in \{1, 2, 3\}$ (panels (*a*)-(*c*)). It is observed that only F_1 and F_2 contain information present in the class variable resulting in positive MI values. Moreover, due to the influence of the noisy variable, $I(C; F_2)$ decreases at increasing noise level, while $I(C; F_1)$ maintains a high constant value. As expected, being F_3 independent of the class variable, $I(C; F_3)$ is always around zero. Accordingly, at the first iteration, F_1 is selected, i.e., $\boldsymbol{F}_s = \{F_1\}$. In the following iterations, the CMI quantities between the class variable C and each remaining features $I(C; F_j|F_1)$, $j = \{2, 3\}$, are computed (panels (*d*) and (*e*)). Being F_3 independent from C, it remains independent also when conditioning on X_1, thus F_2 is selected in the iteration resulting in $\boldsymbol{F}_s = \{F_1, F_2\}$. The searching process thus ends with the computation of the CMI $I(C; F_3|F_1, F_2)$ (panel (*f*)).

The results depicted in Fig. 11.1 demonstrate how, at increasing the level of noise σ, the relevance of the feature F_2 progressively decreases, thus making it difficult the determination of the outcome associated with the class variable C, that depends on both W_1 and W_2. Moreover, it is important to note that, while the values of $I(C; F_3)$ and $I(C; F_3|F_1)$ remain low, being F_3 not affected by the confounding effect introduced by F_3 (panels (*c*) and (*e*)), after the selection of both F_1 and F_2, also $I(C; F_3|F_1, F_2)$ appears influenced by σ, with an increase for low noise levels, as F_3 does not help in recover the original knowledge of F_2, and decreasing for high noise levels, as the confounding effect of W_3 in F_2 begins dominating, making it progressively more independent of W_2 (panel (*f*)).

As regards the effect of the number of neighbors, it is observed that it does not substantially alter the estimated MI and CMI trends. However, when considering $I(C; F_3|F_1, F_2)$, the parameter k influences the magnitude of the estimation bias, with larger neighborhoods leading to greater underestimation of the theoretical value. Such effects are consistent with known limitations of the nearest neighbor estimation approach exacerbated by the increasing dimensionality in the larger joint searching space. Values of k equal to 5 or 10 seem to represent the best tradeoff between estimation stability, with low standard deviation across repetitions, and sensitivity to fine-scale dependencies.

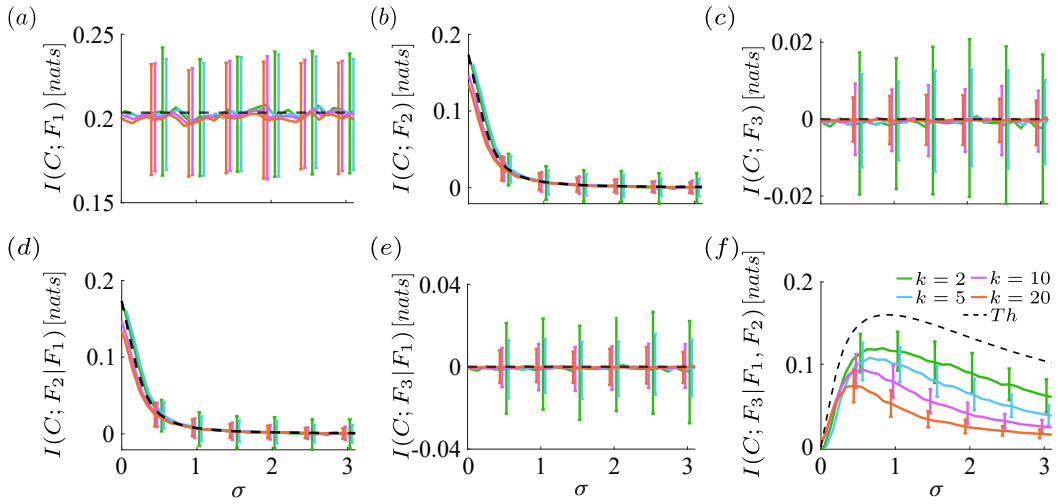

Figure 11.1: Theoretical (dashed lines) and errorplots (MEAN ± 2STD over the realizations) of the estimated MI (panels (*a*)-(*c*))) and CMI (panels (*d*)-(*f*)) for the AND logic-gate as a function of the noise level σ for different values of the parameter k. The figure was modified from Iovino et al. (2026).

11.3. Introduction to a novel feature importance strategy

This section presents the FI strategies introduced in Lazic et al. (2026) adapting the Hi-Fi method to the information-theoretic framework. After describing the proposed greedy algorithm, details on the practical computational steps are provided. Moreover, a couple of validation studies are reported in which the unique, redundant, and synergistic contribution of both Gaussian and non-Gaussian feature sets is investigated.

11.3.1. Description of the feature importance algorithm

Being interested in investigating the importance of the feature variable F_j in determining the class variable C beyond the information brought by the remaining features $\boldsymbol{F}_{\setminus j}$, the CMI measure $I(C;F_j|\boldsymbol{F}_{\setminus j})$ can be computed. This measure was investigated in (Wollstadt et al., 2023) in terms of PID, showing that it collects both unique contribution of the investigated feature and the synergistic effects related to the presence of the other features. To disentangle the unique contribution of F_j in determining C from that deriving from its redundant and synergistic interaction with the variables in $\boldsymbol{F}_{\setminus j}$, the searching approach introduced in Ontivero-Ortega et al. (2025a) in terms of predictability measures is here translated in terms of information-theoretic measures. Specifically, the set of variables in $\boldsymbol{F}_{\setminus j}$ that minimize or maximize the CMI between F_j and C are searched as to allow for the following decomposition:

$$I(C;F_j|\boldsymbol{F}_{\setminus j,max}) = S(C;F_j|\boldsymbol{F}_{\setminus j}) + R(C;F_j|\boldsymbol{F}_{\setminus j}) + U(C;F_j|\boldsymbol{F}_{\setminus j}), \tag{11.3}$$

where the synergistic, redundant and unique contributions can be respectively expressed as:

$$S(C; F_j|\boldsymbol{F}_{\setminus j}) = I(C; F_j|\boldsymbol{F}_{\setminus j,max}) - I(C; F_j), \tag{11.4a}$$

$$R(C; F_j|\boldsymbol{F}_{\setminus j}) = I(C; F_j) - I(C; F_j|\boldsymbol{F}_{\setminus j,min}), \tag{11.4b}$$

$$U(C; F_j|\boldsymbol{F}_{\setminus j}) = I(C; F_j|\boldsymbol{F}_{\setminus j,min}) \tag{11.4c}$$

In order to reduce the computational cost, a greedy approach is adopted to obtain $\boldsymbol{F}_{\setminus j,min}$ and $\boldsymbol{F}_{\setminus j,max}$. Specifically, for determining $\boldsymbol{F}_{\setminus j,min}$, the procedure initializes an empty subset of selected feature $\boldsymbol{F}_0 = \emptyset$ that is then filled at any given step s, with $s = 1, \ldots, M-1$, with the variable $V_s \in \boldsymbol{F}_{\setminus j} \setminus \boldsymbol{F}_{s-1}$ determined such that

$$V_s = \underset{V \in \boldsymbol{F}_{\setminus j} \setminus \boldsymbol{F}_{s-1}}{\arg\min}\, I(C; F_j|\boldsymbol{F}_{s-1}, V). \tag{11.5}$$

If the CMI measure $I(C; F_j|\boldsymbol{F}_{s-1}, V_s)$ is significantly lower than $I(C; F_j|\boldsymbol{F}_{s-1})$ according to surrogate data testing strategy, the feature V_s is retained and the set of selected features updated as $\boldsymbol{F}_s = \{\boldsymbol{F}_{s-1}, V_s\}$; otherwise, if the computed CMI is not significantly lower than that computed at the previous step, V_s is discarded and the search terminates with $\boldsymbol{F}_{\setminus j,min} = \boldsymbol{F}_{s-1}$.

In the case of the $\boldsymbol{F}_{\setminus j,max}$ search, the search start from an empty set $\boldsymbol{F}_0 = \emptyset$ and at each step $s \geq 1$, the selected feature $V_s \in \boldsymbol{F}_{\setminus j} \setminus \boldsymbol{F}_{s-1}$ is determined such that

$$V_s = \underset{V \in \boldsymbol{F}_{\setminus j} \setminus \boldsymbol{F}_{s-1}}{\arg\max}\, I(C; F_j|\boldsymbol{F}_{s-1}, V). \tag{11.6}$$

If the CMI measure $I(C; F_j|\boldsymbol{F}_{s-1}, V_s)$ is significantly higher than $I(C; F_j|\boldsymbol{F}_{s-1})$, the feature V_s is used to update the set of selected feature $\boldsymbol{F}_s = \{\boldsymbol{F}_{s-1}, V_s\}$; contrarily, the search terminates and $\boldsymbol{F}_{\setminus j,max} = \boldsymbol{F}_{s-1}$. After determining both $\boldsymbol{F}_{\setminus j,min}$ and $\boldsymbol{F}_{\setminus j,max}$, the MI and CMI quantities appearing in Eqs. 11.4 can be computed, and used to retrieved unique, redundant, and synergistic features contributions.

As regards the statistical analysis performed to stop the iterative search of $\boldsymbol{F}_{\setminus j,min}$ and $\boldsymbol{F}_{\setminus j,max}$, the statistical analysis of the difference between $I(C; F_j|\boldsymbol{F}_{s-1}, V_s)$ and $I(C; F_j|\boldsymbol{F}_{s-1})$ is performed to test the null hypothesis that the candidate feature V_s does not alter the conditional information shared by C and F_j given $\boldsymbol{F}_{s-1}$, as that if the null hypothesis is verified, V_s will not be included in the sets of selected variables and the search ends. Specifically, the significance of the differences $I(C; F_j|\boldsymbol{F}_{s-1}, V_s) - I(C; F_j|\boldsymbol{F}_{s-1})$ and $I(C; F_j|\boldsymbol{F}_{s-1}) - I(C; F_j|\boldsymbol{F}_{s-1}, V_s)$ respectively tested for determining $\boldsymbol{F}_{\setminus j,max}$ and $\boldsymbol{F}_{\setminus j,min}$, respectively. Accordingly, multiple surrogate data were generated by random shuffling the candidate feature F_s, producing a distribution of surrogate values of the difference measures, so that, if the original measure exceeds a percentile-based threshold defined on the distribution evaluated

on the surrogate data with a significance level of $\alpha = 0.05$, the difference is deemed as significant and the candidate feature add to the set (see Sect. A.2.5 of the Appendix).

11.3.2. *Estimation strategies*

In this section, two mixed estimation approaches are adjusted to the investigated FI strategy, one based on the Gaussianity and the other based on the already employed nearest-neighbor strategy. Mathematical details and extended derivation of the estimate formulations are reported in Lazic et al. (2026).

Gaussian-based framework

In the Gaussian-based framework assumes that, for a given discrete realization of the class variable $C = c$, the underlying joint conditioned space $\{F_j, \boldsymbol{F}_{\setminus j}|C = c\}$ follows a multivariate Gaussian distribution. Accordingly, the joint probability distribution $p(F_j, \boldsymbol{F}_{\setminus j})$ is a Gaussian Mixture Model (GMM) related to both class probability occurrence and conditional probability densities, i.e.,

$$p(F_j, \boldsymbol{F}_{\setminus j}) = \sum_{c \in A_C} p(c) p(F_j, \boldsymbol{F}_{\setminus j}|c). \tag{11.7}$$

To proceed with the feature importance strategy proposed above, the CMI measures

$$\begin{aligned} I(C; F_j|\boldsymbol{F}_{\setminus j}) &= \sum_{c \in A_C} p(c) I(C = c; F_j|\boldsymbol{F}_{\setminus j}) \qquad (11.8a) \\ &= \sum_{c \in A_C} p(c) \int_{\mathcal{D}_{F_j}} \int_{\mathcal{D}_{\boldsymbol{F}_{\setminus j}}} p(f_j, \boldsymbol{f}_{\setminus j}|c) \log \left(\frac{p(\boldsymbol{f}_{\setminus j}) p(f_j, \boldsymbol{f}_{\setminus j}|c)}{p(f_j, \boldsymbol{f}_{\setminus j}) p(\boldsymbol{f}_{\setminus j}|c)} \right) df_j d\boldsymbol{f}_{\setminus j} \end{aligned}$$

need to be computed, with all the terms, apart from $p(c)$, representing the density for either a multivariate Gaussian distribution or a GMM. Since closed-form expressions for the individual specific cross-entropy terms, specifically $H_{F_j, \boldsymbol{F}_{\setminus j}|c}(F_j, \boldsymbol{F}_{\setminus j})$ and $H_{F_j, \boldsymbol{F}_{\setminus j}|c}(\boldsymbol{F})$, are not available, the high-precision numerical Monte Carlo (MC) estimation approach (Metropolis and Ulam, 1949) is used by approximating

$$\hat{I}(C = c; F_j|\boldsymbol{F}_{\setminus j}) = \mathbb{E}_{p_{f_j \boldsymbol{f}_{\setminus j}|c}} \left[\log \frac{p(\boldsymbol{f}_{\setminus j}) p(f_j, \boldsymbol{f}_{\setminus j}|c)}{p(f_j, \boldsymbol{f}_{\setminus j}) p(\boldsymbol{f}_{\setminus j}|c)} \right]. \tag{11.9}$$

To obtain this estimate, many samples are drawn from the conditional distribution space $\{F_j, \boldsymbol{F}_{\setminus j}|C = c\}$ and the log-ratio expression in Eq. 11.9 computed for each sample. The MC estimate of $I(C = c; F_j|\boldsymbol{F}_{\setminus j})$ is then obtained as the average of these expressions across all sample instances.

In this section, MI and CMI terms involved in the algorithm are computed by using the mixed estimation approach detailed in Sect. 5.2.2. Considering the generic step j of the searching algorithm for both $\boldsymbol{F}_{\setminus j,min}$ and $\boldsymbol{F}_{\setminus j,max}$, the CMI terms $I(C;F_j|\boldsymbol{F}_{s-1},V)$ and $I(C;F_j|\boldsymbol{F}_{s-1})$ have to be computed for quantifying the variation in the predictive improvement brought by the candidate variable. Specifically, the values associated with specific outcomes of the class variable C are computed and then averaged according to the occurrence of probability of the samples associated to the different outcomes. Accordingly, for each sample the k^{th} neighbor is searched in the highest-dimensional space $\{F_j,\boldsymbol{F}_{s-1},V\}$ for the samples associated to the class c, i.e., $\{(f_j\boldsymbol{f}_{s-1}v)^c\}$, and then the distance d_c between the specific observation and the detected neighbor is projected in the lower-dimensional spaces $\{\boldsymbol{F}_{s-1},V\}$, $\{F_j,\boldsymbol{F}_{s-1}\}$, and $\{\boldsymbol{F}_{s-1}\}$ to count the samples falling within the distance d_c. Specifically, $m_{\boldsymbol{F}_{s-1}V}$ and $m^c_{\boldsymbol{F}_{s-1}V}$ are counted in the space $\{\boldsymbol{F}_{s-1},V\}$, $m_{F_j\boldsymbol{F}_{s-1}}$ and $m^c_{F_j\boldsymbol{F}_{s-1}}$ in the space $\{F_j,\boldsymbol{F}_{s-1}\}$, and $m_{\boldsymbol{F}_{s-1}}$ and $m^c_{\boldsymbol{F}_{s-1}}$ in the space $\{\boldsymbol{F}_{s-1}\}$ when respectively account for all samples or only those associated to $\{C=c\}$. Moreover, the number of samples $m_{F_j\boldsymbol{F}_{s-1}V}$ falling within d_c when considering all samples in the space $\{F_j,\boldsymbol{F}_{s-1},V\}$ are also counted. In this manner, the following estimation formulas are obtained:

$$\begin{aligned}\hat{I}(C=c;F_j|\boldsymbol{F}_{s-1},V) = \psi(k) + \frac{1}{N_c}\sum_{\{(f_j\boldsymbol{f}_{s-1}v)^c\}}(\psi(m_{\boldsymbol{F}_{s-1}V}+1)\\ -\psi(m_{F_j\boldsymbol{F}_{s-1}V}+1)-\psi(m^c_{\boldsymbol{F}_{s-1}V}+1)),\end{aligned} \tag{11.10a}$$

$$\begin{aligned}\hat{I}(C=c;F_j|\boldsymbol{F}_{s-1}) = \frac{1}{N_c}\sum_{\{(f_j\boldsymbol{f}_{s-1}v)^c\}}(\psi(m_{\boldsymbol{F}_{s-1}}+1)+\psi(m^c_{F_j\boldsymbol{F}_{s-1}}+1)\\ -\psi(m_{F_j\boldsymbol{F}_{s-1}}+1)-\psi(m^c_{\boldsymbol{F}_{s-1}}+1)).\end{aligned} \tag{11.10b}$$

As mentioned above, the first step for the determination of $\boldsymbol{F}_{\setminus j,min}$ is the computation and the significance assessment of the MI term $I(C;F_j)$. Therefore, the specific MI quantity is obtained as

$$\hat{I}(C=c;F_j) = \psi(N)-\psi(N_c)+\psi(k)-\frac{1}{N_c}\sum_{\{f^c_j\}}\psi(m_{F_j}+1), \tag{11.11}$$

where k now denotes the number of neighbors searched in the space $\{F_j\}$ when considering samples attributed to the class variable c and m_{F_j} indicates the number of samples counted when considering all the samples in the space $\{F_j\}$, and then averaged across the outcomes of the class variable.

Once $\boldsymbol{F}_{\setminus j,min}$ and $\boldsymbol{F}_{\setminus j,max}$ are identified, the MI and CMI terms appearing in Eqs. 11.4 have to be computed again considering as neighbor search space $\{F_j,\boldsymbol{F}_{\setminus j,min}\cup$

$\boldsymbol{F}_{\setminus j,max}\}$. To this aim, Eqs. 11.10 are employed by replacing $\boldsymbol{F}_{s-1}$ with $\boldsymbol{F}_{\setminus j,min}$ and $\boldsymbol{F}_{\setminus j,max}$.

11.3.3. Validation on Gaussian and non-Gaussian simulated features

In this section, the validation studies reported in Lazic et al. (2026) to assess the validity of the FI strategy on both Gaussian and non-Gaussian simulated sets of features are shown. In both settings, the unique, redundant, and synergistic contributions of the features in determining a class variable are known a priori; in the first setting, a direct comparison with the theoretical values is also possible.

Validation on Gaussian simulated features

Let us consider a 2-class variable C, i.e., $A_C = \{c_1, c_2\}$, and a set of 6 features, i.e., $\boldsymbol{F} = \{F_1, \ldots, F_6\}$, that are assumed to have a multivariate Gaussian distribution when associated with each specific outcome of the class variable, i.e., $\boldsymbol{F}|c \sim \mathcal{N}(\mu_{\boldsymbol{F}}^{(c)}, \Sigma_{\boldsymbol{F}}^{(c)})$ with $\mu_{\boldsymbol{F}}^{(c)}$ and $\Sigma_{\boldsymbol{F}}^{(c)})$ the mean vector and covariance of $\boldsymbol{F}$ evaluated when $C = c$. By imposing changes in the mean and the variance of the feature variables across the outputs of the class is possible to induce behaviors that elicit specific manner contributions for the feature set. For instance, by changing the mean of a feature variable across class states, i.e., by imposing different values of $\mu_{\boldsymbol{F}_j}^{(c)}$ when varying c, the relevant contribution of F_j is set, while different levels of high-order features interactions are determined by changing the off-diagonal element of the covariance matrix $\Sigma_{\boldsymbol{F}}^{(c)}$; no contributions are evidenced for features that do not present changes of both mean and variance across outputs of the class variable. In the case of the

simulated setting, the system is characterized by the following model parameters:

$$
\begin{aligned}
&p(c_1) = p(c_2) = 0.5,\\
&\mu_{\boldsymbol{F}^{(c_1)}} = [1, 0.5, 0.5, 0, 1, 0],\\
&\mu_{\boldsymbol{F}^{(c_2)}} = [-1, -0.5, -0.5, 0, -1, 0],\\
&\Sigma_{\boldsymbol{F}^{(c_1)}} = \begin{bmatrix} 1 & 0 & 0 & 0 & 0 & 0\\ 0 & 1 & 0.25 & 0 & 0 & 0\\ 0 & 0.25 & 1 & 0 & 0 & 0\\ 0 & 0 & 0 & 1 & 0.5 & 0\\ 0 & 0 & 0 & 0.5 & 1 & 0\\ 0 & 0 & 0 & 0 & 0 & 1 \end{bmatrix},\\
&\Sigma_{\boldsymbol{F}^{(c_2)}} = \begin{bmatrix} 1 & 0 & 0 & 0 & 0 & 0\\ 0 & 1 & 0.25 & 0 & 0 & 0\\ 0 & 0.25 & 1 & 0 & 0 & 0\\ 0 & 0 & 0 & 1 & -0.5 & 0\\ 0 & 0 & 0 & -0.5 & 1 & 0\\ 0 & 0 & 0 & 0 & 0 & 1 \end{bmatrix},
\end{aligned}
\tag{11.12}
$$

for which the feature F_1 exhibits different class-specific mean remaining uncorrelated with the other features; F_2 and F_3 have the same different class-specific means and additionally display a positive correlation for both realizations of C; while F_4 does not exhibit a change in the class-specific mean, F_5 does, and they jointly have a class-dependent covariance value; the feature F_6 has no class-specific change in the probability distribution and is uncorrelated with the other features.

The knn-based estimation method was applied over simulations lasting $N_c = 1000$ samples per realization $C = c$, considering the typical setting $k = 10$ for the number of neighbors. Moreover, the statistical significance of the selected variables was tested generating one-hundred surrogate sequences. The simulation was repeated one-hundred times to assess the confidence intervals of each measure. In this setting, the Gaussian-based framework was employed to determine theoretical values using 10^6 samples for each realization $C = c$.

Fig. 11.2 shows how expected contributions are observed for the simulated setting. Specifically, the change in the mean value across the class outputs for F_1, F_2, F_3, and F_5 is reflected in the unique contribution of that feature variable, with higher magnitude for F_1 and F_5 that present the largest mean change. Presenting a similar class-dependent change in the mean, these latter also exhibit a partially redundant contribution, even if these are not related to each other or with F_2 and F_4 that indeed are correlated to each other resulting in a redundant contribution. Moreover, a synergistic contribution is detected for F_4 and F_5, due to the change in the correlation sign across the outputs of the class. Finally, being the probability density of

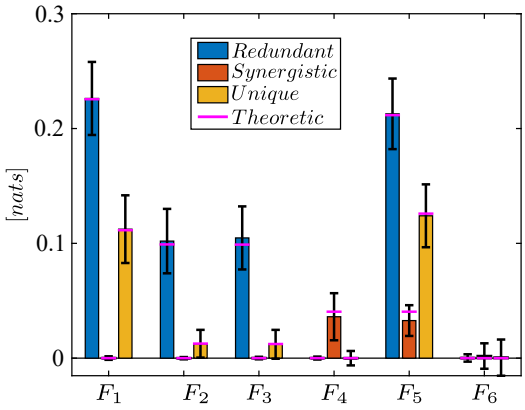

Figure 11.2: Barplots (mean ± 2std) of the unique, redundant and synergistic components of the maximum information shared between the binary class variable C and the features F_j, $j = 1, \dots, 6$; magenta lines represent the theoretical values. The figure was modified from Lazic et al. (2026).

F_6 independent from class and being uncorrelated with the other features, this does not present any contribution. As regards the accuracy of the estimation approach, it can be observed how it is quite higher, with small bias and limited variance of the different contributions across the multiple simulations.

Fig. 11.3 reports the selection of the variables included into the conditioning sets $\boldsymbol{F}_{\setminus j,min}$ and $\boldsymbol{F}_{\setminus j,max}$ during the search for redundant and synergistic contributions to the class outputs. Moreover, Fig. 11.4 shows the order according to which these variables are selected in the iterative procedure. As expected from the marginal predictive capability of these features, it can be observed how the F_1, F_2, F_3 or F_5 are selected into the conditioning set $\boldsymbol{F}_{\setminus j,min}$ when one of them is taken as source variable (Fig. 11.3(a)), in an order generally prioritizing F_1 and F_5 followed by F_2 and F_3 (Fig. 11.4(a)). Moreover, F_4 is also included theoretically into the set $\boldsymbol{F}_{\setminus j,min}$ when F_1, F_2, or F_3 are taken as selected features. In the practical estimation, this selection occurred only in a fraction of realizations (89%, 16% and 17% for F_1, F_2, and F_3, Fig. 11.3(a)) and at the third or fourth iteration of the searching procedure (Fig. 11.4(a)). The inclusion of F_4 is less simple to explain and is related to its synergistic interaction with F_5, indeed its selection along with F_5 further decreases the CMI. As regards the determination of $\boldsymbol{F}_{\setminus j,max}$, the selection involves F_4 and F_5, which are always reciprocally included into $\boldsymbol{F}_{\setminus j,max}$ at the first iteration (Fig. 11.3(b), Fig. 11.4(b)). This selection is meaningful as it relates to the synergistic contribution to the outputs of the class variable C expected for the features F_4 and F_5.

Validation on non-Gaussian simulated features

Let us consider four independent uniformly distributed random feature variables $F_i \sim \mathcal{U}(-1, 1)$, $i \in \{1, \dots, 4\}$ and a class discrete variable generated as $C = \Theta(F_1 \cdot F_2) + \Theta(F_3) + \Theta(F_4)$, where $\Theta(\cdot)$ is the Heaviside function, resulting in values belonging

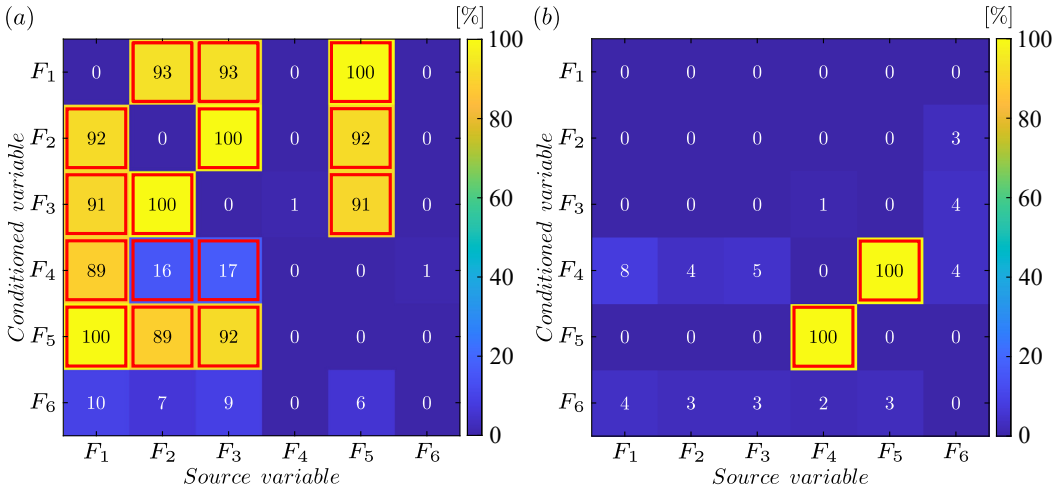

Figure 11.3: Heatmaps showing, for any source variable (columns), the selection of the conditioning variables (rows; cells with red border: theoretical selection; cell color and number: percentage of selections over one-hundred realizations) included within the set $\boldsymbol{F}_{\setminus j,min}$ (panel (*a*)) and within the set $\boldsymbol{F}_{\setminus j,max}$ (panel (*b*)). The figure was modified from Lazic et al. (2026).

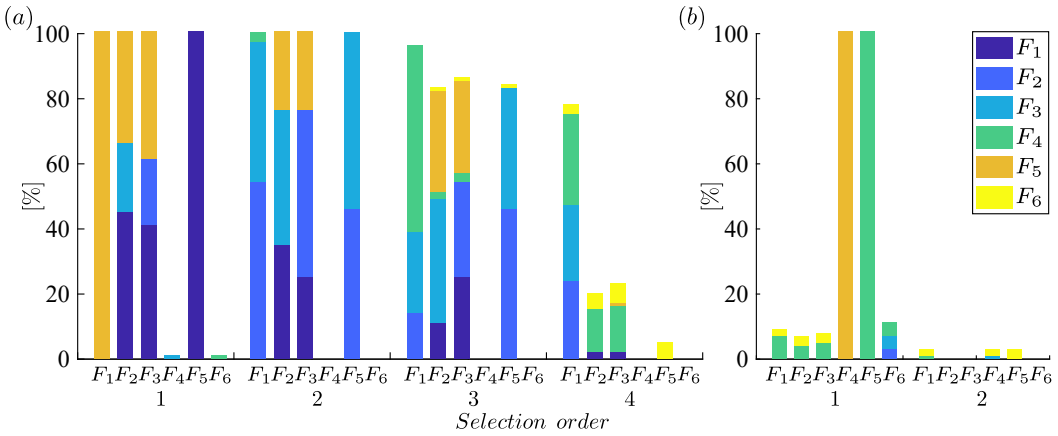

Figure 11.4: Order and percentage of occurrence of the features selected as conditioning variables for the MI between each source feature and the target class during the search for redundancy (panel (*a*), inclusion into $\boldsymbol{F}_{\setminus j,min}$) and synergy (panel (*b*), inclusion into $\boldsymbol{F}_{\setminus j,max}$). The height of each bar quantifies the percentage of times over one-hundred realizations for which a variable was selected for the source feature F_j, $j = 1, \ldots, 6$ at each iteration $s \in \{1, 2, \cdots\}$. The color information represents which variable was selected. The figure was modified from Lazic et al. (2026).

to $A_C = 0, 1, 2, 3$. In assessing the feasibility of the investigated feature importance strategy, two additional features are accounted for defines as $F_5 = F_4 + N$, with $N \sim \mathcal{N}(0, 1)$ and $F_6 \sim \mathcal{U}(-1, 1)$, thus being the former a noisy version of F_4 and the latter an independent feature. Accordingly, it is expected to observe a synergistic contribution of F_1 and F_2, as these interact like in the XOR logic-gate (see Sect. 5.2.3), and a unique contribution of both F_3 and F_4. Moreover, due to the additive nature of the relation generating the class variable C, a synergistic contribution among these four feature variables is expected. Contrarily, as regards the feature F_5, being a noisy version of F_4, is expected to share with it some redundant information, while F_6 is expected to not contribute at all with the class variable.

In this case, the knn-based estimation method was applied over one-hundred realization of the simulation of both $N = 300$ and $N = 1000$ samples and fixing again $k = 10$ for the number of neighbors. Moreover, the statistical significance of the selected variables was tested generating one-hundred surrogate set of features (see Sect. A.2.5 of the Appendix).

Fig. 11.5 confirms the expected synergistic contributions of F_1 and F_2, as well as the unique contribution of both F_3 and F_4; moreover, the redundant contribution of F_4 due to the presence of F_5 is observed. Furthermore, the synergistic contribution related to the additive effect of the features in determining the class C is found. No significant differences are reported for the results obtained with different realization lengths, even if the synergistic contribution appears less evident by decreasing N.

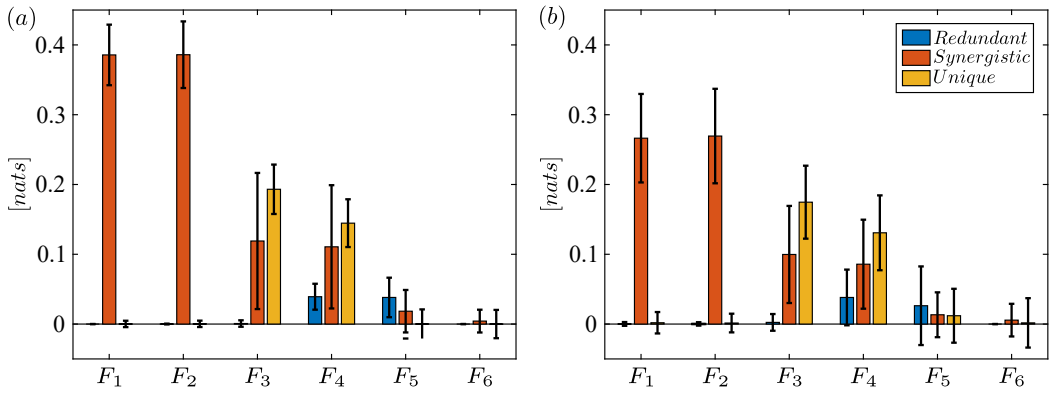

Figure 11.5: Barplots (MEAN ± 2STD across realizations lasting 1000 (panel (*a*)) and 300 (panel (*b*)) samples) of the unique, redundant and synergistic components of the maximum information shared between the four-class variable C and the six features F_j, $j = 1, \ldots, 6$. The figure was modified from Lazic et al. (2026).

11.4. A machine learning approach based on the Partial Information Decomposition framework

As introduced in Sect. 11.1, an alternative approach that can be used to exploit high-order contributions of multiple features in determining a class variable is grounded

in the PID framework. In this section, the recently introduced sPID framework (Barà et al., 2025b) is described and validated in a simulation setting.

11.4.1. *state Partial Information Decomposition framework and estimation strategy*

By considering the class (here also referred to as state) C associated with an investigated network system described by a large set of features $\boldsymbol{F} = \{F_1, \ldots, F_M\}$, the sPID framework quantifies the unique, redundant, and synergistic contributions of these features to the class variable C. Specifically, by treating the class variable C as a discrete-valued target variable V and the set of features $\boldsymbol{F}$ as continuous-valued source variables $\boldsymbol{W} = \{W_1, \ldots, W_M\}$, the PID framework described in Sect. 5.2 can be employed to investigate the mood of interaction between Y and pairs of variables taken from $\boldsymbol{W}$.

Accordingly, the bivariate PID setting is used to characterize the high-order contributions of a pair of features F_i and F_j in determining the class C, which is representative of the overall state of the investigated system. This analysis can be extended to all possible pairs of features in the set, thereby providing a set of measures that lead to a network-based representation of how pairs of features influence the class variable through unique and high-order contributions. The main peculiarities of the sPID are the explicit separation of redundant and synergistic contributions enabled by PID, together with the possibility of assessing how such contributions affect individual outcomes of the class variable through a state-specific analysis. Indeed, the redundant contribution in Eq. 5.7 can be reformulated to account for specific values of the target variable $V = v$, i.e.,

$$I_\cap(V = v; W_\alpha) = \min_{s \in \alpha} I(V = v; W_s), \tag{11.13}$$

and, consequently, also the PI terms in Eq. 5.6 can be expressed with respect to specific outcomes of the target, i.e.,

$$I_\delta(V = v; W_\alpha) = I_\cap(V = v; W_\alpha) - \sum_{\beta \prec \alpha} I_\delta(V = v; W_\beta). \tag{11.14}$$

Within the ML framework, this formulation enables a characterization of the high-order interactions between pairs of feature variables in determining the class variable C by explicitly accounting for their contributions to each specific outcome of the target variable. Moreover, as evidenced for the other ML strategies discussed in the chapter, the computational reliability of the proposed approach depends on the possibility of using the recently proposed estimator for PID that works with discrete target and continuous source variables (Barà et al., 2025a).

11.4.2. Validation on multiple features system

A network system based on the Boolean OR logic-gate was simulated. Considering two independent and uniformly distributed random variables $F_1 \sim \mathcal{U}(a, b)$ and $F_2 \sim \mathcal{U}(c, d)$ with $a = c = -0.5$ and $b = d = 0.5$, the target variable is obtained as $C = \max\{\Theta(F_1), \Theta(F_2)\}$, with $\theta(\cdot)$ the Heaviside function, therefore resulting in $Y = 1$ if at least one of the two feature variable is positive and $Y = 0$ only when both features are non-positive. Additional feature variables were generated by progressively weakening the statistical dependence of one of F_1 with C while maintaining invariant the feature F_2. Specifically, five additional feature variables $F_3, \ldots, F_7$ were obtained by replacing an increasing percentage (20%, 40%, 60%, 80%, and 100%, respectively) of samples of F_1 with random values drawn from the same uniform distribution.

Fifty independent realizations of the system were generated, each consisting of variables with 10000 samples. The sPID framework was then applied by computing, for all possible pairs of feature variables – corresponding to $7 \times 7 = 49$ combinations – the decomposition terms about the information provided about C using the KSG estimation approach described above, with the parameter set to $k = 5$.

Fig. 11.6 presents the average across the realizations of the joint MI (panel (*a*)), the cumulative unique contribution (panel (*b*)) – defined as the sum of the two unique terms – the synergistic contribution (panel (*c*)), and the redundant contribution (panel (*d*)), together with the net balance term (panel (*e*)), computed as the difference between redundant and synergistic contributions. In all panels, F_1 and F_2 correspond to the original variables driving the OR gate, whereas $F_3, \ldots, F_7$ represent progressively randomized versions of F_1. Accordingly, the pair (F_1, F_2) in the upper-left corner represents the reference condition, in which both sources are fully informative and symmetrically contribute to the target. In this case, the decomposition reveals the coexistence of redundancy and synergy. Redundancy arises because each variable individually conveys information about the target, resulting also in an overlapping contribution. At the same time, synergy arises because the outcome $C = 0$ can be only determined from the joint observation of the two variables. As the system transitions from F_1 to progressively randomized variables $F_3, \ldots, F_7$, a gradual loss of information about the target is observed. This is reflected in a decrease in joint MI (panel (*a*)), as well as in both redundancy and synergy decrease (panels (*c*) and (*d*)). The joint MI is indeed entirely carried by the informative variable, while the synergistic contribution vanishes, as the joint observation no longer provides additional information beyond that of individual variables. Moreover, the cumulative unique contribution (panel (*b*)) captures the reduction of the exclusive information carried by each feature variables in the pairs that therefore diminishes toward the lower-right corner. In contrast, the net balance term between redundancy and syn-

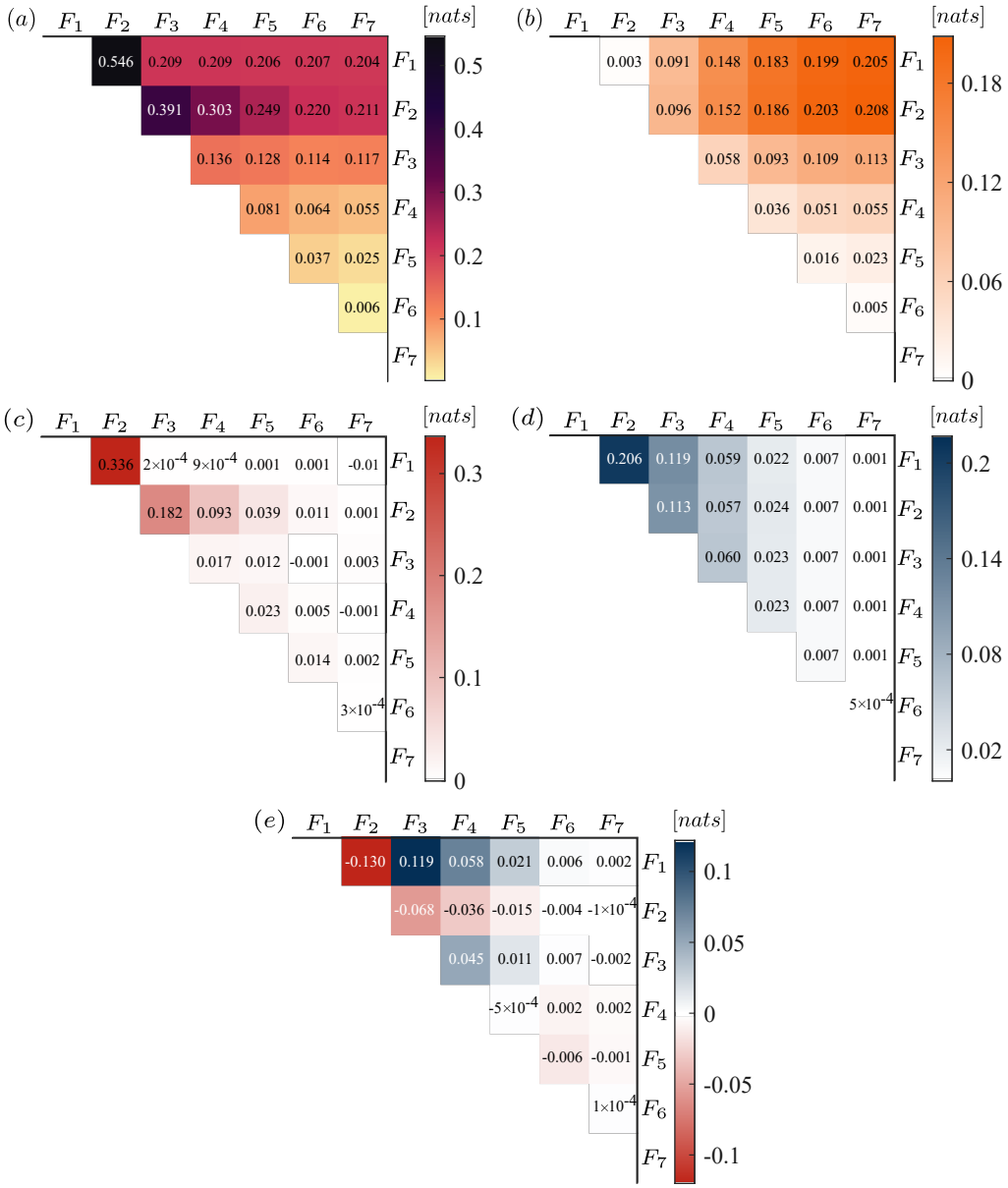

Figure 11.6: Upper triangular heatmaps depicting the average values across realizations of the information shared by each pair of feature variable and class variable (panel (*a*)), as well as their unique (panel (*b*)), synergistic (panel (*c*)) and redundant (panel (*d*)) contributions, as well as the balance between the redundant and synergistic decomposition terms (panel (*e*)). The figure was modified from Barà et al. (2025b).

ergy (panel (*e*)) reveals the evolution of the interaction structure across feature pairs, showing vanishing values when both feature variables become non-informative.

11.5. Overview and conclusions of chapter 11

Feature analysis strategies presented in this chapter address key limitations of widely used information theoretic FS and FI approaches, which often neglect high-order interactions among features. As a result, conventional approaches may incorporate redundant information into classification models while failing to capture synergistic effects that arise when considering the joint contribution of multiple features (Wollstadt et al., 2023; König et al., 2024). Another common limitation concerns the handling of mixed data types, as many existing methods are not directly applicable to settings involving continuous features and discrete class variables without prior data transformation. Even approaches accounting for the high-order features effects generally address this issue by homogenizing the nature of the variables, either through discretization of the continuous variables or through the addition of continuous noise to the discrete ones (Wollstadt et al., 2023; Tsimpiris et al., 2012). The approaches discussed in this chapter have been shown to overcome the aforementioned constraints by exploiting CMI measures and the PID analytical framework, and by leveraging the mixed estimation approaches proposed by Ross (2014) based on the nonlinear nearest-neighbor strategy.

The feasibility of the CMI-based FS and FI strategies presented in Sects. 11.2 and 11.3 has been validated using synthetic datasets in which the roles of features – redundant, relevant, and irrelevant – in determining the class variable are known a priori. Specifically, the results reported in Fig. 11.1 highlight the ability of the proposed approach to correctly selecting relevant features being sensitive to the presence of noisy effects that render certain features irrelevant. Similarly, the results in Fig. 11.2 demonstrate that the estimated unique, redundant, and synergistic contributions of multiple features closely align with the corresponding theoretical values. Moreover, the influence of the estimation parameters on the feasibility of the proposed mixed estimation approach has been evaluated for both FS and FI strategies. Specifically, in the FS case, the effect of the number of neighbors k was investigated, revealing consistent trends in the estimated MI and CMI measures at varying the values of k, despite a known tendency toward underestimation for higher values of k. In the FI case, results reported in Fig. 11.5, obtained under a different simulation setting, show the robustness of the method across varying sample sizes N, although weaker synergistic effects are observed for smaller datasets. Furthermore, the feasibility of the PID-based approach proposed to evaluate high-order contributions in determining the class variable was demonstrated, taking into account the interplay that occurs between pairs of features. Specifically, the results presented in Fig. 11.6

demonstrate the efficacy of the sPID approach in accurately characterizing redundant and synergistic interactions among features, as well as in mitigating high-order behaviors when noise corrupts feature contributions.

In Iovino et al. (2026), the proposed kCMI-FS approach was also evaluated in comparison with widely adopted ML methods. Specifically, this comparison was performed with a counterpart algorithm based on uniform discretization of continuous features, as well as with the CMINN approach by Tsimpiris et al. (2012), using simulated datasets. Overall, kCMI-FS demonstrated greater adaptability, particularly in complex and high-dimensional settings, consistently identifying relevant features, albeit with occasional selection of redundant features. Conversely, CMINN exhibited a more conservative behaviour, yielding smaller and more interpretable subset of features, while the fully discretized approach showed higher variability across datasets, both in terms of selected features and consistency across iterations. Furthermore, kCMI-FS was also evaluated on real-world benchmark databases and compared with the established FS strategies in the Feature Selection Toolbox (FEAST) developed by Brown et al. (2012). Overall, the results of the subsequent classification analysis performed on selected features reveled that kCMI-FS achieves a favorable balance between accuracy, model compactness, and stability across heterogeneous domains, making it particularly suitable for biomedical applications. Accordingly to these observations, kCMI-FS advantages primarily arise from its ability to capture nonlinear and synergistic dependencies, to operate in mixed discrete–continuous spaces, and to produce compact yet informative subsets across heterogeneous datasets.

With regard to the two FI strategies presented in the chapter – the CMI-based approach in Sect. 11.3 and PID-based approach in Sect. 11.4 – both are effecting in capturing high-order effects of features in determining the class variable. However, it is important to emphasize their methodological and practical differences. PID-based approaches aim to decompose MI quantities into predefined atomic components, which requires the specification of a redundancy measure, whose definition is still debated in literature. In contrast, the CMI-based Hi-Fi approach provides a more flexible, data-driven decomposition grounded on traditional information-theoretic measures. Moreover, it enables the CMI estimation without requiring the computation to all possible feature subsets, thereby offering scalability and practical applicability for larger systems. This advantage, however, also represents a limitation, as the proposed Hi-Fi approach does not perform an exhaustive investigation of the feature space, unlike the sPID strategy. In this respect, it is also important to note that the performance of the mixed estimation strategy underlying the CMI-based computation may be negatively influenced by the curse of dimensionality when accounting for the higher dimensional dataset. By contrast, the sPID framework always operates on pairs of features, making it inherently scalable to arbitrar-

ily high-dimensional feature set without occurring in estimation problems. Nevertheless, this pairwise structure constitutes a limitation of the sPID framework, as it does not account for the high-order effects among multiple variable in the broader sense, but rather restricts the analysis to feature pairs–target interplays.

Finally, it is important to acknowledge that the results achieved by the described FI assessment strategies can be employed to establish feature selection strategies that account for the high-order effects of multiple features. For instance, learning models can be trained by considering features that present higher unique or synergistic contributions. Alternatively, features presenting a significant composite score can be considered, as proposed in Iovino et al. (2025) and Ontivero-Ortega et al. (2025b). The latter is defined as the sum of the unique and synergistic contributions to which the redundant contribution is subtracted, thus favoring features that provide both unique and cooperative information while penalizing overlapped information.

Chapter 12

Application of information-theoretic machine learning strategies to physiological data

This chapter presents the findings obtained applying ML strategies grounded on information-theoretic measures to physiological data. In particular, a selection strategy is applied to cardiovascular features to identify the most informative for characterizing sex-related differences in autonomic control mechanisms (Sect. 12.1). High-order feature effects are also evaluated through FI strategies on cardiovascular features, to highlight variations in ANS activity under different physiological stress conditions (Sect. 12.2), and on gene expression features, to identify the most relevant features associated with breast cancer (Sect. 12.3). Finally, a simple application of the sPID framework is presented on cortical data under open- and closed-eyes conditions (Sect. 12.4).

12.1. Conditional Mutual Information-based feature selection for sex differences characterization

Cardiovascular time series collected in Database D on young healthy subjects have been employed in Iovino et al. (2024a) with the aim of selecting the most informative features in a sex classification task. The results of the detailed above FS strategy on physiological features extracted from resting-state 300-point RR, SAP, and DAP time series are here reported.

Feature extraction - Forty-one features were computed in the time, frequency, and information domains from the aforementioned cardiovascular time series. In the time domain, the mean (MEAN), standard deviation (STD), and variance (VAR) indices were extracted. In the frequency domain, the absolute spectral power values evaluated in the low frequency (LF, 0.04-0.15 Hz), high frequency (HF, 0.15-0.4

Hz), and total power (TP, 0-0.4 Hz) bands were computed. The normalized power values in the LF and HF bands were also evaluated (LFn and HFn) along with the respiratory peak frequency in the HF band (fHf). Finally, in the information domain, the entropy (H), the conditional entropy (CE), and the self-entropy (SE) were evaluated by means of the nearest-neighbor estimation strategy (in accordance with the strategies adopted in the applications in Sect. 7.1 and 7.2, the estimation parameters were set to $k = 10$ and $m = 2$). Additional features were evaluated for the RR time series, such as the root mean square of successive differences (RMSSD), the percentage of successive RR intervals differencing more than 50 ms (pNN50), the coefficient variation (CV) computed as the ratio between STD and MEAN of RR, the absolute spectral power in the very low frequency (VLF, 0-0.04 Hz) band, and the symphato-vagal balance index (SVB) obtained as the ratio between LF and HF power for RR.

Feature selection and classification - The CMI-based FS approach described in Sect. 11.2 was applied on the above reported physiological features and the label variable indicative of the sex, i.e., {F, M}. For computing MI and CMI terms, the number of neighbors used by the estimation approach was fixed to $k = 10$. To validate the results of the FS phase, a linear discriminant analysis classifier was used for sex classification. Trained with only the selected features, the dataset was divided into training and test sets using 10-fold cross-validation.

Results and discussion - Fig. 12.1 shows as the proposed feature selection algorithm stopped the search of relevant features after six iterations. Specifically, in the first iteration, only 8 features present significant MI values of which the LFn feature evaluated on RR has the highest value and is thus selected. Proceeding in the iterating search, a totality of six features were selected: MEAN and LFn from RR, MEAN and SE from SAP, and STD and H from DAP.

All the selected features have physiological meaning mainly reflecting autonomic nervous system activity balance and baroreflex sensitivity, that are known to be different between males and females. Females generally exhibit predominant parasympathetic modulation and attenuated sympathetic activity, associated with higher heart rate variability and lower blood pressure variability during resting state (Koenig and Thayer, 2016; Regitz-Zagrosek and Gebhard, 2023). Moreover, estrogen exerts multiple autonomic effects, enhancing vagal tone, baroreflex sensitivity, and reducing sympathetic vasoconstrictor outflow (Philbois et al., 2021).

In Iovino et al. (2024a), it has also been shown how the aforementioned selected features guaranteed an overall good ability of the classifier to discriminate modulation of ANS activity between sexes, with performance comparable to that of the entire feature set and relatively higher performance indicators for the discrimination of females.

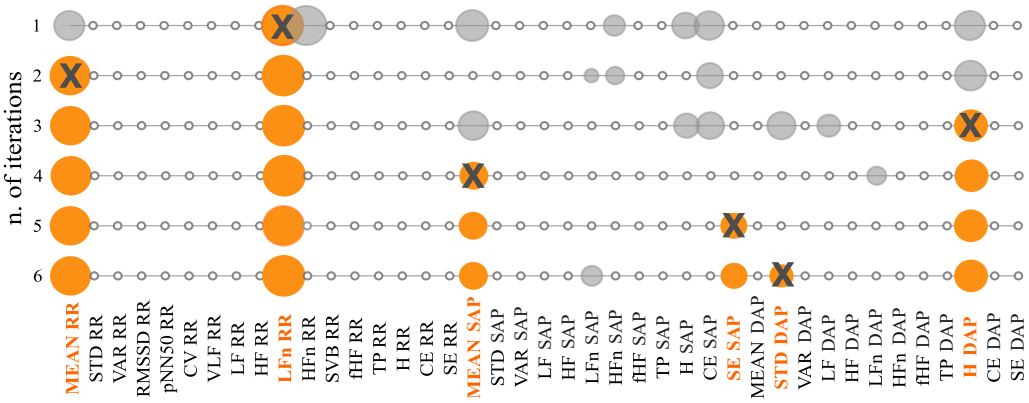

Figure 12.1: Schematic representation of the FS algorithm procedure and results for each iteration. Gray bullets indicate the features presenting a significant MI or CMI value, orange bullets the features selected at each step, while the cross evidences the feature selected at the specific iteration; the size of the bullets is proportional to the value of MI or CMI. The figure was modified from Iovino et al. (2024a).

12.2. Feature importance assessment in cardiovascular variability data for physiological stress classification

In Iovino et al. (2025), the FI strategy detailed in Sect. 11.3 has been applied on cardiovascular variability data with the aim to classify physiological stress. In this context, physiological time series collected in Database B - *version 1* – namely RR, SAP, DAP, and PP time series – were employed to identify the most informative features in distinguishing between resting phase (REST1, herein referred to as REST) and induced orthostatic stress (HUT). The findings related to the feature importance analysis step are reported in the following.

Feature extraction - Fifty-three features were extracted from the aforementioned time series in three domains, i.e., time, frequency, and information. Specifically, in the time domain, metrics such as mean (MEAN), standard deviation (STD), and variance were evaluated for each time series. In the frequency domain, after performing a parametric spectral analysis by fitting an AR model with fixed order $p = 10$, absolute spectral power values are obtained in the low frequency (LF, 0.04-0.15 Hz), high frequency (HF, 0.15-0.4 Hz), and total power (TP, 0-0.4 Hz) bands. Moreover, normalized power values in the LF and HF bands were computed by dividing for TP (LFn and HFn). The respiratory peak frequency in the HF band is also extracted (fHf). In the information domain, entropy (H), conditional entropy (CE), and self-entropy (SE) were calculated using the k-nearest neighbor approach (in accordance with the strategies adopted in the applications in Sect. 7.1 and 7.2, the estimation parameters were set to $k = 10$ and $m = 2$). Additional features were extracted from RR time series, including the root mean square of successive differences (RMSSD), the percentage of successive RR intervals differing more than 50 ms (pNN50), the coefficient of variation (CV) obtained as the ration between STD

and MEAN, the absolute power in the very low frequency (VLF, 0-0.04 Hz), and the sympatho-vagal balance index (SVB) obtained as the ratio between LF and HF power.

Feature importance assessment - As a preliminary step, pairwise correlations among features were computed to identify highly collinear variables, and those exhibiting a coefficient exactly equal to ±1 considered fully redundant and excluded. Specifically, MEAN PP and MEAN RR appeared strongly correlated and the first was removed thus reducing the feature set to fifty-two variables. Then, the analysis proceed within a 10-fold cross-validation framework, for which within each fold, features were normalized to zero-mean and unit variance on both training and test sets and used as input for the application of the Hi-Fi decomposition strategy. Specifically, the Gaussian-based framework reported in Sect. 11.3.2 was employed to obtain the unique, redundant and synergistic contribution of each feature.

Results and discussion - Fig. 12.2 shows the results of the FI analysis depicting the unique, redundant, and synergistic information contributions of each feature expressed as mean and variability values across the 10-fold cross-validation providing insights into the contribution and stability of each feature in stress classification across different folds. It can be observed how SVB RR consistently exhibits the highest unique contribution, thus suggesting how RR taken separately provides relevant and non-redundant insights on determining physiological stress states. On the other hand, SAP and DAP features present a balanced contribution between redundant and both unique and synergistic information, suggesting their contribution both individually and in interaction with other features. Finally, PP features reveal high synergistic contribution, e.g., in the case of VAR, suggesting that PP features may act as complementary variable. Overall, these results highlight heterogeneous contributions among cardiovascular features, with RR playing a dominant and independent role and PP contributing primarily in a synergistic fashion.

Among the features exhibiting the higher unique contributions are the entropy-domain features, such as SE and CE for both RR and PP, and the frequency-domain features, such as HF and LF for both RR and PP. This result can be related to their strong relation with ANS control. As demonstrated in Chapter 7, SE and CE provide complementary insights into the complexity and regularity of cardiac dynamics, that are known to vary with physiological stress (Javorka et al., 2018). In a similar manner, frequency-domain features have been shown to reflect sympathetic and parasympathetic activities, which exhibit a significant modulation between rest and stress conditions (Malliani et al., 1991). With regard to features that exhibit a high redundant contribution, these are features that capture similar physiological mechanisms, as often observed for time- and information-domain features. Indeed, these features covary due to their shared physiological underpinnings (Porta et al., 2017a). Conversely, features exhibiting high synergy, such as VAR and some en-

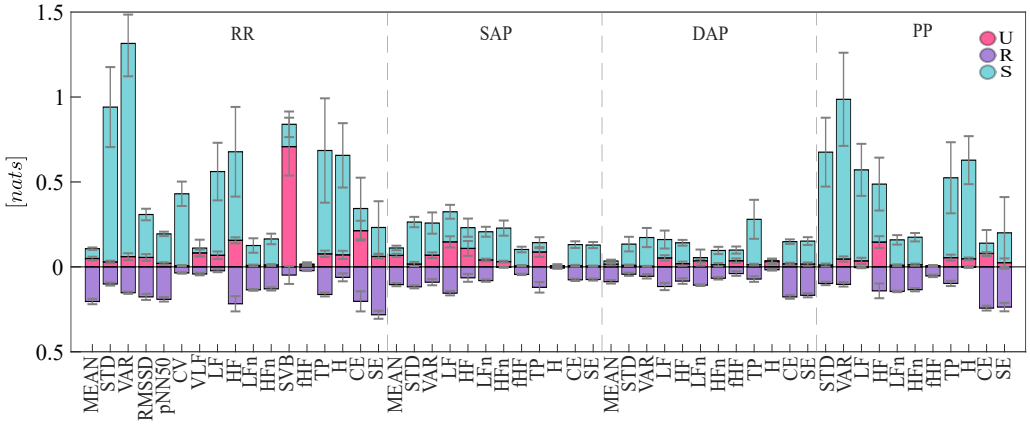

Figure 12.2: Errorbar graphs (MEAN ± 2STD) of unique (U), redundant (R), and synergistic (S) contributions of each cardiovascular feature computed across the 10 folds. R values are reported using a secondary axis (oriented downwards) to highlight their role in the selection criterion, specifically against the sum of U and S. The figure was modified from Iovino et al. (2025).

tropy indices, are likely to capture interaction effects between different regulatory components (e.g., sympathetic modulation combined with nonlinear heart rate dynamics) (Scagliarini et al., 2024). These findings overall highlight how the complex physiological ANS response to stress is more accurately captured when considering the joint behaviour of features.

12.3. Feature importance assessment in gene expression measurements for breast cancer detection

This section employs gene expression data from breast cancer tissues collected in Database L to investigate the contributions of gene expression in determining molecular subtypes. The presented results are reported in Lazic et al. (2026).

Feature importance assessment - The FI strategy presented in Sect. 11.3 was applied considering the four molecular subtypes as outputs of the class variable and the expression levels of the 50 genes as feature variables. Specifically, after increasing the number of data by generating a bootstrapped dataset with 572 samples and one-hundred sampling repetitions to ensure the same class counts, the nearest-neighbor-based approach was applied by fixing a number of neighbors $k = 10$ and using one-hundred surrogate samples to determine the selection criteria (see Sect. A.2.5 of the Appendix).

Results and discussion - Fig. 12.3 shows the top-ranked contributors according to the estimated average CMI between the class variable and each of the feature variables, conditioned on the subset of features that maximizes the measure. The results reveal that the majority of the genes that are documented in the literature as

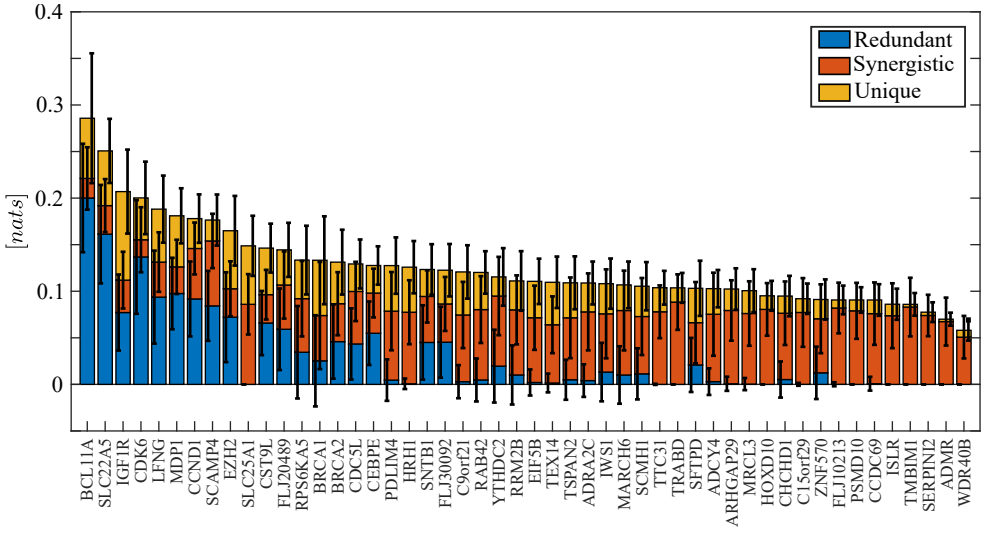

Figure 12.3: Errorbar graphs (MEAN ± 2STD) of unique, redundant, and synergistic contributions of each gene computed across 100 bootstrap samples. Genes are ordered according to a decreasing CMI. The figure was taken from Barà et al. (2025b).

being associated with breast cancer, i.e., SCL11A, SLC22A5, CDK6, IGF1R, LFNG, CCND1, EZH2, BRCA1, BRCA2, and TEX14 (Janssen et al., 2023; Westphal et al., 2025), exhibit high CMI values. These findings are in accordance also with previous studies that employed FS strategies (Covert et al., 2020; Catav et al., 2021; Janssen et al., 2023). Furthermore, as also noted by Catav et al. (2021), the relevant contributions from MDP1, SCAMP4, SLC25A1, and CST9L genes are observed, even if some of these are not directly related to breast cancer from literature. However, SLC25A1 has been reported by Catalina-Rodriguez et al. (2012) to exhibit elevated expression in breast cancer tissues, suggesting a potential relevance to subtype differentiation.

Focusing on the ten most important genes, it appears that the contribution is predominantly associated with redundant components. This result is corroborated in part by Westphal et al. (2025), who, performing a PID-based analysis, revealed lower contribution of synergy and redundancy. In this view, it is important to emphasize the distinction between the two employed approaches. Indeed, they defined feature-wise synergy and redundancy (FWS and FWR) measures through the concept of interaction information. An analysis of the selection order (not included in the thesis) revealed shared redundancy between BCL11A and SLC22A5, which is consistent with their subtype-specific functions. BCL11A has been associated with the basal-like phenotype (Katnik et al., 2023), while SLC22A5 has been linked to luminal phenotypes and is recognized as an estrogen receptor-regulated gene (Wang et al., 2012; Orrantia-Borunda et al., 2022). Furthermore, LFNG and BCL11A exhibit redundant information, likely due to their shared association with the basal-like subtype (Xu et al., 2012).

12.4. state Partial Information Decomposition application on cortical data

In this section, the application of the sPID reported in Barà et al. (2025b) on a human brain network described by cortical data collected on resting state subjects with open and closed eyes is reported. Specifically, data described in Database I are employed after preprocessing steps to recontruct brain source activity from scalp signals.

Data preprocessing - Electroencephalographic data were filtered through a zero phase-shift band-pass filter between 0.3 and 40 Hz and processed via Independent Component Analysis (ICA) to remove artifacts resulting from eye blinks, eye movements, and cardiac activity. These were then re-referenced to a common average voltage and down-sampled to f_s =128 Hz. Finally, data windows of 8 seconds – corresponding to 1024 samples – were selected from each subject and condition via an iterative test that checked the restricted weak stationarity of the signals in mean and variance (Magagnin et al., 2011). The scalp signals were projected via spectral inverse operators to their cortical sources using the CiftiStorm pipeline. This is a MATLAB toolbox for spectral analysis and inverse solution of electroencephalographic and magnetoencephalographic data, therefore employed to obtain head and source models and to retrieve the lead fields required to solve the inverse reconstruction problem (Areces-Gonzalez et al., 2024).

More specifically, a spectral analysis was conducted through a k-order orthogonal wavelet decomposition of the data, employing the Maximal Overlap Discrete Wavelet Transform method (MODWT) (Percival and Walden, 2000). The wavelet transform was applied to vector-valued functions representing the EEG signals, yielding components with spectral peaks in the frequency bands $\left(\frac{f_s}{2^{k+1}}, \frac{f_s}{2^k}\right]$. A maximum wavelet order $k = 7$ was selected to obtain waveforms peaking around the fundamental EEG frequency bands, namely, the gamma band (γ, 32-64 Hz) for $k = 1$, the beta band (β, 16-32 Hz) for $k = 2$, the alpha band (α, 8-16 Hz) for $k = 3$, the theta band (θ, 4-8 Hz) for $k = 4$, the high delta band (high-δ, 2-4 Hz) for $k = 5$, the mid delta band (mind-δ, 1-2 Hz) for $k = 6$, and the low delta band (low-δ, 0.5-1 Hz) for $k = 7$. The inverse solution was subsequently obtained using the Spectral Structured Sparse Bayesian Learning (SSSBL) method. This approach operates via an optimal quasilinear operator applied to the wavelet-domain data (Paz-Linares et al., 2023), which is optimized to identify source activity patterns generated by cortical oscillatory networks across the considered frequency bands in resting-state EEG. Quasilinearity consists in a key property of the SSSBL approach, enabling robust regularization via nonlinear priors – specifically, the Elastic Net Nuclear Norm – thereby mitigating spatial distortions and leakage effects in the reconstructed source time series (Gonzalez-Moreira et al., 2018). Furthermore, this approach contributes to limiting nonlinear distortions in both the time and frequency domains. For the anatomical

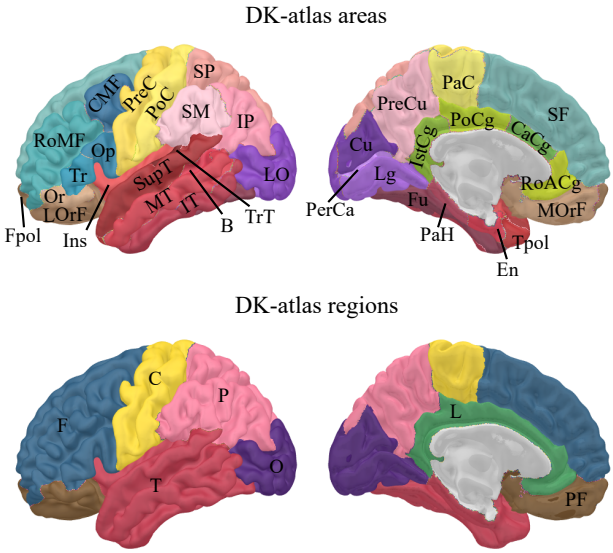

Figure 12.4: Graphical representation of brain areas according to DK atlas and their grouping in large regions. In yellowish the central (C) cortex (pre central, PreC; post central, PoC; para central, PaC), in bluish the frontal (F) cortex (rostral middle frontal, RoMF; caudal middle frontal, CMF; pars opercularis, Op; pars triangularis, Tr; superior frontal, SF), in greenish the lateral (L) cortex (isthmus cingulate, IstCg; posterior cingulate, PoCg; caudal lanterior cingulate, CaCg; rostral anterior cingulate, RoACg), in purplish the occipital (O) cortex (lateral occipital, LO; cuneus, Cu; pericalcarine, PerCa; lingual, Lg), in pinkish the parietal (P) cortex (superior parietal, SP; supra marginal, SM; inferior parietal, IP; pre cuneus, PreCu), in brownish the prefrontal (PF) cortex (pars orbitalis, Or; lateral orbitofrontal, LOrF; frontal pole, Fpol; medial orbitofrontal, MOrF), and in reddish the temporal (T) cortex (insula, Ins; superior temporal, SupT; middle temporal, MT; inferior temporal, IT; transverse temporal, TrT; bankssts, B; fusiform, Fu; para hippocampal, PaH; enterhinal, En; temporal pole, Tpol). The figure was modified from Barà et al. (2025b).

segmentation, the Desikan-Killany (DK) atlas was adopted, comprising of 34 cortical regions for hemisphere (both left (L) and right (R)) (Desikan et al., 2006). The DK areas and their aggregation in larger cortical areas are graphical illustrated in Fig. 12.4.

Data and statistical analysis - The sPID analysis was performed on the reconstructed cortex signals to investigate the nature of the information carried about the experimental condition (eyes open vs. eyes closed). Specifically, the samples of the signals from different cortical areas were considered as realizations of the source variables, while the acquisition phase was treated as a binary output of the target variable ($Q = 2$). Thus, $N_c = 1024$ samples for each of the Q conditions were analyzed for each subject, for a total data length of 2048 samples. The analysis was performed for each of pair of the 68 brain areas, thus repeated for the 2278 possible combinations. The PID method was applied by using a number of neighbors $k = 5$. The unique contributions of pairs of areas were summed to obtained a combined unique information. Moreover, the redundancy-synergy balance computed as the

difference between redundant and synergistic contributions from each pair of areas.

The statistical significance of the joint MI, as well as of the cumulative unique, redundant, and synergistic contributions was assessed by generating fifty surrogate data (see Sect. A.2.5 of the Appendix). Specifically, the measures computed on the original data were compared with a significance threshold derived from the distributions of the measures evaluated on multiple surrogate data obtained by shuffling the samples of the target variable. Specifically, unique, redundant, and synergistic PID terms were deemed as statistically significant if their value computed on the original data exceeds the $100(1-\alpha)^{th}$ percentile of the distribution obtained on surrogate data, with a significance level of $\alpha = 0.05$. Differently, in accordance with the Bonferroni correction, the joint MI was deemed as statistically significant if at least of the decomposition contribution is assessed as significant by using a threshold of $100(1-\alpha)^{th}$ with a significance level $\alpha = 0.05/3$. To simplify the reading of the results, averaged significance for the larger cortical regions have been obtained for each measure, considering the mean of the terms associated with pairs of cortical areas corresponding to those regions.

Results and discussion - Fig. 12.5 shows high values of joint MI between the acquisition state and pairs of signals across most cortical areas, with the exception of central, lateral and parietal regions. An overall average significance of 97.64% is observed in the whole cortex (panel (*a*)). In addition to a moderately elevated synergistic contribution observed when at least one of the source variables is taken from areas in the occipital regions – particularly in the right hemisphere (panel (*c*)) – high joint MI values are primarily associated with redundant contributions arising from pairs of regions in frontal, prefrontal, occipital, and temporal regions (panel (*d*)). Moreover, significant unique contributions are observed in interactions involving one of these regions with the other regions of the cortex, i.e., central, lateral, and parietal (panel (*b*)). As expected, high values are reflected in higher significance, with overall higher significance for the redundant contribution. Regions characterized by strong redundant contributions are also highlighted in terms of net balance, whereas the remaining areas display a more balanced profile or a slight predominance of synergistic effects (panel *e*).

The observed findings are consistent with the established role of the occipital cortex in early visual processing, for which an increased synchronized activity in the α band is exhibited by the occipital cortex when the eyes are closed (Parks and Madden, 2013). A high joint MI between the cuneus (Cu), pericalcarine (PerCa) and lingual (Lg) areas, constituting the visual network (VN), and the other cortex regions is indeed observed. Furthermore, these regions exhibit a high degree of synergistic and redundant contributions, with a predominance of the latter. The presence of significant redundant information exchange within and between frontal, temporal, and occipital regions suggests highly correlated oscillatory dynamics in these re-

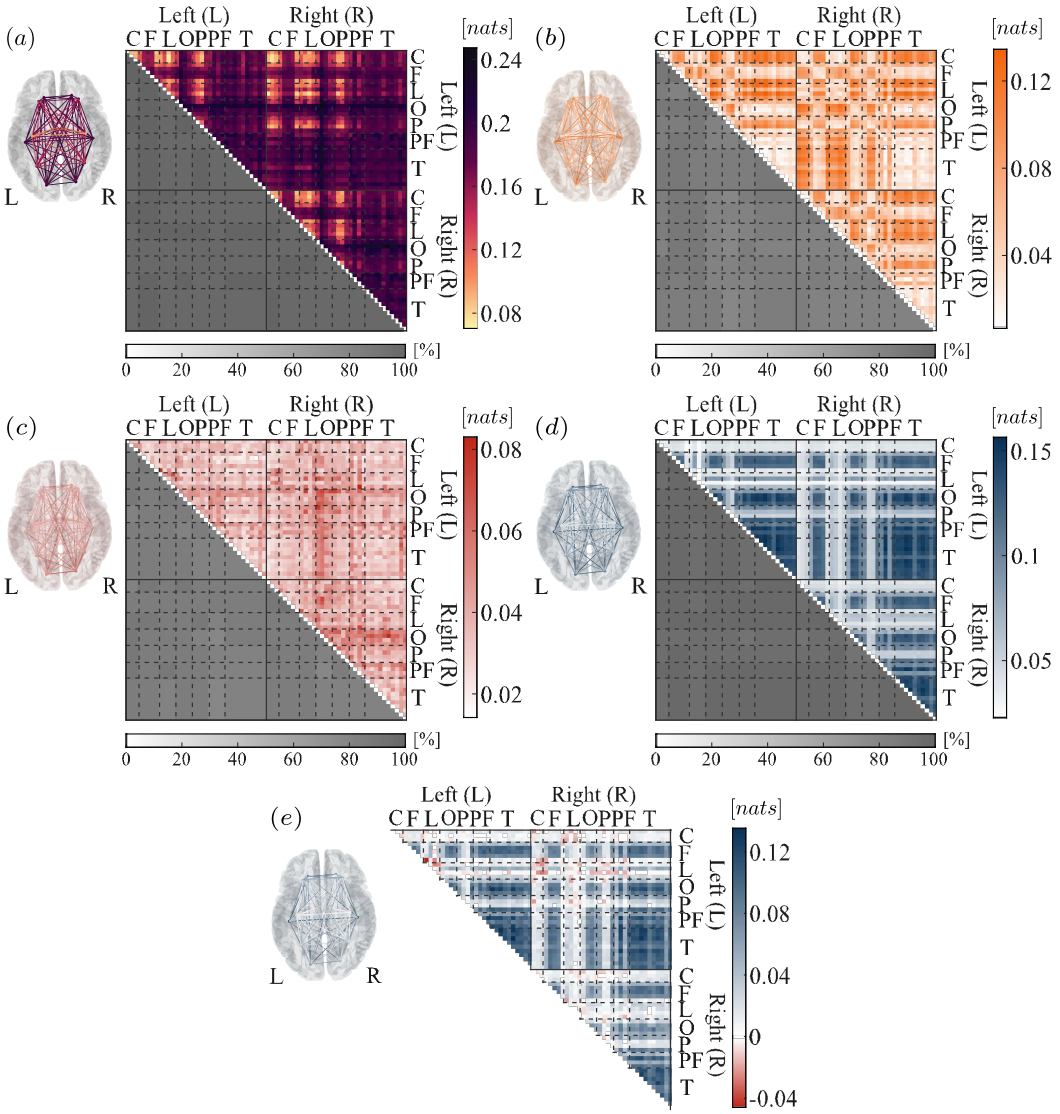

Figure 12.5: Heatmaps depicting in the upper triangular the average values across subjects of the information shared by each pair of cortical source and the acquisition phase (panel (*a*)), as well as their unique (panel (*b*)), synergistic (panel (*c*)) and redundant (panel (*d*)) contributions, as well as the balance between the redundant and synergistic decomposition terms (panel (*e*)), and in lower triangular the correspondent average significance evaluated within and between left (L) and right (R) cortical regions (central (C), frontal (F), lateral (L), occipital (O), parietal (P), prefrontal (PF), and temporal (T)). On the left, a 3D cortex representation considering the average values of the corresponding measure within (colored nodes in the centroid of each region) and between (colored links between pairs of centroids) cortical regions. The figure was taken from Barà et al. (2025b).

gions, we could refer to the role of the dorsal attention network (DAN). It comprises the frontal eyes field (FEF), which is associated with the activity of the middle frontal gyrus structural area in the frontal cortex region – corresponding to caudal middle frontal (CMF) and rostral middle frontal (RoMF) DK atlas areas (Blanke et al., 2000). The FEF has been observed to be involved in the voluntary shifts of visual attention and in the eye movement control (Lynch and Tian, 2006), with a high alpha activity in the response preparation to a visual stimulus (Popov et al., 2017) and when eyes are closed (Marx et al., 2004). Similarly, although the temporal cortex is recognized as being predominantly implicated in higher-level visual functions – such as object recognition and feature integration (Grill-Spector and Malach, 2004) – its involvement during simple visual tasks comprising repeated or familiar stimuli reveals an early recruitment and top-down facilitation mechanisms (Bar et al., 2006; Bell et al., 2009) that, together with a hierarchical and parallel organization of the ventral visual stream which enables the rapid transmission of visual information from occipital areas to temporal regions (Felleman and Van Essen, 1991; Lamme and Roelfsema, 2000), results in dynamics similar to the VN. It is noteworthy that the prevalence of redundant information shared between pairs of cortical sources and the acquisition phase is consistent with the concept that redundancy is related to robustness, a notion enforced particularly in neuroscience applications of PID related to the study of human sources of visual information (Luppi et al., 2024).

12.5. Overview and conclusions of chapter 12

The applications presented in this chapter highlight the importance of adopting a multivariate perspective in feature analysis when designing ML strategies. In this context, the evaluation of high-order redundant and synergistic information plays a crucial role in guiding feature selection and improving model performance. Moreover, for the network perspective proposed for the functional description of the human organism in the thesis and for the results showed throughout, these remarks became particularly relevant when considering biomedical and clinical applications.

The synergy-aware evaluation and selection pipelines applied in Sects. 12.1 and 12.2 enable the identification of cardiovascular features that are not only individually relevant but also complementary, thereby enhancing both interpretability and performance in tasks such as sex-related differences in autonomic control and stress detection. In both cases, the selected feature subsets – obtained through an iterative CMI evaluation in the former and through the preservation of unique and synergistic contributions while discarding the redundant one in the latter – capture complementary aspects of autonomic regulation. These include features indicative of slow tonic variations in cardiac timing as well as faster oscillatory components associated with the sympathetic and parasympathetic modulation (Pernice et al. (2019);

Ontivero-Ortega et al. (2025b)). The joint selection of features derived from both ECG and ABP signals support that discriminative information is distributed across coupled physiological systems rather than confined to individual organ systems. Overall, these findings emphasize the importance of accounting for the complex interplay among physiological signals, in line with the results presented in Part III, and demonstrate how information-theoretic tools enables a richer and more interpretable assessment of ANS dynamics. The inclusion of high-order physiological features related to the redundant and synergistic interactions among multiple organ systems could further enhance model feasibility and should be investigated.

By quantifying the unique, redundant, and synergistic contribution of each feature within a set, the proposed Hi-Fi feature importance strategy allows for the identification of features with independent informative contribution as well as features sharing physiological information. For example, in the stress discrimination task in Sect. 12.2, higher unique contributions are associated with entropy- and frequency-domains cardiovascular features, which are known to present a strong relation with ANS control, while higher redundant contributions are observed for features capturing similar physiological mechanisms, such as those in time- and information-domains. Additionally, as shown in the simulation analysis (see Sect. 11.3.3), the proposed strategy enables to track the conditioning variables involved in the determination of each informative contribution, thereby offering a deeper understanding of interactions among features.

The applicability of the CMI-based FI strategy is further demonstrated in Sect. 12.3 on gene expression data. The identified informative genes are consistent with previous works investigating biomarkers associated with breast cancer tissues (Catav et al., 2021; Westphal et al., 2025; Janssen et al., 2023), thus supporting the applicability of the proposed approach on different domains.

Finally, the state-PID approach applied on cortical data in Sect. 12.4 enables the assessment of how interactions between pairs of cortical regions help distinguishing between eyes-open and eyes-closed conditions. The results reveal intricate patterns of information exchange arising from the pairwise interplay between cortical areas even for these simple states. While a predominance of redundant interactions is observed – in line with previous studies on brain dynamics (Luppi et al., 2024) – higher synergistic contributions are highlighted for areas related to the occipital region, which are known to play an important role in visual tasks and exhibiting synchronized oscillatory activity (Parks and Madden, 2013).

Part V

Conclusions

Chapter 13

Concluding remarks and future directions

This thesis provides a comprehensive investigation of the behavior of complex systems through the application of information-theoretic tools, with a particular focus on the analysis of high-dimensional data, such as those characterizing physiological network dynamics and those commonly encountered in machine learning problems. This chapter summarizes the main contributions of the thesis, highlighting strengths and limitations of the proposed analytical frameworks for the functional analysis of complex systems, with particular emphasis on estimation-related aspects (Sect. 13.1). It also discusses the key findings obtained from the analysis of physiological data presented in Part III (Sect. 13.2) and from biomedical features analysis presented in Part IV (Sect. 13.3). In this context, the limitations of the proposed approaches are evidenced, and potential directions for future research are outlined (Sect. 13.4).

13.1. Opportunities and challenges in estimating complex system behavior using information-theoretic measures

The usefulness of information-theoretic frameworks for the investigation of complex system behavior is widely recognized in literature. By leveraging the inherently stochastic nature of real-world dynamics, entropy-based measures enable the extraction of meaningful insights from the variability of the observed data, thereby providing a unified analytical framework (Shannon, 1948; Cover, 1999). Indeed, in contrast to other approaches that focus on specific aspects of system behavior – often providing fragmented and partial characterizations – information-theoretic methods account for the stochastic, multivariate, nonlinear, and nonstationary properties of complex systems typically associated with complex self-organized, multiscale, and emergent dynamics. Within this context, a key strength of the framework of in-

formation dynamics, as highlighted throughout this thesis, lies in its ability to support a hierarchical analysis of the system dynamics. This enables the investigation of individual system components, of the coupling and causal relationships between pairs of elements, and, more generally, of the collective behaviors that emerge from interactions among multiple components (Faes et al., 2022). From this perspective, combining insights derived from measures such as entropy rate or information storage (Lizier (2012a); Barà et al. (2023c, 2024c)) with those obtained from frameworks such as MIR or PrI decomposition (Faes et al. (2015c); Mijatovic et al. (2021); Barà et al. (2023b)), which are used to characterize directional and pairwise interactions, as well as from PID-based approaches that quantify redundant and synergistic information sharing (Williams and Beer (2010); Barà et al. (2025a)), enables a more comprehensive understanding of complex dynamics. This hierarchical integrated approach provides insights that cannot be achieved by examining isolated components or focusing on a single aspect of system behavior.

A crucial aspect in assessing the effectiveness of the aforementioned information-theoretic approaches for describing complex system behavior concerns the practical estimation of entropy-based quantities from finite, real-world data, which are often affected by noise and nonstationarity. This thesis has explored several estimation strategies, distinguishing between methods for continuous and discrete data – the latter typically requiring quantization, with an associated loss of information – as well as between parametric and model-free approaches. Among these, linear parametric methods represent the simplest and most computationally efficient solution, and have demonstrated high practical feasibility, particularly in the analysis of high-dimensional data with pronounced oscillatory content (Barrett et al., 2010; Sparacino, 2026). However, these approaches rely on the assumption of Gaussianity and linearity, which limits their ability to capture the nonlinear dynamics that commonly characterize complex systems. Although it has been shown that stationary processes can, in principle, be represented as autoregressive models without loss of information – at the expense of increasing model order (Barnett and Seth, 2014) – this representation may still obscure relevant nonlinear interactions. On the other hand, model-free approaches ensure a greater flexibility in capturing both linear and nonlinear dynamics. Among them, nearest-neighbor estimation strategies have proven particularly effective, showing robustness to noise and nonstationarity while preserving the information contained in continuous-valued data (Kozachenko, 1987; Xiong et al., 2017). Nevertheless, despite the availability of bias-correction strategies (Kraskov et al., 2004), these methods remain affected by the curse of dimensionality and present very high computational demand, which limit their applicability in high-dimensional settings and in the analysis of groupwise interactions. Discrete-based estimation strategies are even more affected by the curse of dimensionality and introduce additional limitations due to information loss asso-

ciated with lower-resolution data representation (Faes and Porta (2014); Barà et al. (2024c, 2023b)). Indeed, the binning procedure reduces the resolution of the amplitude dynamics, while the permutation-based strategy completely disregards amplitude information (Azami et al., 2023; Bandt and Pompe, 2002). Although empirical rules have been proposed to mitigate these issues, these often excessively reduce the data representation restricting amplitude resolution and the effective memory of the system. Consequently, these methods are less suitable for high-dimensional and short data lengths, but they can be favored for real-time applications due to their simplicity and low computational costs. Finally, acknowledging the importance of preserving the intrinsic nature of the observed data, mixed estimation strategies based on model-free nearest neighbor approaches were adopted to work with both continuous and discrete data (Ross (2014); Barà et al. (2025a)).

In summary, the selection of the most appropriate estimation strategy is a non-trivial task that must account for multiple factors. These include the characteristics of the data – such as noise levels, stationarity, sample size, and oscillatory content – as well as the properties of the underlying system – including the presence of nonlinear dynamics, dimensionality, and the strength of the phenomena of interest. Furthermore, the choice should be guided also by the objective of the analysis, requiring a balance between estimation feasibility and robustness, computational costs and time, methodological simplicity, and interpretability of the results.

13.2. Information-theoretic insights into physiological dynamics

Given the aforementioned ability of the information-theoretic analytical framework in investigating complex, high-dimensional systems through a hierarchical evaluation of the underlying dynamics, its relevance for the emerging field of Network Physiology is quite evident (Faes et al. (2022), Sparacino (2026)). The feasibility of these investigations in evaluating physiological dynamics related to individual organ systems, as well as to regulatory control mechanisms involving multiple organ systems has been demonstrated by numerous works in literature and by the applications presented in this thesis.

With a particular focus on cardiovascular and cardiorespiratory short-term dynamics, the reported findings support the effectiveness of complexity, coupling, and causality measures in characterizing healthy physiological states. For instance, the activation of the sympathetic branch of the autonomic nervous system and the enhancement of baroreflex sensitivity under postural stress conditions – such as those induced by the head-up tilt maneuver – are reflected in well-established trends, including a decrease in entropy rate of cardiac and respiratory dynamics (Volpes et al., 2022a; Barà et al., 2023b) and an increase in causal influence from arterial pressure to heart rate (Barà et al., 2023a,b, 2026b). Similarly, the enhancement of respiratory

sinus arrhythmia during controlled breathing protocols is associated with reduced complexity of ventilatory activity and diminished influence of breathing activity on cardiac dynamics, as quantified via transfer entropy measures, during forced breathing activity (Barà et al., 2023b, 2024c). Beyond these well-established mechanisms, less explored dynamics – such as those involving arterial compliance – have also been investigated, revealing its important role within cardiovascular and cardiorespiratory regulatory network. In particular, it has been observed how postural stress is associated with a decreased influence of heart period on arterial compliance, a stronger influence of compliance on arterial pressure, and a decreased influence of compliance on respiration (Barà et al., 2026b). Furthermore, applications to altered physiological or pathological conditions, including aging and diseases such as acute myocardial infarction and heart failure, indicate a general weakening of regulatory mechanisms compared to healthy states (Platiša et al., 2023; Cimignolo et al., 2025a). Finally, the application of the proposed frameworks on other physiological dynamics, such as brain activity and brain-heart interactions (Barà et al., 2023c), demonstrates their potentiality and versatility to provide novel insights in research areas often characterized by heterogeneous and less defined findings (Vergara et al., 2025c).

The practical limitations mentioned above, particularly those related to the model-free estimation approaches, have constrained the investigation of physiological dynamics to the analysis of individual organs or pairwise interactions. High-order interactions among physiological variables have instead been restricted to static analysis that, neglecting temporal dependencies, reduces data dimensionality and thereby facilitates the application of model-free approaches at the price of discarding the investigation of temporal dynamics exerted over multiple time lags. Despite this limitation, such approaches have provided novel insights into the redundant and synergistic contributions of systolic and diastolic arterial pressure components in determining the mean arterial pressure (Sparacino et al., 2025d), as well as into the interplay of cardiac and arterial pressure dynamics across ventilatory phases (Barà et al., 2024a).

Another important aspect emerging from the applications reported in the thesis is the opportunity to compare the results achieved using different analytical frameworks and estimation strategies. In particular, the combined use of linear parametric and model-free nonlinear strategies enables a deeper understanding of the nonlinear characterization of physiological dynamics. For example, findings in Volpes et al. (2022a) and Barà et al. (2023a, 2026b) highlight the well-known tendency toward linearization of cardiovascular and cardiorespiratory dynamics during the execution of tasks enhancing sympathetic activity. Furthermore, comparisons involving discrete-based strategies with different estimating parameters provide insights into key characteristics of the data, such as amplitude variability – affected by the

number of quantization levels in quantization procedures – and the effective memory of the system, as reflected by the choice of embedding dimension. For instance, results reported in Barà et al. (2023b, 2024c) show that low amplitude resolution or insufficient embedding dimension may hinder well-known cardiovascular and cardiorespiratory dynamic trends with postural stress or controlled breathing.

13.3. Enhancing machine learning interpretability via information-theoretic methods

Both grounded on probability theory, the frameworks of information theory and machine learning are inherently interconnected. The information-theoretic foundations underlying several ML strategies are well-known in literature (Principe and Xu, 1999; MacKay, 2003), and in recent years entropy-based measures have emerged as powerful tools for addressing ML challenges related to the models interpretability and the management of high-dimensional dataset (Haroutunian and Gharagyozyan, 2025). These aspects are especially relevant in applications involving physiological data and healthcare settings, where the interpretability of classification or clustering findings is essential to derive physiological insights. At the same time, the ability to handle large volume of data has become important, given the availability of data collected both in clinical settings and through the increasingly popular wearable devices continuously monitoring physiological parameters.

With a focus on ML feature analysis strategies, information-theoretic measures have been employed to develop algorithms capable of assessing feature relevance in predicting discrete labels associated with the investigated system, thereby enabling the selection of the most informative variables (Iovino et al., 2026; Lazic et al., 2026; Barà et al., 2025b). In this context, metrics that capture the high-order interplays between multiple features are particularly relevant, as they allow redundant information to be excluded from learning processes while preserving the synergistic information emerging from the joint consideration of multiple features (Wollstadt et al., 2023). Overall, this leads to improved performance and robustness in both supervised or unsupervised learning outcomes. In addition, it is important to highlight that an additional factor which contributes to the feasibility of these approaches lies in the utilization of estimation strategies that are suited to typical ML settings, involving continuous feature variables and a discrete class variable (Barà et al., 2025a).

13.4. Future directions

Throughout the thesis, several limitations of the investigated analytical frameworks have been identified. In this section, potential directions for future research are out-

lined, with the primary aim of fostering methodological advancements applicable across a broad range of complex systems in different domains. In addition, possible extensions within the specific fields of network physiology and machine learning are discussed.

While the analysis of individual and pairwise dynamics in network systems is well established in the literature and has been extensively explored in this thesis, groupwise analysis remains less developed. Recent advances highlight the lack of consensus on appropriate metrics for quantifying high-order interactions, particularly with regard to the definition of redundancy. Furthermore, significant challenges are related to the estimation of such measures, largely due to the curse of dimensionality, which becomes increasingly critical in multivariate settings. In this context, future research should focus on the development of well-defined information-theoretic metrics for high-order interactions satisfying desirable theoretical properties, as well as on the design of improved model-free estimation techniques capable of mitigating dimensionality-related issues. Approaches based on non-uniform embedding, as well as methods that explicitly account for the nonstationary and multiscale nature of complex dynamics, constitute promising directions.

Further efforts should be also directed toward integrating the proposed analytical framework within the context of wearable technologies for the continuous monitoring of physiological parameters. In particular, given the widespread use of wearable devices for cardiovascular assessment, the implementation of relatively simple algorithms – such as those evaluating the complexity of heart rate or arterial pressure dynamics – could enable real-time analysis and personalized health assessment. However, with a view toward combining the analysis of multimodal data from different physiological sources in portable, real-time monitoring systems, further investigations are needed to assess the feasibility of ultra-short-term analyses across various physiological signals. The development of such bivariate and multivariate settings would be likely associated with the use of linear parametric strategies, due to the mentioned longer-data requirement of model-free strategies.

Finally, the presented framework is closely connected to the potential integration with machine learning methodologies, which play a central role in clinical applications such as early disease detection, patient monitoring, and personalized treatment planning. In this regard, incorporating high-order information-theoretic measures into the set of investigated physiological features represents a promising direction. Moreover, the development of a unified machine learning pipeline – encompassing signal preprocessing, feature extraction and importance assessment, and the development of supervised and unsupervised learning algorithms – would facilitate the creation of fully interpretable models, which are of particular importance in healthcare applications.

Appendix

The information-theoretic measures computed throughout this thesis are statistically assessed using surrogate data analysis approach. In this appendix, the general principles underlying this this validation framework are first introduced (Sect. A.1). followed by a detailed description of the specific strategies employed to to assess the different metrics (Sect. A.2). These aspects have been extensively addressed in Pinto et al. (2024) and Cimignolo et al. (2025a), and are here briefly recalled.

A.1. Surrogate data analysis framework

The intrinsic variability of dynamic systems requires the use of suitable statistical strategies to assess the significance and reliability of estimated information-theoretic measures. This is commonly achieved by using surrogate data analysis, a flexible framework that can be applied to a wide range of signals, allowing for the exploration of key properties of the underlying dynamics (Lucio et al., 2012; Lancaster et al., 2018). Additionally, as will be discussed in more detail in the following, these methods can be easily applied to static and dynamic information measures, allowing the testing of specific hypotheses related to the observed data (Jamšek et al., 2010; Cliff et al., 2021). Originally introduced to detect the presence of nonlinearity in time series dynamics (Theiler et al., 1992; Schreiber and Schmitz, 1996), surrogate data approaches were first applied for evaluating the significance of brain coupling dynamics (Lachaux et al., 1999) and then broadly extended to several information-theoretic measures (Theiler et al., 1992; Faes et al., 2008c; Lancaster et al., 2018). This approach represented a substantial improvement over commonly used practices based on arbitrary thresholding, which offer an approximate assessments and fail to account for estimation-related factors. By contrast, by defining a threshold level based on statistical criteria derived from the sampling distribution of the es-

timator under investigation, surrogate data methods provide a more rigorous and powerful framework for statistical assessment.

Surrogate data analysis methods are generally classified into typical realizations and constrained realizations (Schreiber and Schmitz, 2000; Lancaster et al., 2018). In the former, a data model is first fitted and then Monte Carlo realizations are generated from it for comparison with the observed data, requiring a priori knowledge of the model and its parameters. In the latter, surrogate data are generated directly from the original data, preserving all its characteristics except for the specific property under investigation (Theiler and Prichard, 1996). Constrained realizations are more widely used and specifically intended for hypothesis testing; however, they are not suitable for estimating confidence intervals (Theiler and Prichard, 1996).

More generally referred to as surrogate data analysis, the constrained realization approach involves two steps: selecting an appropriate discriminating statistic and properly formulating the null hypothesis to be tested. Specifically, a null hypothesis is defined by assuming the absence of a particular feature in the observed data. Surrogate data consistent with this hypothesis are generated and a discriminating statistic is computed for both the original and surrogate data. If the statistic computed on the original data is significantly different from the distribution derived from the surrogate, the null hypothesis is rejected, indicating that the null hypothesis is not adequate in describing data (Schreiber and Schmitz, 2000; Lancaster et al., 2018). Because surrogate distributions are not necessarily normal, significance is typically assessed by using a non-parametric test, where the significance threshold is determined through percentile-based strategies applied on the surrogate distribution (Theiler et al., 1992; Schreiber and Schmitz, 2000). The number of surrogate data N_s to be generated depends on whether a one-sided or two-sided test is being conducted, as well as on the percentile-based threshold $(1 - \alpha) \times 100\%$ used for the significance assessment. In a one-sided test, the null hypothesis is rejected only if the discriminating statistic from the original data deviates from the surrogate distribution in a single direction. In contrast, a two-sided test considers deviation in both directions, allowing the statistic to be either higher or lower in the surrogates than in the original data. Accordingly, a number of surrogates at least equal to $10/\alpha$ and $20/\alpha$ should be generated to have a feasible significance assessment when using one-sided and two-sided test, respectively (Schreiber and Schmitz, 2000). If multiple statistical tests are performed, the probability of obtaining significant results by chance increases. In such cases, it is imperative to adapt the significance level in order to prevent the erroneous rejection of the null hypothesis. One possible approach is to implement the Bonferroni correction, whereby the threshold level is adjusted to α/n, with n representing the number of tested hypotheses (Lancaster et al., 2018).

A.2. Integrating information-theoretic and surrogate data analysis frameworks

In this section, surrogate data analysis strategies are discussed with a particular focus on the investigated information-theoretic metrics. More specifically, the aim is to assess the significance of self-dependencies, as well as of coupling and causality dependencies evaluated within and among nodes of both static and dynamic networks. In addition, the presence of significant nonlinearity in the behavior of both single nodes and in their interactions is investigated. The following surrogate data strategies are employed throughout the thesis for testing the significance of the quantities computed at the level of individual realizations of the observed variables.

A.2.1. Surrogates for testing auto-dependencies in univariate processes

The statistical assessment of measures evaluating auto-dependencies in univariate processes – such as entropy rate and information storage, described in Chapter 3 and involved in the decomposition strategies presented in Chapter 4 – is performed by using the *Random Shuffling* surrogates. In the standard approach, as adopted in this thesis, the temporal order of the samples in the observed time series is randomly permuted under the null hypothesis that the process does not exhibit self-dependencies. This procedure generates independent and identically distributed realizations that preserve the original mean, variance, and probability distribution, while completely destroying the temporal structure of the signal (Theiler et al. (1992); Barà et al. (2023b)). Accordingly, entropy rate values are considered as statistically significant when the value computed on the original series is lower than the $100\alpha^{th}$ percentile of the surrogate distribution, whereas information storage is deemed as significant when its value exceeds the $100(1-\alpha)^{th}$ percentile.

More recently, a refined surrogate-based approach for testing auto-dependencies was proposed by Pinto et al. (2024). In this framework, after constructing the observation matrix for a given embedding dimension, the shuffling procedure is applied only to the column representing the present state of the time series. This removes dependencies between present and past samples while preserving the embedded past structure, enabling a more targeted assessment of dynamical dependencies.

A.2.2. Surrogates for testing dynamic coupling in bivariate processes

The statistically significance of coupling and causality measures described in Chapter 4 – including mutual information rate and the partial information, as well as related quantities of transfer entropy, cross entropy, joint entropy rate, and conditional self-entropy – is assessed in this thesis using the *Temporal Shift* surrogate strategy. In this approach, surrogate data are generated by destroying the coupling

between two processes while maintaining individual statistical properties. This is achieved by temporally shifting one of the two time series – typically with circular wrapping – while leaving the other unchanged (Barà et al., 2023b). Accordingly, coupling measures are evaluated against the null hypothesis that the two processes are statistically independent. In this case, the lag of the temporal shift must be set accounting for the possible interaction delay between the two processes. By repeating the surrogate generating procedure multiple times, the values computed on the original data are deemed as statistically significant if they fall below the $100\alpha^{th}$ percentile for conditional entropy-based measures, or above the $(1-\alpha)^{th}$ percentile for mutual information or conditional mutual information measures.

Also in this case, recent refined surrogate-based strategies have been proposed (Pinto et al., 2024). In particular, after constructing the observation matrix of the two processes, a shuffling procedure is applied among the row of the sub-matrix representative of the realizations of one of the two processes. This procedure disrupts the coupling between the processes while preserving the internal temporal structure of each signal, enabling a more controlled assessment of interdependence.

A.2.3. Surrogates for testing nonlinear dynamics in univariate processes

The presence of nonlinearity in univariate metrics is assessed using the *Iterative Amplitude Adjusted Fourier Transform* (IAAFT) surrogate method (Schreiber and Schmitz, 1996). This approach iteratively adjust the Fourier amplitudes of the original time series to generate surrogate data that preserve the linear properties of the signal, i.e., its power spectrum and amplitude distribution, while destroying nonlinear temporal dependencies. As a result, the generated surrogates represent realizations of linear stochastic processes with the same autocorrelation structure and probability distribution as the original data, with the power spectrum approximating that of the original series depending on the number of iterations (Pinto et al., 2024). Accordingly, the metrics are evaluated under the null hypothesis that the observed data originate from a Gaussian linear stochastic process. The surrogate procedure is repeated multiple time to construct surrogate distribution, and the null hypothesis is rejected if the entropy rate computed on the original series falls below the $100\alpha^{th}$ percentile or the information storage exceeds the $(1-\alpha)^{th}$ percentile of the surrogate distribution, thereby indicating the presence of nonlinear dynamics.

A.2.4. Surrogates for testing nonlinear interactions in bivariate processes

The presence of nonlinear interactions in bivariate processes can be assessed using the *bivariate Iterative Amplitude Adjusted Fourier Transform* surrogate method (Lancaster et al., 2018). In this approach, the same random phase shifts are applied to the Fourier components of both series, thereby preserving not only individual spectra

of the two processes, but also their cross-spectral structure, while disrupting nonlinear dependencies between the past and present states (Prichard and Theiler, 1994). Accordingly, interaction measures are evaluated under the null hypothesis that the bivariate process exhibits only linear correlations, or equivalently, the data arises from a multivariate Gaussian process.

As in the univariate case, the null hypothesis is rejected if the conditional entropy-based measures computed on the original data falls below the $100\alpha^{th}$ percentile or the mutual information or conditional mutual information measures exceeds the $(1-\alpha)^{th}$ percentile of the surrogate distribution, thereby indicating the presence of nonlinear interaction dynamics.

A.2.5. Surrogate for testing dependencies among variables

To test dependencies in among node activities in a static network, the *Random Shuffling* approach can be employed. As already mentioned, this method consists in generating independent realizations of the original variables – presenting their marginal properties, such as mean, variance, and probability distribution – by randomly permuting the sample order. In this way, any dependence between variables is destroyed, and interaction measures computed on surrogate data are expected to be centered around zero. consequently, the value obtained on the original data is deemed as statistically significant if it exceeds the $100(1-\alpha)^{th}$ percentile of the surrogate distribution.

In this thesis, this strategy was used to assess the significance of the high-order measures described in Chapter 5. In particular, the significance of the MI terms involved by the PID framework was evaluated by randomizing the samples of one of the two variables. To account for multiple hypothesis testing, significance thresholds were adjusted using Bonferroni correction (see details in Sect. 5.2.3).

The same approach was also applied to evaluate the statistical significance of the quantities involved in the feature selection and feature importance strategies described in Chapter 11. As detailed in Sects. 11.2 and 11.3, the significance of the MI term between the class variable C and a candidate feature F_j was tested under the null hypothesis of independence of the feature with the class, implemented by random shuffling of the samples of F_j. In the FS procedure, the significance of the CMI terms, computed between C and F_j conditioned on the set of selected features $\boldsymbol{F}_s$, was assessed under the null hypothesis of independence between C and $\boldsymbol{F}_s$, achieved by random shuffling of the samples of C (Iovino et al., 2026). Similarly, in the FI strategy, the significance of the differences between CMI values computed at consecutive iterative steps was evaluated by generating surrogate data through random shuffling of the candidate feature F_j, under the null hypothesis that F_j does not contribute to the observed variation (Lazic et al., 2026).

Bibliography

H. Akaike. A new look at the statistical model identification. *IEEE transactions on automatic control*, 19(6):716–723, 1974.

D. Al-Shammary, M. Radhi, A. H. Alsaeedi, A. M. Mahdi, A. Ibaida, and K. Ahmed. Efficient ECG classification based on the probabilistic kullback-leibler divergence. *Informatics in medicine unlocked*, 47:101510, 2024.

P. J. Allen, O. Josephs, and R. Turner. A method for removing imaging artifact from continuous EEG recorded during functional MRI. *Neuroimage*, 12(2):230–239, 2000.

C. Alonso-Montes, I. Diez, L. Remaki, I. Escudero, B. Mateos, Y. Rosseel, D. Marinazzo, S. Stramaglia, and J. M. Cortes. Lagged and instantaneous dynamical influences related to brain structural connectivity. *Frontiers in Psychology*, 6:1024, 2015.

J. M. Amigó, K. Keller, and V. A. Unakafova. On entropy, entropy-like quantities, and applications. *Discrete Contin. Dyn. Syst. B*, 20:3301–3343, 2015.

D. Anastassiou. Computational analysis of the synergy among multiple interacting genes. *Molecular systems biology*, 3:83, 2007.

P. W. Anderson. More is different: broken symmetry and the nature of the hierarchical structure of science. *Science*, 177(4047):393–396, 1972.

Y. Antonacci, L. Astolfi, G. Nollo, and L. Faes. Information transfer in linear multivariate processes assessed through penalized regression techniques: validation and application to physiological networks. *Entropy*, 22(7):732, 2020.

Y. Antonacci, C. Barà, A. Zaccaro, F. Ferri, L. Augugliaro, and L. Faes. Investigating the heartbeat-evoked cortical responses through parametric time-varying information measures. In *2022 12th Conference of the European Study Group on Cardiovascular Oscillations (ESGCO)*, pages 1–2. IEEE, 2022.

Y. Antonacci, C. Barà, A. Zaccaro, F. Ferri, R. Pernice, and L. Faes. Time-varying information measures: an adaptive estimation of information storage with application to brain-heart interactions. *Frontiers in Network Physiology*, 3:1242505, 2023.

Y. Antonacci, C. Barà, L. Sparacino, I. Pirovano, A. Mastropietro, G. Rizzo, and L. Faes. Spectral information dynamics of cortical signals uncover the hierarchical organization

of the human brain's motor network. *IEEE Transactions on Biomedical Engineering*, 72(5): 1655–1664, 2024.

Y. Antonacci, C. Barà, G. de Felice, A. Sferlazza, R. Pernice, and L. Faes. Exploring transient neurophysiological states through local and time-varying measures of information dynamics. *Applied Mathematics and Computation*, 500:129437, 2025a.

Y. Antonacci, C. Bará, L. Sparacino, G. Mijatovic, L. Minati, and L. Faes. A method for the time-frequency analysis of high-order interactions in non-stationary physiological networks. *Journal of Neural Engineering*, 22(6):066001, 2025b.

A. Areces-Gonzalez, D. Paz-Linares, U. Riaz, Y. Wang, M. Li, F. A. Razzaq, J. F. Bosch-Bayard, E. Gonzalez-Moreira, L. B. C. C. (LBCC), G. B. C. (GBC), et al. Ciftistorm pipeline: facilitating reproducible eeg/meg source connectomics. *Frontiers in Neuroscience*, 18:1237245, 2024.

R. L. Armentano, J. G. Barra, J. Levenson, A. Simon, and R. H. Pichel. Arterial wall mechanics in conscious dogs: assessment of viscous, inertial, and elastic moduli to characterize aortic wall behavior. *Circulation research*, 76(3):468–478, 1995.

J. Arnhold, P. Grassberger, K. Lehnertz, and C. E. Elger. A robust method for detecting interdependences: application to intracranially recorded eeg. *Physica D: Nonlinear Phenomena*, 134(4):419–430, 1999.

V. Arshinov and C. Fuchs. *Causality, emergence, self-organisation*. NIA-Priroda Moscow, 2003.

S. Arya, D. M. Mount, N. S. Netanyahu, R. Silverman, and A. Y. Wu. An optimal algorithm for approximate nearest neighbor searching fixed dimensions. *Journal of the ACM (JACM)*, 45(6):891–923, 1998.

H. Azami, L. Faes, J. Escudero, A. Humeau-Heurtier, L. E. Silva, et al. Entropy analysis of univariate biomedical signals: Review and comparison of methods. *Frontiers in Entropy across the Disciplines: Panorama of Entropy: Theory, Computation, and Applications*, pages 233–286, 2023.

D. Azzalini, I. Rebollo, and C. Tallon-Baudry. Visceral signals shape brain dynamics and cognition. *Trends in cognitive sciences*, 23(6):488–509, 2019.

M. Babo-Rebelo, C. G. Richter, and C. Tallon-Baudry. Neural responses to heartbeats in the default network encode the self in spontaneous thoughts. *Journal of Neuroscience*, 36(30): 7829–7840, 2016.

Y. Bai, K. L. Siu, S. Ashraf, L. Faes, G. Nollo, and K. H. Chon. Nonlinear coupling is absent in acute myocardial patients but not healthy subjects. *American Journal of Physiology-Heart and Circulatory Physiology*, 295(2):H578–H586, 2008.

S. S. Band, A. Yarahmadi, C.-C. Hsu, M. Biyari, M. Sookhak, R. Ameri, I. Dehzangi, A. T. Chronopoulos, and H.-W. Liang. Application of explainable artificial intelligence in medical health: A systematic review of interpretability methods. *Informatics in Medicine Unlocked*, 40:101286, 2023.

C. Bandt and B. Pompe. Permutation entropy: a natural complexity measure for time series. *Physical review letters*, 88(17):174102, 2002.

M. Bar, K. S. Kassam, A. S. Ghuman, J. Boshyan, A. M. Schmid, A. M. Dale, M. S. Hämäläinen, K. Marinkovic, D. L. Schacter, B. R. Rosen, et al. Top-down facilitation of visual recognition. *Proceedings of the national academy of sciences*, 103(2):449–454, 2006.

C. Barà, R. Pernice, L. Sparacino, Y. Antonacci, M. Javorka, and L. Faes. Analysis of cardiac pulse arrival time series at rest and during physiological stress. In *2022 IEEE 21st Mediterranean Electrotechnical Conference (MELECON)*, pages 926–931. IEEE, 2022a.

C. Barà, R. Pernice, L. Sparacino, S. Mangione, M. Javorka, and L. Faes. Transfer entropy analysis of pulse arrival time-heart period interactions during physiological stress. In *2022 12th Conference of the European Study Group on Cardiovascular Oscillations (ESGCO)*, pages 1–2. IEEE, 2022b.

C. Barà, R. Pernice, L. Sparacino, Y. Antonacci, M. Javorka, and L. Faes. Comparison of linear model-based and nonlinear model-free directional coupling measures: Analysis of cardiovascular and cardiorespiratory interactions at rest and during physiological stress. In *Mediterranean Conference on Medical and Biological Engineering and Computing*, pages 155–163. Springer, 2023a.

C. Barà, L. Sparacino, R. Pernice, Y. Antonacci, A. Porta, D. Kugiumtzis, and L. Faes. Comparison of discretization strategies for the model-free information-theoretic assessment of short-term physiological interactions. *Chaos: An Interdisciplinary Journal of Nonlinear Science*, 33(3), 2023b.

C. Barà, A. Zaccaro, Y. Antonacci, M. Dalla Riva, A. Busacca, F. Ferri, L. Faes, and R. Pernice. Local and global measures of information storage for the assessment of heartbeat-evoked cortical responses. *Biomedical Signal Processing and Control*, 86:105315, 2023c.

C. Barà, Y. Antonacci, M. Javorka, and L. Faes. An approach to decompose the information shared between cardiovascular and respiratory physiological systems. In *Computing in Cardiology Conference (CinC)*, volume 51, 2024a.

C. Barà, Y. Antonacci, M. Javorka, and L. Faes. Role of arterial pressure changes on the time-lagged baroreflex response. In *2024 13th Conference of the European Study Group on Cardiovascular Oscillations (ESGCO)*, pages 1–2. IEEE, 2024b.

C. Barà, R. Pernice, C. A. Catania, M. Hilal, A. Porta, A. Humeau-Heurtier, and L. Faes. Comparison of entropy rate measures for the evaluation of time series complexity: Simulations and application to heart rate and respiratory variability. *Biocybernetics and Biomedical Engineering*, 44(2):380–392, 2024c.

C. Barà, Y. Antonacci, M. Iovino, I. Lazic, and L. Faes. Partial information decomposition for discrete target and continuous source random variables. *Phys. Rev. E*, 112:L012301, Jul 2025a.

C. Barà, Y. Antonacci, L. Sparacino, A. A. Gonzalez, M. Zhao, L. Fu, P. A. Valdes-Sosa, H. Ito, M. Frasca, L. Faes, and L. Minati. Redundant and synergistic interactions in a complex network of single-transistor electronic chaotic oscillators and in neurophysiological recordings. *Submitted to Chaos: An Interdisciplinary Journal of Nonlinear Science. arXiv preprint arXiv:2512.13570*, 2025b.

C. Barà, Y. Antonacci, L. Sparacino, S. Stramaglia, and L. Faes. Investigating high-order

interactions among physiological variables using predictability and information-theoretic measures. In *2025 47th Annual International Conference of the IEEE Engineering in Medicine and Biology Society (EMBC)*, pages 1–4. IEEE, 2025c.

C. Barà, Y. Antonacci, L. Sparacino, H. Pinto, M. Javorka, S. Stramaglia, and L. Faes. Investigating high-order behaviors in multivariate cardiovascular interactions via nonlinear prediction and information-theoretic tools. *IEEE Transactions on Biomedical Engineering.*, 2026a.

C. Barà, L. Sparacino, L. Faes, and M. Javorka. Direct causality measures unravel complex networks of cardiovascular dynamics and their modifications with postural stress. *PLOS Computational Biology*, 22(3):e1014075, 2026b.

R. Barbieri, E. C. Matten, A. A. Alabi, and E. N. Brown. A point-process model of human heartbeat intervals: new definitions of heart rate and heart rate variability. *American Journal of Physiology-Heart and Circulatory Physiology*, 288(1):H424–H435, 2005.

L. Barnett and A. K. Seth. The MVGC multivariate granger causality toolbox: a new approach to granger-causal inference. *Journal of neuroscience methods*, 223:50–68, 2014.

L. Barnett and A. K. Seth. Granger causality for state-space models. *Physical Review E*, 91(4): 040101, 2015.

L. Barnett, A. B. Barrett, and A. K. Seth. Granger causality and transfer entropy are equivalent for gaussian variables. *Physical review letters*, 103(23):238701, 2009.

A. B. Barrett. Exploration of synergistic and redundant information sharing in static and dynamical gaussian systems. *Physical Review E*, 91(5):052802, 2015.

A. B. Barrett, L. Barnett, and A. K. Seth. Multivariate granger causality and generalized variance. *Physical Review E—Statistical, Nonlinear, and Soft Matter Physics*, 81(4):041907, 2010.

R. P. Bartsch, A. Y. Schumann, J. W. Kantelhardt, T. Penzel, and P. C. Ivanov. Phase transitions in physiologic coupling. *Proceedings of the National Academy of Sciences*, 109(26):10181–10186, 2012.

R. P. Bartsch, K. K. Liu, A. Bashan, and P. C. Ivanov. Network physiology: how organ systems dynamically interact. *PloS one*, 10(11):e0142143, 2015.

G. Baselli, A. Porta, and M. Pagani. Coupling arterial windkessel with peripheral vasomotion: modeling the effects on low-frequency oscillations. *IEEE transactions on biomedical engineering*, 53(1):53–64, 2005.

A. Bashan, R. P. Bartsch, J. W. Kantelhardt, S. Havlin, and P. C. Ivanov. Network physiology reveals relations between network topology and physiological function. *Nature communications*, 3(1):702, 2012.

F. Battiston, G. Cencetti, I. Iacopini, V. Latora, M. Lucas, A. Patania, J.-G. Young, and G. Petri. Networks beyond pairwise interactions: Structure and dynamics. *Physics reports*, 874:1–92, 2020.

R. Battiti. Using mutual information for selecting features in supervised neural net learning. *IEEE Transactions on neural networks*, 5(4):537–550, 1994.

A. H. Bell, F. Hadj-Bouziane, J. B. Frihauf, R. B. Tootell, and L. G. Ungerleider. Object representations in the temporal cortex of monkeys and humans as revealed by functional magnetic resonance imaging. *Journal of neurophysiology*, 101(2):688–700, 2009.

G. G. Belz. Elastic properties and windkessel function of the human aorta. *Cardiovascular drugs and therapy*, 9(1):73–83, 1995.

T. Benichou, B. Pereira, M. Mermillod, I. Tauveron, D. Pfabigan, S. Maqdasy, and F. Dutheil. Heart rate variability in type 2 diabetes mellitus: A systematic review and meta–analysis. *PloS one*, 13(4):e0195166, 2018.

C. Berge. *Hypergraphs: combinatorics of finite sets*, volume 45. Elsevier, 1984.

D. Bernardi and B. Lindner. A frequency-resolved mutual information rate and its application to neural systems. *Journal of neurophysiology*, 113(5):1342–1357, 2015.

D. P. Bernstein. Continuous noninvasive real-time monitoring of stroke volume and cardiac output by thoracic electrical bioimpedance. *Critical care medicine*, 14(10):898–901, 1986.

G. G. Berntson, J. T. Cacioppo, and K. S. Quigley. Respiratory sinus arrhythmia: Autonomic origins, physiological mechanisms, and psychophysiological implications. *Psychophysiology*, 30(2):183–196, 1993.

G. G. Berntson, J. T. Cacioppo, P. F. Binkley, B. N. Uchino, K. S. Quigley, and A. Fieldstone. Autonomic cardiac control. iii. psychological stress and cardiac response in autonomic space as revealed by pharmacological blockades. *Psychophysiology*, 31(6):599–608, 1994.

N. Bertschinger, J. Rauh, E. Olbrich, and J. Jost. Shared information—new insights and problems in decomposing information in complex systems. In *Proceedings of the European conference on complex systems 2012*, pages 251–269. Springer, 2012.

N. Bertschinger, J. Rauh, E. Olbrich, J. Jost, and N. Ay. Quantifying unique information. *Entropy*, 16(4):2161–2183, 2014.

V. Binson, S. Thomas, M. Subramoniam, J. Arun, S. Naveen, and S. Madhu. A review of machine learning algorithms for biomedical applications. *Annals of Biomedical Engineering*, 52(5):1159–1183, 2024.

C. M. Bishop and N. M. Nasrabadi. *Pattern recognition and machine learning*, volume 4. Springer, 2006.

O. Blanke, L. Spinelli, G. Thut, C. M. Michel, S. Perrig, T. Landis, and M. Seeck. Location of the human frontal eye field as defined by electrical cortical stimulation: anatomical, functional and electrophysiological characteristics. *Neuroreport*, 11(9):1907–1913, 2000.

S. Boccaletti, V. Latora, Y. Moreno, M. Chavez, and D.-U. Hwang. Complex networks: Structure and dynamics. *Physics reports*, 424(4-5):175–308, 2006.

A. Borst and F. E. Theunissen. Information theory and neural coding. *Nature neuroscience*, 2 (11):947–957, 1999.

L. Breiman. Random forests mach. learn., 45 (1), 5–32. *ed*, 2001.

S. L. Bressler and A. K. Seth. Wiener–granger causality: a well established methodology. *Neuroimage*, 58(2):323–329, 2011.

G. Brown, A. Pocock, M.-J. Zhao, and M. Luján. Conditional likelihood maximisation: a

unifying framework for information theoretic feature selection. *The journal of machine learning research*, 13:27–66, 2012.

T. E. Brown, L. A. Beightol, J. Koh, and D. L. Eckberg. Important influence of respiration on human RR interval power spectra is largely ignored. *Journal of applied physiology*, 75(5): 2310–2317, 1993.

F. Buccelletti, E. Gilardi, E. Scaini, L. Galiuto, R. Persiani, A. Biondi, F. Basile, and N. G. Silveri. Heart rate variability and myocardial infarction: systematic literature review and metanalysis. *European Review for Medical & Pharmacological Sciences*, 13(4), 2009.

T. G. Buchman. Physiologic failure: multiple organ dysfunction syndrome. In *Complex systems science in biomedicine*, pages 631–640. Springer, 2006.

R. L. Buckner, J. R. Andrews-Hanna, and D. L. Schacter. The brain's default network: anatomy, function, and relevance to disease. *Annals of the new York Academy of Sciences*, 1124(1):1–38, 2008.

D. A. Burton, K. Stokes, and G. M. Hall. Physiological effects of exercise. *Continuing Education in Anaesthesia, Critical Care & Pain*, 4(6):185–188, 2004.

T. Buzug and G. Pfister. Optimal delay time and embedding dimension for delay-time coordinates by analysis of the global static and local dynamical behavior of strange attractors. *Physical review A*, 45(10):7073, 1992.

B. Cairo, V. Bari, F. Gelpi, B. De Maria, and A. Porta. Assessing cardiorespiratory interactions via lagged joint symbolic dynamics during spontaneous and controlled breathing. *Frontiers in Network Physiology*, 3:1211848, 2023.

O. G. Cameron. *Visceral sensory neuroscience: Interoception*. Oxford University Press, 2001.

O. G. Cameron. Visceral brain–body information transfer. *Neuroimage*, 47(3):787–794, 2009.

A. J. Camm, M. Malik, J. T. Bigger, G. Breithardt, S. Cerutti, R. J. Cohen, P. Coumel, E. L. Fallen, H. L. Kennedy, R. E. Kleiger, et al. Heart rate variability: standards of measurement, physiological interpretation and clinical use. Task force of the european society of cardiology and the north american society of pacing and electrophysiology. *Circulation*, 93(5):1043–1065, 1996.

D. Candia-Rivera. Brain-heart interactions in the neurobiology of consciousness. *Current Research in Neurobiology*, 3:100050, 2022.

D. Candia-Rivera, V. Catrambone, R. Barbieri, and G. Valenza. Integral pulse frequency modulation model driven by sympathovagal dynamics: Synthetic vs. real heart rate variability. *Biomedical Signal Processing and Control*, 68:102736, 2021.

D. Candia-Rivera, L. Faes, F. de Vico Fallani, and M. Chavez. Measures and models of brain-heart interactions. *IEEE Reviews in Biomedical Engineering*, 2025.

J. Cannon. The fractal geometry of nature. by benoit b. mandelbrot. *The American Mathematical Monthly*, 91(9):594–598, 1984.

C. A. Carrington and M. J. White. Spontaneous baroreflex sensitivity in young and older people during voluntary and electrically evoked isometric exercise. *Age and Ageing*, 31(5): 359–364, 2002.

R. Castaldo, L. Montesinos, P. Melillo, C. James, and L. Pecchia. Ultra-short term hrv features as surrogates of short term HRV: A case study on mental stress detection in real life. *BMC medical informatics and decision making*, 19(1):12, 2019.

P. Castiglioni, G. Merati, G. Parati, and A. Faini. Sample, fuzzy and distribution entropies of heart rate variability: What do they tell us on cardiovascular complexity? *Entropy*, 25 (2):281, 2023.

P. Castiglioni, A. Zaza, G. Merati, and A. Faini. On the autonomic control of heart rate variability: How the mean heart rate affects spectral and complexity analysis and a way to mitigate its influence. *Mathematics*, 13(18):2955, 2025.

O. Catalina-Rodriguez, V. K. Kolukula, Y. Tomita, A. Preet, F. Palmieri, A. Wellstein, S. Byers, A. J. Giaccia, E. Glasgow, C. Albanese, et al. The mitochondrial citrate transporter, cic, is essential for mitochondrial homeostasis. *Oncotarget*, 3(10):1220, 2012.

A. Catav, B. Fu, Y. Zoabi, A. L. W. Meilik, N. Shomron, J. Ernst, S. Sankararaman, and R. Gilad-Bachrach. Marginal contribution feature importance-an axiomatic approach for explaining data. In *International Conference on Machine Learning*, pages 1324–1335. PMLR, 2021.

V. Catrambone, R. Barbieri, H. Wendt, P. Abry, and G. Valenza. Functional brain–heart interplay extends to the multifractal domain. *Philosophical Transactions of the Royal Society A: Mathematical, Physical and Engineering Sciences*, 379(2212), 2021.

A. Chaddha, M. Rafanelli, M. Brignole, R. Sutton, K. E. Wenzke, S. L. Wasmund, R. L. Page, and M. H. Hamdan. The pathophysiologic mechanisms associated with hypotensive susceptibility. *Clinical Autonomic Research*, 26(4):261–268, 2016.

K. Chakir, S. K. Daya, T. Aiba, R. S. Tunin, V. L. Dimaano, T. P. Abraham, K. Jaques, E. W. Lai, K. Pacak, W.-Z. Zhu, et al. Mechanisms of enhanced β-adrenergic reserve from cardiac resynchronization therapy. *Circulation*, 119(9):1231–1240, 2009.

G. Chandrashekar and F. Sahin. A survey on feature selection methods. *Computers & electrical engineering*, 40(1):16–28, 2014.

C. Chen, Y. Jin, I. L. Lo, H. Zhao, B. Sun, Q. Zhao, J. Zheng, and X. D. Zhang. Complexity change in cardiovascular disease. *International journal of biological sciences*, 13(10):1320, 2017.

C.-M. Chen, S. Anastasova, K. Zhang, B. G. Rosa, B. P. Lo, H. E. Assender, and G.-Z. Yang. Towards wearable and flexible sensors and circuits integration for stress monitoring. *IEEE Journal of Biomedical and Health Informatics*, 24(8):2208–2215, 2019.

J. Chen, L. Song, M. Wainwright, and M. Jordan. Learning to explain: An information-theoretic perspective on model interpretation. In *International conference on machine learning*, pages 883–892. PMLR, 2018.

W. Chen, J. Zhuang, W. Yu, and Z. Wang. Measuring complexity using FuzzyEn, ApEn, and SampEn. *Medical engineering & physics*, 31(1):61–68, 2009.

W. G. Chen, D. Schloesser, A. M. Arensdorf, J. M. Simmons, C. Cui, R. Valentino, J. W. Gnadt, L. Nielsen, C. S. Hillaire-Clarke, V. Spruance, et al. The emerging science of interoception:

sensing, integrating, interpreting, and regulating signals within the self. *Trends in neurosciences*, 44(1):3–16, 2021.

D. Chicharro. On the spectral formulation of granger causality. *Biological cybernetics*, 105: 331–347, 2011.

D. Chicharro, A. Ledberg, et al. Framework to study dynamic dependencies in networks of interacting processes. *Phys. Rev. E*, 86(4):041901, 2012.

S. A. Chouhan. Supervised information gain-based feature selection for multimodal physiological signals in stress prediction. *Scientific Reports*, 2026.

S. Cimignolo, C. Barà, R. Pernice, L. Faes, G. Nollo, and M. Masè. A framework based on information dynamics to assess and dissect complex cardiovascular interactions across pathophysiological states. *Submitted to Biocybernetics and Biomedical Engineering*, 2025a.

S. Cimignolo, C. Barà, R. Pernice, M. Masè, G. Nollo, and L. Faes. Assessment of cardiovascular coupling during rest and postural stress using mutual information rate. In *Proceedings of the Nineth National Congress of Bioengineering*. Pàtron editore, 2025b.

O. M. Cliff, L. Novelli, B. D. Fulcher, J. M. Shine, and J. T. Lizier. Assessing the significance of directed and multivariate measures of linear dependence between time series. *Physical Review Research*, 3(1):013145, 2021.

G. D. Clifford, F. Azuaje, P. Mcsharry, et al. ECG statistics, noise, artifacts, and missing data. *Advanced methods and tools for ECG data analysis*, 6(1):18, 2006.

F. Coelho, A. P. Braga, and M. Verleysen. A mutual information estimator for continuous and discrete variables applied to feature selection and classification problems. *International Journal of Computational Intelligence Systems*, 9(4):726–733, 2016.

J. Cohen. *Statistical power analysis for the behavioral sciences*. routledge, 2013.

M. A. Cohen and J. A. Taylor. Short-term cardiovascular oscillations in man: measuring and modelling the physiologies. *The Journal of physiology*, 542(3):669–683, 2002.

W. H. Cooke, J. B. Hoag, A. A. Crossman, T. A. Kuusela, K. U. Tahvanainen, and D. L. Eckberg. Human responses to upright tilt: a window on central autonomic integration. *The Journal of physiology*, 517(2):617–628, 1999.

T. M. Cover. *Elements of information theory*. John Wiley & Sons, 1999.

I. Covert, S. M. Lundberg, and S.-I. Lee. Understanding global feature contributions with additive importance measures. *Advances in neural information processing systems*, 33:17212–17223, 2020.

I. Csiszár. I-divergence geometry of probability distributions and minimization problems. *The annals of probability*, pages 146–158, 1975.

D. Cuesta-Frau. Slope entropy: A new time series complexity estimator based on both symbolic patterns and amplitude information. *Entropy*, 21(12):1167, 2019.

D. Cuesta Frau, P. Miró Martínez, S. Oltra Crespo, A. Molina Picó, B. Vargas, P. González, C. Mahabala, and H. D. Pradeepa. Classification of fever patterns using a single extracted entropy feature: A feasibility study based on sample entropy. *Mathematical Biosciences and Engineering*, 17(1):235–249, 2019.

R. S. Cunha, B. Pannier, A. Benetos, J.-P. Siché, G. M. London, J. M. Mallion, and M. E. Safar. Association between high heart rate and high arterial rigidity in normotensive and hypertensive subjects. *Journal of hypertension*, 15(12):1423–1430, 1997.

M. Dani, P. Taraborrelli, D. Panagopoulos, A. Dirksen, M. Torocastro, R. Sutton, and P. B. Lim. New horizons in the ageing autonomic nervous system: orthostatic hypotension and supine hypertension. *Age and Ageing*, 51(8):afac150, 2022.

M. Dastgoshadeh and Z. Rabiei. Detection of epileptic seizures through EEG signals using entropy features and ensemble learning. *Frontiers in human neuroscience*, 16:1084061, 2023.

C. Daubert, N. Behar, R. P. Martins, P. Mabo, and C. Leclercq. Avoiding non-responders to cardiac resynchronization therapy: a practical guide. *European heart journal*, 38(19): 1463–1472, 2017.

Š. David and M. Javorka. Noninvasive arterial compliance estimation. *Physiological Research*, 70(Suppl 4):S483, 2021.

B. De Maria, L. A. Dalla Vecchia, R. Maestri, G. D. Pinna, M. Parati, F. Perego, V. Bari, B. Cairo, F. Gelpi, M. T. La Rovere, et al. Lack of association between heart period variability asymmetry and respiratory sinus arrhythmia in healthy and chronic heart failure individuals. *PLoS One*, 16(2):e0247145, 2021.

R. W. DeBoer, J. M. Karemaker, and J. Strackee. Hemodynamic fluctuations and baroreflex sensitivity in humans: a beat-to-beat model. *American Journal of Physiology-Heart and Circulatory Physiology*, 253(3):H680–H689, 1987.

E. A. Deitch. Multiple organ failure pathophysiology and potential future therapy. *Annals of surgery*, 216(2):117–134, 1992.

M. Del Greco, G. Nollo, M. Disertori, G. Sanna, and A. Maggioni. Non-invasive assessment of the arrhythmogenic substrate after myocardial infarction in thrombolytic era: Gissi-3 arrhythmias substudy. 1998.

R. S. Desikan, F. Ségonne, B. Fischl, B. T. Quinn, B. C. Dickerson, D. Blacker, R. L. Buckner, A. M. Dale, R. P. Maguire, B. T. Hyman, et al. An automated labeling system for subdividing the human cerebral cortex on mri scans into gyral based regions of interest. *Neuroimage*, 31(3):968–980, 2006.

S. Dhesi, E. Lockwood, and R. K. Sandhu. Troubleshooting cardiac resynchronization therapy in nonresponders. *Canadian Journal of Cardiology*, 33(8):1060–1065, 2017.

M. Di Rienzo, P. Castiglioni, G. Mancia, A. Pedotti, and G. Parati. Advancements in estimating baroreflex function. *IEEE Engineering in Medicine and Biology Magazine*, 20(2):25–32, 2001.

D. Dias and J. Paulo Silva Cunha. Wearable health devices—vital sign monitoring, systems and technologies. *Sensors*, 18(8):2414, 2018.

T. E. Dick, Y.-H. Hsieh, R. R. Dhingra, D. M. Baekey, R. F. Galán, E. Wehrwein, and K. F. Morris. Cardiorespiratory coupling: common rhythms in cardiac, sympathetic, and respiratory activities. *Progress in brain research*, 209:191–205, 2014.

G. Dirlich, L. Vogl, M. Plaschke, and F. Strian. Cardiac field effects on the EEG. *Electroencephalography and clinical neurophysiology*, 102(4):307–315, 1997.

D. P. Doane. Aesthetic frequency classifications. *The American Statistician*, 30(4):181–183, 1976.

R. Draelos. Connections: Log-Likelihood, Cross-Entropy, KL-Divergence, Logistic Regression, and Neural Networks. *GlassBox Medicine*, 2019.

A. E. Draghici and J. A. Taylor. The physiological basis and measurement of heart rate variability in humans. *Journal of physiological anthropology*, 35(1):22, 2016.

N. R. Draper and H. Smith. *Applied regression analysis*, volume 326. John Wiley & Sons, 1998.

T. E. Duncan. On the calculation of mutual information. *SIAM Journal on Applied Mathematics*, 19(1):215–220, 1970.

D. L. Eckberg. Point: counterpoint: respiratory sinus arrhythmia is due to a central mechanism vs. respiratory sinus arrhythmia is due to the baroreflex mechanism. *Journal of applied physiology*, 2009.

D. A. Ehrlich, K. Schick-Poland, A. Makkeh, F. Lanfermann, P. Wollstadt, and M. Wibral. Partial information decomposition for continuous variables based on shared exclusions: Analytical formulation and estimation. *Physical Review E*, 110(1):014115, 2024.

M. Elstad, L. Walløe, K. H. Chon, and K. Toska. Low-frequency fluctuations in heart rate, cardiac output and mean arterial pressure in humans: what are the physiological relationships? *Journal of hypertension*, 29(7):1327–1336, 2011.

M. Elstad, E. L. O'Callaghan, A. J. Smith, A. Ben-Tal, and R. Ramchandra. Cardiorespiratory interactions in humans and animals: rhythms for life. *American Journal of Physiology-Heart and Circulatory Physiology*, 315(1):H6–H17, 2018.

B. Fadlallah, B. Chen, A. Keil, and J. Príncipe. Weighted-permutation entropy: A complexity measure for time series incorporating amplitude information. *Physical Review E—Statistical, Nonlinear, and Soft Matter Physics*, 87(2):022911, 2013.

L. Faes and A. Porta. Conditional entropy-based evaluation of information dynamics in physiological systems. In *Directed information measures in neuroscience*, pages 61–86. Springer, 2014.

L. Faes, G. Nollo, and K. H. Chon. Assessment of granger causality by nonlinear model identification: application to short-term cardiovascular variability. *Annals of biomedical engineering*, 36(3):381–395, 2008a.

L. Faes, A. Porta, and G. Nollo. Mutual nonlinear prediction as a tool to evaluate coupling strength and directionality in bivariate time series: comparison among different strategies based on k nearest neighbors. *Physical Review E—Statistical, Nonlinear, and Soft Matter Physics*, 78(2):026201, 2008b.

L. Faes, H. Zhao, K. H. Chon, and G. Nollo. Time-varying surrogate data to assess nonlinearity in nonstationary time series: application to heart rate variability. *IEEE transactions on biomedical engineering*, 56(3):685–695, 2008c.

L. Faes, G. Nollo, and A. Porta. Information domain approach to the investigation of cardiovascular, cardio-pulmonary, and vasculo-pulmonary causal couplings. *Frontiers in physiology*, 2:80, 2011.

L. Faes, S. Erla, and G. Nollo. Measuring connectivity in linear multivariate processes: definitions, interpretation, and practical analysis. *Computational and mathematical methods in medicine*, 2012(1):140513, 2012a.

L. Faes, G. Nollo, and A. Porta. Non-uniform multivariate embedding to assess the information transfer in cardiovascular and cardiorespiratory variability series. *Computers in biology and medicine*, 42(3):290–297, 2012b.

L. Faes, S. Erla, A. Porta, and G. Nollo. A framework for assessing frequency domain causality in physiological time series with instantaneous effects. *Philosophical Transactions of the Royal Society A: Mathematical, Physical and Engineering Sciences*, 371(1997):20110618, 2013a.

L. Faes, G. Nollo, and A. Porta. Compensated transfer entropy as a tool for reliably estimating information transfer in physiological time series. *Entropy*, 15(1):198–219, 2013b.

L. Faes, D. Marinazzo, A. Montalto, and G. Nollo. Lag-specific transfer entropy as a tool to assess cardiovascular and cardiorespiratory information transfer. *IEEE Transactions on Biomedical Engineering*, 61(10):2556–2568, 2014a.

L. Faes, G. Nollo, F. Jurysta, and D. Marinazzo. Information dynamics of brain–heart physiological networks during sleep. *New Journal of Physics*, 16(10):105005, 2014b.

L. Faes, D. Kugiumtzis, G. Nollo, F. Jurysta, and D. Marinazzo. Estimating the decomposition of predictive information in multivariate systems. *Physical Review E*, 91(3):032904, 2015a.

L. Faes, D. Marinazzo, F. Jurysta, and G. Nollo. Linear and non-linear brain–heart and brain–brain interactions during sleep. *Physiological measurement*, 36(4):683–698, 2015b.

L. Faes, A. Porta, and G. Nollo. Information decomposition in bivariate systems: theory and application to cardiorespiratory dynamics. *Entropy*, 17(1):277–303, 2015c.

L. Faes, D. Marinazzo, G. Nollo, and A. Porta. An information-theoretic framework to map the spatiotemporal dynamics of the scalp electroencephalogram. *IEEE Transactions on Biomedical Engineering*, 63(12):2488–2496, 2016a.

L. Faes, A. Porta, G. Nollo, and M. Javorka. Information decomposition in multivariate systems: definitions, implementation and application to cardiovascular networks. *Entropy*, 19(1):5, 2016b.

L. Faes, M. Gómez-Extremera, R. Pernice, P. Carpena, G. Nollo, A. Porta, and P. Bernaola-Galván. Comparison of methods for the assessment of nonlinearity in short-term heart rate variability under different physiopathological states. *Chaos: An Interdisciplinary Journal of Nonlinear Science*, 29(12), 2019a.

L. Faes, M. A. Pereira, M. E. Silva, R. Pernice, A. Busacca, M. Javorka, and A. P. Rocha. Multiscale information storage of linear long-range correlated stochastic processes. *Physical Review E*, 99(3):032115, 2019b.

L. Faes, G. Mijatovic, Y. Antonacci, R. Pernice, C. Barà, L. Sparacino, M. Sammartino, A. Porta, D. Marinazzo, and S. Stramaglia. A new framework for the time-and frequency-domain assessment of high-order interactions in networks of random processes. *IEEE Transactions on Signal Processing*, 70:5766–5777, 2022.

L. Faes, L. Sparacino, G. Mijatovic, Y. Antonacci, L. Ricci, D. Marinazzo, and S. Stramaglia. Partial information rate decomposition. *Physical Review Letters*, 135(18):187401, 2025.

K. Falconer. Box counting dimensions. *Fractal geometry. Chichester: John Wiley & Sons*, pages 38–44, 1990.

J. D. Farmer and J. J. Sidorowich. Predicting chaotic time series. *Physical review letters*, 59(8): 845, 1987.

J. P. Fauvel, C. Cerutti, P. Quelin, M. Laville, M. P. Gustin, C. Z. Paultre, and M. Ducher. Mental stress–induced increase in blood pressure is not related to baroreflex sensitivity in middle-aged healthy men. *Hypertension*, 35(4):887–891, 2000.

D. J. Felleman and D. C. Van Essen. Distributed hierarchical processing in the primate cerebral cortex. *Cerebral cortex (New York, NY: 1991)*, 1(1):1–47, 1991.

A. Fernández, J. Quintero, R. Hornero, P. Zuluaga, M. Navas, C. Gómez, J. Escudero, N. García-Campos, J. Biederman, and T. Ortiz. Complexity analysis of spontaneous brain activity in attention-deficit/hyperactivity disorder: diagnostic implications. *Biological psychiatry*, 65(7):571–577, 2009.

A. Finnegan and J. S. Song. Maximum entropy methods for extracting the learned features of deep neural networks. *PLoS computational biology*, 13(10):e1005836, 2017.

R. Foote. Mathematics and complex systems. *science*, 318(5849):410–412, 2007.

J.-O. Fortrat, Y. Yamamoto, and R. L. Hughson. Respiratory influences on non-linear dynamics of heart rate variability in humans. *Biological cybernetics*, 77(1):1–10, 1997.

M. D. Fox and M. E. Raichle. Spontaneous fluctuations in brain activity observed with functional magnetic resonance imaging. *Nature reviews neuroscience*, 8(9):700–711, 2007.

A. M. Fraser and H. L. Swinney. Independent coordinates for strange attractors from mutual information. *Physical review A*, 33(2):1134, 1986.

K. J. Friston, L. Harrison, and W. Penny. Dynamic causal modelling. *Neuroimage*, 19(4): 1273–1302, 2003.

C. O. Fritz, P. E. Morris, and J. J. Richler. Effect size estimates: current use, calculations, and interpretation. *Journal of experimental psychology: General*, 141(1):2, 2012.

D. Galletly and P. Larsen. Relationship between cardioventilatory coupling and respiratory sinus arrhythmia. *British Journal of Anaesthesia*, 80(2):164–168, 1998.

F. Gelpi, B. Cairo, V. Bari, B. De Maria, A. S. Salinet, M. Y. Lam, O. Llwyd, J. Ince, J. S. Minhas, R. B. Panerai, et al. Cerebrovascular variability interactions after acute ischemic stroke: insights from directionality analysis based on transfer entropy. *Journal of Applied Physiology*, 139(2):341–354, 2025.

J. Geweke. Measurement of linear dependence and feedback between multiple time series. *Journal of the American statistical association*, 77(378):304–313, 1982.

F. Ghasemi, B. S. Neysiani, and N. Nematbakhsh. Feature selection in pre-diagnosis heart coronary artery disease detection: a heuristic approach for feature selection based on information gain ratio and gini index. In *2020 6th International Conference on Web Research (ICWR)*, pages 27–32. IEEE, 2020.

J. S. Gibson, G. Lee, and C.-F. Wu. Least-squares estimation of input/output models for distributed linear systems in the presence of noise. *Automatica*, 36(10):1427–1442, 2000.

L. H. Gilpin, D. Bau, B. Z. Yuan, A. Bajwa, M. Specter, and L. Kagal. Explaining explanations: An overview of interpretability of machine learning. In *2018 IEEE 5th International Conference on data science and advanced analytics (DSAA)*, pages 80–89. IEEE, 2018.

J.-M. Girault and A. Humeau-Heurtier. Centered and averaged fuzzy entropy to improve fuzzy entropy precision. *Entropy*, 20(4):287, 2018.

L. Glass. Synchronization and rhythmic processes in physiology. *Nature*, 410(6825):277–284, 2001.

A. L. Goldberger. Giles f. filley lecture. complex systems. *Proceedings of the American Thoracic Society*, 3(6):467–471, 2006.

A. L. Goldberger, L. A. Amaral, L. Glass, J. M. Hausdorff, P. C. Ivanov, R. G. Mark, J. E. Mietus, G. B. Moody, C.-K. Peng, and H. E. Stanley. Physiobank, physiotoolkit, and physionet: components of a new research resource for complex physiologic signals. *circulation*, 101(23):e215–e220, 2000.

A. L. Goldberger, C.-K. Peng, and L. A. Lipsitz. What is physiologic complexity and how does it change with aging and disease? *Neurobiology of aging*, 23(1):23–26, 2002.

C. Gómez, J. T. Lizier, M. Schaum, P. Wollstadt, C. Grützner, P. Uhlhaas, C. M. Freitag, S. Schlitt, S. Bölte, R. Hornero, et al. Reduced predictable information in brain signals in autism spectrum disorder. *Frontiers in neuroinformatics*, 8:9, 2014.

E. Gonzalez-Moreira, D. Paz-Linares, A. Areces-Gonzalez, R. Wang, J. Bosch-Bayard, M. L. Bringas-Vega, and P. A. Valdes-Sosa. Caulking the leakage effect in meeg source connectivity analysis. *arXiv preprint arXiv:1810.00786*, 2018.

J. M. Gorman and R. P. Sloan. Heart rate variability in depressive and anxiety disorders. *American heart journal*, 140(4):S77–S83, 2000.

C. W. J. Granger. Economic processes involving feedback. *Information and control*, 6(1):28–48, 1963.

P. Grassberger and I. Procaccia. Measuring the strangeness of strange attractors. *Physica D: nonlinear phenomena*, 9(1-2):189–208, 1983.

A. Greco, L. Faes, V. Catrambone, R. Barbieri, E. P. Scilingo, and G. Valenza. Lateralization of directional brain-heart information transfer during visual emotional elicitation. *American Journal of Physiology-Regulatory, Integrative and Comparative Physiology*, 317(1):R25–R38, 2019.

D. J. Grieve, J. A. Byrne, A. C. Cave, and A. M. Shah. Role of oxidative stress in cardiac remodelling after myocardial infarction. *Heart, Lung and Circulation*, 13(2):132–138, 2004.

V. Griffith. *Quantifying synergistic information*. California Institute of Technology, 2014.

K. Grill-Spector and R. Malach. The human visual cortex. *Annu. Rev. Neurosci.*, 27(1):649–677, 2004.

P. Grossman and E. W. Taylor. Toward understanding respiratory sinus arrhythmia: Relations to cardiac vagal tone, evolution and biobehavioral functions. *Biological psychology*, 74(2):263–285, 2007.

P. Grossman, F. H. Wilhelm, and M. Spoerle. Respiratory sinus arrhythmia, cardiac vagal control, and daily activity. *American Journal of Physiology-Heart and Circulatory Physiology*, 287(2):H728–H734, 2004.

D. Gu, A. Lin, and G. Lin. Sleep and cardiac signal processing using improved multivariate partial compensated transfer entropy based on non-uniform embedding. *Chaos, Solitons & Fractals*, 159:112061, 2022.

A. J. Gutknecht, M. Wibral, and A. Makkeh. Bits and pieces: Understanding information decomposition from part-whole relationships and formal logic. *Proceedings of the Royal Society A: Mathematical, Physical and Engineering Sciences*, 477(2251), 2021.

A. J. Gutknecht, A. Makkeh, and M. Wibral. From babel to boole: The logical organization of information decompositions. *Proceedings of the Royal Society A: Mathematical, Physical and Engineering Sciences*, 481(2310), 2025.

I. Guyon and A. Elisseeff. An introduction to variable and feature selection. *Journal of machine learning research*, 3(Mar):1157–1182, 2003.

P. Guzik, T. Krauze, A. Wykretowicz, and J. Piskorski. Healthy young poles–hypol database with synchronised beat-to-beat heart rate and blood pressure signals: Hypol–cardiovascular time series database. *Journal of Medical Science*, 92(4):e941–e941, 2023.

M. Harder, C. Salge, and D. Polani. Bivariate measure of redundant information. *Physical Review E—Statistical, Nonlinear, and Soft Matter Physics*, 87(1):012130, 2013.

M. E. Haroutunian and G. A. Gharagyozyan. Information theory tools and techniques to overcome machine learning challenges. *Mathematical Problems of Computer Science*, 63:25–41, 2025.

M. E. Haroutunian, D. G. Asatryan, and K. A. Mastoyan. Analyzing the quality of distorted images by the normalized mutual information measure. *Mathematical Problems of Computer Science*, 61:7–14, 2024.

S. He, K. Sun, and R. Wang. Fractional fuzzy entropy algorithm and the complexity analysis for nonlinear time series. *The European Physical Journal Special Topics*, 227:943–957, 2018.

R. Hornero, D. Abásolo, N. Jimeno, C. I. Sánchez, J. Poza, and M. Aboy. Variability, regularity, and complexity of time series generated by schizophrenic patients and control subjects. *IEEE Transactions on Biomedical Engineering*, 53(2):210–218, 2006.

B.-G. Hu. Information theory and its relation to machine learning. In *Proceedings of the 2015 Chinese Intelligent Automation Conference: Intelligent Information Processing*, pages 1–11. Springer, 2015.

Q. Hu, Y. Wei, J. Pang, and M. Liang. Unsupervised domain adaptation for brain structure segmentation via mutual information maximization alignment. *Biomedical Signal Processing and Control*, 90:105784, 2024.

H. V. Huikuri, T. Seppanen, M. J. Koistinen, K. J. Airaksinen, M. Ikaheimo, A. Castellanos, and R. J. Myerburg. Abnormalities in beat-to-beat dynamics of heart rate before the spontaneous onset of life-threatening ventricular tachyarrhythmias in patients with prior myocardial infarction. *Circulation*, 93(10):1836–1844, 1996.

J. P. Huke and D. S. Broomhead. Embedding theorems for non-uniformly sampled dynamical systems. *Nonlinearity*, 20(9):2205, 2007.

R. A. Ince. Measuring multivariate redundant information with pointwise common change in surprisal. *Entropy*, 19(7):318, 2017.

J. Innes, S. De Cort, W. Kox, and A. Guz. Within-breath modulation of left ventricular function during normal breathing and positive-pressure ventilation in man. *The Journal of physiology*, 460(1):487–502, 1993.

M. Iovino, I. Lazic, C. Barà, L. Faes, and R. Pernice. Conditional mutual information-based feature selection for sex differences characterization. In *2024 13th Conference of the European Study Group on Cardiovascular Oscillations (ESGCO)*, pages 1–2. IEEE, 2024a.

M. Iovino, I. Lazic, T. Loncar-Turukalo, M. Javorka, R. Pernice, and L. Faes. Comparison of automatic and physiologically-based feature selection methods for classifying physiological stress using heart rate and pulse rate variability indices. *Physiological Measurement*, 45 (11):115004, 2024b.

M. Iovino, M. Ontivero-Ortega, C. Barà, S. Stramaglia, M. Javorka, R. Pernice, and L. Faes. Assessing feature importance in cardiovascular variability for the classification of physiological stress. In *2025 IEEE International Conference on Omni-layer Intelligent Systems (COINS)*, pages 1–6. IEEE, 2025.

M. Iovino, I. Lazic, C. Barà, D. Kugiumtzis, L. Faes, and R. Pernice. A principled and data-efficient information-theoretic method for feature selection. *IEEE Journal of Biomedical and Health Informatics*, pages 1–13, 2026.

P. C. Ivanov. Long-range dependence in heartbeat dynamics. In *Processes with long-range correlations: Theory and applications*, pages 339–372. Springer, 2003.

P. C. Ivanov. The new field of network physiology: building the human physiolome, 2021.

P. C. Ivanov and R. P. Bartsch. Network physiology: mapping interactions between networks of physiologic networks. In *Networks of Networks: the last Frontier of Complexity*, pages 203–222. Springer, 2014.

R. G. James, N. Barnett, and J. P. Crutchfield. Information flows? a critique of transfer entropies. *Physical review letters*, 116(23):238701, 2016.

J. Jamšek, M. Paluš, and A. Stefanovska. Detecting couplings between interacting oscillators with time-varying basic frequencies: Instantaneous wavelet bispectrum and information theoretic approach. *Physical Review E—Statistical, Nonlinear, and Soft Matter Physics*, 81(3): 036207, 2010.

B. Janssen, J. Oosting, D. W. Slaaf, P. B. Persson, and H. Struijker-Boudier. Hemodynamic basis of oscillations in systemic arterial pressure in conscious rats. *American Journal of Physiology-Heart and Circulatory Physiology*, 269(1):H62–H71, 1995.

J. Janssen, V. Guan, and E. Robeva. Ultra-marginal feature importance: Learning from data with causal guarantees. In *International conference on artificial intelligence and statistics*, pages 10782–10814. PMLR, 2023.

M. Javorka, Z. Turianikova, I. Tonhajzerova, K. Javorka, and M. Baumert. The effect of or-

thostasis on recurrence quantification analysis of heart rate and blood pressure dynamics. *Physiological measurement*, 30(1):29, 2008.

M. Javorka, J. Krohova, B. Czippelova, Z. Turianikova, Z. Lazarova, K. Javorka, and L. Faes. Basic cardiovascular variability signals: mutual directed interactions explored in the information domain. *Physiological Measurement*, 38(5):877, 2017.

M. Javorka, J. Krohova, B. Czippelova, Z. Turianikova, Z. Lazarova, R. Wiszt, and L. Faes. Towards understanding the complexity of cardiovascular oscillations: Insights from information theory. *Computers in biology and medicine*, 98:48–57, 2018.

E. T. Jaynes. Information theory and statistical mechanics. *Physical review*, 106(4):620, 1957.

P. M. Jeyanthi, T. Choudhury, D. Hack-Polay, T. P. Singh, and S. Abujar. *Decision intelligence analytics and the implementation of strategic business management*. Springer, 2022.

X. Jia, L. Ren, and J. Cai. Clinical implementation of ai technologies will require interpretable ai models. *Medical physics*, (1):1–4, 2020.

Y. Jia, H. Gu, and Q. Luo. Sample entropy reveals an age-related reduction in the complexity of dynamic brain. *Scientific reports*, 7(1):7990, 2017.

Y. Jiang, A. Yabluchanskiy, J. Deng, F. A. Amil, S. S. Po, and T. W. Dasari. The role of age-associated autonomic dysfunction in inflammation and endothelial dysfunction. *Geroscience*, 44(6):2655–2670, 2022.

M. Jozwiak, S. Millasseau, J.-L. Teboul, R. Lombardi, R. Devanlay, E. Umbdenstock, L. Morand, J. Dellamonica, and D. Chemla. Value and variability of pulse shape indicator for estimating mean arterial pressure in the radial and femoral arteries. *Journal of the American Heart Association*, 13(3):e031969, 2024.

P. Kakria, N. Tripathi, and P. Kitipawang. A real-time health monitoring system for remote cardiac patients using smartphone and wearable sensors. *International journal of telemedicine and applications*, 2015(1):373474, 2015.

A. Kamiya, T. Kawada, and M. Sugimachi. Systems physiology of the baroreflex during orthostatic stress: from animals to humans. *Frontiers in physiology*, 5:256, 2014.

A. Kapidžić, M. M. Platiša, T. Bojić, and A. Kalauzi. Nonlinear properties of cardiac rhythm and respiratory signal under paced breathing in young and middle-aged healthy subjects. *Medical engineering & physics*, 36(12):1577–1584, 2014.

D. Kaplan and L. Glass. *Understanding nonlinear dynamics*. Springer Science & Business Media, 2012.

J. M. Karemaker. Counterpoint: respiratory sinus arrhythmia is due to the baroreflex mechanism. *Journal of applied physiology*, 106(5):1742–1743, 2009.

E. Katnik, A. Gomułkiewicz, A. Piotrowska, J. Grzegrzółka, A. Rusak, A. Kmiecik, K. Ratajczak-Wielgomas, and P. Dziegiel. Bcl11a expression in breast cancer. *Current Issues in Molecular Biology*, 45(4):2681–2698, 2023.

M. B. Kennel, R. Brown, and H. D. Abarbanel. Determining embedding dimension for phase-space reconstruction using a geometrical construction. *Physical review A*, 45(6):3403, 1992.

H. Kerner, J. Campbell, and M. Strickland. Introduction to machine learning. In *Machine learning for planetary science*, pages 1–24. Elsevier, 2022.

S. S. Khalsa, D. Rudrauf, J. S. Feinstein, and D. Tranel. The pathways of interoceptive awareness. *Nature neuroscience*, 12(12):1494–1496, 2009.

S. Khan, S. Bandyopadhyay, A. R. Ganguly, S. Saigal, D. J. Erickson III, V. Protopopescu, and G. Ostrouchov. Relative performance of mutual information estimation methods for quantifying the dependence among short and noisy data. *Physical Review E—Statistical, Nonlinear, and Soft Matter Physics*, 76(2):026209, 2007.

J. W. Kim, H. S. Seok, and H. Shin. Is ultra-short-term heart rate variability valid in non-static conditions? *Frontiers in physiology*, 12:596060, 2021.

D. P. Kingma and M. Welling. Auto-encoding variational bayes. *arXiv preprint arXiv:1312.6114*, 2013.

J. Koenig and J. F. Thayer. Sex differences in healthy human heart rate variability: A meta-analysis. *Neuroscience & Biobehavioral Reviews*, 64:288–310, 2016.

H. Koepchen. Physiology of rhythms and control systems: an integrative approach. In *Rhythms in Physiological Systems: Proceedings of the International Symposium at Schloß Elmau, Bavaria, October 22–25, 1990*, pages 3–20. Springer, 1991.

A. N. Kolmogorov. A new metric invariant of transitive dynamical systems and automorphisms of lebesgue spaces. *Trudy Matematicheskogo Instituta imeni VA Steklova*, 169:94–98, 1985.

G. König, E. Günther, and U. von Luxburg. Disentangling interactions and dependencies in feature attribution. *arXiv preprint arXiv:2410.23772*, 2024.

A. Kos and A. Umek. Wearable sensor devices for prevention and rehabilitation in healthcare: Swimming exercise with real-time therapist feedback. *IEEE internet of things journal*, 6(2):1331–1341, 2018.

L. Kozachenko. Sample estimate of the entropy of a random vector. *Probl. Pered. Inform.*, 23: 9, 1987.

A. Kraskov, H. Stögbauer, and P. Grassberger. Estimating mutual information. *Physical Review E—Statistical, Nonlinear, and Soft Matter Physics*, 69(6):066138, 2004.

J. Krohova, B. Czippelova, Z. Turianikova, Z. Lazarova, R. Wiszt, M. Javorka, and L. Faes. Information domain analysis of respiratory sinus arrhythmia mechanisms. *Physiological Research*, 67:S611–S618, 2018.

J. Krohova, L. Faes, B. Czippelova, R. Pernice, Z. Turianikova, R. Wiszt, N. Mazgutova, A. Busacca, and M. Javorka. Vascular resistance arm of the baroreflex: methodology and comparison with the cardiac chronotropic arm. *Journal of Applied Physiology*, 128(5):1310–1320, 2020.

J. C. Krohova, B. Czippelova, Z. Turianikova, R. Pernice, A. Busacca, L. Faes, and M. Javorka. Input for baroreflex analysis: which blood pressure signal should be used? *Journal of Physiology & Pharmacology*, 73(5), 2022.

D. Kugiumtzis. Transfer entropy on rank vectors. *Journal of Nonlinear Systems and Applications*, 73:81, 2012.

D. Kugiumtzis. Partial transfer entropy on rank vectors. *The European Physical Journal Special Topics*, 222(2):401–420, 2013.

J.-P. Lachaux, E. Rodriguez, J. Martinerie, and F. J. Varela. Measuring phase synchrony in brain signals. *Human brain mapping*, 8(4):194–208, 1999.

J. Ladyman, J. Lambert, and K. Wiesner. What is a complex system? *European Journal for Philosophy of Science*, 3:33–67, 2013.

V. A. Lamme and P. R. Roelfsema. The distinct modes of vision offered by feedforward and recurrent processing. *Trends in neurosciences*, 23(11):571–579, 2000.

G. Lancaster, D. Iatsenko, A. Pidde, V. Ticcinelli, and A. Stefanovska. Surrogate data for hypothesis testing of physical systems. *Physics reports*, 748:1–60, 2018.

P. Lantelme, C. Mestre, M. Lievre, A. Gressard, and H. Milon. Heart rate: an important confounder of pulse wave velocity assessment. *Hypertension*, 39(6):1083–1087, 2002.

I. Lazic, C. Barà, M. Iovino, S. Stramaglia, K. Kasas-Lazetic, N. Jakovljević, and L. Faes. Information-theoretic quantification of high-order feature effects in classification problems. *Chaos, Solitons & Fractals*, 204:117724, 2026.

S. Lee, H. B. Hwang, S. Park, S. Kim, J. H. Ha, Y. Jang, S. Hwang, H.-K. Park, J. Lee, and I. Y. Kim. Mental stress assessment using ultra short term HRV analysis based on non-linear method. *Biosensors*, 12(7):465, 2022.

P. Lehrer and D. Eddie. Dynamic processes in regulation and some implications for biofeedback and biobehavioral interventions. *Applied psychophysiology and biofeedback*, 38:143–155, 2013.

J. Lei, M. G'Sell, A. Rinaldo, R. J. Tibshirani, and L. Wasserman. Distribution-free predictive inference for regression. *Journal of the American Statistical Association*, 113(523):1094–1111, 2018.

A. Lempel and J. Ziv. On the complexity of finite sequences. *IEEE Transactions on information theory*, 22(1):75–81, 2003.

D. D. Lewis. Feature selection and feature extraction for text categorization. In *Speech and Natural Language: Proceedings of a Workshop Held at Harriman, New York, February 23-26, 1992*, 1992.

F. Leyva, S. Nisam, and A. Auricchio. 20 years of cardiac resynchronization therapy. *Journal of the American College of Cardiology*, 64(10):1047–1058, 2014.

K. Li, L. Guo, J. Nie, G. Li, and T. Liu. Review of methods for functional brain connectivity detection using fmri. *Computerized medical imaging and graphics*, 33(2):131–139, 2009.

P. Li, C. Liu, K. Li, D. Zheng, C. Liu, and Y. Hou. Assessing the complexity of short-term heartbeat interval series by distribution entropy. *Medical & biological engineering & computing*, 53:77–87, 2015.

A. Liardi, K. J. Down, G. Blackburne, M. Neri, and P. A. Mediano. The mathematical landscape of partial information decomposition: A comprehensive review of properties and measures. *arXiv preprint arXiv:2603.06678*, 2026.

D. Lin. Robustness and perturbation in the modeled cascade heart rate variability. *Physical Review E*, 67(3):031914, 2003.

L. A. Lipsitz and A. L. Goldberger. Loss of 'complexity'and aging: potential applications of fractals and chaos theory to senescence. *Jama*, 267(13):1806–1809, 1992.

J. T. Lizier. *The local information dynamics of distributed computation in complex systems*. Springer Science & Business Media, 2012a.

J. T. Lizier. *The local information dynamics of distributed computation in complex systems*. Springer Science & Business Media, 2012b.

J. T. Lizier. Measuring the dynamics of information processing on a local scale in time and space. In *Directed information measures in neuroscience*, pages 161–193. Springer, 2014.

D. Lombardi and S. Pant. Nonparametric k-nearest-neighbor entropy estimator. *Physical Review E*, 93(1):013310, 2016.

J. Lucio, R. Valdés, and L. Rodríguez. Improvements to surrogate data methods for nonstationary time series. *Physical Review E—Statistical, Nonlinear, and Soft Matter Physics*, 85(5): 056202, 2012.

S. M. Lundberg and S.-I. Lee. A unified approach to interpreting model predictions. *Advances in neural information processing systems*, 30, 2017.

A. I. Luppi, F. E. Rosas, P. A. Mediano, D. K. Menon, and E. A. Stamatakis. Information decomposition and the informational architecture of the brain. *Trends in cognitive sciences*, 28(4):352–368, 2024.

H. Lütkepohl. *New introduction to multiple time series analysis*. Springer Science & Business Media, 2005.

J. Lynch and J.-R. Tian. Cortico-cortical networks and cortico-subcortical loops for the higher control of eye movements. *Progress in brain research*, 151:461–501, 2006.

D. J. MacKay. *Information theory, inference and learning algorithms*. Cambridge university press, 2003.

V. Magagnin, T. Bassani, V. Bari, M. Turiel, R. Maestri, G. D. Pinna, and A. Porta. Non-stationarities significantly distort short-term spectral, symbolic and entropy heart rate variability indices. *Physiological measurement*, 32(11):1775–1786, 2011.

V. Mäki-Marttunen, I. Diez, J. M. Cortes, D. R. Chialvo, and M. Villarreal. Disruption of transfer entropy and inter-hemispheric brain functional connectivity in patients with disorder of consciousness. *Frontiers in neuroinformatics*, 7:24, 2013.

A. Makkeh, A. J. Gutknecht, and M. Wibral. Introducing a differentiable measure of pointwise shared information. *Physical Review E*, 103(3):032149, 2021.

F. Malizia, A. Corso, L. V. Gambuzza, G. Russo, V. Latora, and M. Frasca. Reconstructing higher-order interactions in coupled dynamical systems. *Nature Communications*, 15(1): 5184, 2024.

A. Malliani, M. Pagani, F. Lombardi, and S. Cerutti. Cardiovascular neural regulation explored in the frequency domain. *Circulation*, 84(2):482–492, 1991.

S. C. Malpas. Neural influences on cardiovascular variability: possibilities and pitfalls. *American Journal of Physiology-Heart and Circulatory Physiology*, 282(1):H6–H20, 2002.

G. Manis, M. Aktaruzzaman, and R. Sassi. Bubble entropy: An entropy almost free of parameters. *IEEE Transactions on Biomedical Engineering*, 64(11):2711–2718, 2017.

M. M. N. Mannan, M. A. Kamran, and M. Y. Jeong. Identification and removal of physiological artifacts from electroencephalogram signals: A review. *Ieee Access*, 6:30630–30652, 2018.

D. Marinazzo, M. Pellicoro, and S. Stramaglia. Nonlinear parametric model for granger causality of time series. *Physical Review E—Statistical, Nonlinear, and Soft Matter Physics*, 73 (6):066216, 2006.

E. Martinez-Gutierrez, A. Jimenez-Marin, S. Stramaglia, and J. M. Cortes. The structure of anticorrelated networks in the human brain. *Frontiers in Network Physiology*, 2:946380, 2022.

C. Marullo and E. Agliari. Boltzmann machines as generalized hopfield networks: a review of recent results and outlooks. *Entropy*, 23(1):34, 2020.

E. Marx, A. Deutschländer, T. Stephan, M. Dieterich, M. Wiesmann, and T. Brandt. Eyes open and eyes closed as rest conditions: impact on brain activation patterns. *Neuroimage*, 21(4):1818–1824, 2004.

R. M. May. Simple mathematical models with very complicated dynamics. *Nature*, 261 (5560):459–467, 1976.

R. McCraty and S. B. Schafer. Exploring dimensions of the media dream: Functional context in collective personae. In *Exploring the collective unconscious in the age of digital media*, pages 1–39. IGI Global Scientific Publishing, 2016.

W. McGill. Multivariate information transmission. *Transactions of the IRE Professional Group on Information Theory*, 4(4):93–111, 1954.

M. A. Méndez, P. Zuluaga, R. Hornero, C. Gómez, J. Escudero, A. Rodríguez-Palancas, T. Ortiz, and A. Fernández. Complexity analysis of spontaneous brain activity: effects of depression and antidepressant treatment. *Journal of psychopharmacology*, 26(5):636–643, 2012.

C. Merkwirth, U. Parlitz, and W. Lauterborn. Fast nearest-neighbor searching for nonlinear signal processing. *Physical Review E*, 62(2):2089, 2000.

N. Metropolis and S. Ulam. The Monte Carlo method,-J. Amer. statistical assoc. 1949.

D. T. Mihailović, G. Mimić, E. Nikolić-Djorić, and I. Arsenić. Novel measures based on the kolmogorov complexity for use in complex system behavior studies and time series analysis. *Open Physics*, 13(1), 2015.

G. Mijatovic, Y. Antonacci, T. Loncar-Turukalo, L. Minati, and L. Faes. An information-theoretic framework to measure the dynamic interaction between neural spike trains. *IEEE Transactions on Biomedical Engineering*, 68(12):3471–3481, 2021.

G. Mijatovic, C. Barà, R. Pernice, T. Loncar-Turukalo, G. Nollo, and L. Faes. Exploring the short-term memory of heart rate variability through model-free information measures. In *2023 45th Annual International Conference of the IEEE Engineering in Medicine & Biology Society (EMBC)*, pages 1–4. IEEE, 2023.

M. Mohri, A. Rostamizadeh, and A. Talwalkar. *Foundations of machine learning*. MIT press, 2018.

C. Molnar, G. Casalicchio, and B. Bischl. Interpretable machine learning–a brief history, state-of-the-art and challenges. In *Joint European conference on machine learning and knowledge discovery in databases*, pages 417–431. Springer, 2020.

E. F. Morales and H. J. Escalante. A brief introduction to supervised, unsupervised, and reinforcement learning. In *Biosignal processing and classification using computational learning and intelligence*, pages 111–129. Elsevier, 2022.

J. Morales, P. Borzée, D. Testelmans, B. Buyse, S. Van Huffel, and C. Varon. Linear and nonlinear quantification of the respiratory sinus arrhythmia using support vector machines. *Frontiers in Physiology*, 12:623781, 2021.

F. Mosteller and J. W. Tukey. Data analysis and regression. a second course in statistics. *Addison-Wesley series in behavioral science: quantitative methods*, 1977.

R. Mukkamala, K. Toska, and R. J. Cohen. Noninvasive identification of the total peripheral resistance baroreflex. *American Journal of Physiology-Heart and Circulatory Physiology*, 284 (3):H947–H959, 2003.

T. J. Mullen, M. L. Appel, R. Mukkamala, J. M. Mathias, and R. J. Cohen. System identification of closed-loop cardiovascular control: effects of posture and autonomic blockade. *American Journal of Physiology-Heart and Circulatory Physiology*, 272(1):H448–H461, 1997.

G. Nollo, L. Faes, A. Porta, B. Pellegrini, F. Ravelli, M. Del Greco, M. Disertori, and R. Antolini. Evidence of unbalanced regulatory mechanism of heart rate and systolic pressure after acute myocardial infarction. *American Journal of Physiology-Heart and Circulatory Physiology*, 283(3):H1200–H1207, 2002.

G. Nollo, L. Faes, A. Porta, R. Antolini, and F. Ravelli. Exploring directionality in spontaneous heart period and systolic pressure variability interactions in humans: implications in the evaluation of baroreflex gain. *American Journal of Physiology-Heart and Circulatory Physiology*, 288(4):H1777–H1785, 2005.

D. Nuzzi, S. Stramaglia, M. Javorka, D. Marinazzo, A. Porta, and L. Faes. Extending the spectral decomposition of granger causality to include instantaneous influences: application to the control mechanisms of heart rate variability. *Philosophical Transactions of the Royal Society A*, 379(2212):20200263, 2021.

J. Oleksakova, M. Javorka, B. Czippelova, N. Mazgutova, M. Grofik, L. Babalova, P. Skacik, and E. Kurca. Autonomic control of heart and vessels in patients with very early stage of parkinson disease. *Physiological Measurement*, 44(5):054002, 2023.

M. Ontivero-Ortega, L. Faes, J. M. Cortes, D. Marinazzo, and S. Stramaglia. Assessing high-order effects in feature importance via predictability decomposition. *Physical Review E*, 111(3):L033301, 2025a.

M. Ontivero-Ortega, M. Iovino, R. Pernice, C. Barà, M. Javorka, L. Faes, and S. Stramaglia. Assessment of sex-related differences in cardiovascular control using high-order feature importance. *The European Physical Journal Special Topics*, pages 1–12, 2025b.

M. O'Rourke. Arterial stiffness, systolic blood pressure, and logical treatment of arterial hypertension. *Hypertension*, 15(4):339–347, 1990.

C. Orphanidou. A review of big data applications of physiological signal data. *Biophysical reviews*, 11(1):83–87, 2019.

E. Orrantia-Borunda, P. Anchondo-Nuñez, L. E. Acuña-Aguilar, F. O. Gómez-Valles, and C. A. Ramírez-Valdespino. Subtypes of breast cancer. *Breast Cancer [Internet]*, 2022.

N. H. Packard, J. P. Crutchfield, J. D. Farmer, and R. S. Shaw. Geometry from a time series. *Physical review letters*, 45(9):712, 1980.

M. Pagani and D. Lucini. Autonomic dysregulation in essential hypertension: insight from heart rate and arterial pressure variability. *Autonomic Neuroscience*, 90(1-2):76–82, 2001.

A. Pakman, A. Nejatbakhsh, D. Gilboa, A. Makkeh, L. Mazzucato, M. Wibral, and E. Schneidman. Estimating the unique information of continuous variables. *Advances in neural information processing systems*, 34:20295–20307, 2021.

J. Pan and W. J. Tompkins. A real-time qrs detection algorithm. *IEEE transactions on biomedical engineering*, (3):230–236, 2007.

T. G. Papaioannou, A. D. Protogerou, D. Vrachatis, G. Konstantonis, E. Aissopou, A. Argyris, E. Nasothimiou, E. J. Gialafos, M. Karamanou, D. Tousoulis, et al. Mean arterial pressure values calculated using seven different methods and their associations with target organ deterioration in a single-center study of 1878 individuals. *Hypertension Research*, 39(9): 640–647, 2016.

A. Papana and D. Kugiumtzis. Evaluation of mutual information estimators for time series. *International Journal of Bifurcation and Chaos*, 19(12):4197–4215, 2009.

A. Papana, D. Kugiumtzis, and P. Larsson. Detection of direct causal effects among parts of the brain of epileptic patients. *International Journal of Bifurcation and Chaos*, 2012.

A. Papoulis. *Random variables and stochastic processes*. McGraw Hill, 1965.

G. Parati, A. Frattola, M. Di Rienzo, P. Castiglioni, and G. Mancia. Broadband spectral analysis of blood pressure and heart rate variability in very elderly subjects. *Hypertension*, 30(4):803–808, 1997.

G. Parati, M. Di Rienzo, L. Ulian, C. Santucciu, A. Girard, J.-L. Elghozi, and G. Mancia. Clinical relevance blood pressure variability. *Journal of hypertension. Supplement: official journal of the International Society of Hypertension*, 16(3):S25–33, 1998.

G. Parati, J. P. Saul, and P. Castiglioni. Assessing arterial baroreflex control of heart rate: new perspectives. *Journal of hypertension*, 22(7):1259–1263, 2004.

D. Parbat and M. Chakraborty. Multiscale entropy analysis of single lead ecg and ecg derived respiration for ai based prediction of sleep apnea events. *Biomedical Signal Processing and Control*, 87:105444, 2024.

H.-D. Park and O. Blanke. Heartbeat-evoked cortical responses: Underlying mechanisms, functional roles, and methodological considerations. *NeuroImage*, 197:502–511, 2019.

E. L. Parks and D. J. Madden. Brain connectivity and visual attention. *Brain connectivity*, 3 (4):317–338, 2013.

D. Paz-Linares, E. Gonzalez-Moreira, A. Areces-Gonzalez, Y. Wang, M. Li, M. Vega-Hernandez, Q. Wang, J. Bosch-Bayard, M. L. Bringas-Vega, E. Martinez-Montes, et al.

Minimizing the distortions in electrophysiological source imaging of cortical oscillatory activity via spectral structured sparse bayesian learning. *Frontiers in Neuroscience*, 17: 978527, 2023.

L. Pecchia, R. Castaldo, L. Montesinos, and P. Melillo. Are ultra-short heart rate variability features good surrogates of short-term ones? state-of-the-art review and recommendations. *Healthcare technology letters*, 5(3):94–100, 2018.

C.-K. Peng, S. Havlin, J. Hausdorff, J. Mietus, H. Stanley, and A. Goldberger. Fractal mechanisms and heart rate dynamics: long-range correlations and their breakdown with disease. *Journal of electrocardiology*, 28:59–65, 1995.

H. Peng, F. Long, and C. Ding. Feature selection based on mutual information criteria of max-dependency, max-relevance, and min-redundancy. *IEEE Transactions on pattern analysis and machine intelligence*, 27(8):1226–1238, 2005.

D. B. Percival and A. T. Walden. *Wavelet methods for time series analysis*, volume 4. Cambridge university press, 2000.

R. Pernice, M. Javorka, J. Krohova, B. Czippelova, Z. Turianikova, A. Busacca, and L. Faes. Comparison of short-term heart rate variability indexes evaluated through electrocardiographic and continuous blood pressure monitoring. *Medical & biological engineering & computing*, 57(6):1247–1263, 2019.

R. Pernice, I. Lazic, C. Barà, L. Sparacino, G. Mijatovic, T. Loncar-Turukalo, and L. Faes. Assessment of cardiorespiratory interactions during spontaneous and controlled breathing: Non-linear model-free analysis. In *2022 12th Conference of the European Study Group on Cardiovascular Oscillations (ESGCO)*, pages 1–2, 2022a.

R. Pernice, L. Sparacino, C. Barà, Y. Antonacci, and L. Faes. Assessment of cardiorespiratory interactions during spontaneous and controlled breathing: Linear parametric analysis. In *2022 12th Conference of the European Study Group on Cardiovascular Oscillations (ESGCO)*, pages 1–2. IEEE, 2022b.

R. Pernice, L. Sparacino, V. Bari, F. Gelpi, B. Cairo, G. Mijatovic, Y. Antonacci, D. Tonon, G. Rossato, M. Javorka, et al. Spectral decomposition of cerebrovascular and cardiovascular interactions in patients prone to postural syncope and healthy controls. *Autonomic Neuroscience*, 242:103021, 2022c.

H. Phan, K. Mikkelsen, O. Y. Chén, P. Koch, A. Mertins, P. Kidmose, and M. De Vos. Personalized automatic sleep staging with single-night data: a pilot study with kullback–leibler divergence regularization. *Physiological measurement*, 41(6):064004, 2020.

S. V. Philbois, T. P. Facioli, A. C. Gastaldi, J. A. Rodrigues, J. Tank, T. H. Fares, K. P. Rodrigues, and H. C. Souza. Important differences between hypertensive middle-aged women and men in cardiovascular autonomic control—a critical appraisal. *Biology of sex Differences*, 12(1):11, 2021.

M. Piepoli, P. Sleight, S. Leuzzi, F. Valle, G. Spadacini, C. Passino, J. Johnston, and L. Bernardi. Origin of respiratory sinus arrhythmia in conscious humans: an important role for arterial carotid baroreceptors. *Circulation*, 95(7):1813–1821, 1997.

S. M. Pincus. Approximate entropy as a measure of system complexity. *Proceedings of the national academy of sciences*, 88(6):2297–2301, 1991.

S. M. Pincus. Greater signal regularity may indicate increased system isolation. *Mathematical biosciences*, 122(2):161–181, 1994.

M. R. Pinsky. The effects of mechanical ventilation on the cardiovascular system. *Critical Care Clinics*, 6(3):663–678, 1990.

H. Pinto, Y. Antonacci, R. Pernice, C. Barà, M. Javorka, L. Faes, and A. P. Rocha. Decomposing the mutual information rate of heart period and respiration variability series to assess cardiorespiratory interactions. In *2023 45th Annual International Conference of the IEEE Engineering in Medicine & Biology Society (EMBC)*, pages 1–4. IEEE, 2023.

H. Pinto, I. Lazic, Y. Antonacci, R. Pernice, D. Gu, Barà, L. Faes, and A. P. Rocha. Testing dynamic correlations and nonlinearity in bivariate time series through information measures and surrogate data analysis. *Frontiers in network physiology*, 4:1385421, 2024.

H. Pinto, Y. Antonacci, C. Barà, R. Pernice, I. Lazic, L. Faes, and A. P. Rocha. Estimating the mutual information rate of short time series from coupled dynamic systems. *Communications in Nonlinear Science and Numerical Simulation*, page 109383, 2025.

I. Pirovano, Y. Antonacci, A. Mastropietro, C. Barà, L. Sparacino, E. Guanziroli, F. Molteni, M. Tettamanti, L. Faes, and G. Rizzo. Rehabilitation modulates high-order interactions among large-scale brain networks in subacute stroke. *IEEE Transactions on Neural Systems and Rehabilitation Engineering*, 31:4549–4560, 2023.

M. M. Platiša, N. N. Radovanović, R. Pernice, C. Barà, S. U. Pavlović, and L. Faes. Information-theoretic analysis of cardio-respiratory interactions in heart failure patients: effects of arrhythmias and cardiac resynchronization therapy. *Entropy*, 25(7):1072, 2023.

T. Popov, S. Kastner, and O. Jensen. Fef-controlled alpha delay activity precedes stimulus-induced gamma-band activity in visual cortex. *Journal of Neuroscience*, 37(15):4117–4127, 2017.

A. Porta, G. Baselli, D. Liberati, N. Montano, C. Cogliati, T. Gnecchi-Ruscone, A. Malliani, and S. Cerutti. Measuring regularity by means of a corrected conditional entropy in sympathetic outflow. *Biological cybernetics*, 78:71–78, 1998.

A. Porta, G. Baselli, F. Lombardi, N. Montano, A. Malliani, and S. Cerutti. Conditional entropy approach for the evaluation of the coupling strength. *Biological cybernetics*, 81(2): 119–129, 1999.

A. Porta, S. Guzzetti, N. Montano, R. Furlan, M. Pagani, A. Malliani, and S. Cerutti. Entropy, entropy rate, and pattern classification as tools to typify complexity in short heart period variability series. *IEEE Transactions on Biomedical Engineering*, 48(11):1282–1291, 2002.

A. Porta, S. Guzzetti, E. Borroni, R. Furlan, N. Montano, and A. Malliani. Role of the autonomic nervous system in generating non-linear dynamics in short-term heart period variability. *Biomedizinische Technik. Biomedical engineering*, 51(4):174–177, 2006.

A. Porta, L. Faes, M. Masé, G. D'addio, G. Pinna, R. Maestri, N. Montano, R. Furlan, S. Guzzetti, G. Nollo, et al. An integrated approach based on uniform quantization for the evaluation of complexity of short-term heart period variability: application to 24h

holter recordings in healthy and heart failure humans. *Chaos: An Interdisciplinary Journal of Nonlinear Science*, 17(1), 2007a.

A. Porta, T. Gnecchi-Ruscone, E. Tobaldini, S. Guzzetti, R. Furlan, and N. Montano. Progressive decrease of heart period variability entropy-based complexity during graded head-up tilt. *Journal of applied physiology*, 103(4):1143–1149, 2007b.

A. Porta, T. Bassani, V. Bari, G. D. Pinna, R. Maestri, and S. Guzzetti. Accounting for respiration is necessary to reliably infer granger causality from cardiovascular variability series. *IEEE transactions on biomedical engineering*, 59(3):832–841, 2011a.

A. Porta, A. M. Catai, A. C. Takahashi, V. Magagnin, T. Bassani, E. Tobaldini, P. Van De Borne, and N. Montano. Causal relationships between heart period and systolic arterial pressure during graded head-up tilt. *American Journal of Physiology-Regulatory, Integrative and Comparative Physiology*, 300(2):R378–R386, 2011b.

A. Porta, T. Bassani, V. Bari, E. Tobaldini, A. C. Takahashi, A. M. Catai, and N. Montano. Model-based assessment of baroreflex and cardiopulmonary couplings during graded head-up tilt. *Computers in biology and medicine*, 42(3):298–305, 2012.

A. Porta, L. Faes, V. Bari, A. Marchi, T. Bassani, G. Nollo, N. M. Perseguini, J. Milan, V. Minatel, A. Borghi-Silva, et al. Effect of age on complexity and causality of the cardiovascular control: comparison between model-based and model-free approaches. *PloS one*, 9(2): e89463, 2014.

A. Porta, A. Marchi, V. Bari, K. Heusser, J. Tank, J. Jordan, F. Barbic, and R. Furlan. Conditional symbolic analysis detects nonlinear influences of respiration on cardiovascular control in humans. *Philosophical Transactions of the Royal Society a: Mathematical, Physical and Engineering Sciences*, 373(2034):20140096, 2015.

A. Porta, B. De Maria, V. Bari, A. Marchi, and L. Faes. Are nonlinear model-free conditional entropy approaches for the assessment of cardiac control complexity superior to the linear model-based one? *IEEE Transactions on Biomedical Engineering*, 64(6):1287–1296, 2016.

A. Porta, V. Bari, B. De Maria, A. C. Takahashi, S. Guzzetti, R. Colombo, A. M. Catai, F. Raimondi, and L. Faes. Quantifying net synergy/redundancy of spontaneous variability regulation via predictability and transfer entropy decomposition frameworks. *IEEE Transactions on Biomedical Engineering*, 64(11):2628–2638, 2017a.

A. Porta, V. Bari, G. Ranuzzi, B. De Maria, and G. Baselli. Assessing multiscale complexity of short heart rate variability series through a model-based linear approach. *Chaos: An Interdisciplinary Journal of Nonlinear Science*, 27(9), 2017b.

A. Porta, V. Bari, F. Gelpi, B. Cairo, B. De Maria, D. Tonon, G. Rossato, and L. Faes. On the different abilities of cross-sample entropy and k-nearest-neighbor cross-unpredictability in assessing dynamic cardiorespiratory and cerebrovascular interactions. *Entropy*, 25(4): 599, 2023.

D. Prichard and J. Theiler. Generating surrogate data for time series with several simultaneously measured variables. *Physical review letters*, 73(7):951, 1994.

J. C. Principe and D. Xu. An introduction to information theoretic learning. In *IJCNN'99. In-*

ternational Joint Conference on Neural Networks. Proceedings (Cat. No. 99CH36339), volume 3, pages 1783–1787. IEEE, 1999.

J. R. Quinlan. Induction of decision trees. *Machine learning*, 1(1):81–106, 1986.

N. N. Radovanović, S. U. Pavlović, G. Milašinović, and M. M. Platiša. Effects of cardiac resynchronization therapy on cardio-respiratory coupling. *Entropy*, 23(9):1126, 2021.

M. E. Raichle. The brain's default mode network. *Annual review of neuroscience*, 38(1):433–447, 2015.

A. Raimondi, R. Saputo, M. Javorka, L. Faes, and R. Pernice. Ultra-short-term analysis of cardiovascular interactions at rest and during stress conditions using mutual information rate. In *9th National Congress of Bioengineering—GNB*, 2025a.

A. Raimondi, R. Saputo, M. Javorka, L. Faes, R. Pernice, et al. Ultra-short-term analysis of cardiovascular interactions at rest and during orthostatic stress using model-free mutual information rate. In *Fourth International Summer Institute on Network Physiology (ISINP 2025)-Scientific Program*, pages 115–117. https://isinp. github. io/isinp-4/wp-content/uploads/2025/03/ISINP-Booklet . . . , 2025b.

R. A. Rayan, A. Suruliandi, and S. Raja. Modified mutual information feature selection algorithm to predict covid-19 using clinical data. *Computer Methods in Biomechanics and Biomedical Engineering*, pages 1–21, 2024.

V. Regitz-Zagrosek and C. Gebhard. Gender medicine: effects of sex and gender on cardiovascular disease manifestation and outcomes. *Nature Reviews Cardiology*, 20(4):236–247, 2023.

J. S. Richman and J. R. Moorman. Physiological time-series analysis using approximate entropy and sample entropy. *American journal of physiology-heart and circulatory physiology*, 278(6):H2039–H2049, 2000.

F. Riganello, S. K. Larroque, M. A. Bahri, L. Heine, C. Martial, M. Carrière, V. Charland-Verville, C. Aubinet, A. Vanhaudenhuyse, C. Chatelle, et al. A heartbeat away from consciousness: heart rate variability entropy can discriminate disorders of consciousness and is correlated with resting-state fMRI brain connectivity of the central autonomic network. *Frontiers in neurology*, 9:769, 2018.

B. Rim, N.-J. Sung, S. Min, and M. Hong. Deep learning in physiological signal data: A survey. *Sensors*, 20(4):969, 2020.

J. Rissanen. Modeling by shortest data description. *Automatica*, 14(5):465–471, 1978.

T. Robiglio, M. Neri, D. Coppes, C. Agostinelli, F. Battiston, M. Lucas, and G. Petri. Synergistic signatures of group mechanisms in higher-order systems. *Physical review letters*, 134 (13):137401, 2025.

R. Romero-Ortuño, N. Martínez-Velilla, R. Sutton, A. Ungar, A. Fedorowski, R. Galvin, O. Theou, A. Davies, R. B. Reilly, J. Claassen, et al. Network physiology in aging and frailty: the grand challenge of physiological reserve in older adults, 2021.

F. Rosas, V. Ntranos, C. J. Ellison, S. Pollin, and M. Verhelst. Understanding interdependency through complex information sharing. *Entropy*, 18(2):38, 2016.

F. Rosas, P. A. Mediano, M. Ugarte, and H. J. Jensen. An information-theoretic approach to self-organisation: Emergence of complex interdependencies in coupled dynamical systems. *Entropy*, 20(10):793, 2018.

F. E. Rosas, P. A. Mediano, M. Gastpar, and H. J. Jensen. Quantifying high-order interdependencies via multivariate extensions of the mutual information. *Physical Review E*, 100(3): 032305, 2019.

F. E. Rosas, P. A. Mediano, H. J. Jensen, A. K. Seth, A. B. Barrett, R. L. Carhart-Harris, and D. Bor. Reconciling emergences: An information-theoretic approach to identify causal emergence in multivariate data. *PLoS computational biology*, 16(12):e1008289, 2020.

F. E. Rosas, P. A. Mediano, A. I. Luppi, T. F. Varley, J. T. Lizier, S. Stramaglia, H. J. Jensen, and D. Marinazzo. Disentangling high-order mechanisms and high-order behaviours in complex systems. *Nature Physics*, 18(5):476–477, 2022.

M. G. Rosenblum, J. Kurths, A. Pikovsky, C. Schafer, P. Tass, and H.-H. Abel. Synchronization in noisy systems and cardiorespiratory interaction. *IEEE Engineering in Medicine and Biology Magazine*, 17(6):46–53, 1998.

B. C. Ross. Mutual information between discrete and continuous data sets. *PloS one*, 9(2): e87357, 2014.

M. Rostaghi and H. Azami. Dispersion entropy: A measure for time-series analysis. *IEEE Signal Processing Letters*, 23(5):610–614, 2016.

N. F. Rulkov, M. M. Sushchik, L. S. Tsimring, and H. D. Abarbanel. Generalized synchronization of chaos in directionally coupled chaotic systems. *Physical Review E*, 51(2):980, 1995.

J. Runge, J. Heitzig, V. Petoukhov, and J. Kurths. Escaping the curse of dimensionality in estimating multivariate transfer entropy. *Physical review letters*, 108(25):258701, 2012.

B. Rush, L. A. Celi, and D. J. Stone. Applying machine learning to continuously monitored physiological data. *Journal of clinical monitoring and computing*, 33(5):887–893, 2019.

H. Samet. K-nearest neighbor finding using maxnearestdist. *IEEE Transactions on Pattern Analysis and Machine Intelligence*, 30(2):243–252, 2007.

G. Santamaría-Bonfil, N. Fernández, and C. Gershenson. Measuring the complexity of continuous distributions. *Entropy*, 18(3):72, 2016.

I. D. Sant'anna, E. B. de Sousa, A. V. de Moraes, D. L. Loures, E. T. Mesquita, and A. C. L. da Nóbrega. Cardiac function during mental stress: cholinergic modulation with pyridostigmine in healthy subjects. *Clinical Science*, 105(2):161–165, 2003.

B. Santosa. Multiclass classification with cross entropy-support vector machines. *Procedia Computer Science*, 72:345–352, 2015.

R. Saputo, C. Barà, I. Franzone, M. Javorka, R. Pernice, and L. Faes. Partial decomposition of information dynamics elicits unique and shared modes of cardiovascular and cardiorespiratory control in response to autonomic stressors. *The European Physical Journal Special Topics*, pages 1–21, 2026.

J. P. Saul, R. D. Berger, M. H. Chen, and R. J. Cohen. Transfer function analysis of auto-

nomic regulation. ii. respiratory sinus arrhythmia. *American Journal of Physiology-Heart and Circulatory Physiology*, 256(1):H153–H161, 1989.

T. Scagliarini, L. Sparacino, L. Faes, D. Marinazzo, and S. Stramaglia. Gradients of o-information highlight synergy and redundancy in physiological applications. *Frontiers in Network Physiology*, 3:1335808, 2024.

R. Schandry, B. Sparrer, and R. Weitkunat. From the heart to the brain: a study of heartbeat contingent scalp potentials. *International Journal of Neuroscience*, 30(4):261–275, 1986.

L. Schiatti, G. Nollo, G. Rossato, and L. Faes. Extended granger causality: a new tool to identify the structure of physiological networks. *Physiological measurement*, 36(4):827–843, 2015.

K. Schick-Poland, A. Makkeh, A. J. Gutknecht, P. Wollstadt, A. Sturm, and M. Wibral. A partial information decomposition for discrete and continuous variables. *arXiv preprint arXiv:2106.12393*, 2021.

J. Schmitz, D. Claus, B. Neundörfer, and H. Handwerker. Comparison of different algorithms for evaluation of respiratory sinus arrhytmia: cross-correlation function histogram analysis and regression analysis. *Physiol Res*, 44(3):197–203, 1995.

T. Schreiber. Measuring information transfer. *Physical review letters*, 85(2):461, 2000.

T. Schreiber and A. Schmitz. Improved surrogate data for nonlinearity tests. *Physical review letters*, 77(4):635, 1996.

T. Schreiber and A. Schmitz. Surrogate time series. *Physica D: Nonlinear Phenomena*, 142(3-4): 346–382, 2000.

S. Schulz, F.-C. Adochiei, I.-R. Edu, R. Schroeder, H. Costin, K.-J. Bär, and A. Voss. Cardiovascular and cardiorespiratory coupling analyses: a review. *Philosophical Transactions of the Royal Society A: Mathematical, Physical and Engineering Sciences*, 371(1997):20120191, 2013.

S. Schulz, M. Bolz, K.-J. Bär, and A. Voss. Central-and autonomic nervous system coupling in schizophrenia. *Philosophical Transactions of the Royal Society A: Mathematical, Physical and Engineering Sciences*, 374(2067), 2016.

G. Schwarz. Estimating the dimension of a model. *The annals of statistics*, pages 461–464, 1978.

S. A. Sepúlveda-Fontaine and J. M. Amigó. Applications of entropy in data analysis and machine learning: a review. *Entropy*, 26(12):1126, 2024.

V. Sequeira and J. van der Velden. Historical perspective on heart function: the frank–starling law. *Biophysical reviews*, 7(4):421–447, 2015.

A. K. Seth. Measuring autonomy and emergence via granger causality. *Artificial life*, 16(2): 179–196, 2010.

F. Shaffer and J. P. Ginsberg. An overview of heart rate variability metrics and norms. *Frontiers in public health*, 5:290215, 2017.

F. Shaffer, R. McCraty, and C. L. Zerr. A healthy heart is not a metronome: an integrative review of the heart's anatomy and heart rate variability. *Frontiers in psychology*, 5:1040, 2014.

F. Shaffer, S. Shearman, and Z. M. Meehan. The promise of ultra-short-term (UST) heart rate variability measurements. *Biofeedback*, 44(4):229–233, 2016.

F. Shaffer, Z. M. Meehan, and C. L. Zerr. A critical review of ultra-short-term heart rate variability norms research. *Frontiers in neuroscience*, 14:594880, 2020.

C. E. Shannon. A mathematical theory of communication. *The Bell system technical journal*, 27(3):379–423, 1948.

L. Shekerdemian and D. Bohn. Cardiovascular effects of mechanical ventilation. *Archives of disease in childhood*, 80(5):475–480, 1999.

A. F. Siegenfeld and Y. Bar-Yam. An introduction to complex systems science and its applications. *Complexity*, 2020(1):6105872, 2020.

Y. G. Sinai. On the notion of entropy of a dynamical system. In *Doklady of Russian Academy of Sciences*, volume 124, pages 768–771, 1959.

V. Solo. State-space analysis of granger-geweke causality measures with application to fmri. *Neural computation*, 28(5):914–949, 2016.

H.-S. Song and P. M. Lehrer. The effects of specific respiratory rates on heart rate and heart rate variability. *Applied psychophysiology and biofeedback*, 28(1):13–23, 2003.

L. Sparacino. *Spectral Information Dynamics in Network Neuroscience and Physiology*. Studies in Computational Intelligence. Springer Nature Switzerland, 2026. ISBN 9783032054166. URL https://books.google.it/books?id=U5mlEQAAQBAJ.

L. Sparacino, R. Pernice, C. Barà, D. Švec, M. Javorka, and L. Faes. Spectral analysis of the beat-to-beat variability of arterial compliance. In *2022 12th Conference of the European Study Group on Cardiovascular Oscillations (ESGCO)*, pages 1–2. IEEE, 2022.

L. Sparacino, Y. Antonacci, C. Barà, D. Švec, M. Javorka, and L. Faes. A method to assess linear self-predictability of physiologic processes in the frequency domain: application to beat-to-beat variability of arterial compliance. *Frontiers in Network Physiology*, 4:1346424, 2024.

L. Sparacino, Y. Antonacci, G. Mijatovic, and L. Faes. Measuring hierarchically-organized interactions in dynamic networks through spectral entropy rates: theory, estimation, and illustrative application to physiological networks. *Neurocomputing*, 630:129675, 2025a.

L. Sparacino, C. Barà, Y. Antonacci, M. Javorka, and L. Faes. Decomposition of the dynamic information shared in complex networks of physiological variables. In *Computing in Cardiology Conference (CinC)*, 2025b.

L. Sparacino, G. Mijatovic, Y. Antonacci, L. Ricci, D. Marinazzo, S. Stramaglia, and L. Faes. Decomposing multivariate information rates in networks of random processes. *Physical Review E*, 112(4):044313, 2025c.

L. Sparacino, R. Pernice, C. Barà, R. Saputo, M. Javorka, and L. Faes. Investigating the effect of systolic and diastolic arterial pressures on mean pressure through partial information decomposition. In *2025 47th Annual International Conference of the IEEE Engineering in Medicine and Biology Society (EMBC)*, pages 1–4. IEEE, 2025d.

L. Sparacino, H. Pinto, C. Barà, Y. Antonacci, R. Pernice, A. P. Rocha, and L. Faes. Quantifying coupling and causality in dynamic bivariate systems: a unified framework for time-

domain, spectral, and information-theoretic analysis. *Frontiers in Network Physiology*, 5: 1687132, 2026.

T. Spindelböck, S. Ranftl, and W. von der Linden. Cross-entropy learning for aortic pathology classification of artificial multi-sensor impedance cardiography signals. *Entropy*, 23 (12):1661, 2021.

N. Spolaôr, R. Fonseca-Pinto, A. I. Mendes, L. A. Ensina, W. S. Takaki, A. R. Parmezan, C. V. Nogueira, C. S. Coy, F. C. Wu, and H. D. Lee. Evaluating intelligent methods for decision making support in dermoscopy based on information gain and ensemble. In *Computational Intelligence for Business Analytics*, pages 111–127. Springer, 2021.

P. A. Stokes and P. L. Purdon. A study of problems encountered in granger causality analysis from a neuroscience perspective. *Proceedings of the national academy of sciences*, 114(34): E7063–E7072, 2017.

S. Stramaglia, T. Scagliarini, Y. Antonacci, and L. Faes. Local granger causality. *Physical Review E*, 103(2):L020102, 2021.

S. Stramaglia, L. Faes, J. M. Cortes, and D. Marinazzo. Disentangling high-order effects in the transfer entropy. *Physical Review Research*, 6(3):L032007, 2024.

H. A. Sturges. The choice of a class interval. *Journal of the american statistical association*, 21 (153):65–66, 1926.

J. Sugawara, C. K. Willie, T. Miyazawa, H. Komine, P. N. Ainsle, and S. Ogoh. Effects of transient change in carotid arterial stiffness on arterial baroreflex during mild orthostatic stimulation. *Artery Research*, 6(3):130–135, 2012.

G. Sugihara, R. May, H. Ye, C.-h. Hsieh, E. Deyle, M. Fogarty, and S. Munch. Detecting causality in complex ecosystems. *science*, 338(6106):496–500, 2012.

J. Svacinova, M. Javorka, Z. Nováková, E. Závodná, B. Czippelova, and N. Honzíková. Development of causal interactions between systolic blood pressure and inter-beat intervals in adolescents. *Physiological research*, 64(6):821, 2015.

D. Svec, B. Czippelova, J. C. Krohova, N. Mazgutova, R. Wiszt, Z. Turianikova, L. Matuskova, and M. Javorka. Short-term arterial compliance changes in the context of systolic blood pressure influence. *Physiological Research*, 70(Suppl 3):S339, 2021.

P. Taggart. Brain-heart interactions and cardiac ventricular arrhythmias. *Netherlands Heart Journal*, 21(2):78–81, 2013.

A. C. Takahashi, A. Porta, R. C. Melo, R. J. Quitério, E. da Silva, A. Borghi-Silva, E. Tobaldini, N. Montano, and A. M. Catai. Aging reduces complexity of heart rate variability assessed by conditional entropy and symbolic analysis. *Internal and emergency medicine*, 7(3):229–235, 2012.

F. Takens. Dynamical systems and turbulence. *Warwick, 1980*, pages 366–381, 1981.

F. Takens. Detecting strange attractors in turbulence. In *Dynamical Systems and Turbulence, Warwick 1980: proceedings of a symposium held at the University of Warwick 1979/80*, pages 366–381. Springer, 2006.

I. Tan, B. Spronck, H. Kiat, E. Barin, K. D. Reesink, T. Delhaas, A. P. Avolio, and M. Butlin. Heart rate dependency of large artery stiffness. *Hypertension*, 68(1):236–242, 2016.

M. Tao, K. Poskuviene, N. F. Alkayem, M. Cao, and M. Ragulskis. Permutation entropy based on non-uniform embedding. *Entropy*, 20(8):612, 2018.

W. O. Tatum, B. A. Dworetzky, and D. L. Schomer. Artifact and recording concepts in eeg. *Journal of clinical neurophysiology*, 28(3):252–263, 2011.

J. Theiler. Estimating fractal dimension. *Journal of the optical society of America A*, 7(6):1055–1073, 1990.

J. Theiler and D. Prichard. Constrained-realization monte-carlo method for hypothesis testing. *Physica D: Nonlinear Phenomena*, 94(4):221–235, 1996.

J. Theiler, S. Eubank, A. Longtin, B. Galdrikian, and J. D. Farmer. Testing for nonlinearity in time series: the method of surrogate data. *Physica D: Nonlinear Phenomena*, 58(1-4):77–94, 1992.

N. Timme, W. Alford, B. Flecker, and J. M. Beggs. Synergy, redundancy, and multivariate information measures: an experimentalist's perspective. *Journal of computational neuroscience*, 36(2):119–140, 2014.

E. Tobaldini, L. Nobili, S. Strada, K. R. Casali, A. Braghiroli, and N. Montano. Heart rate variability in normal and pathological sleep. *Frontiers in physiology*, 4:294, 2013.

K. Tomczak, P. Czerwińska, and M. Wiznerowicz. Review the cancer genome atlas (tcga): an immeasurable source of knowledge. *Contemporary Oncology/Współczesna Onkologia*, 2015 (1):68–77, 2015.

G. D. Tourassi, E. D. Frederick, M. K. Markey, and C. E. Floyd Jr. Application of the mutual information criterion for feature selection in computer-aided diagnosis. *Medical physics*, 28(12):2394–2402, 2001.

J. K. Triedman and J. P. Saul. Blood pressure modulation by central venous pressure and respiration. buffering effects of the heart rate reflexes. *Circulation*, 89(1):169–179, 1994.

L. T. Trujillo. K-th nearest neighbor (KNN) entropy estimates of complexity and integration from ongoing and stimulus-evoked electroencephalographic (EEG) recordings of the human brain. *Entropy*, 21(1):61, 2019.

Z. Trunkvalterova, M. Javorka, I. Tonhajzerova, J. Javorkova, Z. Lazarova, K. Javorka, and M. Baumert. Reduced short-term complexity of heart rate and blood pressure dynamics in patients with diabetes mellitus type 1: multiscale entropy analysis. *Physiological measurement*, 29(7):817, 2008.

A. Tsimpiris, I. Vlachos, and D. Kugiumtzis. Nearest neighbor estimate of conditional mutual information in feature selection. *Expert Systems with Applications*, 39(16):12697–12708, 2012.

Y. Tzeng, P. Larsen, and D. Galletly. Cardioventilatory coupling in resting human subjects. *Experimental physiology*, 88(6):775–782, 2003.

A. M. Unakafov and K. Keller. Conditional entropy of ordinal patterns. *Physica D: Nonlinear Phenomena*, 269:94–102, 2014.

M. Ursino and E. Magosso. Role of short-term cardiovascular regulation in heart period variability: a modeling study. *American Journal of Physiology-Heart and Circulatory Physiology*, 284(4):H1479–H1493, 2003.

V. A. Vakorin, O. A. Krakovska, and A. R. McIntosh. Confounding effects of indirect connections on causality estimation. *Journal of neuroscience methods*, 184(1):152–160, 2009.

P. A. Valdes-Sosa, A. Roebroeck, J. Daunizeau, and K. Friston. Effective connectivity: influence, causality and biophysical modeling. *Neuroimage*, 58(2):339–361, 2011.

M. Valente, M. Javorka, A. Porta, V. Bari, J. Krohova, B. Czippelova, Z. Turianikova, G. Nollo, and L. Faes. Univariate and multivariate conditional entropy measures for the characterization of short-term cardiovascular complexity under physiological stress. *Physiological measurement*, 39(1):014002, 2018.

G. Valenza, A. Greco, C. Gentili, A. Lanata, L. Sebastiani, D. Menicucci, A. Gemignani, and E. P. Scilingo. Combining electroencephalographic activity and instantaneous heart rate for assessing brain–heart dynamics during visual emotional elicitation in healthy subjects. *Philosophical Transactions of the Royal Society A: Mathematical, Physical and Engineering Sciences*, 374(2067), 2016.

J. R. Vergara and P. A. Estévez. A review of feature selection methods based on mutual information. *Neural computing and applications*, 24(1):175–186, 2014.

V. R. Vergara, C. Bara, R. Pernice, A. Zaccaro, F. Ferri, L. Faes, and Y. Antonacci. Exploring the predictability of eeg signals timed with the heartbeat: A model-based approach for the temporal and spatial characterization of the brain dynamics. In *Mediterranean Conference on Medical and Biological Engineering and Computing*, pages 135–144. Springer, 2023.

V. R. Vergara, C. Barà, I. Franzone, A. Zaccaro, F. Ferri, L. Faes, and Y. Antonacci. A statistical framework for the analysis of heartbeat-evoked brain potentials. In *Proceedings of the Nineth National Congress of Bioengineering*. Pàtron editore, 2025a.

V. R. Vergara, C. Barà, A. Zaccaro, F. Ferri, F. Jurysta, L. Faes, and Y. Antonacci. Information-theoretic analysis of eeg wave amplitude and heart rate variability reveals the time scale-dependent nature of brain–heart interactions. *IEEE Open Journal of Engineering in Medicine and Biology*, 6:499–506, 2025b. doi: 10.1109/OJEMB.2025.3590598.

V. R. Vergara, C. Barà, A. Zaccaro, F. Ferri, F. Jurysta, L. Faes, and Y. Antonacci. Information-theoretic analysis of eeg wave amplitude and heart rate variability reveals the time scale-dependent nature of brain-heart interactions. *IEEE Open Journal of Engineering in Medicine and Biology*, 2025c.

R. Vicente, M. Wibral, M. Lindner, and G. Pipa. Transfer entropy—a model-free measure of effective connectivity for the neurosciences. *Journal of computational neuroscience*, 30(1): 45–67, 2011.

I. Vlachos and D. Kugiumtzis. Nonuniform state-space reconstruction and coupling detection. *Physical Review E—Statistical, Nonlinear, and Soft Matter Physics*, 82(1):016207, 2010.

G. Volpes, C. Barà, A. Busacca, S. Stivala, M. Javorka, L. Faes, and R. Pernice. Feasibility of ultra-short-term analysis of heart rate and systolic arterial pressure variability at rest and during stress via time-domain and entropy-based measures. *Sensors*, 22(23):9149, 2022a.

G. Volpes, C. Barà, S. Valenti, M. Javorka, A. Busacca, L. Faes, and R. Pernice. Feasibility of ultra-short term complexity analysis of heart rate variability in resting state and during

orthostatic stress. In *2022 12th Conference of the European Study Group on Cardiovascular Oscillations (ESGCO)*, pages 1–2. IEEE, 2022b.

G. T. Walker. On periodicity in series of related terms. *Proceedings of the Royal Society of London. Series A, Containing Papers of a Mathematical and Physical Character*, 131(818):518–532, 1931.

C. Wang, I. P. Uray, A. Mazumdar, J. A. Mayer, and P. H. Brown. Slc22a5/octn2 expression in breast cancer is induced by estrogen via a novel intronic estrogen-response element (ere). *Breast cancer research and treatment*, 134(1):101–115, 2012.

C. Wang, T. He, H. Zhou, Z. Zhang, and C. Lee. Artificial intelligence enhanced sensors-enabling technologies to next-generation healthcare and biomedical platform. *Bioelectronic Medicine*, 9(1):17, 2023.

Z. Wang and Q. Zhu. A cross-entropy based feature selection method for binary valued data classification. In *International Conference on Intelligent Systems Design and Applications*, pages 1406–1416. Springer, 2021.

C. Westphal, S. Hailes, and M. Musolesi. Partial information decomposition for data interpretability and feature selection. In *International Conference on Artificial Intelligence and Statistics*, pages 1873–1881. PMLR, 2025.

M. Wibral, B. Rahm, M. Rieder, M. Lindner, R. Vicente, and J. Kaiser. Transfer entropy in magnetoencephalographic data: quantifying information flow in cortical and cerebellar networks. *Progress in biophysics and molecular biology*, 105(1-2):80–97, 2011.

M. Wibral, J. T. Lizier, S. Vögler, V. Priesemann, and R. Galuske. Local active information storage as a tool to understand distributed neural information processing. *Frontiers in neuroinformatics*, 8:1, 2014a.

M. Wibral, R. Vicente, and J. T. Lizier. *Directed information measures in neuroscience*, volume 724. Springer, 2014b.

N. Wiener. The theory of prediction mcgraw-hill: New york. *Ny, Usa*, pages 165–183, 1956.

M. Wiesenfeldt, U. Parlitz, and W. Lauterborn. Mixed state analysis of multivariate time series. *International Journal of Bifurcation and Chaos*, 11(08):2217–2226, 2001.

P. L. Williams. *Information dynamics: Its theory and application to embodied cognitive systems*. PhD thesis, Indiana University, 2011.

P. L. Williams and R. D. Beer. Nonnegative decomposition of multivariate information. *arXiv preprint arXiv:1004.2515*, 2010.

A. Wolf, J. B. Swift, H. L. Swinney, and J. A. Vastano. Determining lyapunov exponents from a time series. *Physica D: nonlinear phenomena*, 16(3):285–317, 1985.

P. Wollstadt, S. Schmitt, and M. Wibral. A rigorous information-theoretic definition of redundancy and relevancy in feature selection based on (partial) information decomposition. *Journal of Machine Learning Research*, 24(131):1–44, 2023.

S. W. Wong, N. Massé, D. S. Kimmerly, R. S. Menon, and J. K. Shoemaker. Ventral medial prefrontal cortex and cardiovagal control in conscious humans. *Neuroimage*, 35(2):698–708, 2007.

L. Xiao-Feng and W. Yue. Fine-grained permutation entropy as a measure of natural complexity for time series. *Chinese Physics B*, 18(7):2690, 2009.

H.-B. Xie, W.-X. He, and H. Liu. Measuring time series regularity using nonlinear similarity-based sample entropy. *Physics Letters A*, 372(48):7140–7146, 2008.

W. Xiong, L. Faes, and P. C. Ivanov. Entropy measures, entropy estimators, and their performance in quantifying complex dynamics: Effects of artifacts, nonstationarity, and long-range correlations. *Physical review E*, 95(6):062114, 2017.

K. Xu, J. Usary, P. C. Kousis, A. Prat, D.-Y. Wang, J. R. Adams, W. Wang, A. J. Loch, T. Deng, W. Zhao, et al. Lunatic fringe deficiency cooperates with the met/caveolin gene amplicon to induce basal-like breast cancer. *Cancer cell*, 21(5):626–641, 2012.

A. Zaccaro, M. G. Perrucci, E. Parrotta, M. Costantini, and F. Ferri. Brain-heart interactions are modulated across the respiratory cycle via interoceptive attention. *NeuroImage*, 262: 119548, 2022.

K. C. Zekios, E.-T. Mouchtouri, P. Lekkas, D. N. Nikas, and T. M. Kolettis. Sympathetic activation and arrhythmogenesis after myocardial infarction: where do we stand? *Journal of cardiovascular development and disease*, 8(5):57, 2021.

A. Zhang, Z. Wu, E. Wu, M. Wu, M. P. Snyder, J. Zou, and J. C. Wu. Leveraging physiology and artificial intelligence to deliver advancements in health care. *Physiological Reviews*, 2023.

J. Zhu, C. Ma, Y. Zhang, H. Huang, D. Kong, and W. Ni. Multi-label diagnosis of arrhythmias based on a modified two-category cross-entropy loss function. *Electronics*, 12(24):4976, 2023.

S. J. Zieman, V. Melenovsky, and D. A. Kass. Mechanisms, pathophysiology, and therapy of arterial stiffness. *Arteriosclerosis, thrombosis, and vascular biology*, 25(5):932–943, 2005.

Scientific curriculum

Chiara Barà was born in Cefalù, Italy, on February 11, 1997. In 2016, she enrolled in the Biomedical Engineering program at the University of Palermo (Palermo, Italy), where she received a B.Sc. degree in Biomedical Engineering in July 2019. She continued her studies at the University of Palermo, where she obtained a M.Sc. degree in Biomedical Engineering (cum laude) in October 2021. Driven by her interest in the processing and analysis of physiological signals, during her master's thesis, entitled "Misure locali di informazione nei segnali elettrofisiologici per lo studio delle interazioni cuore-cervello", she investigated the application of information-theoretic measures to study physiological dynamics underlying brain-heart interactions. In March 2022, she completed a post-graduate internship of twenty days at University of Trento (Trento, Italy), and began a eight-months post-graduate research fellowship at Biosignals and Information Theory Laboratory (BITLAB), Department of Engineering, University of Palermo, during which she focused on the development and application of signal processing algorithms, which particular highlight on cardiovascular signals. In November 2022, she joined the PhD program in Information and Communication Technologies (cycle XXXVIII), under the supervision of Prof. Luca Faes, continuing her research activities within the BITLAB. Her research has primarily focused on addressing estimation challenges in the analysis of complex network dynamics using information-theoretic measures. In particular, it aims to support a hierarchical evaluation of system behavior, ranging from individual components to groupwise interactions, with a specific emphasis on physiological dynamics and organ networks. In November 2025, she began a post-graduate research fellowship at Institute of Intelligent Industrial Technologies and Systems for Advanced Manufacturing, National Research Council (Milan, Italy).

List of publications

Articles in peer-reviewed journals

1. G. Volpes, **C. Barà**, A. Busacca, S. Stivala, M. Javorka, L. Faes, R. Pernice (2022). "Feasibility of Ultra-Short-Term Analysis of Heart Rate and Systolic Arterial Pressure Variability at Rest and during Stress via Time-Domain and Entropy-Based Measures". *Sensors, 22(23), 9149.*
   doi: 10.3390/s22239149

2. L. Faes, G. Mijatovic, Y. Antonacci, R. Pernice, **C. Barà**, L. Sparacino, M. Sammartino, A. Porta, D. Marinazzo, S. Stramaglia (2022). "A New Framework for the Time- and Frequency-Domain Assessment of High-Order Interactions in Networks of Random Processes". *IEEE Transactions on Signal Processing, 70, 5766-5777.*
   doi: 10.1109/TSP.2022.3221892

3. I. Pirovano, A. Mastropietro, Y. Antonacci, **C. Barà**, E. Guanziroli, F. Molteni, L. Faes, G. Rizzo (2022). "Resting state EEG directed functional connectivity unveils changes in motor network organization in subacute stroke patients after rehabilitation". *Frontiers in Physiology, 13, 862207.*
   doi: 10.3389/fphys.2022.862207

4. M.M. Platiša, N.N. Radovanović, R. Pernice, **C. Barà**, S.U. Pavlović, L. Faes (2023). "Information-Theoretic Analysis of Cardio-Respiratory Interactions in Heart Failure Patients: Effects of Arrhythmias and Cardiac Resynchronization Therapy". *Entropy, 25(7), 1072.*
   doi: 10.3390/e25071072

5. **C. Barà**, L. Sparacino, R. Pernice, Y. Antonacci, A. Porta, D. Kugiumtzis, L. Faes (2023). "Comparison of discretization strategies for the model-free

information-theoretic assessment of short-term physiological interactions". *Chaos: An Interdisciplinary Journal of Nonlinear Science, 33(3). Editor's peak selection.*
doi: 10.1063/5.0140641

6. **C. Barà**, A. Zaccaro, Y. Antonacci, M. Dalla Riva, A. Busacca, F. Ferri, L. Faes, R. Pernice (2023). "Local and global measures of information storage for the assessment of heartbeat-evoked cortical responses". *Biomedical Signal Processing and Control, 86, 105315.*
doi: 10.1016/j.bspc.2023.105315

7. Y. Antonacci, **C. Barà**, A. Zaccaro, F. Ferri, R. Pernice, L. Faes (2023). "Time-Varying Information Measures: An Adaptive Estimation of Information Storage with Application to Brain-Heart Interactions". *Frontiers in Network Physiology, 3, 124250.*
doi: 10.3389/fnetp.2023.1242505

8. I. Pirovano, Y. Antonacci, A. Mastropietro, **C. Barà**, L. Sparacino, E. Guanziroli, F. Molteni, M. Tettamanti, L. Faes, G. Rizzo (2023). "Rehabilitation modulates high-order interactions among large-scale brain networks in subacute stroke". *IEEE Transactions on Neural Systems and Rehabilitation Engineering,31, 4549-4560.*
doi: 10.1109/TNSRE.2023.3332114

9. L. Sparacino, Y. Antonacci, **C. Barà**, A. Valenti, A. Porta, L. Faes (2023). "A method to assess Granger causality, isolation and autonomy in the time and frequency domains: theory and application to cerebrovascular variability". *IEEE Transactions on Biomedical Engineering, vol. 71, no. 5, pp. 1454-1465.*
doi: 10.1109/TBME.2023.3340011

10. L. Sparacino, Y. Antonacci, **C. Barà**, D. Švec, M. Javorka, L. Faes (2024). "A method to assess linear self-predictability of physiologic processes in the frequency domain: application to beat-to-beat variability of arterial compliance". *Frontiers in Network Physiology, 4, 1346424.*
doi: 10.3389/fnetp.2024.1346424

11. G. Volpes, S. Valenti, G. Genova, **C. Barà**, A. Parisi, L. Faes, A. Busacca, R. Pernice (2024). "Wearable Ring-Shaped Biomedical Device for Physiological Monitoring through Finger-Based Acquisition of Electrocardiographic, Photoplethysmographic, and Galvanic Skin Response Signals: Design and Preliminary Measurements". *Biosensors, 14(4), 205.*
doi: 10.3390/bios14040205

12. **C. Barà**, R. Pernice, C.A. Catania, M. Hilal, A. Porta, A. Humeau-Heurtier, L. Faes (2024). "Comparison of entropy rate measures for the evaluation of time series complexity: Simulations and application to heart rate and respiratory variability". *Biocybernetics and Biomedical Engineering, 44(2), 380-392.*

doi: 10.1016/j.bbe.2024.04.004

13. H. Pinto, I. Lazic, Y. Antonacci, R. Pernice, D. Gu, **C. Barà**, L. Faes, A.P. Rocha (2024). "Testing Dynamic Correlations and Nonlinearity in Bivariate Time Series through Information Measures and Surrogate Data Analysis". *Frontiers in Network Physiology, 4, 1385421.*
doi: 10.3389/fnetp.2024.1385421

14. Y. Antonacci, **C. Barà**, L. Sparacino, I. Pirovano, A. Mastropietro, G. Rizzo, L. Faes (2024). "Spectral Information Dynamics of Cortical Signals Uncover the Hierarchical Organization of the Human Brain's Motor Network". *IEEE Transactions on Biomedical Engineering.*
doi: 10.1109/TBME.2024.3516943

15. J.V.N. Tegnitsap, Z.T. Njitacke, **C. Barà**, T. Fonzin Fozin, H.B. Fotsin, P.A. Valdes-Sosa, N. Yoshimura, L. Minati (2025). "A van der Pol-like complementary chaotic oscillator: Design, physical realizations, dynamics, and physiological data augmentation prospect", *Chaos, Solitons & Fractals 191, 115886.*
doi: 10.1016/j.chaos.2024.115886

16. Y. Antonacci, **C. Barà**, G. De Felice, A. Sferlazza, R. Pernice, L. Faes (2025). "Exploring Transient Neurophysiological States Through Local and Time-varying Measures of Information Dynamics". *Applied Mathematics and Computation, 500, 129437.*
doi: 10.1016/j.amc.2025.129437

17. Z.T. Njitacke, J. V. N. Tegnitsap, M. Zhao, **C. Barà**, T. F. Fozin; J. Awrejcewicz, N. Yoshimura, P. A. Valdes-Sosa, C. Letellier, L. Minati (2025). "Chaotic dynamics, topological analysis and flat analog control by physiological signals of a neurally-inspired system". *Chinese Journal of Physics, 96, 20-52.*
doi: 10.1016/j.cjph.2025.04.006

18. **C. Barà**, Y. Antonacci, M. Iovino, I. Lazic, L. Faes (2025). "Partial information decomposition for mixed discrete and continuous random variables". *Physical Review E 112 (1), L012301.*
doi: 10.1103/58bg-5n9s

19. V. R. Vergara, **C. Barà**, A. Zaccaro, F. Ferri, F. Jurysta, L. Faes, Y. Antonacci (2025). "Information-theoretic analysis of EEG wave amplitude and heart rate variability reveals the time scale-dependent nature of brain-heart interactions". *IEEE Open Journal of Engineering in Medicine and Biology, vol. 6, pp. 499-506.*
doi: 10.1109/OJEMB.2025.3590598

20. H. Pinto, Y. Antonacci, **C. Barà**, R. Pernice, I. Lazic, L. Faes, A. P. Rocha (2025). "Estimating the Mutual Information Rate of Short Time Series from Coupled

Dynamic Systems". *Communications in Nonlinear Science and Numerical Simulation, 152, 109383.*
doi: 10.1016/j.cnsns.2025.109383

21. Y. Antonacci, **C. Barà**, L. Sparacino, G. Mijatovic, L. Minati, L. Faes (2025). "A Method for the Time-Frequency Analysis of High-Order Interactions in Non-Stationary Physiological Networks". *Journal Neural Engineering, 22, 066001.*
doi: 10.1088/1741-2552/ae15c0

22. D. Fruet, **C. Barà**, R. Pernice, M. Iovino, L. Faes, G. Nollo (2025). "A Signal Normalization Approach for Robust Driving Stress Assessment Using Multi-Domain Physiological Data". *Eng 6, no. 11: 288.*
doi: 10.3390/eng6110288

23. I. Lazic, **C. Barà**, M. Iovino, S. Stramaglia, K. Kasas-Lazetic, N. Jakovljevic, L. Faes (2025). "Information-theoretic Quantification of High-order Feature Effects in Classification Problems". *Chaos Solitons and Fractals, 204, 117724.*
doi: 10.1016/j.chaos.2025.117724

24. M. Ontivero-Ortega, M. Iovino, R. Pernice, **C. Barà**, M, Javorka, L. Faes, S. Stramaglia (2025). "Assessment of Sex-Related Differences in Cardiovascular Control using High-Order Feature Importance". *The European Physical Journal Special Topics, 1-12.*
doi: 10.1140/epjs/s11734-025-02076-y

25. L. Sparacino, H. Pinto, **C. Barà**, Y. Antonacci, R. Pernice, A.P. Rocha, L. Faes (2025). "Quantifying Coupling and Causality in Bivariate Systems: a Unified Framework for Time, Frequency, and Information-Theoretic Analysis". *Frontiers in Network Physiology, 5, 1687132.*
doi: 10.3389/fnetp.2025.1687132

26. **C. Barà**, L. Sparacino, L. Faes, M. Javorka (2025). "Direct causality measures unravel complex networks of cardiovascular oscillations and their modifications with postural stress". *PLOS Computational Biology 22(3): e1014075.*
doi: 10.1371/journal.pcbi.1014075

27. M. Iovino, I. Lazic, **C. Barà**, D. Kugiumtzis, L. Faes, R. Pernice (2026). "A Principled and Data-Efficient Information-Theoretic Method for Feature Selection". *IEEE Journal of Biomedical and Health Informatics.*
doi: 10.1109/JBHI.2026.3679377

28. R. Saputo, **C. Barà**, I. Franzone, M. Javorka, R. Pernice, L. Faes (2026). "Partial Decomposition of Information Dynamics Elicits Unique and Shared Modes of Cardiovascular and Cardiorespiratory Control in Response to Autonomic Stressors". *The European Physical Journal Special Topics, 1-21.*
doi: 10.1140/epjs/s11734-026-02270-6

29. **C. Barà**, Y. Antonacci, H. Pinto, L. Sparacino, M. Javorka, S. Stramaglia, L. Faes (2026). "Investigating High-Order Behaviors in Multivariate Cardiovascular Interactions via Nonlinear Prediction and Information-Theoretic Tools". *IEEE Transactions on Biomedical Engineering*.
doi: 10.1109/TBME.2026.3689598

Submitted

30. **C. Barà**, Y. Antonacci, L. Sparacino, A.A. Gonzalez, M. Zhao, L. Fu, P. Valdes-Sosa, H. Ito, M. Frasca, L. Faes, L. Minati (2025). "Redundant and synergistic interactions in a complex network of single-transistor electronic chaotic oscillators and in neurophysiological recordings". *Submitted to Chaos.*
doi: 10.48550/arXiv.2512.13570
31. S. Cimignolo, **C. Barà**, R. Pernice, L. Faes, G. Nollo, M. Masè (2025). "A Framework Based on Information Dynamics to Assess and Dissect Complex Cardiovascular Interactions Across Pathophysiological States". *Submitted to Biocybernetics and Biomedical Engineering.*
32. H. Pinto, C. Dias, V.R. Vergara, **C. Barà**, R. Pernice, A. P. Rocha, L. Faes, Y. Antonacci (2026). "Time–Frequency Linear Interdependence Measures Reveal Multivariate Patterns of Cerebrovascular–Autonomic Interactions in Traumatic Brain Injury". *Submitted to Biomedical Signal Processing and Control.*

Conference proceedings

1. **C. Barà**, R. Pernice, L. Sparacino, M. Javorka, L. Faes (2022). "Transfer Entropy Analysis of Pulse Arrival Time - Heart Period Interactions during Physiological Stress". *12th conference of the European Study Group on Cardiovascular Oscillation (ESGCO).*
2. Y. Antonacci, **C. Barà**, A. Zaccaro, M. Dalla Riva, M. Pavone, F. Ferri, L. Faes (2022). "Investigating the Heartbeat-evoked cortical responses through Time-Varying Information Measures based on adaptive Autoregressive Models". *12th conference of the European Study Group on Cardiovascular Oscillation (ESGCO).*
3. R. Pernice, I. Lazic, **C. Barà**, L. Sparacino, L. Faes (2022). "Assessment of Cardiorespiratory Interactions during Control Breathing: non-liner model-free analysis". *12th conference of the European Study Group on Cardiovascular Oscillation (ESGCO).*
4. R. Pernice, L. Sparacino, **C. Barà**, S. Mangione, L. Faes (2022). "Assessment

of Cardiorespiratory Interactions during Control Breathing: linear parametric analysis". *12th conference of the European Study Group on Cardiovascular Oscillation (ESGCO)*.

5. G. Volpes, **C. Barà**, S. Valenti, M. Javorka, A. Busacca, L. Faes, R. Pernice. (2022). "Feasibility of Ultra-short Term Complexity Analysis of Heart Rate Variability in Resting State and During Orthostatic Stress". *12th conference of the European Study Group on Cardiovascular Oscillation (ESGCO)*.
6. L. Sparacino, R. Pernice, **C. Barà**, M. Javorka, D. Švec, L. Faes (2022). "Spectral analysis of beat-to-beat variability of arterial compliance". *12th conference of the European Study Group on Cardiovascular Oscillation (ESGCO)*.
7. G. Mijatovic, **C. Barà**, R. Pernice, T. Loncar-Turukalo, G. Nollo, L. Faes (2023). "Exploring the Short-Term Memory of Heart Rate Variability through Model-Free Information Measures". *45th Annual International Conference of the IEEE Engineering in Medicine and Biology Society (EMBC).*
8. H. Pinto, Y. Antonacci, R. Pernice, **C. Barà**, M. Javorka, L. Faes, A.P. Rocha (2023). "Decomposing the Mutual Information Rate of Heart Period and Respiration Variability Series to Assess Cardiorespiratory Interactions". *45th Annual International Conference of the IEEE Engineering in Medicine and Biology Society (EMBC).*
9. L. Faes, R. Pernice, **C. Barà**, Y. Antonacci (2023). "Mutual Information Rate Decomposition as a Tool to Investigate Coupled Dynamical Systems: Estimation Approaches, Simulations and Application to Physiological Signals". *XLIII Dynamics Days Europe 2023.*
10. **C. Barà**, R. Pernice, L. Sparacino, Y. Antonacci, M. Javorka, L. Faes (2023). "Comparison of Linear Model-Based and Nonlinear Model-Free Directional Coupling Measures: Analysis of Cardiovascular and Cardiorespiratory Interactions at Rest and During Physiological Stress". *16th Mediterranean Conference on Medical and Biological Engineering and Computing (MEDICON) and the 5th International Conference on Medical and Biological engineering (CMBEBIH).*
11. V.R. Vergara, **C. Barà**, R. Pernice, A. Zaccaro, F. Ferri, L. Faes, Y. Antonacci (2023). "Exploring the Predictability of EEG Signals Timed with the Heartbeat: A Model-Based Approach for the Temporal and Spatial Characterization of the Brain Dynamics". *16th Mediterranean Conference on Medical and Biological Engineering and Computing (MEDICON) and the 5th International Conference on Medical and Biological engineering (CMBEBIH).*
12. R. Pernice, **C. Barà**, Y. Antonacci, L. Faes (2024). "Assessment of complexity and dynamical coupling between complex system using Entropy Rate and Mutual Information Rate Measures: simulations and application to physiolog-

ical data". *Book of Abstracts of AMS-UNI International Joint Meeting 2024.*

13. **C. Barà**, Y. Antonacci, M. Javorka, L. Faes (2024). "An Approach to Decompose the Information Shared between Cardiovascular and Respiratory Physiological Systems". *51st international Computing in Cardiology (CinC) conference.*

14. **C. Barà**, Y. Antonacci, M. Javorka, L. Faes (2024). "Role of Arterial Pressure Changes on the Time-Lagged Baroreflex Response". *13th Conference of the European Study Group on Cardiovascular Oscillations (ESGCO).*

15. S. Castelbuono, **C. Barà**, R. Pernice, L. Faes, D. Bellavia (2024). "Ultra-Short-Term Heart Rate Variability of Home-Monitored Heart Failure Patients: a Case Study". *13th Conference of the European Study Group on Cardiovascular Oscillations (ESGCO).*

16. V.R. Vergara, **C. Barà**, F. Jurysta, L. Faes, Y. Antonacci (2024). "Investigating Dynamic Brain-Heart Interactions during sleep with Information-Theoretic Measures". *13th Conference of the European Study Group on Cardiovascular Oscillations (ESGCO).*

17. M. Iovino, I. Lazic, **C. Barà**, L. Faes, R. Pernice (2024). "Conditional Mutual Information-based Feature Selection for Sex Differences Characterization". *13th Conference of the European Study Group on Cardiovascular Oscillations (ESGCO).*

18. H. Pinto, C. Dias, **C. Barà**, Y. Antonacci, L. Faes, A.P. Rocha (2025). "Exploring the Mutual Information Rate Decomposition in Situations of Pathological Stress". *International Conference on Congress of the Portuguese Statistical Society.*

19. S. Lombardi, R. Pernice, **C. Barà**, L. Curcio, A. Busacca, L. Bocchi (2025). "Impact of Acquisition Conditions on PPG Signal Characteristics: A Mathematical Modelling Approach". *IX Congress of the National Group of Bioengineering (GNB).*

20. S. Cimignolo, **C. Barà**, R. Pernice, M. Masè, G. Nollo, L. Faes (2025). "Assessment of cardiovascular coupling during rest and postural stress using Mutual Information Rate". *IX Congress of the National Group of Bioengineering (GNB).*

21. V. R. Vergara, **C. Barà**, I. Franzone, A. Zaccaro, F. Ferri, L. Faes, Y. Antonacci (2025). "A Statistical Framework for the Analysis of Heartbeat-Evoked Brain Potentials". *IX Congress of the National Group of Bioengineering (GNB).*

22. G. Genova, **C. Barà**, M. Iovino, G. Chiarello, R. Pernice, A. Parisi, G.C. Giaconia, F. Ficuciello, C. Iacono, A. Smaldone, R. La Rocca, A. Busacca, S. Stivala (2025). "Design of a non-invasive multiparametric biomedical device for surgeon monitoring during robotic-aided procedures". *IX Congress of the National Group of Bioengineering (GNB).*

23. **C. Barà**, Y. Antonacci, L. Sparacino, S. Stramaglia, L. Faes (2025). "Investigating High-Order Interactions among Physiological Variables using Predictability and Information-Theoretic Measures". *47th Annual International Conference of the IEEE Engineering in Medicine and Biology Society (EMBC).*
24. L. Sparacino, R. Pernice, **C. Barà**, R. Saputo, M. Javorka, L. Faes (2025). "The effect of systolic and diastolic arterial pressures on mean arterial pressure: a partial information decomposition strategy". *47th Annual International Conference of the IEEE Engineering in Medicine and Biology Society (EMBC).*
25. M. Iovino, M. Ontivero-Ortega, **C. Barà**, S. Stramaglia, M. Javorka, R. Pernice, L. Faes (2025). "Assessing Feature Importance in Cardiovascular Variability for the Classification of Physiological Stress". *IEEE International Conference on Omni-layer Intelligent systems (IEEE COINS).*
26. L. Sparacino, **C. Barà**, Y. Antonacci, M. Javorka, L. Faes (2025). "Decomposition of the dynamic information shared in complex networks of physiological variables". *52th international Computing in Cardiology (CinC) conference.*

Submitted

27. **C. Barà**, Y. Antonacci, M. Lavit Nicora, C. Zanco, M. Mondellini, M. Malosio, G. Tauro, G. Rizzo, A. Mastropietro (2026). "Time-Resolved Assessment of Brain and Cardiac Activity during Robot-Assisted Movements". *5th IEEE International Conference on Metrology for eXtended Reality, Artificial Intelligence and Neural Engineering (MetroXRAINE)*.
28. **C. Barà**, V.R. Vergara, Y. Antonacci, M. Mondellini, M. Lavit Nicora, G. Rizzo, L. Faes, A. Mastropietro (2026). "Regulatory brain-body networks underlying different levels of robot-assisted movements". *14th Conference of the European Study Group on Cardiovascular Oscillations (ESGCO)*.

Acknowledgements

The research presented in this thesis was carried out in the *Biosignals and Information Theory Laboratory (BITLAB)* in the Department of Engineering, University of Palermo, Palermo (Italy), under the supervision of Prof. Luca Faes, to whom I am deeply grateful for sharing his knowledge and expertise, and for helping me appreciate the importance and beauty of research. I would also like to extend my heartfelt thanks to the senior researchers of the laboratory, Dr. Riccardo Pernice and Dr. Yuri Antonacci, for the valuable scientific insights and moral support they provided throughout my three years of doctoral studies. Moreover, I am sincerely grateful to all my colleagues, who made this journey both stimulating and rewarding. From a scientific perspective, our continuous discussions and interactions greatly enriched my work; on a personal level, they contributed to creating a pleasant and supportive environment. For this reason, I would like to thank Valeria, Roberta, Marta, Irene, Anna, Hélder, Salvatore C., Salvatore S., Gabriele, Simone, and Giuseppe, and especially Laura, who shared this journey with me from the very beginning and with whom I experienced many wonderful scientific adventures.

Established and newly formed research collaborations were fundamental to the development of this work, as they provided access to the investigated datasets and offered valuable methodological and interpretative contributions. First, I would like to thank the people supporting me during the periods I spent in foreign academic institutions. I am particularly grateful to Prof. Michal Javorka of the *Department of Physiology, Comenius University, Jessenius Faculty of Medicine, Martin (Slovakia)*, for his insightful guidance on clinical and research questions related to cardiovascular dynamics, for his great contribution to the physiological interpretation of many of the results presented in this thesis, as well as for providing a dataset extensively analyzed in this work. I also wish to thank Ivan Lažić, with whom I closely collaborated during my time at the *Faculty of Technical Sciences, University of Novi Sad*

(Serbia), and the Prof. Ludovico Minati, who gave me the opportunity to broader my knowledge in fields beyond physiological applications during my stay at the *University of Electronic Science and Technology of China (UESTC), Chengdu (Cina)*. In addition, I would like to thank Prof. Alberto Porta from the *Laboratorio di Modellistica di Sistemi Complessi, IRCCS Policlinico San Donato, San Donato Milanese, Milano (Italy)*, Prof. Giandomenico Nollo from the *University of Trento, Trento (Italy)*, Prof. Francesca Ferri from the *Department of Neuroscience, Imaging and Clinical Sciences, University of Chieti-Pescara, Chieti (Italy)*, Giovanna Rizzo from the *Institute of Intelligent Industrial Technologies and Systems for Advanced Manufacturing*, *National Research Council, Milan (Italy)*, and Prof. Przemyslaw Guzik from the *Poznan University of Medical Sciences, Poznan (Poland)*, for providing datasets that were instrumental for the analyses conducted during my research.